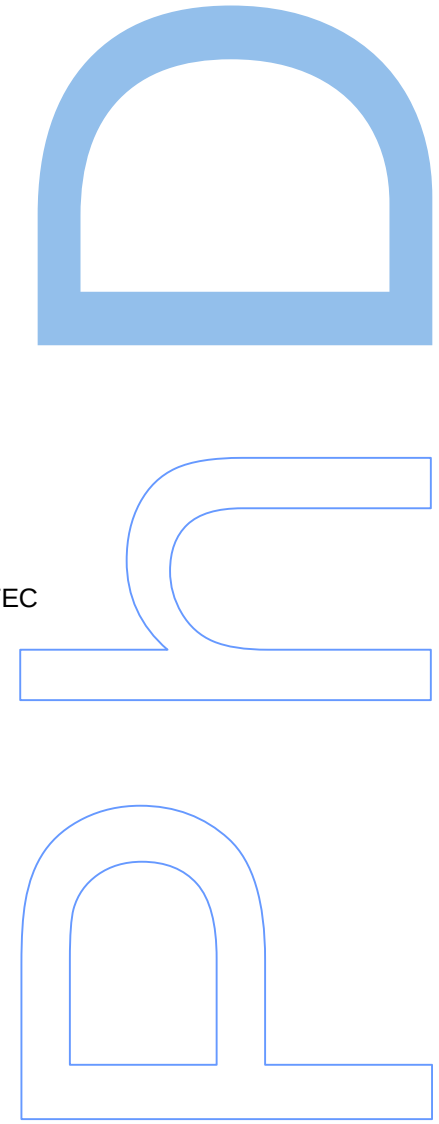
Fabrication and characterization of spin torque vortex oscillators

Leandro Jorge Ferreira Martins
Doutoramento em Física
Departamento de Física e Astronomia
2022

Orientador
Dr. Ricardo Ferreira, Líder do grupo de Spintrónica do INL

Coorientadores
Dr. João Ventura, Investigador principal e vice presidente do IFIMUP e CEMUP-MNTEC
Dr. Paulo Freitas, Vice-diretor do INL e líder do grupo de Nanodispositivos



Agradecimentos

Se me pedissem para descrever o meu percurso doutoral numa frase, seria sem dúvida "correr na areia". De facto, não há melhor analogia para estes pequenos avanços conseguidos com um enorme esforço. O doutoramento é ótimo para uma pessoa perceber as suas limitações, mas também para se congratular com aquilo que é possível atingir quando a tendência para se desistir à primeira é posta de parte. Quanto tempo fora de horas passado na sala limpa (em dezembro de 2019, depois do jantar de Natal do INL, ainda houve tempo de madrugada para progredir na VPW24); quantas idas ao INL depois de jantar para garantir que uma noite de simulações não é desperdiçada; quantos dias desesperado por não ter "resultados de jeito". Mas no fim, a nossa contribuição fica sempre clarificada, o que só pode ser um motivo de orgulho.

Alex Jenkins was my shadow supervisor. He is a great guy with a tremendous sense of humour. His random singing is always a treat ("tell me lies, tell me sweet little lies"). I would like to thank him for his kindness and patience put in my learning process. Most of my simulations and lab skills are due to him.

Uma palavra também para o Ricardo Ferreira, o meu orientador principal. É um prazer enorme ter um supervisor que, mesmo nos momentos mais atarefados e difíceis (ou seja, quase sempre), conseguia encontrar tempo para vir à minha secretária e, com toda a amabilidade, clarificar as minhas dúvidas. Sempre apreciei a capacidade do Ricardo de colocar as pessoas à vontade. É uma sorte ter tido um orientador principal com tanto conhecimento da área e, ao mesmo tempo, tão gentil.

Também para o meu orientador João Ventura, um agradecimento forte pela sua disposição em ajudar-me, sempre o mais rápido possível. Sem ele, não teria sido possível esta oportunidade de trabalhar numa parceria entre o IFIMUP e o INL.

Gostaria de agradecer a todos os meus colegas do INL pelos ótimos momentos passados nos últimos quatro anos, tal como pelo apoio prestado. Também à Fundação para a Ciência e a Tecnologia é devido um reconhecimento pelo financiamento proporcionado durante o meu doutoramento (SFRH/BD/128833/2017).

Um reconhecimento à minha família (aos três anjos e aos que ainda cá estão) pelo esforço enorme que fizeram para que eu aqui chegasse - nada paga essa dedicação! À Thaís por (qual Lupin!) me ter dado sempre um chocolate nos momentos mais difíceis.

Abstract

This thesis comprises the fabrication and characterization of MgO-based magnetic tunnel junctions (MTJs) working as spin torque vortex oscillators (STVOs). The research was developed at the International Iberian Nanotechnology Laboratory (INL) in Braga, as the result of a partnership between the latter and the Institute of Physics for Advanced Materials, Nanotechnology and Photonics (IFIMUP) from the University of Porto. This work aims to be a relevant contribution for a better understanding of such devices, showing their limitations and possible solutions to surpass them and, at the same time, showing their potential to become an efficient class of spintronic hardware in the future.

It is demonstrated that STVOs working as rectifiers show a different detection (i.e. DC voltage) depending on the chirality of the vortex magnetic state induced in the MTJ free layer. Based on this behaviour, it is proposed to use such devices as non-volatile artificial synapses, whose weight can be switched in a binary and non-volatile scheme simply by changing the vortex chirality that is stable at remanence. The physical origin of this phenomenon is clarified by micromagnetic simulations showing that the break of symmetry is caused by the radial Oersted field (created by the input RF signal) that promotes the free layer dynamics for a sufficiently large vortex core displacement, relative to its central position.

Still with rectification measurements, it is demonstrated how the polycrystalline structure of the STVO affects its static and dynamic properties. In particular, the focus goes to the behaviour of the vortex in the free layer. It is shown that for sufficiently low power excitations (roughly $\mathrm{P_{RF}} < 10\,\mu\mathrm{W}$, being $\mathrm{P_{RF}}$ the power of the RF input signal), the vortex shows a local gyrotropic mode, characterized by a low amplitude ($\sim 1\,\mu\mathrm{V}$) and high frequency ($\sim 1\,\mathrm{GHz}$) oscillation of the vortex core, dictated by local pinning sites created by the polycrystalline structure. So, as $\mathrm{P_{RF}}$ increases, it is possible to define a threshold power, above which the vortex core is capable of escaping from the pinning site, thus starting to oscillate at the high amplitude ($\sim 1\,\mathrm{mV}$) and low frequency ($\sim 100\,\mathrm{MHz}$) collective mode, this time dictated by the properties (e.g. aspect ratio, saturation magnetization) of the free layer as a whole.

Important results are also presented for the synchronization of a pair of STVOs working as RF sources. In this context, a new patterning process is developed for the fabrication of adjacent pairs of STVOs with an edge-to-edge distance ($\mathrm{d_{ee}}$) down to 100 nm and with independent top contacts. Experimentally, this new design gives more flexibility to evaluate the synchronization via magneto-dipolar coupling, since the DC bias current can be individually controlled, while having a simultaneous access to the dynamics of each individual STVO. Both frequency and time domain measurements confirm a successful synchronization for a pair of STVOs with $\mathrm{d_{ee}} = 100\,\mathrm{nm}$, characterized by a phase difference expected for two non-identical STVOs.

Finally, a new fabrication process is successfully implemented for the patterning of STVOs on top of 300 nm-thick oxide membranes. The objective is to obtain a transparent substrate below each STVO nanopillar, so that it is possible to obtain devices ready to be probed by scanning transmission X-ray microscopy (STXM), with particular focus in the behaviour of the free layer vortex state. This process comprises, not only the standard patterning of the frontside MTJ devices, but also the microfabrication of the oxide membranes on the backside of the silicon substrate. The membrane design allows a nominal maximum angle of 45° between the X-ray propagation direction and the direction perpendicular to the substrate surface, thus giving the STXM the possibility to be sensible to the in-plane vortex magnetization. The uniformity of the backside process is limited, so at the wafer level, the process shows an open membranes yield of $\sim$ 50%.

Keywords: magnetic tunnel junction, spin torque vortex oscillator, chirality, non-volatile synapse, local and collective gyrotropic modes, independent top contacts, magneto-dipolar coupling, synchronization.

Resumo

Esta tese inclui a fabricação e a caracterização de junções magnéticas de efeito túnel (MTJs) funcionando como osciladores por transferência de spin com vórtice (STVOs). Esta investigação foi desenvolvida no Laboratório Ibérico e Internacional de Nanotecnologia (INL) em Braga, como resultado de uma parceria entre o último e o Instituto de Física de Materiais Avançados, Nanotecnologia e Fotónica (IFIMUP) da Universidade do Porto. Este trabalho pretende ser um contributo relevante para melhorar a compreensão deste tipo de dispositivos, mostrando as suas limitações e possíveis soluções para as ultrapassar e, ao mesmo tempo, mostrar o seu potencial para serem no futuro uma nova classe de hardware eficiente.

Para STVOs funcionando como retificadores, é demonstrado que a sua detecção (ou seja, a tensão contínua de saída) é diferente dependendo da quiralidade do vórtice magnético induzido na camada livre da MTJ. Baseado neste comportamento, propõe-se o uso destes dispositivos como sinapses artificiais não-voláteis, cujo peso pode ser comutado de uma maneira binária e não-volátil, simplesmente mudando a quiralidade do vórtice que é estável no estado remanente. A origem física deste fenómeno é clarificada a partir de simulações micromagnéticas, de onde se conclui que a quebra de simetria é causada pelo campo radial de Oersted (criado pelo sinal RF de entrada) que promove a dinâmica na camada livre quando o deslocamento do núcleo do vórtice é suficientemente alto, relativamente à sua posição central.

Ainda com medidas de retificação, é demonstrada a maneira como a estrutura policristalina do STVO afeta as suas propriedades estáticas e dinâmicas. Especificamente, o foco vai para o comportamento do vórtice na camada livre. É mostrado que, para uma potência de excitação suficientemente baixa (aproximadamente, $\mathrm{P_{RF}} < 10\,\mu\mathrm{W}$, sendo $\mathrm{P_{RF}}$ a potência do sinal RF de entrada), o vórtice apresenta um modo girotrópico local, caracterizado por uma oscilação do seu núcleo com uma baixa amplitude ($\sim 1\,\mu\mathrm{V}$) e alta frequência ($\sim 1\,\mathrm{GHz}$), imposto por locais de fixação criados pela estrutura policristalina. Portanto, aumentando $\mathrm{P_{RF}}$, é possível definir uma potência limite, acima da qual o núcleo do vórtice é capaz de escapar do ponto de fixação, desta maneira passando a oscilar a uma alta amplitude ($\sim 1\,\mathrm{mV}$) e a uma baixa frequência ($\sim 100\,\mathrm{MHz}$), de acordo com um modo colétivo, desta vez imposto pelas propriedades (por exemplo, a proporção das dimensões ou a magnetização de saturação) da camada livre como um todo.

Também foram obtidos resultados importantes relativamente à sincronização de pares de STVOs funcionando como fontes de sinais RF. Neste contexto, um novo processo de padronização foi desenvolvido para a fabricação de pares adjacentes de STVOs com uma distância entre pilares ($\mathrm{d_{ee}}$) tão baixa quanto 100 nm e apresentando contactos eléctricos independentes. Experimentalmente, este novo design possibilita uma maior flexibilidade para uma sincronização via acoplamento magnético

dipolar, uma vez que a corrente elétrica pode ser controlada individualmente enquanto se tem acesso simultâneo à dinâmica de cada STVO. Ambos as medições no domínio da frequência e do tempo confirmam o sucesso da sincronização para um par de STVOs com $\mathrm{d_{ee}} = 100\,\mathrm{nm}$, caracterizada por uma diferença de fase esperada para dois STVOs não-idênticos.

Finalmente, um novo processo de fabricação foi implementado para a padronização de STVOs sustentados em membranas de óxido com uma espessura de 300 nm. O objectivo é obter um substrato transparente abaixo de cada nanopilar, de forma a que se obtenham dispositivos prontos a serem examinados por microscopia de raios X, com particular foco no comportamento do vórtice na camada livre. Este processo compreende, não só a fabricação padrão dos STVOs na parte da frente do substrato, mas também a microfabricação das membranas de óxido na parte de trás do substrato de silício. O design da membrana possibilita um ângulo máximo nominal de 45° entre o direção de propagação dos raios X e a direção perpendicular à superfície do substrato, desta maneira dando a possibilidade à microscopia de ser sensível à componente planar da magnetização do vórtice. A uniformidade do processo no lado de trás é limitada, portanto, ao nível do substrato completo, o processo mostra um rendimento de $\sim$50% de STVOs com membranas abertas.

Palavras-chave: junção magnética de efeito túnel, oscilador por transferência de spin com vórtice, quiralidade, sinapse não-volátil, modos girotrópicos locais e colétivos, contactos elétricos independentes, acoplamento magnético dipolar, sincronização.

Thesis structure

This thesis describes the fabrication and characterization of vortex-based magnetic tunnel junctions (MTJs), targeting a wide range of applications.

Chapter 1 is a simple theoretical description that gives the context of this thesis and the Physics required to understand the work presented after. It includes a short introduction to the Spintronics field, but its focus goes to two distinct phenomena verified in MTJs: the tunnel magnetoresistance (TMR) and the spin-transfer torque (STT) effect.

Chapter 2 describes the main experimental techniques used at INL for the fabrication and characterization of vortex-based magnetic tunnel junctions.

Chapter 3 explains in detail the cleanroom-based process performed to deposit and pattern the different MTJ devices characterized in this thesis.

Chapter 4 proposes that an MTJ working as a rectifier can be used as an artificial non-volatile synapse. This conclusion is taken based on the different detections measured for distinct vortex chiralities. The physical understanding of the experimental data was achieved by micromagnetic simulations, leading to the radial Oersted field created by the input RF signal as the responsible for the non-volatile phenomenon.

Chapter 5 shows that the polycrystalline structure of the MTJ free layer can change significantly the static and dynamic behaviour of the vortex. As in chapter 4, the dynamic results were obtained from the rectification capabilities of the MTJs. By sweeping the power of the input RF signal, it is possible to make a distinction between a local and a collective mode associated with vortex oscillations at different frequencies and different amplitudes.

Chapter 6 presents a new nanofabrication design that was successfully used to synchronize a pair of MTJs via magneto-dipolar coupling. This new design allows the fabrication of MTJ nanopillars with an edge-to-edge distance down to 100 nm and with independent top contacts, meaning that the dynamics of each MTJ can be individually manipulated for a flexible synchronization.

Chapter 7 describes a new fabrication process performed at INL for the patterning of MTJs on top of 300 nm-thick oxide membranes. In addition to the standard frontside process, the method involves a microfabrication process of the backside of the substrate. In the end, the objective is to obtain MTJs with a transparent oxide substrate, suitable for vortex imaging by transmission X-ray microscopy.

Chapter 8 enumerates the main conclusions that can be drawn from the work performed in this thesis. Possible solutions to continue this research in the future are also presented.

List of Figures

1.1 Schematic illustration of electron tunneling in an MTJ. (a) The magnetizations of the FM layers are parallel (low resistance state). (b) The magnetizations are anti-parallel (large resistance state). $\mathrm{D_{i\uparrow}}$ and $\mathrm{D_{i\downarrow}}$ represent the density of electronic states at the Fermi level for the two spin-states at the electrode i (i = 1, 2). 26

1.2 Relevant atomic orbitals for 3d metals, organized by symmetry groups. 28

1.3 Schematic representations of electron tunneling through (a) an amorphous $\mathrm{AlO_x}$ and (b) a crystalline MgO(001) barrier. 29

1.4 Tunneling DOS ($\mathrm{k_{||}} = 0$) for the possible coupling symmetries across an epitaxial Fe(001) / MgO(001) / Fe(001) MTJ. The black arrows denote the magnetization direction at each FM layer. 30

1.5 Cross-sectional TEM images obtained before and after the annealing of CoFeB / MgO / CoFeB MTJs. 31

1.6 TMR ratio for a CoFeB/MgO/CoFeB-based MTJ as a function of the RA product at room temperature. 32

1.7 (a) General bottom-pinned MTJ stack used in this thesis. (b) Typical VSM loop obtained for an unpatterned MTJ. The arrows represent the direction of the magnetization of each FM layer at different stages of the loop. 33

1.8 Illustration of the STT principle. The electrons travel (a) from the reference to the free layer, favouring the parallel configuration and (b) from the free to the reference layer, favouring the anti-parallel configuration. Below each MTJ illustration the dynamics of $\mathbf{M_{free}}$ is highlighted based on Eq. (1.11). 34

1.9 Possible combinations for a remanent vortex state based on its two main properties: chirality (C) and polarity (P). A positive chirality (+C) denotes a clockwise circulation of the magnetic moments, whereas a positive polarity (+P) is associated with magnetic moments at the vortex core pointing in the positive out-of-plane direction (i.e. white dot at the core region). Vice-versa for -C and -P. 36

1.10 (a) Magnetic phase diagram of a patterned FM layer, where the radius (R) and the thickness (L) are normalized to the exchange length $\mathrm{L_E} = 18\,\mathrm{nm}$, obtained from calculations. The red area highlights a metastable region. (b) Magnetic phase diagram obtained from patterned MTJs at INL ($\mathrm{L_E} = 5\mathrm{nm}$). 37

1.11 Illustration of the different forces acting on the vortex core during gyrotropic dynamics induced by a spin-polarized current with in-plane ($p_{x,y}$) and out-of-plane (p_z) components. The forces are represented based on the assumption of a uniform polarizer. . . . 38
1.12 (a) Power spectral density (PSD) measured as a function of the frequency and DC current applied through an MTJ with a nominal diameter of 300 nm. The measurement is performed when the vortex of the free layer has a negative (top) and a positive (bottom) chirality at zero field. The MTJ stack is also described on top, where the thickness is presented in nanometers. (b) Illustration of the experimental setup. 40
1.13 Amplitude of the steady-state oscillation (average value of the magnetization component in the xx axis) presented as a function of the applied DC bias current density. The free layer is simulated as a circular nanodisk with a vortex magnetic state, a diameter of 300 nm and a thickness of 9.0 nm. The inset shows the magnetic configuration of the non-uniform polariser. The simulations were performed at zero perpendicular field. . 41

2.1 Illustration of the magnetron sputtering principle. The purple region below the target represents the plasma ignition. The non-static substrate configuration is in accordance with the sputtering systems used at INL. 43
2.2 (a) Simple illustration of the 10 cathodes configuration in the UHV deposition chamber of MTM. The green arrow indicates the dynamic deposition with a non-static substrate. (b) Image inside the UHV chamber of the MTM selectable target and the corresponding grounded shield. As a consequence of the magnetron configuration, the target wear is not uniform. (c) Illustration of the three linearly disposed cathodes configuration in the UHV deposition chamber of FTM. 44
2.3 Thickness of an FeB layer and substrate velocity as a function of the wafer position along the notch. 46
2.4 Uniformity measurement of a Ru layer deposited by MTM in a 200 mm Si oxidized wafer. The data was obtained by measuring the sheet resistance over the Ru surface. The map comprises an area with a diameter larger than 154.2 mm (i.e. larger than 6 inches). 47
2.5 General illustration of the deposition chamber of a PECVD system. Insulation parts are represented in yellow. 47
2.6 Illustration of the Nordiko 7500 ion beam gun, along with both neutralizers and the rotary table. Insulation parts are represented in yellow. 49
2.7 Working module of the Nordiko 7500. The ion beam gun is embedded in the chamber door. The rotary table is placed in a 90° position between the sample surface and the ion beam. 50
2.8 (a) SIMS data obtained from a nanopillar definition process. The milling aims to etch the sample until the bottom contact (i.e. buffer structure below the MTJ). The Cu peaks are not shown in order to highlight the lower W and Ru peak signals. (b) Illustration of the sample stack after definition (thickness in nanometers). The TiWN layers can be recognized by the W signal and the CuN by the Cu signal. The milling definition was stopped at the third Ru peak, which corresponds to the middle Ru layer of the buffer. Starting from the bottom, the MTJ corresponds to the AFM / SAF / insulating barrier / free layer structure. 52

2.9 Etching fabrication. (a) After coating and according to the design, the polymer mask is set on the sample. (b) An etching technique is performed, removing both the exposed material and the polymer. (c) A strip technique allows to completely remove the polymer, thus obtaining the desired pattern in the sample. 53
2.10 Microfabrication step by DWL lithography. (a) The material to pattern is coated with PR. (b) The laser exposure is performed according to the digital mask. (c) Considering a positive PR, the development leads to the removal of the exposed region. (d) The ion milling process removes the material where the PR was removed. (e) Finally, a PR strip (plasma asher or acetone bath) allows to make a complete removal of the PR, thus obtaining the desired pattern in the material. 55
2.11 SEM top view images of circular 600 nm test structures, obtained after development for two different e-beam doses. 57
2.12 (a) Top view of a standard 0.5 cm^2 substrate used for VSM measurements. By definition, the annealing is always performed to define the easy axis in the 0° direction. (b) VSM measurements obtained at the easy axis for a Ta(10) / $\mathrm{CoFe_{40}B_{20}}$(2.0) / MgO(7.9 $\Omega\mu m^2$) / Ta(10) / Ru(7) nanostructure, before and after two different annealing conditions. (c) VSM measurements obtained for a Ta(5) / CuN(50) / Ta(5) / CuN(50) / Ta(5) / Ru(5) / IrMn(6) / $\mathrm{CoFe_{30}}$(2.0) / Ru(0.7) / $\mathrm{CoFe_{40}B_{20}}$(2.6) / MgO(9 $\mathrm{k\Omega\mu m^2}$) / $\mathrm{CoFe_{40}B_{20}}$(2.0) / Ta(5) / Ru(10) MTJ, before and after annealing. The sample was annealed at 330 °C for 2 h, with an applied field of 1 T. 58
2.13 Data obtained from the standard recipe used in this thesis. The plot shows the temperature as a function of time. 59
2.14 (a) Illustration of the OPM Nanocalc setup, measuring the thickness of a $\mathrm{SiO_2}$ layer. (b) XY stage of the Nanocalc setup placed at the INL cleanroom. (c) Nanocalc measurement of a 3μm $\mathrm{SiO_2}$ layer. The reflectance of the sample as a function of the light wavelength is depicted by the black curve. The red curve represents the fit performed by the software from which the thickness is extracted. 60
2.15 (a) Overview of the VSM setup at INL. (b) Amplified view showing the vertical insertion of the sample holder between the pick-up coils. Although covered by the pick-up coils, a Hall probe is also present to measure the magnetic field of the electromagnets. 61
2.16 VSM measurement performed in a nanostructure with a magnetic layer of FeB, whose stack is presented in Table 2.7. The magnetic moment (m) is presented as a function of the in-plane magnetic field (H). The thickness of FeB and the area of the sample are used to calculate the magnetization presented in Table 2.7. 62
2.17 Illustration of CIPT measurements, representing the two probe spacing limits. (a) The probes are too close, so the current flows only through the top FM layer. (b) The large probe spacing creates a parallel current propagation through both FM layers. 63
2.18 Setup of the CIPT tester at INL. On the right side, there is a zoom in at the cantilevers region. 63

2.19 Experimental data obtained using the CIPT method and respective fit to the theory based on the analytical solution of Eq. (2.12). $\mathrm{R_{sq}}$ refers to the MTJ sheet resistance in the parallel configuration and $\mathrm{MR_{cip}}$ is the current in-plane magnetoresistance measured as a function of the probe spacing. In this specific measurement, from the fit results $\mathrm{RA} = 1.63\,\Omega\mu\mathrm{m}^2$, $\mathrm{TMR} = 98.04\,\%$, $\mathrm{R_T} = 1.13\,\Omega$, $\mathrm{R_B} = 0.28\,\Omega$ and $\lambda = 1.075\,\mu\mathrm{m}$. 64
2.20 Illustration of the setup for measurements at the probe station. 65
2.21 (a) TMR ratio a function of the RA product obtained for a set of 379 nanopillars with a nominal diameter of 375 nm. (b) Example of a transfer curve obtained from one of those devices and from which the magnetoresistive parameters are calculated. 65
2.22 (a) Image of all the instruments available for RF measurements. The ones used in this thesis are labelled. (b) Image of the setup mounted in the pneumatic table. 66

3.1 Optical microscopy image of a four-contact device. Useful information: bottom contact (BC) and top contact (TC). 68
3.2 (a) Optical microscopy image of a two-contact device. (b) Zoom in at the central region, where the field line is defined on top of the nanopillar. Useful information: bottom contact (BC), top contact (TC) and field line (FL). 69
3.3 (a) Optical microscopy image of a individual top contacts device. (b) Zoom in at the central region, where each nanopillar i is electrically connected with an individual top contact $\mathrm{ITC_i}$ (i = 1, 2, 3 or 4). Useful information: bottom contact (BC), top contact (TC), field line creating a magnetic field in the xx direction ($\mathrm{FL_x}$) and field line creating a magnetic field in the yy direction ($\mathrm{FL_y}$). 70
3.4 Illustration of the mask used at the first optical lithography. On the left side, a cross section of the sample shows the etching performed until the Si substrate at the trench regions. Useful information: capping structure (CS) and bottom contact (BC). The alignment marks are magnified for clarity. 71
3.5 (a)-(c) SEM images obtained for two pillars defined with different milling conditions. On top of each image, the pillar stack corresponds to the MTJ composition below the sacrificial structure (thickness in nanometers). The images were saved at a tilting angle of (a) 30° and (b) 40°. From the same two wafers, two identical pillars were chosen for a focus ion beam cut, so that (b)-(d) show the correspondent SEM images of the pillar cross sections. 72
3.6 $\mathrm{SiO_2}$ deposition sequence before planarization. Each step shows a SEM image and an illustration (not at scale). The test pillars have a TiWN(15) / AlSiCu(400) / TiWN(15) stack and 600 nm of diameter. (a) Starting from a defined pillar, $\mathrm{SiO_2}$ is deposited to fulfil a nominal thickness of (b) 200 nm, (c) 800 nm and (d) 1600 nm. 74
3.7 Illustration and corresponding SEM images of the planarization process for a real MTJ pillar, (a) after an oxide deposition step and (b) after the last milling when the pillar is open on top for electric contact. The diameter of the pillar is 300 nm. 75
3.8 Mask used for pillar cap and bottom pad definition (i.e. green regions). On the right, two cross sections show the profile after the etching process. Useful information: capping structure (CS) and bottom contact (BC). 76

3.9 Mask used for the bottom contact definition (i.e. red region), along with a cross section at the bottom pad after etching. Useful information: bottom contact (BC). 76
3.10 Mask used for the via fabrication to the pillar cap (i.e. yellow region), along with a cross section at the bottom pad and pillar region after etching. Useful information: capping structure (CS) and bottom contact (BC). 77
3.11 Mask used for the via fabrication to the bottom pad (i.e. purple region), along with a cross section at the bottom pad after etching. Useful information: bottom contact (BC). . 78
3.12 Mask used for the top pad definition (i.e. blue regions). 78
3.13 Mask used for the vias to MTJ pads (i.e. light blue regions). 79
3.14 (a) Mask used for the field lines definition (i.e. dark blue region). (b) Zoom in at the pillar region showing the field line defined on top of the pillar (the MTJ size is magnified for clarity). Useful information: bottom contact (BC), top contact (TC) and field line (FL). 79

4.1 Illustration of a simple artificial neural network for image recognition. 82
4.2 (a)-(b) Experimental synchronization maps, measured as a function of the input RF signals $\mathrm{f_A}$ and $\mathrm{f_B}$, (a) before and (b) after 86 training steps. Each colour region corresponds to a different synchronization state between the four oscillators and the input. Dots with different colours correspond to different vowels and their spread is a consequence of being spoken by different people. (c) Illustration of the experimental setup, where four oscillators working as neurons are connected in series. The inputs $\mathrm{f_A}$ and $\mathrm{f_B}$ are transmitted by a field line as two microwave fields. (d) The vowel recognition rate is presented as a function of the number of training steps. 84
4.3 (a) Illustration of the spin diode concept. (b) RF detection performed by a nanopillar acting as a spin torque nano-detector (V labels a voltmeter). (c) Example of a spin diode measurement performed at INL for a vortex-based magnetic tunnel junction with a diameter of 1 μm. An in-plane magnetic field of 39 Oe was applied in the easy axis during the measurement. 85
4.4 Top view of the fabrication design with the integrated field line fabricated on top of the MTJ pillar. 88
4.5 (a) Transfer curve explaining the three-step initialization process for an MTJ with a diameter of 1.0 μm. The resistance of the MTJ is depicted as a function of the DC current $\mathrm{I_{FL}}$ applied through the integrated field line. In this example, an applied DC current of -5.0 mA sets the vortex with a negative chirality (C = -1). The insets show how each chirality is associated with a different circulation of the in-plane magnetic moments of the vortex. (b) Illustration of the experimental setup used for initialization. The field line is roughly 600 nm on top of the free layer. 89
4.6 (a) Again, an illustration of the experimental setup used for initialization is presented, now with a pulse generator. (b) The initialization is performed with pulses controlled by three main parameters: width (w), amplitude ($\mathrm{V_A}$) and offset ($\mathrm{V_{off}}$). (c) Probability of having a negative chirality, presented as a function of the DC current applied to the MTJ during the initialization. For each $\mathrm{I_{DC}}$ setpoint, the probability is calculated based on 100 repetitions of the initialization. The pulse parameters were constant over the full measurement. 90

4.7 Illustration of the experimental setup used for spin diode measurements. 91
4.8 Spin diode measurements presented as a function of the input RF current density for (a) positive and (b) negative chiralities. (c) Spin diode measurement obtained for an input RF current density of $2.8 \times 10^9\,\mathrm{A/m^2}$. 92
4.9 (a) Rectified voltage measured at a fixed frequency of 60 MHz and presented as a function of the input RF current density. (b) The same results are now presented in the operational window, where the synaptic weights are defined by the slope of each linear fit. (c) Synaptic weights presented as function of the input frequency for both chiralities. The absolute difference between the two weights is also depicted. 93
4.10 Spin diode measurements obtained for an STVO with a diameter of (a) 1.0 μm and (b) 0.9 μm, for an RF input power of 0.398 mW. The four possible programmable sums of the output voltages are presented in (c) as a function of the input RF power for a frequency of 60 MHz. 95
4.11 Simulated $\Delta \mathrm{M_Y}$ time traces obtained for both chiralities at an in-plane field of 39.8 Oe, for (a) positive and (b) negative polarities. Both OFT and STT are considered. The results are obtained for a frequency of 81 MHz and an RF current density of $3.0 \times 10^9\,\mathrm{A/m^2}$. 96
4.12 Complete and partial R-H loops obtained for a bias DC current of 0.1 mA. These results are obtained from the MTJ device whose spin diode measurements are presented in Fig. 4.8. 97
4.13 (a) Simulated rectified voltage calculated as a function of the input RF current density for the two different vortex chiralities at a fixed frequency of 81 MHz. An in-plane magnetic field of 39.8 Oe is applied in the yy direction. 97
4.14 The simulated spin diode spectra for (a) positive and (b) negative chiralities are presented for different excitation mechanisms: spin-transfer torque (STT), Oersted field torque (OFT) and for both mechanisms (OFT + STT). The results were obtained for an RF current density of $3.0 \times 10^9\,\mathrm{A/m^2}$. The inset in (a) shows the STT-driven resonance fitted with Eq. (4.7). (c) – (e) Time-averaged phase difference between $\Delta \mathrm{M_Y}$ and $\mathrm{J_{RF}}$, as defined in Eq. (4.8), presented as a function of the $\mathrm{J_{RF}}$ frequency for different oscillation-driven mechanisms and chiralities. (f) – (g) Simulated $\Delta \mathrm{M_Y}$ time traces obtained for both chiralities. Similar to (a) and (b), different excitation mechanisms are considered. The results were obtained for an RF current density of $3.0 \times 10^9\,\mathrm{A/m^2}$ at a frequency of 81 MHz whose time traces are also presented. 99
4.15 (a)-(f) Simulated rectified voltage calculated as a function of the in-plane magnetic field applied in the yy direction for the two different vortex chiralities. Again, the simulated spin diode measurements are presented for different excitation mechanisms: spin-transfer torque (STT), Oersted field torque (OFT) and both (OFT + STT). The results were obtained for an RF current density of $2.8 \times 10^9\,\mathrm{A/m^2}$. The simulated spin diode outputs are presented for a setpoint field of (g) 6.0 Oe and (h) 18.0 Oe. Both OFT and STT are considered. The calculation of $\mathrm{V_{REC}}$ is explained in (g) as the module of the peak-to-valley voltage. (i) Illustration of the simulated nanodisk, showing the vortex core offset for both chiralities when an in-plane field of 18 Oe is applied. 101

4.16 (a) Rectified voltage calculated as a function of the in-plane magnetic field applied according to the in-plane easy axis for the two different vortex chiralities. The results were obtained for an MTJ device with a diameter of 1.0 μm and an RF input power of 0.398 mW. (b) The results are zoomed in at the field range where the vortex core passes through the center of the nanopillar. (c) As an example, the spin diode outputs are presented for a setpoint field of -40.8 Oe and $\mathrm{V_{REC}}$ is calculated as the peak-to-valley or valley-to-peak voltage. 102
4.17 (a) The experimental $\Delta \mathrm{V}(\mathrm{f_{MAX}})$ is depicted in (c) as a function of the in-plane field. (a) and (b) show $\mathrm{V^{+}}(\mathrm{f_{MAX}})$ and $\mathrm{V^{-}}(\mathrm{f_{MAX}})$, respectively, used to calculate $\Delta \mathrm{V}(\mathrm{f_{MAX}})$. For each field setpoint, $\Delta \mathrm{V}(\mathrm{f_{MAX}})$ is calculated at the frequency $\mathrm{f_{MAX}}$ that maximizes the difference. (d) Example of the $\Delta \mathrm{V}$ calculation for a field setpoint of 15.1 Oe. 103
4.18 Simulated difference of the output voltage ($\Delta \mathrm{V}$) calculated for C = +1 and C = -1. 104
4.19 Spin diode spectra obtain for an in-plane field of (a) 13.6 Oe, (b) -4.5 Oe and (c) -19.6 Oe. These results were obtained at C = +1 and for the MTJ device whose results are also shown in Fig 4.16. 105

5.1 The top view of the two-contact design is used to illustrate the experimental setup, which allows to measure both static and dynamic characteristics of each individual nanopillar. 109
5.2 (a) Resistance of an STVO measured as a function of the in-plane field applied by the electromagnet ($\mathrm{H_{EM}}$). The results are presented in a field range where the vortex is nucleated and a small DC current of 0.1 mA is applied to the MTJ. The inset shows the complete transfer curve, where a DC current of -5.0 mA is applied to the nanopillar. (b) Simulated $\mathrm{M_Y}$ calculated as a function of the in-plane field in the yy direction, for a nanodisk with a diameter of 500 nm, showing two possible structures: amorphous and polycrystalline. (c) Simulated position of the vortex core calculated as a function of the in-plane field in the yy direction. Some colour dots make the connection between the core position in (c) and $\mathrm{M_Y}$ in (b). 110
5.3 (a) $\mathrm{dR_{MTJ}}$ calculated from Eq. (5.1) and presented as a function of both electromagnet and field line in-plane fields. A small DC current of 0.1 mA is applied to the MTJ with a diameter of 500 nm. (b) An equivalent analysis is performed for the simulated nanodisk, also with a diameter of 500 nm. 111
5.4 (a) $\mathrm{dR_{MTJ}}$ calculated as a function of $\mathrm{H_{EM}}$ and $\mathrm{H_{FL}}$, focused in a central pinning site. (b) For the same field setpoints, the resonance frequency of the local gyrotropic oscillation is calculated from spin diode measurements. (c) Spin diode spectra are presented for different values of $\mathrm{H_{EM}}$, in accordance with the field sweep illustrated in (a) by an horizontal white line. These results are obtained from an MTJ with a diameter of 600 nm, the resistance is measured with a DC current of 0.1 mA and the spin diode spectra are measured with an input RF power of 10 μW. 113

5.5 (a) Illustration of the nanodisk used in the toy model. Regions 1 and 2 are identified by different colours and the diameters are also indicated. (b) Total energy density of the vortex core and (c) frequency of the gyrotropic oscillation simulated in the toy model as a function of the vortex core position in the xx axis of the simulation plane [the light blue arrow in (a) illustrates the core displacement]. The results are presented for two different conditions: (i) no defect in the center (black) and (ii) 8% variation of both saturation magnetization and exchange coupling in the central region (red). 114
5.6 Spin diode spectra presented as a function of the input RF power. The MTJ device has a diameter of 500 nm and the field setpoints are $(\mathrm{H_{EM}}\,,\,\mathrm{H_{FL}}) = (5.3\,,\,-18.4)\,\mathrm{Oe}$. For clarity, the data is divided into two frequency domains: (a) collective and (b) local frequency range. The same distinction is made in (c) and (d), where two spin diode spectra are depicted as examples below and above the threshold for a collective oscillation. 115
5.7 (a) $\mathrm{dR_{MTJ}}$ calculated as a function of $\mathrm{H_{EM}}$ and $\mathrm{H_{FL}}$ for a nanopillar with a diameter of 600 nm. The MTJ resistance is monitored by injecting a DC current of 0.1 mA. (d) The amplitude of the rectified voltage of the collective mode is presented for the field window defined in (a). A fixed input RF power of 12.6 $\mu\mathrm{W}$ is applied. 116
5.8 MTJ resistance measured as a function of the external field for an MTJ device with the stack A (top) and stack B (bottom). Both measurements are obtained from devices with a nominal diameter of 500 nm and by applying a DC current of 1.0 mA. 117
5.9 (a) Resistance as a function of the external field, measured in the vortex nucleation region for an MTJ device with the stack A. The field sweep is performed in a zigzag fashion, as exemplified in the inset. (b) Resistance of the same MTJ device measured at remanence as a function of the number of passes through zero field. In (c) and (d) the analysis is similar to the one performed in (a) and (b), but now for an MTJ device with the stack B. Here, the MTJ devices are the same as the ones used in Fig. 5.8 and the resistance is measured by applying a DC current of 1.0 mA. 118

6.1 (a) Illustration of a simple STNO stack, where the reference layer (RL) acts as the polarizer. A spin-polarized current promotes a steady-state magnetic precession in the free layer (FL). (b) Output voltage obtained from the STNO dynamics. 121
6.2 Main patterned STNO geometries: (a) nanocontact and (b) nanopillar. 121
6.3 Illustration of the main stack configurations used for STNO fabrication: (a) a simple trilayer structure with free (FL) and reference (RL) FM layers and (b) a trilayer structure with insertion of a perpendicular magnetic polarizer (Pol.). For both, the free FM layer may have different magnetic states: 1) in-plane, 2) out-of-plane or 3) vortex. 122
6.4 Illustration of the magnetization precession of a free FM layer. The blue curve represents a perfect non-realistic precession, whereas the red curve shows a realistic phenomenon, with an amplitude perturbation at t = 2 adding phase noise to the system. 124

6.5 (a) Illustration of two nanocontacts fabricated for synchronization via spin wave propagation. (b) Power spectral density (PSD) measured as a function of the DC bias current ($\mathrm{I_{DC}}$) applied to a pair of nanocontacts. The synchronization is achieved roughly for $\mathrm{I_{DC}} > 45\,\mathrm{mA}$. (c) Illustration of the two adjacent pillars fabricated for synchronization via magneto-dipolar coupling. (d) The PSD is presented as a function of the perpendicular field ($\mathrm{H_{perp}}$) when the vortices have opposite polarities, showing a synchronized state roughly for $\mathrm{H_{perp}} < 0.6\,\mathrm{kOe}$. (e) Illustration of the setup used for synchronization via electric coupling. (f) The dynamic properties (output power and linewidth) are presented for the free running oscillations (green and orange) and for the synchronized state (red). 125
6.6 Synchronization method of two STNOs, obtained from theory. It shows the frequency of oscillators "1" and "2" as a function of the DC current applied to the oscillator "2". The dashed lines indicate the free running frequencies of each oscillator. The synchronization is represented by a purple solid line, with $\Delta\omega_\mathrm{s} = \omega_\mathrm{max} - \omega_\mathrm{min}$. The inset shows the free running frequencies of each STNO as a function of the applied DC current. . . . 127
6.7 (a) Top view of the ITC design in the central region. (b) Illustration of the ITC design near the nanopillars. (c) Each $\mathrm{MTJ_i}$ is electrically connected with an individual top contact $\mathrm{ITC_i}$ (i = 1, 2, 3 or 4). When changing the number of MTJs per device, the design with four ITCs is maintained. Useful information: bottom contact (BC), field line creating a magnetic field in the xx direction ($\mathrm{FL_x}$), field line creating a magnetic field in the yy direction ($\mathrm{FL_y}$) and distance between consecutive nanopillars (d). 129
6.8 SEM images obtained for four MTJ nanopillars with a diameter of 300 nm after (a) definition and (b) planarization. The nominal edge-to-edge distance between pillars is 100 nm. The images are obtained at a tilting angle of 40°. 130
6.9 Top view SEM images obtained for an ITC device after (a) development and (b) resist strip. The nominal distance between consecutive ITCs is 100 nm. 130
6.10 Yield of the MTJ nanopillars presented as a function of the edge-to-edge distance. For each distance, the calculation is based on 10 ITC devices with different configurations: (a) four, (b) three, (c) two and (d) one MTJs per device, as illustrated in Fig. 6.7c. The value n represents the number of nanopillars measured in the 10 ITC devices. 132
6.11 Illustration of the experimental setup used for the characterization of MTJ nanopillars with ITCs. Depending on the purpose, the STVO signals can be visualized via a spectrum analyser after power combining or individually via two oscilloscope channels. . . . 133
6.12 (a)-(b) Power spectral density (PSD) individually measured from two STVOs ($\mathrm{STVO_1}$ and $\mathrm{STVO_2}$) with an edge-to-edge distance of 100 nm. (a) Spectrum obtained for $\mathrm{STVO_1}$ as a function of the DC current $\mathrm{I_1}$ (the DC current $\mathrm{I_2}$ applied to $\mathrm{STVO_2}$ is kept at zero). (b) Spectrum obtained for $\mathrm{STVO_2}$ as a function of the DC current $\mathrm{I_2}$ (the DC current $\mathrm{I_1}$ applied to $\mathrm{STVO_1}$ is kept at zero). (c) Time trace obtained for $\mathrm{STVO_1}$ at $\mathrm{I_1} = -10.0\mathrm{mA}$. (d) Time trace obtained for $\mathrm{STVO_2}$ at $\mathrm{I_2} = -5.0\mathrm{mA}$. Each time trace is presented after application of a band pass filter between 150 MHz and 400 MHz. A perpendicular magnetic field of 2.8 kOe was applied during the measurements. 134

6.13 (a) Power spectral density (PSD) measured for two STVOs ($\mathrm{STVO_1}$ and $\mathrm{STVO_2}$) with an edge-to-edge distance of 100 nm, as a function of the DC current $\mathrm{I_1}$ passing through $\mathrm{STVO_1}$. The DC current $\mathrm{I_2}$ applied to $\mathrm{STVO_2}$ is $-5.0\,\mathrm{mA}$. (b) Example of the PSD obtained for $\mathrm{I_1} = -10.0\,\mathrm{mA}$ and $\mathrm{I_2} = -5.0\,\mathrm{mA}$ for single (black and red) and combined (blue) oscillations. (c) Linewidth, (d) output power and (e) frequency calculated as a function of $\mathrm{I_1}$ for $\mathrm{I_2} = 0.0\,\mathrm{mA}$ (black) and $\mathrm{I_2} = -5.0\,\mathrm{mA}$ (blue). For an easy comparison, the parameters obtained for an isolated oscillation of $\mathrm{STVO_2}$ at $\mathrm{I_2} = -5.0\,\mathrm{mA}$ (red) are also shown without any connection with the $\mathrm{I_1}$ axis. A perpendicular magnetic field of 2.8 kOe was applied during the measurements. 136
6.14 (a) The instantaneous phase difference ($\Delta\Psi$) is presented as a function of time, for different values of $\mathrm{I_1}$ passing through $\mathrm{STVO_1}$. The DC current passing through $\mathrm{STVO_2}$ is $-5.0\,\mathrm{mA}$. $\Delta\Psi$ is zoomed in for (b) $\mathrm{I_1} = -8.0\,\mathrm{mA}$ and (c) $\mathrm{I_1} = -8.6\,\mathrm{mA}$. A perpendicular magnetic field of 2.8 kOe was applied during the measurements. 137
6.15 Power spectral density (PSD) measured for two STVOs ($\mathrm{STVO_1}$ and $\mathrm{STVO_2}$) 1 μm apart, as a function of the DC current $\mathrm{I_{FL}}$ passing through the field line. The measurement is performed for (a) an individual oscillation of $\mathrm{STVO_1}$ ($\mathrm{I_1} = -4.0\mathrm{mA}$), (b) an individual oscillation of $\mathrm{STVO_2}$ ($\mathrm{I_2} = -4.0\mathrm{mA}$) and (c) the combined dynamics ($\mathrm{I_1} = \mathrm{I_2} = -4.0\mathrm{mA}$). A perpendicular magnetic field of 5.6 kOe was applied during the measurements. 138
6.16 (a) Linewidth and (b) output power calculated as a function of $\mathrm{I_{FL}}$ for the individual oscillation of $\mathrm{STVO_1}$ (black) and $\mathrm{STVO_2}$ (red) and for the combined dynamics (blue). The $\mathrm{I_{FL}}$ range is chosen based on the data shown in Fig. 6.15c, where both STVOs merge into the same oscillating frequency. In (b), the orange dashed line corresponds to the sum of the output power of each individual oscillator ($\mathrm{P_1}$ for $\mathrm{STVO_1}$ and $\mathrm{P_2}$ for $\mathrm{STVO_2}$). (c) The instantaneous phase difference ($\Delta\Psi$) is presented as a function of time for $\mathrm{I_{FL}} = 22\mathrm{mA}$. Two channels of the oscilloscope were used to save the time traces of each STVO. 139
6.17 Power spectral density (PSD) measured for two STVOs ($\mathrm{STVO_1}$ and $\mathrm{STVO_2}$) 400 nm apart, as a function of the DC current $\mathrm{I_{FL}}$ passing through the field line. The measurement is performed for $\mathrm{I_1} = \mathrm{I_2} = -4.0\mathrm{mA}$. (b) The instantaneous phase difference ($\Delta\Psi$) is presented as a function of time for $\mathrm{I_{FL}} = -58\,\mathrm{mA}$. Two channels of the oscilloscope were used to save the time traces of each STVO. A perpendicular magnetic field of 5.6 kOe was applied during the measurements. 141
6.18 (a)-(c) Power spectral density (PSD) measured for two STVOs ($\mathrm{STVO_1}$ and $\mathrm{STVO_2}$) 400 nm apart, as a function of the RF field frequency $\mathrm{f_{SH}}$ applied through the field line with a constant power of 10 mW. The spectra are measured for three different conditions of the DC bias current: (a) $\mathrm{I_1} = -4.0\,\mathrm{mA}$ applied to $\mathrm{STVO_1}$ only, (b) $\mathrm{I_2} = -4.0\,\mathrm{mA}$ applied to $\mathrm{STVO_2}$ only and (c) $\mathrm{I_1} = \mathrm{I_2} = -4.0\,\mathrm{mA}$ applied to both $\mathrm{STVO_1}$ and $\mathrm{STVO_2}$. (d) The linewidth of the locked state is calculated as a function of $\mathrm{f_{SH}}$ for the conditions presented in (a) and (b). (e)-(f) The phase deviation θ translating the locking between each STVO and the external RF field is presented for different values of $\mathrm{f_{SH}}$, considering the conditions in (c). Throughout these measurements, a DC current of -66 mA in the field line and a perpendicular field of 5.6 kOe were applied. 142

6.19 The phase deviation θ between $\mathrm{STVO_2}$ and the second harmonic is calculated for different values of the bias DC current $\mathrm{I_1}$ applied to $\mathrm{STVO_1}$. The DC current applied to $\mathrm{STVO_2}$ is constant ($\mathrm{I_2} = -4.0\,\mathrm{mA}$). The results are calculated for two different frequencies of the external RF field: (a) $\mathrm{f_{SH}} = 750\,\mathrm{MHz}$ and (b) $\mathrm{f_{SH}} = 780\,\mathrm{MHz}$. The inset highlights the magnitude of the phase slips. 143

7.1 Optical microscope images showing the three design types fabricated on top of $\mathrm{SiN_x}$ membranes. Both frontside and backside images of each design are shown on top and on the bottom of the figure, respectively. The contact pads refer to the bottom contact (B), top contact (T) and field line (F). On the bottom left side, the main regions are labelled with the backside materials: the 200 μm Si step between consecutive membrane windows and the remaining $\mathrm{SiO_2}$ outside the membrane regions, where the patterning is not performed. As an example, the membrane length is measured for type 3. 147

7.2 (a) R-H loop of an MTJ device with a nominal diameter of 500 nm. The measurement is obtained by applying a DC current of 1.0 mA. (b) Statistical analysis of 38 identical devices, comparing the TMR ratio as a function of the RA product, when the latter is calculated based on the nominal area of the pillar (black scatter) or based in the FIB image (red scatter). (c) SEM image showing the cross section of an STVO after a FIB cut. The MTJ diameter is measured in the bottom contact and on top of the pillar cap (distance in nanometers) and each value is compared with the nominal MTJ diameter of 500 nm. Here, all the MTJs are chosen from the wafer that includes the devices fabricated on top of membranes. 148

7.3 (a) Illustration of the marks used for the backside alignment. (b) Simple sketch of the final setup used for the backside alignment. On the bottom, the perfect overlap between the frontside marks (in red) and the screen saved backside marks (in green) represents the configuration that one should see from the bottom view microscopes for a successfully aligned backside exposure. 150

7.4 Illustrations of the substrate cross section, showing the different steps towards the hard mask definition. Substrate after (a) the backside alignment, (b) the first optical lithography and (c) the second optical lithography. For clarity, the images are not at scale. 151

7.5 Illustrations of the substrate cross section, showing the different steps towards the membrane definition. Substrate after (a) the Si step definition, (b) the hard mask removal and (c) the substrate removal up to the membrane. (c) also illustrates the 200 μm Si step required for a maximum X-ray incidence angle of 45°. For clarity, the images are not at scale. 152

7.6 (a) STXM image obtained from an STVO fabricated on top of a 300 nm-thick $\mathrm{SiN_x}$ membrane. Courtesy of the “Unite Mixte de Physique CNRS/Thales” center. (b) Spin diode measurements obtained for an MTJ device with a nominal diameter of 600 nm. The measurements are obtained at zero external magnetic field. 153

List of Tables

2.1 Examples of standard recipes used for sputtering deposition (nominal thickness t). The materials highlighted in red (blue) correspond to depositions at the MTM (FTM) tool. As explained in the main text, the MgO recipes are defined aiming a specific RA product. Each recipe contains: the number of cyclical paths below the target (N), the linear velocity of the substrate (v), the power of the sputtering source (P), the Ar flow and, for specific cases, the N_2 flow. 45

2.2 Setpoint conditions at the PECVD tool for the deposition of SiO_2 used in the MTJ fabrication. 48

2.3 Standard recipe parameters used at Nordiko 7500. Following the setpoint parameters, an example of a reading during a milling process is presented. 51

2.4 Etching rates of different materials, obtained using the standard recipe of Table 2.3 at two incidence angles. 51

2.5 Recipe parameters used for PR strip in the plasma asher. 56

2.6 Example of the parameters measured during a strip process. 56

2.7 Magnetization (M) calculated from VSM data and presented for different magnetic materials. Each magnetic layer is inserted in a specific stack (magnetic layer highlighted in red) that is deposited in the VSM substrates. All the thicknesses shown in the stack column are presented in nanometers. All the three samples were measured as deposited. 62

4.1 Summary of STND performances from the literature, where the sensitivity (S) and frequency of operation (f) are the indicative parameters. Regarding the magnetic properties of the MTJ, FL and RL refer to the free and reference layers, respectively, which may present an in-plane ($\rightarrow$), a perpendicular ($\uparrow$) or a vortex magnetic state. It should be emphasized that, considering the way that each reference exposes its experimental results, some of them above are approximations. 86

5.1 Material composition of stack A and stack B, as described in the main text (thickness in nanometers). 117

6.1 Summary of STNO performances from the literature, where the frequency (f), output power ($\mathrm{P_{out}}$) and linewidth (Γ) are the indicative parameters. FL and RL refer to the free and reference layers, respectively, which may present an in-plane ($\rightarrow$), a perpendicular ($\uparrow$) or a vortex magnetic state. The STNO may also have a magnetic polarizer (Pol.). It should be emphasized that, considering the way that each reference exposes its experimental results, some of them above are approximations. The values of $\mathrm{P_{out}}$ and Γ refer to the best result obtained at each reference, which does not imply that both are obtained simultaneously for the same experimental conditions. 123
6.2 Description of the two MTJ stacks used for ITC patterning. The thickness is presented in nanometers. 131
6.3 Recipe parameters used at Nordiko 7500 for ITCs definition. The neutralizer setpoints are in accordance with Table 2.3. 131

Contents

List of Abbreviations **23**

1 Introduction **24**
1.1 Spintronics: general overview . . . 24
1.2 Tunnel magnetoresistance . . . 26
1.2.1 Julliere's model . . . 26
1.2.2 Slonczewski's model . . . 27
1.3 Different types of tunneling . . . 28
1.3.1 Incoherent tunneling through an amorphous barrier . . . 29
1.3.2 Coherent tunneling through a crystalline barrier . . . 29
1.4 CoFeB/MgO/CoFeB trilayer system . . . 31
1.5 Resistance-area product in MgO-based MTJs . . . 31
1.6 General MTJ structure . . . 32
1.7 The spin-transfer torque effect . . . 32
1.7.1 STT-induced dynamics in a FM layer with an uniform magnetization . . . 33
1.7.2 STT-induced dynamics in a FM layer with a magnetic vortex . . . 36

2 Experimental techniques **42**
2.1 Sputtering deposition systems . . . 42
2.1.1 Timaris sputtering tools . . . 42
2.2 Plasma enhanced chemical vapour deposition . . . 46
2.3 Ion beam milling (Nordiko 7500) . . . 48
2.4 Lithography techniques . . . 53
2.4.1 Direct write laser lithography . . . 54
2.4.2 Photoresist strip by plasma asher . . . 55
2.4.3 Direct write electron-beam lithography . . . 56
2.5 Magnetic annealing treatment . . . 57
2.6 Characterization techniques . . . 59
2.6.1 Optical interferometer (OPM Nanocalc) . . . 59
2.6.2 Vibrating sample magnetometer . . . 60
2.6.3 Current in-plane tunneling method . . . 61
2.6.4 Semi-automatic transport measurement setup . . . 64
2.6.5 RF setup . . . 66

3 Micro and nanofabrication **68**
3.1 Device geometries . . . 68
3.2 Process steps . . . 69
3.2.1 MTJ stack deposition and annealing . . . 69
3.2.2 Sacrificial structure deposition . . . 71
3.2.3 Trenches definition . . . 71
3.2.4 Pillar definition . . . 72
3.2.5 Ion beam planarization . . . 73
3.2.6 Pillar cap and bottom pads definition . . . 75
3.2.7 Bottom contact definition . . . 76
3.2.8 Via to pillar cap . . . 77
3.2.9 Via to the bottom contact . . . 78
3.2.10 Top contact definition . . . 79
3.2.11 Field line definition . . . 79

4 Bio-inspired capabilities for vortex-based spin torque nano-oscillators **81**
4.1 Artificial neural networks . . . 81
4.2 Spintronics hardware for neuromorphic computing . . . 83
4.3 RF detection in magnetic tunnel junctions . . . 85
4.4 MTJ design and stack . . . 87
4.5 Vortex initialization . . . 88
4.6 Non-volatile synapse based on a vortex nano-oscillator . . . 91
4.6.1 Experimental synaptic weights . . . 91
4.6.2 Simulated synaptic weights . . . 95
4.6.3 Evolution of the non-volatile effect with the core displacement . . . 100
4.7 Conclusion . . . 105

5 Collective versus local oscillations linked to the granular nanostructure of a vortex nano-oscillator **107**
5.1 Effect of structural defects on the dynamics of a vortex-based nano-oscillator . . . 107
5.2 Nanofabrication and experimental setup . . . 108
5.3 Identification of pinning sites based on static measurements . . . 109
5.4 Vortex dynamics in a polycrystalline magnetic medium . . . 112
5.4.1 Local dynamics . . . 112
5.4.2 Transition to collective dynamics . . . 115
5.5 Hysteretic behaviour of the vortex displacement . . . 116
5.6 Conclusion . . . 119

6 Magnetic dipolar synchronization of spin torque vortex oscillators with independent top contacts **120**
6.1 Spin torque nano-oscillator . . . 120
6.1.1 Device architectures . . . 121
6.1.2 Magnetic and stack configurations . . . 122
6.1.3 Performance parameters . . . 123

6.2 Synchronization of STNOs . . . 126
6.2.1 State of the art . . . 126
6.2.2 Synchronization from the universal nonlinear auto-oscillator model . . . 127
6.3 Dipolar coupling of STVOs in an ITC geometry . . . 128
6.3.1 ITCs nanofabrication . . . 128
6.3.2 Experimental setup . . . 132
6.3.3 Steady-state dynamics of coupled STVOs . . . 134
6.3.4 Second harmonic injection locking with coupled STVOs . . . 140
6.4 Conclusion . . . 144

7 Fabrication of spin torque vortex oscillators on top of SiN_x membranes 145
7.1 Vortex imaging by transmission X-ray microscopy . . . 145
7.2 Geometries . . . 146
7.3 Fabrication steps . . . 147
7.3.1 Substrate preparation . . . 147
7.3.2 Frontside patterning . . . 148
7.3.3 Backside patterning: membrane definition . . . 149
7.4 Discussion and conclusion . . . 152

8 Conclusion and outlook 155

Bibliography 159

List of Abbreviations

AFM	Antiferromagnetic
CVD	Chemical Vapour Deposition
DC	Direct Current
FM	Ferromagnetic
INL	International Iberian Nanotechnology Laboratory
ITC	Independent Top Contact
MRAM	Magnetic Random-Access Memory
MTJ	Magnetic Tunnel Junction
PECVD	Plasma Enhanced CVD
PR	Photoresist
PVD	Physical Vapour Deposition
RA	Resistance-Area
RF	Radio Frequency
SAF	Synthetic Antiferromagnetic Structure
SEM	Scanning Electron Microscopy
SHIL	Second Harmonic Injection Locking
STT	Spin-Transfer Torque
STND	Spin Torque Nano Detector
STNO	Spin Torque Nano Oscillator
STVO	Spin Torque Vortex Oscillator
TEM	Transmission Electron Microscopy
VSM	Vibrating Sample Magnetometer

Chapter 1

Introduction

1.1 Spintronics: general overview

Spintronics is a multidisciplinary field that studies spin-dependent effects in solid-state systems. The interest is focused in the electron spin state, whose manipulation can be used to tune the magnetic properties of materials. The appearance of Spintronics is the acknowledgement that, not only the charge, but also the spin carries important information.

The first magnetoresistive phenomenon, discovered by William Thomson in 1857 [1], was the anisotropic magnetoresistance (AMR) effect. It was observed that the resistance of ferromagnetic (FM) 3d materials depends on the angle between its magnetization and the direction of the current flow. Typical AMR ratios for FM thin films go roughly up to 5% [2], which was enough for their integration as magnetic sensors in read heads of hard disk drives (HDDs).

A major breakthrough happened in 1988, when the giant magnetoresistance (GMR) effect was discovered [3, 4]. This effect may be demonstrated in a spin valve, most simply defined as two FM layers (e.g. Co, Fe, CoFe, CoFeB) separated by a non-magnetic conductive layer (e.g. Cu, Cr). Due to the spin-dependent scattering, the spin valve conductance varies according to its magnetic configuration, i.e. parallel (higher conductance $\mathrm{G_P}$) or anti-parallel (lower conductance $\mathrm{G_{AP}}$) magnetizations. For this purpose, the fabrication aims to fix the magnetization of one of the FM layers (reference layer), leaving the magnetization of the second FM layer (free layer) loose to be manipulated. The pinning of the reference layer may be achieved by means of an exchange interaction with an adjacent AFM layer [5], by insertion of a SAF structure [6] (see section 1.6) or simply by fabrication of a spin valve with magnetically asymmetric FM layers [7]. To quantify the conductance (G) variation, a magnetoresistance (MR) ratio must be defined as

$$MR = \frac{G_P - G_{AP}}{G_{AP}} = \frac{R_{AP} - R_P}{R_P}, \tag{1.1}$$

where the same labelling is used for the spin valve resistance R. At room temperature, GMR ratios up to $\sim$20% were obtained using spin valves [8], which allowed their application in magnetic sensors technology [9], namely as HDD read heads [10].

Starting in a spin valve, the substitution of the non-magnetic conductive layer by an insulating barrier (e.g. $\mathrm{AlO_x}$, MgO) results in a magnetic tunnel junction (MTJ). An ultra-thin insulating barrier

($\sim 1\,\mathrm{nm}$) guarantees the electric conduction by tunneling, being the barrier thickness a parameter to tune the MTJ resistance. As GMR, but now due to the spin-dependent tunneling [11], the tunnel magnetoresistance (TMR) effect is also translated into a variation of the MTJ conductance with the magnetic configuration, whose ratio may also be calculated from Eq. (1.1). Although it was experimentally demonstrated in 1975 [11], the TMR effect only started to play an important role in 1995, when it was obtained an appreciable TMR ratio of 18% at room temperature for $\mathrm{AlO_x}$-based MTJs [12]. Over the years, that value has been increased up to 80% [13]. Even so, there was still plenty of room for improvements. In 2001, theory predicted TMR values up to 1000% by using a crystalline MgO barrier [14, 15]. The possibility for improvement was experimentally demonstrated in 2004, when many scientific reports started to present TMR ratios above 200% at room temperature for MgO-based MTJs [16–18], thus making them the optimized MTJ stack used nowadays in research.

The development of Spintronics devices had a decisive contribution from the spin-transfer torque (STT) effect in magnetic nanostructures, introduced in 1996 by Berger [19] and Slonczewski [20]. Both predicted that an electric current flowing perpendicular to the plane of a magnetic multilayer can manipulate the magnetization of a magnetic layer. The experimental demonstrations came right after, showing, in a magnetic multilayer, that the STT effect leads to magnetization precession [7, 21, 22] and complete switching [23, 24].

These advances paved the way for a new generation of Spintronics devices, whose main representation nowadays in the market is the STT-based magnetic random-access memory (STT-MRAM) with storage capacity up to 1 Gb [25]. Specifically, each memory cell is an MTJ fabricated in a nanopillar geometry, whose bit (i.e. '0' or '1') is dictated by its resistance. While a low density DC current is used to read the bit, a large density DC current ($\sim 1\,\mathrm{MA/cm^2}$) allows to write in the cell by STT-driven switching of the free layer. This is an important improvement for low power consumption and high density storage, because the switching DC current decreases with the miniaturization of the cell, in contrast with conventional MRAM cells, where the writing is performed by magnetic fields coming from adjacent field lines, whose intensity for switching increases with the miniaturization [26].

The control of the magnetization dynamics is also an important topic in Spintronics, aiming for the development of spin-torque nano-oscillators (STNOs) [27] and spin-torque nano-detectors (STNDs) [28]. To be competitive as RF generators and a viable substitute for standard voltage-controlled oscillators, STNOs need to optimize their output power and spectral purity. The fabrication of MTJs with a magnetic vortex in the free layer [29, 30] and the synchronization of STNOs [31, 32] increased the output power up to $\sim 10\,\mu\mathrm{W}$ [33] and linewidth down to $\sim 50\,\mathrm{kHz}$ [34], near the upper limit for applications of $\sim 10\,\mathrm{kHz}$ [35]. Regarding STNDs, since the first experimental demonstration of STT-driven RF detection in MTJs [36], the sensitivity (i.e. the ratio between the output rectified voltage and the power of the input RF signal) of STNDs has progressively been increased by careful engineering of the free layer properties. Tuning the perpendicular magnetic anisotropy of the free layer [37–39] allowed to obtain sensitivities up to $\sim 10^5\,\mathrm{mV/mW}$ which surpasses the performance of standard Schottky diodes ($\sim 10^3\,\mathrm{mV/mW}$ [37]). The use of vortex-based STNDs, beyond high sensitivities ($\sim 10^4\,\mathrm{mV/mW}$), also bring the advantage of having a detection, above threshold, independent of the input RF signal amplitude, based on the resonant expulsion of the vortex core [40, 41].

In recent years, researchers have been involved in exciting emergent spintronic fields [35]. Neuromorphic computing is a notable example [42]. In this thesis, the work performed in chapter 4 gives a contribution to that particular field. The main motivation is the already proved possibility of spintronic

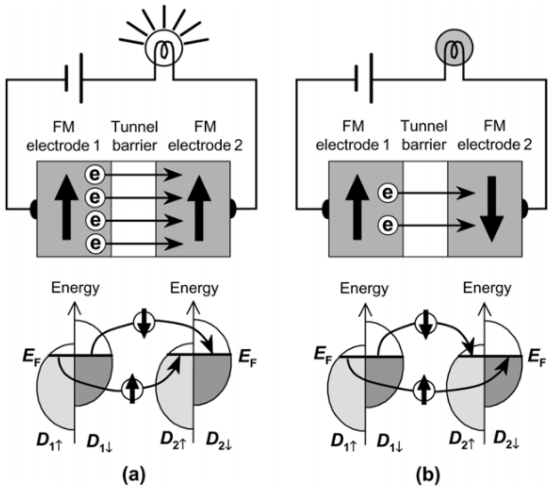


Figure 1.1: Schematic illustration of electron tunneling in an MTJ. (a) Magnetizations of the FM layers are parallel (low resistance state). (b) Magnetizations are anti-parallel (large resistance state). $\mathrm{D_{i\uparrow}}$ and $\mathrm{D_{i\downarrow}}$ represent the density of electronic states at the Fermi level for the two spin-states at the electrode i (i = 1, 2). Adapted from [49].

devices to emulate the functions of neurons [43–45] and synapses [46, 47]. Nowadays, much of the work performed in this field shares the objective of scaling up this concept and build a new class of low-power hardware for unconventional computing [48], aiming to solve the "von-Neumann bottleneck" that results from the continuous data transfer between the separate memory and processor in conventional systems.

1.2 Tunnel magnetoresistance

1.2.1 Julliere's model

The first step towards a clear understanding of the spin role was the suggestion that the electrical conduction in FM metals could be described as two independent propagation channels for electrons with opposite spin-states [50, 51]. From the magnetic properties of a FM metal (i.e. non-zero spontaneous magnetization), results an unbalance of the density of states (DOS) for opposite spin-states at the Fermi level, meaning the presence of a spin-polarized current in the FM metal, i.e. spins will tend to align parallel to the local magnetization. The spin-polarization $(\mathrm{P_0})$ is defined as

$$P_0 = \frac{D^{\uparrow} - D^{\downarrow}}{D^{\uparrow} + D^{\downarrow}}, \tag{1.2}$$

where $\mathrm{D^{\uparrow}}$ and $\mathrm{D^{\downarrow}}$ represent the DOS at the Fermi level for electrons with opposite spin-states. Moreover, in a series of experiment using FM/insulator/superconductor junctions, Tedrow and Meservey showed that the current remains spin-polarized while tunneling through the insulator [52, 53].

In 1975, Julliere measured the tunnel conductance in a Fe/Ge-O/Co MTJ [11]. For the first time, a change of the MTJ conductance (i.e. TMR effect) depending on its magnetic configuration was

experimentally demonstrated. In addition to the experimental evidence, Julliere proposed a model to explain the physical phenomenon, based on two assumptions. Considering the results of Tedrow and Meservey, the first states that an electron maintains its spin-state while tunneling, so that, as depicted in Fig. 1.1, electrons with a specific spin-state from one of the FM layers will tunnel only to unfilled states of the same spin. Therefore, in the parallel configuration, the majority-spin (minority-spin) electrons tunnel to the majority-spin (minority-spin) states, while in the anti-parallel configuration, the majority-spin (minority-spin) electrons tunnel to the minority-spin (majority-spin) states. Finally, the second assumption states that the electric current associated with the tunneling of electrons with a specific spin-state is proportional to the product of their effective DOS in the initial and final FM layers. In this way, one reaches the final Julliere's equation [11]:

$$TMR = \frac{2P_1P_2}{1 - P_1P_2}, \tag{1.3}$$

where $\mathrm{P_1}$ and $\mathrm{P_2}$ refer to the spin-polarization in each of the FM layers. Julliere's model proves that the TMR effect is only possible due to the existence of a spin-polarized current tunneling through the MTJ. For amorphous $\mathrm{AlO_x}$-based MTJs, the Julliere's model describes quite well the experimental results [12, 13]. However, this model is oversimplified, because it neglects the band structure effects in the FM electrodes and insulating barrier, so that the insulator role in the tunneling phenomenon is completely neglected. As a clear example, De Teresa *et al.* showed that a $\mathrm{Co/I/La_{0.7}Sr_{0.3}MnO_3}$ MTJ (I = $\mathrm{SrTiO_3}$, $\mathrm{Al_2O_3}$ or $\mathrm{Ce_{0.69}La_{0.31}O_{1.845}}$) presents a different Co spin-polarization, depending on the insulating barrier [54]. These results clearly demonstrate that the spin-polarization of the tunneling electrons is not only dependent on the nature of the FM material, being instead the result of the chosen FM/insulator/FM structure.

1.2.2 Slonczewski's model

The TMR ratio derivation from the Julliere's model [Eq. (1.3)] was obtained considering the DOS of electrons at the Fermi level for both FM electrodes. Nevertheless, this approach is insufficient to derive a theory that could translate the experimental results, mainly in the case of crystalline insulating barriers. It was already referred in section 1.2.1 that the band structure at each electrode, i.e. the Bloch state associated with each tunneling electron, is completely neglected. To improve the analysis, Slonczewski introduced a model to describe the tunneling phenomenon where the wave vector $\mathbf{k_F}$ at the Fermi level of a given electron is introduced or, in an equivalent way, the velocity $\mathbf{v_F}$ [55]. The model states that the electron tunneling probability is directly dependent on its velocity in the electrode/barrier interface. In this analysis, two identical FM electrodes are separated by an insulating barrier described as a squared potential, with energy height ϕ and thickness d. Considering the free-electron approximation, as an electron tunnels through the barrier, the correspondent Bloch state experiences a decay rate of

$$\kappa(E) = \sqrt{k_{\parallel}^2 + \frac{2m_e}{\hbar}(\phi - E)}, \tag{1.4}$$

where $\mathrm{k_{\parallel}}$ refers to the wave vector component parallel to the electrode/barrier interface. This means that electrons propagating in a direction perpendicular to the interface ($\mathbf{k} \approx \mathbf{k}_{\perp}$ and $\mathbf{k}_{\parallel} \approx 0$) will suffer a lower decay, so that the probability of tunneling will be higher. Solving the Schrödinger's equation for

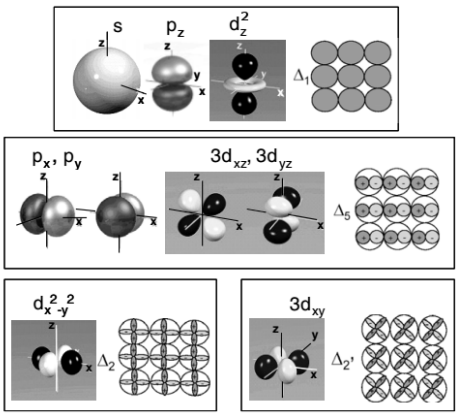


Figure 1.2: Relevant atomic orbitals for 3d metals, organized by symmetry groups. Adapted from [57].

the three parts of the junction and applying the boundary conditions in the interfaces (i.e. guarantee the continuity of the wave function), the conductance becomes

$$G = G_0(1 + P^2 \cos\theta), \tag{1.5}$$

where θ is the angle between the magnetization directions and P the new spin-polarization, given by

$$P = \frac{(k_{F\uparrow} - k_{F\downarrow})(\kappa^2 - k_{F\uparrow}k_{F\downarrow})}{(k_{F\uparrow} + k_{F\downarrow})(\kappa^2 + k_{F\uparrow}k_{F\downarrow})} = P_0 \frac{\kappa^2 - k_{F\uparrow}k_{F\downarrow}}{\kappa^2 + k_{F\uparrow}k_{F\downarrow}}. \tag{1.6}$$

$\mathrm{k_{F\uparrow}}$ and $\mathrm{k_{F\downarrow}}$ denote the wave vector of the majority and minority-spin electrons at the Fermi level ($\mathrm{E_F}$), respectively. Using the relation $\mathrm{D(E_F)} \propto \mathrm{k_F}$ [56], one obtains the right part of Eq. (1.6), being $\mathrm{P_0}$ the spin-polarization from the Julliere's model in Eq. (1.2). $\mathrm{G_0}$ is the mean surface conductance, corresponding to the conductance when the magnetizations are perpendicular, given by

$$G_0 = \frac{\kappa}{\hbar d}\left[\frac{e\kappa(\kappa^2 + k_\uparrow k_\downarrow)(k_\uparrow + k_\downarrow)}{\pi(\kappa^2 + k_\uparrow^2)(\kappa^2 + k_\downarrow^2)}\right]^2 e^{-2\kappa d}. \tag{1.7}$$

Beyond the analytical details, the important here is to emphasize that the electron properties must be considered in the calculation of the spin-polarization. On considering only the electronic DOS at the Fermi level, one is oversimplifying the phenomenon.

1.3 Different types of tunneling

Here, it is described how the crystallographic nature of the barrier influences the tunneling phenomenon. In single-crystal systems, electrons are described by Bloch wave functions, which have the form [58]:

$$\Psi_{\mathbf{k}}(\mathbf{r}) = u_{\mathbf{k}}(\mathbf{r}) exp(i\mathbf{k}.\mathbf{r}), \tag{1.8}$$

where $\mathrm{u_k(r)}$ has the periodicity of the lattice. This theoretical introduction is extremely relevant, because for a specific Bloch state in one of the electrodes, the tunneling probability depends mainly on

the rate of decay of its wave function in the barrier. The spatial shape of an atomic orbital gives information about its symmetry and depends on the electronic state. Thus, one can organize the atomic orbitals into symmetry groups. For a specific group, all the atomic orbitals have the same modulation regarding the component in the plane (xy plane in Fig. 1.2) perpendicular to the propagation direction (z direction in Fig. 1.2) or, in other words, the component in the plane parallel to the electrode/insulator interface. This selection comes from the direct influence of the xy oscillations on the rate of decay that a Bloch state experiences while tunneling [57]. Thus, as depicted in Fig. 1.2, one can identify the Δ_1 (s, p_z and d_z^2), Δ_5 (p_x, p_y, p_z, d_{xz} and d_{yz}), Δ_2 ($d_{x^2-y^2}$) and $\Delta_{2'}$ (d_{xy}) symmetries.

1.3.1 Incoherent tunneling through an amorphous barrier

When the insulating barrier is amorphous, there is no crystallographic symmetry on its structure. This means that Bloch states, regardless of their symmetry, will experience the same decay rate when coupling with evanescent states of the barrier, i.e. the tunneling probability is independent of the Bloch state symmetry of the electron (Fig. 1.3a). This phenomenon is known as incoherent tunneling, which is what the Julliere's model implies by neglecting both electron and barrier properties.

In 3d FM metals and alloys, Bloch states with Δ_1 symmetry have a large positive spin-polarization at the Fermi level, while Bloch states with Δ_2 and Δ_5 symmetries have a smaller positive or even negative spin-polarization [49, 59]. For an AlO_x barrier, a symmetry filtering of the tunneling electrons does not exist, so that high and low polarized symmetry states will tunnel with the same probability through the barrier. From this incoherent tunneling results a low overall spin-polarization that can explain the lower experimental TMR results obtained for AlO_x-based MTJs (up to $\sim 80\%$ at room temperature [13]), when compared with the results obtained for crystalline MgO-based MTJs.

1.3.2 Coherent tunneling through a crystalline barrier

The coherent tunneling process is the responsible for the largest TMR values obtained in MTJs [16, 18, 60]. As depicted in Fig. 1.3b, the crystalline MgO(001) barrier "selects" the tunneling electrons based on their Bloch state symmetry in the electrode. This means that the tunneling probability strongly depends on the electron orbital symmetry, so that a symmetry filtering is effectively implemented.

Butler [59] made the calculation of the transmission probability for the different Bloch states that can couple with the evanescent states in a Fe(001)/ MgO(001)/Fe(001) MTJ (Fig. 1.4), where the Fe

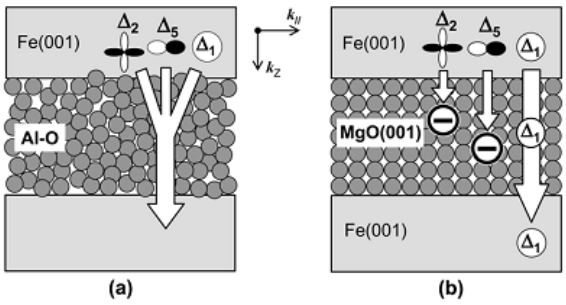


Figure 1.3: Schematic representations of electron tunneling through (a) an amorphous AlO_x and (b) a crystalline MgO(001) barrier. Adapted from [49].

electrodes have a body-centered cubic (bcc) symmetry. The calculation was made for wave functions with $k_{||} = 0$, which are transmitted from the electrode/barrier interface, where $k_{||}$ is the component of the wave vector in the plane parallel to the same interface.

For the parallel configuration, in the majority-spin channel (Fig. 1.4a), the Δ_1 states are the only showing a small decay. In the minority-spin channel (Fig. 1.4b), the Δ_1 states are absent, while all the other symmetries suffer a significant decay. Thus, in the parallel alignment, most of the current is a consequence of the tunneling of electrons in Δ_1 symmetry states. In this context, the absence of the Δ_1 states in the minority-spin channel must be explained. The band dispersion of bcc Fe in the [001] direction ($k_{||} = 0$) shows that all the Δ_1 states below the Fermi level belong to the majority-spin band, so that the Δ_1 band is fully spin-polarized ($P_{\Delta_1} = 1$) and no minority-spin states contribute to the tunneling current [49].

For the anti-parallel configuration (Figs. 1.4c-d), the decay behaviour for the Δ_2, $\Delta_{2'}$ and Δ_5 symmetries is almost unchanged when compared with the parallel configuration, so the conductance will be small. Moreover, in the majority-minority channel (Fig. 1.4c), the Δ_1 states suffer a lower decay in the barrier, but they do not contribute to the current because no propagation in the minority-spin channel is allowed (once again, the Δ_1 band is fully spin-polarized in both Fe layers, which explains why the Δ_1 decay in Fig. 1.4c is maintained at the Fe layer on the right). The conclusion is that a much higher conductance is obtained in the parallel configuration, where highly spin-polarized electrons in Δ_1 states dominate the tunneling. It should be emphasized that not only bcc Fe(001) shows these

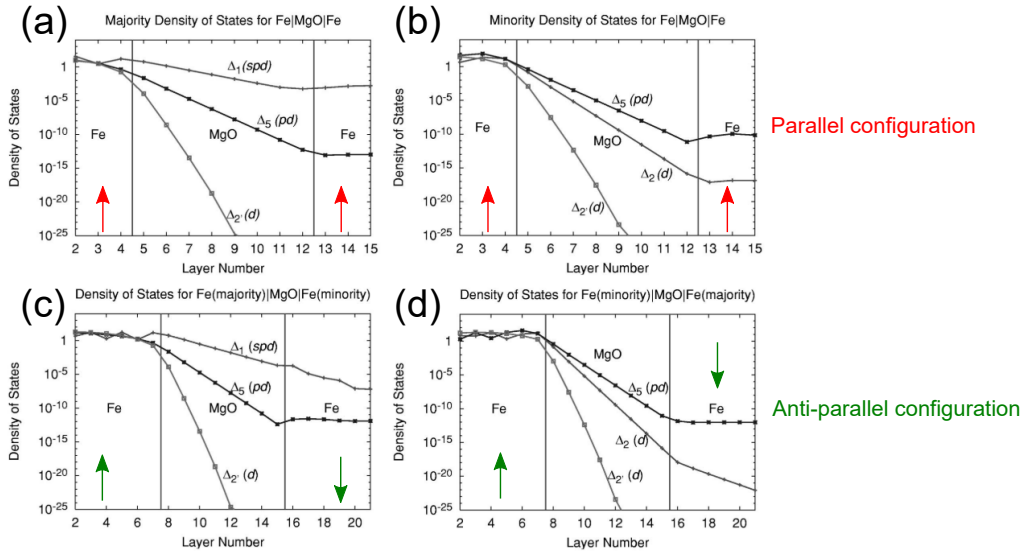


Figure 1.4: Tunneling DOS ($k_{||} = 0$) for the possible coupling symmetries across an epitaxial Fe(001)/MgO(001)/Fe(001) MTJ. The arrows denote the magnetization direction at each FM layer. Adapted from [59].

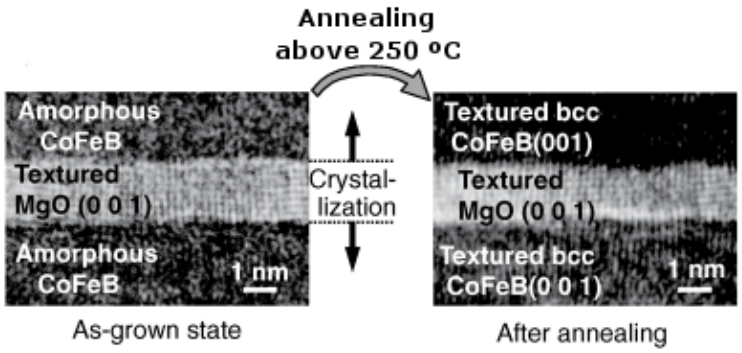


Figure 1.5: Cross-sectional TEM images obtained before and after the annealing of CoFeB/MgO/CoFeB MTJs. Adapted from [61].

promising results, but also other FM metals, mainly alloys based on Fe and Co (e.g. CoFe and CoFeB).

1.4 CoFeB/MgO/CoFeB trilayer system

Since the first theoretical predictions of high TMR values in Fe/MgO/Fe MTJs [14, 15], MgO-based MTJs have been intensively studied, using not only Fe electrodes but also its alloys [17, 18, 60]. In particular, MTJs with CoFeB FM electrodes present results up to 600% at room temperature [60], thus having the largest potential for applications. The advantages of using CoFeB FM electrodes are directly related with the crystalline properties of the CoFeB/MgO/CoFeB structure after sputtering deposition. Fig. 1.5 shows two TEM images of an CoFeB/MgO/CoFeB-based MTJ, before and after an annealing treatment. On the left side, the image shows that both CoFeB FM layers acquire an amorphous structure after sputtering deposition. Remarkably, the MgO barrier grows in a crystalline structure. An annealing treatment (Fig. 1.5 on the right) promotes the crystallization of the CoFeB layers in a body-centered cubic (bcc) structure. Considering that the $Co_{60}Fe_{20}B_{20}$ alloy, above an amorphous SiO_2 layer, crystallizes in a face-centered cubic (fcc) structure [62], this means that the MgO(001) barrier plays an important role in defining the bcc crystallization of the CoFeB layers. This process is a solid-phase epitaxy, where the MgO(001) barrier serves as a template for the crystallization of the FM layers, which is essential for the coherent tunneling of Δ_1 states.

1.5 Resistance-area product in MgO-based MTJs

For the characterization and comparison of MTJs, a very useful parameter is the resistance-area (RA) product. Two MTJs with the same RA product have the same barrier thickness. Figure 1.6 shows the typical experimental behaviour of the TMR ratio as a function of RA in CoFeB/MgO/CoFeB-based MTJs. The relation between RA and the thickness of the insulating barrier is given by [63]

$$RA = B \cdot \exp(C \cdot t_{MgO}), \tag{1.9}$$

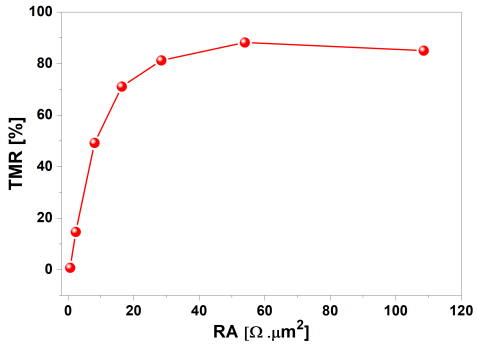


Figure 1.6: TMR ratio for a CoFeB/MgO/CoFeB-based MTJ as a function of the RA product at room temperature.

where B and C are fitting parameters from the deposition system (see section 2.1) and t_{MgO} the thickness of the MgO barrier. For higher RA values, i.e. thicker barriers, the TMR tends to saturate, which proves the majority tunneling of highly spin-polarized Δ_1 states. As the thickness of the barrier decreases, the DOS decay in the barrier starts to be insufficient to prevent the tunneling of other symmetries beyond Δ_1. The tunneling of different symmetries decreases the spin-polarization and the TMR ratio. The defects of the MgO barrier are particularly relevant for this RA product range ($< 10\,\Omega\mu m^2$), where the MgO barrier presents a thickness below 1 nm [64]. From a material point of view, defects may arise from pinholes joining the two electrodes [65] and from the existence of regions with an ultra-thin amorphous MgO induced by the roughness of the stack [62].

1.6 General MTJ structure

In this thesis, all MTJs have been fabricated following the general stack illustrated in Fig. 1.7a. The bent arrow of the free layer represents a vortex magnetic state, which was common for all the patterned MTJs. The reference layer is created by deposition of a synthetic antiferromagnetic (SAF) structure, i.e. pinned FM layer / metallic spacer / reference FM layer. It makes use of the interlayer exchange coupling (i.e. RKKY interaction) between the pinned and the reference layer, being the magnetic configuration (parallel or anti-parallel) ruled by the thickness of the metallic spacer. The SAF is designed with an anti-parallel configuration to minimize the stray field acting on the free layer. The deposition of an AFM layer adjacent to the first FM layer allows to pin its magnetization by an exchange bias interaction. Figure 1.7b shows a VSM magnetic loop obtained from an unpatterned MTJ. The SAF gives a stability range, roughly from -1 kOe to 2 kOe, where only the switching of the free layer is visible.

1.7 The spin-transfer torque effect

The most obvious way to manipulate an MTJ magnetic state is by an external magnetic field. Nevertheless, it was already emphasized that an electric current gets spin-polarized as it propagates through a FM layer, leading to the possibility of manipulating the magnetization of the free FM layer by transfer of angular momentum from the spin-polarized electrons. This is the so-called spin-transfer

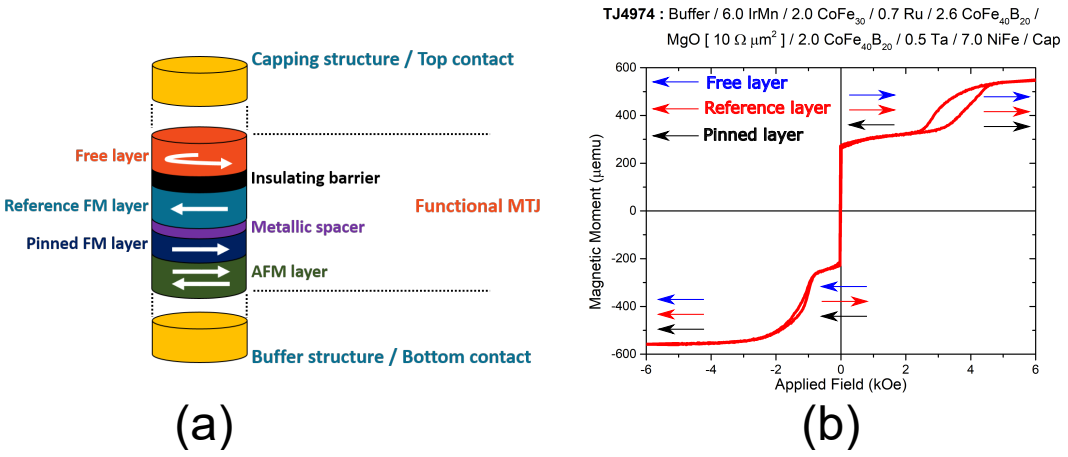


Figure 1.7: (a) General bottom-pinned MTJ stack used in this thesis. (b) Typical VSM loop obtained for an unpatterned MTJ. The arrows represent the direction of the magnetization of each FM layer at different stages of the loop.

torque (STT) effect [19, 20]. A current-based manipulation of an MTJ magnetic state promotes two main phenomena that are essential for applications: i) the complete current-induced switching of the magnetization of the free layer [66], which is the base of the STT-MRAM and ii) a stable magnetic precession of the same magnetization [67], fundamental for the development of functional STNO and STND devices.

1.7.1 STT-induced dynamics in a FM layer with an uniform magnetization

Consider the MTJ depicted in Fig. 1.8, where an antiparallel configuration of the magnetizations is present. Each magnetization state is described by the Landau-Lifshitz-Gilbert (LLG) equation, given by [68]

$$\frac{d\vec{M}}{dt} = -\gamma\vec{M} \times \vec{H}_{eff} + \frac{\alpha}{M_S}\vec{M} \times \frac{d\vec{M}}{dt}. \tag{1.10}$$

The first term on the right side of Eq. (1.10) represents the torque exerted by the effective magnetic field ($\mathbf{H_{eff}}$) on $\mathbf{M}$, where γ is the gyromagnetic ratio. $\mathbf{H_{eff}}$ is defined as the sum of all the internal and external magnetic fields acting on $\mathbf{M}$. If $\mathbf{H_{eff}}$ and $\mathbf{M}$ are not collinear and no damping is considered, a stable precession of the magnetization around the direction of the effective field is induced. The second term in Eq. (1.10) represents the damping torque that tends to align the magnetization towards the direction of the effective field, where α is the Gilbert damping and $\mathrm{M_S}$ the saturation magnetization of the FM layer.

It was already described in section 1.6 that the magnetization of the reference layer ($\mathbf{M_{ref}}$) is strongly stabilized by an RKKY interaction with an underlying exchange-biased FM layer, while the magnetization of the free layer ($\mathbf{M_{free}}$) is relatively free to rotate. Although showing an anti-parallel configuration, the magnetizations in Fig. 1.8 are not collinear. Instead, there is a small misalignment between them. That scheme aims to represent a real system for T $\neq$ 0 K, in which the internal energy

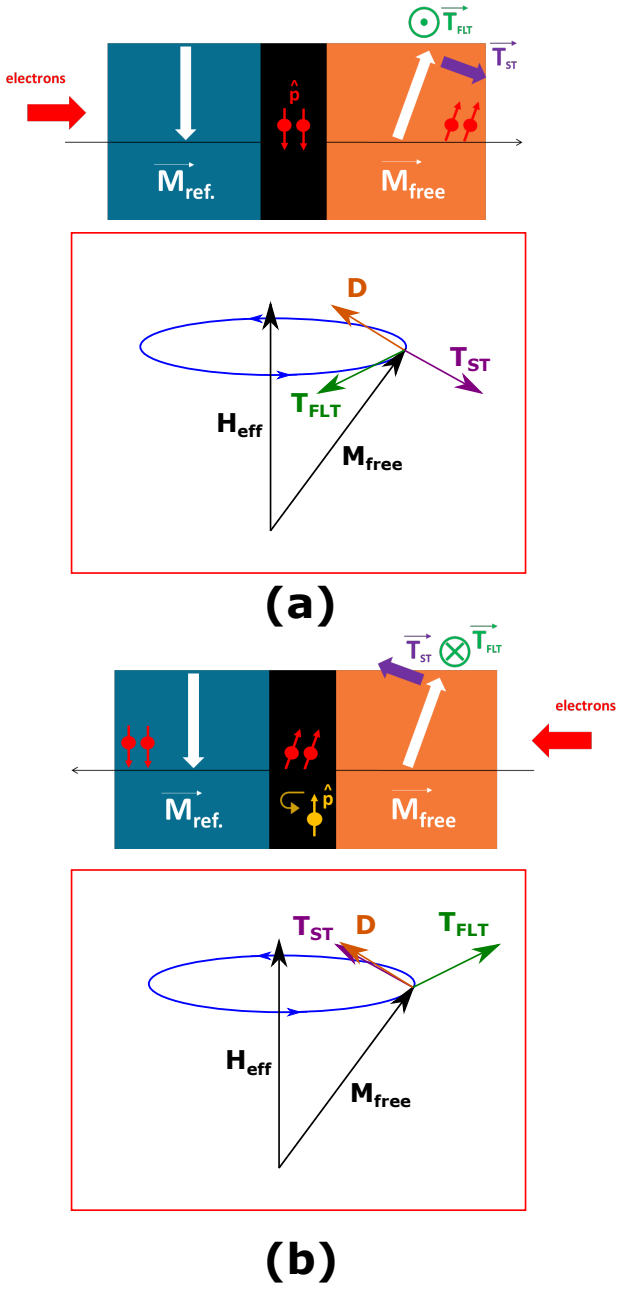


Figure 1.8: Illustration of the STT principle. The electrons travel (a) from the reference to the free layer, favouring the parallel configuration and (b) from the free to the reference layer, favouring the anti-parallel configuration. Below each MTJ illustration the dynamics of $\mathbf{M_{free}}$ is highlighted based on Eq. (1.11).

is enough to promote a small random precession of $\mathbf{M_{free}}$ around $\mathbf{H_{eff}}$ [69]. The thermal fluctuations are translated into a thermal magnetic field ($\mathbf{H_{th}}$) that varies randomly over time. $\mathbf{H_{th}}$ should be added to $\mathbf{H_{eff}}$ to give a non-deterministic behaviour for the precession of $\mathbf{M_{free}}$. The effect of thermal fluctuations is only being considered for $\mathbf{M_{free}}$, but even if it is extended to $\mathbf{M_{ref}}$ the conclusion is the same: at any time, there is a high probability to have non-collinear magnetizations for the MTJ depicted in Fig. 1.8, either for a parallel or anti-parallel configuration. For the MTJ shown in Fig. 1.8, as it will be explained below, the condition of having non-collinear magnetizations is mandatory to promote the STT effect.

In Fig. 1.8a, the electrons become majority spin-polarized according to $\mathbf{M_{ref}}$ while propagating through the reference layer. After tunneling, the electrons will realign their spins, now according to $\mathbf{M_{free}}$. Nevertheless, there has to be conservation of the angular momentum, so a change of the spin-polarization is followed by a variation of the local magnetization, which is translated into a spin torque, Slonczewski torque $\mathbf{T_{ST}}$, that tends to rotate $\mathbf{M_{free}}$ and promote a parallel configuration. As the electric current is inverted (Fig. 1.8b), the electrons become spin-polarized according to $\mathbf{M_{free}}$. At the interface between the barrier and the reference layer, the electrons spin-polarized in the opposite direction of $\mathbf{M_{ref}}$ will be in majority "reflected" back to the free layer. This is a consequence of the low density of states at the Fermi level that the reference layer presents for electrons with a spin state opposite to $\mathbf{M_{ref}}$. By STT effect, the accumulated electrons in the free layer will tend to rotate $\mathbf{M_{free}}$ away from $\mathbf{M_{ref}}$, in this way sustaining even more the existent anti-parallel configuration. At this point, it is clear that the direction of the electric current has an important role in defining the rotation of $\mathbf{M_{free}}$ towards (parallel configuration) or away (anti-parallel) from $\mathbf{M_{ref}}$. This process allows to change the magnetization of the free layer based exclusively on the electric current that passes through the junction. Since $\mathbf{M_{ref}}$ is stabilized, this process does not admit any change in the magnetization of the reference layer.

Beyond $\mathbf{T_{ST}}$, Fig. 1.8 shows an additional STT component $\mathbf{T_{FLT}}$, perpendicular to the plane defined by both magnetizations. This out-of-plane component is called field-like torque [70], since it acts as an external magnetic field with the direction of $\hat{\mathbf{p}}$, so that it can modify the energy landscape seen by $\mathbf{M_{free}}$. Inserting the STT effect into Eq. (1.10), the time behaviour of the free layer magnetization is given by [20, 68]

$$\frac{d\vec{M}_{free}}{dt} = -\gamma\vec{M}_{free} \times \vec{H}_{eff} + \frac{\alpha}{M_S}\vec{M}_{free} \times \frac{d\vec{M}_{free}}{dt} + (\vec{T}_{ST} + \vec{T}_{FLT}), \tag{1.11}$$

being

$$\vec{T}_{ST} = -\eta_{ST} \cdot [\hat{m}_{free} \times (\hat{m}_{free} \times \hat{p})] \tag{1.12}$$

and

$$\vec{T}_{FLT} = -\eta_{FLT} \cdot (\hat{m}_{free} \times \hat{p}), \tag{1.13}$$

where $\hat{\mathbf{m}}_{\mathbf{free}}$ and $\hat{\mathbf{p}}$ are unit vectors in the direction of $\mathbf{M_{free}}$ and of the spin-polarization, respectively. Each STT component has a spin-torque efficiency, i.e. η_{ST} and η_{FLT}, whose magnitude depends on the system parameters, namely the spin-polarization, the current density and the angle between $\hat{\mathbf{m}}_{\mathbf{free}}$ and $\hat{\mathbf{p}}$.

Based on Eq. (1.12), it is clear that $\mathbf{T_{ST}}$ may either counter (Fig. 1.8a) or reinforce the damping torque $\mathbf{D}$ (Fig. 1.8b) depending on the current direction. When $\mathbf{T_{ST}}$ counters the damping, the dynamics of $\mathbf{M_{free}}$ will be dictated by the current magnitude. If the current is below the critical value for

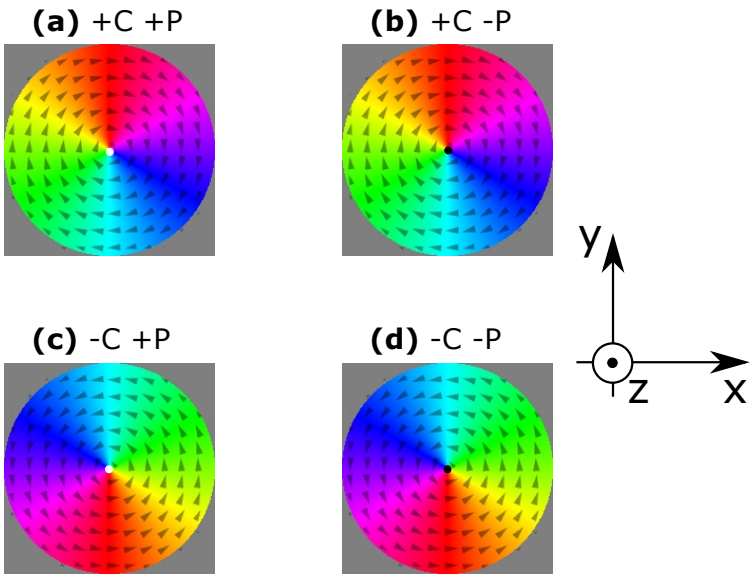


Figure 1.9: Possible combinations for a remanent vortex state based on its two main properties: chirality (C) and polarity (P). A positive chirality (+C) denotes a clockwise circulation of the magnetic moments, whereas a positive polarity (+P) is associated with magnetic moments at the vortex core pointing in the positive out-of-plane direction (i.e. white dot at the core region). Vice-versa for -C and -P.

switching, $\mathbf{T_{ST}}$ opposes the damping but it is weaker in magnitude, so the effective damping torque is decreased, but it cannot counter the damping motion that tends to align $\mathbf{M_{free}}$ with the effective field. If the current is increased below the switching threshold, $\mathbf{T_{ST}}$ is able to overcome the damping torque, increasing the angle between $\mathbf{M_{free}}$ and the effective field. Nevertheless, $\mathbf{T_{ST}}$ and $\mathbf{D}$ are angular dependent, so a possible dynamic equilibrium can be achieved for a certain angle. In that case, the energy gained from STT is balanced by the energy lost from damping, so that a self-sustained precessional motion is achieved, which is the basics of a STNO. If the current magnitude goes above the switching threshold, the $\mathbf{T_{ST}}$ magnitude is sufficient to tilt the magnetization for switching, as it should happen in a STT-MRAM. As for $\mathbf{T_{FLT}}$, experimental results in MgO-based MTJs show that η_{FLT} goes up to $25\,\% - 40\,\%$ of η_{ST} [71–73], which means that it cannot be generally discarded. In fact, it has been demonstrated that $\mathbf{T_{FLT}}$ plays an important role in MgO-based MTJs, namely in STT-induced domain-wall motion [73] and in the dynamics of high order vortex modes [74].

1.7.2 STT-induced dynamics in a FM layer with a magnetic vortex

A spin-polarized current may also promote a precessional motion in magnetic materials with a non-uniform magnetization distribution. To minimize the energy of the magnetic system, the material may present different magnetic distributions, depending on its dimensions. For larger samples (i.e. macroscopic dimensions), a multi-domain configuration is obtained. As the sample shrinks, the system evolves to a single domain configuration with a uniform magnetization, whose magnetic moments

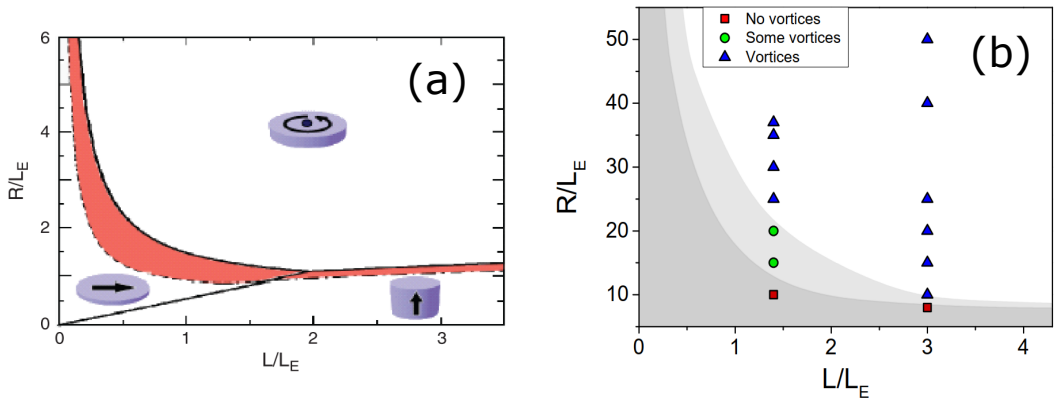


Figure 1.10: (a) Magnetic phase diagram of a patterned FM layer, where the radius (R) and the thickness (L) are normalized to the exchange length $\mathrm{L_E} = 18\mathrm{nm}$, obtained from calculations. The red area highlights the range of the dimensions where the vortex is metastable. Adapted from [75]. (b) Magnetic phase diagram obtained from two different patterned MTJ wafers presenting a different thickness for the free layer, i.e. 9 nm and 17 nm. Exchange length, $\mathrm{L_E} = 5\,\mathrm{nm}$ [76].

can be more or less twisted (according to the material geometry and dimensions) to minimize the demagnetizing energy. Here, the interest relies on the non-uniform magnetic states that the material presents for intermediate dimensions, specifically the vortex, defined as a curling of in-plane magnetic moments with a progressive increase of their out-of-plane component towards the vortex core. Its magnetic shape is characterized by two main topological numbers. Figure 1.9 shows the possible vortex states based on the four combinations of those numbers. The chirality C indicates the sense of the magnetic moments circulation around the core, which can be either clockwise ($\mathrm{C} = +1$ or +C) or counter-clockwise ($\mathrm{C} = -1$ or -C). The polarity P specifies the out-of-plane direction of the core, i.e. $\mathrm{P} = +1$ or +P for $+\hat{\mathrm{z}}$ and $\mathrm{P} = -1$ or -P for $-\hat{\mathrm{z}}$.

At the remanent state, a stable vortex may be obtained for magnetic materials by engineering their dimensions [77–80]. For a patterned circular FM layer, whose magnetic phase diagram is depicted in Fig. 1.10a, the L/R ratio must be properly chosen to obtain a vortex [81], where L is the thickness and R the radius of the layer. L and R are normalized to the exchange length $\mathrm{L_E}$ [82] of permalloy, so that they are small enough to consider the formation of magnetic domains and domain walls energetically unfavoured. For $\mathrm{R} \leq \mathrm{L_E}$ (if the layer is too thick), it acquires an out-of-plane magnetization, whereas for $\mathrm{L} \leq \mathrm{L_E}$ (if the layer is too flat), an in-plane magnetization is achieved. Naturally, the vortex state appears for an intermediate L/R ratio. Previous experimental results obtained at INL [76] show a good agreement with the calculations (see Fig. 1.10b).

External perturbations lead to interesting dynamics for a magnetic vortex, namely by application of an external magnetic field [84] or, more importantly, by STT effect through a spin-polarized current, allowing the excitation of its fundamental gyrotropic mode [29, 85]. Figure 1.11 illustrates the gyrotropic mode, characterized by a precession with constant amplitude of the core around the center of the magnetic medium. In MgO-based MTJs, considering the chosen materials and geometries, the

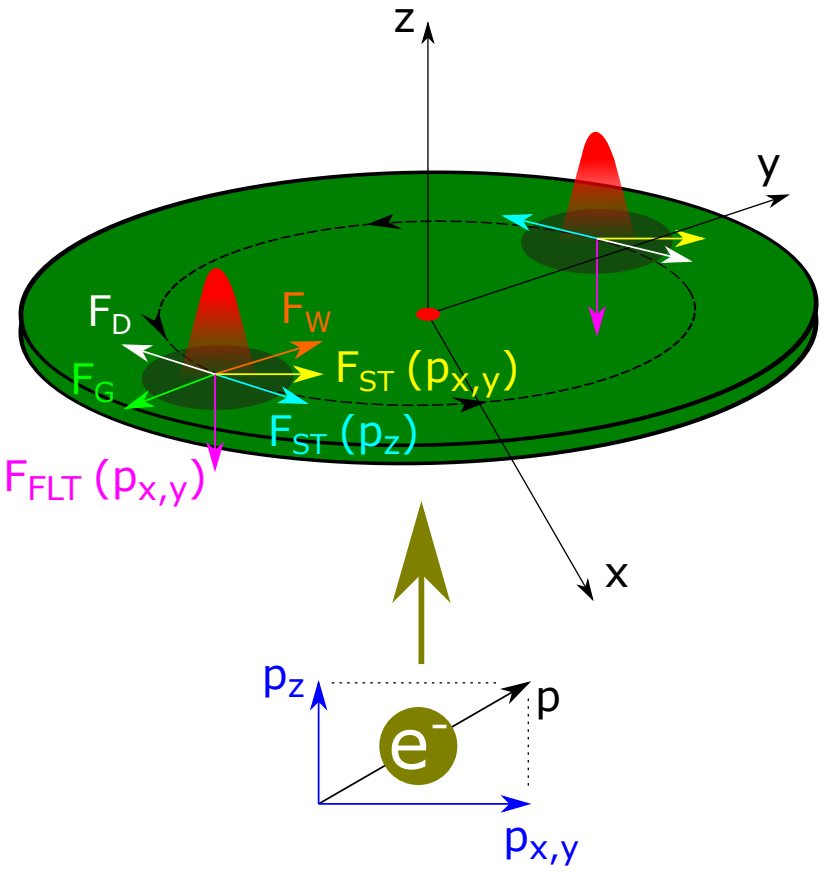


Figure 1.11: Illustration of the different forces acting on the vortex core during gyrotropic dynamics induced by a spin-polarized current with in-plane ($\mathrm{p_{x,y}}$) and out-of-plane ($\mathrm{p_z}$) components. The forces are represented based on the assumption of a uniform polarizer. The core is represented at two positions, one semi-cycle away from each other. Adapted from [83].

fundamental vortex precession tends to fall into the MHz range [86]. This low frequency dynamics must satisfy the Thiele equation [87]. Inserting the STT effect, the modified equation, showing the forces acting on the vortex core, becomes

$$\vec{F}_G + \vec{F}_W + \vec{F}_D + (\vec{F}_{ST} + \vec{F}_{FLT}) = 0 \tag{1.14}$$

where

$$\vec{F}_G = \vec{G} \times \frac{d\vec{X}}{dt}\,, \tag{1.15}$$

$$\vec{F}_W = -\frac{\partial W(\vec{X})}{\partial \vec{X}}\,, \tag{1.16}$$

and

$$\vec{F}_D = -D\frac{d\vec{X}}{dt}\,. \tag{1.17}$$

X = (x, y) is the vortex core in-plane position, D the damping factor that quantifies the "resistance" of the system to the gyroscopic motion, W(**X**) = W(0) + 1/2 κ $|\mathbf{X}|^2$ the potential energy of the shifted vortex and $\mathbf{G} = -\hat{\mathbf{z}}\ 2\pi \mathrm{pLM_S}/\gamma$ the gyrovector, being κ the vortex stiffness, $\hat{\mathbf{z}}$ the unit vector in the direction perpendicular to the layer surface, p the core polarity, $\mathrm{M_S}$ the saturation magnetization and γ the gyromagnetic ratio. $\mathbf{F_{ST}}$ and $\mathbf{F_{FLT}}$ come from the Slonczewski and field-like torque, respectively. After a perturbation and without damping, the first two terms on the left side of Eq. (1.14) represent the original Thiele equation, i.e. an ideal vortex core rotates indefinitely in a perfect circular trajectory with a radius for which the gyrotropic force ($\mathbf{F_G}$) balances the restoring force ($\mathbf{F_W}$) that tends to minimize the energy of the system. The existence of $\mathbf{F_G}$ can be understood making the analogy with the Magnus force in aero-dynamics, where the rotation of a moving object in a fluid tends to change its linear velocity vector.

Figure 1.11 also shows the different forces acting on the vortex core in the linear regime, i.e. $\mathbf{F_D}$ and $\mathbf{F_W}$ are linear for a small displacement of the vortex core position, as defined in the work of Dussaux *et al.* [83]. The perturbation comes from an applied DC current with a spin-polarization

$$\vec{p} = \vec{p}_{x,y} + \vec{p}_z \tag{1.18}$$

where $\mathbf{p_{x,y}}$ and $\mathbf{p_z}$ are the in-plane and out-of-plane components, respectively. Considering the energy dissipation of the vortex core during its rotation, the STT forces acting on the core are given by [83]

$$\vec{F}_{ST} = \vec{F}_{ST}(p_z) + \vec{F}_{ST}(p_{x,y}) = \frac{h\,|\vec{p}|\,J}{4\,|e|}\,(\,|\vec{p}_z|\,|\vec{X}|\,\hat{\mathbf{u}}_\theta + |\vec{p}_{x,y}|\,ln(2)\,b\,C\,\hat{\mathbf{p}}_{\mathbf{x,y}}\,) \tag{1.19}$$

and

$$\vec{F}_{FLT}(p_{x,y}) = -\frac{h\,|\vec{p}|\,J}{4\,|e|}\,C\,\lambda\,R\,\xi\,(\hat{\mathbf{z}} \times \hat{\mathbf{p}}) \tag{1.20}$$

where h is the Planck constant, e the electron charge, J the current density, $\hat{\mathbf{u}}_\theta$ the unit vector tangent to the vortex trajectory, $\hat{\mathbf{p}}_{\mathbf{x,y}}$ the unit vector in the direction of $\mathbf{p_{x,y}}$, b the vortex core radius, C the vortex chirality, R the vortex radius, ξ the relative efficiency of the field-like torque in relation with the Slonczewski torque and λ the mean in-plane magnetization increase with the vortex shift from remanence (at first order approximation, $\lambda = 2/3$). Coming from the Slonczewski torque, $\mathbf{F_{ST}}(\mathbf{p_z})$ promotes the gyrotropic rotation of the core and depends directly on the existence of an out-of-plane component for the spin-polarization. On the other hand, the in-plane component leads to an additional force $\mathbf{F_{ST}}(\mathbf{p_{x,y}})$ associated with the Slonczewski torque and to $\mathbf{F_{FLT}}(\mathbf{p_{x,y}})$ associated with the field-like torque. As depicted in Fig. 1.11, these two additional components tend to displace the core from its trajectory led by $\mathbf{F_{ST}}(\mathbf{p_z})$. For a uniform polarizer, i.e. J and $\mathbf{p}$ constant in time and space, $\mathbf{F_{ST}}(\mathbf{p_{x,y}})$ and $\mathbf{F_{FLT}}(\mathbf{p_{x,y}})$ are constant over the oscillation cycle, so that, as depicted in Fig. 1.11, the energy gain caused by $\mathbf{F_{ST}}(\mathbf{p_{x,y}})$ and $\mathbf{F_{FLT}}(\mathbf{p_{x,y}})$ at one point of the cycle is lost one semi-cycle after. By considering the Oersted field created by the DC current, another important result from Ref. [83] is the threshold current density $\mathrm{J_{th}}$ for a sustained vortex oscillation, given by

$$J_{th} = \frac{D\,\frac{k_{ms}}{|\vec{G}|}}{\frac{h\,|\vec{p_z}|\,|\vec{p}|}{4\,|e|} - D\,\frac{k_{Oe}}{|\vec{G}|}}. \tag{1.21}$$

In Eq. (1.21), $\mathrm{J_{th}}$ depends on the vortex stiffness κ, given by

$$\kappa = k_{ms} + k_{Oe}\,J = \frac{10}{9}\,\mu_0\,M_S^2\,\frac{L^2}{R} + [0.85\,C\,\mu_0\,M_S\,R\,L]\,J. \tag{1.22}$$

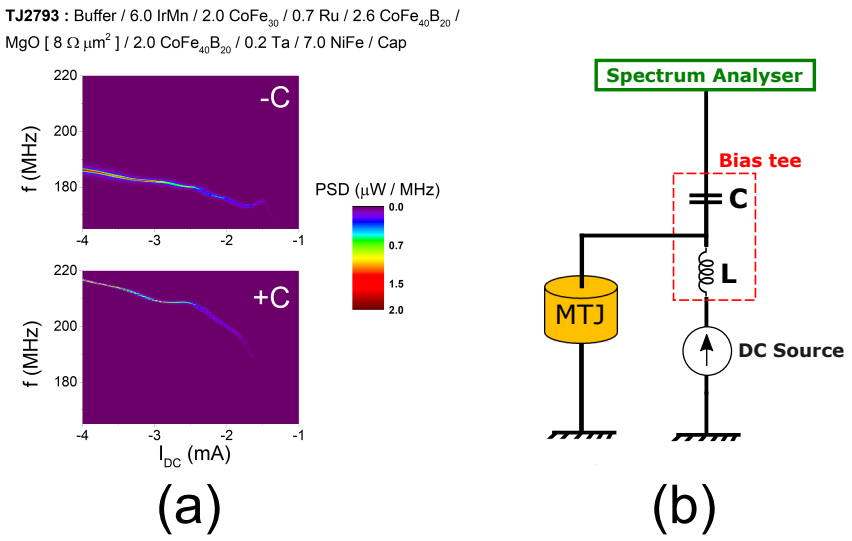


Figure 1.12: (a) Power spectral density (PSD) measured as a function of the frequency and DC current applied through an MTJ with a nominal diameter of 300 nm. The measurement is performed when the vortex of the free layer has a negative (top) and a positive (bottom) chirality at zero field. The MTJ stack is also described on top, where the thickness is presented in nanometers. (b) Illustration of the experimental setup.

So, the vortex stiffness has two distinct contributions: $\mathrm{k_{ms}}$ coming from the magnetostatic energy and $\mathrm{k_{Oe}}$ coming from the Oersted field confinement. Considering that $\mathrm{k_{Oe}}$ depends on the vortex chirality, Eq. (1.21) predicts two different $\mathrm{J_{th}}$ for vortices with opposite chiralities. A similar conclusion can be drawn from the resonance frequency that, for a stable precession, is given by

$$f = \frac{1}{2\pi}\frac{\kappa}{G} = \frac{1}{2\pi}\frac{k_{ms} + k_{Oe}\,J}{G}, \tag{1.23}$$

which should also be different for opposite chiralities. These calculations are only true for small displacements of the vortex core, but their qualitative conclusion - that the chirality leads to a splitting of the vortex dynamics - remains valid for analyses that admit a larger core displacement (i.e. non-linear regime), as performed still in Ref. [83] or, more recently, in the work of Araujo *et al.* [88]. At INL, this frequency splitting has been experimentally verified in our MgO-based MTJs. Figure 1.12a shows the power spectral density (PSD) of an MTJ device with a diameter of 300 nm and a vortex magnetic state in the free layer, as a function of the frequency and DC current. The measurement is performed for the two chiralities and the frequency splitting is evident through all the DC current domain. The spectra is collected with a spectrum analyser after filtering through a bias tee (Fig. 1.12b). The vortex dynamics are obtained at zero in-plane and perpendicular fields, which go against Eqs. (1.19) and (1.20) that predict a non-zero perpendicular component of the spin-polarization for steady-state oscillations, if a uniform planar polarizer is considered. In fact, as described on top of Fig. 1.12a, the reference layer of CoFeB (working as the polarizer) is designed with a thickness of 2.6 nm,

so that it presents an in-plane uniform magnetization at remanence. So, in our understanding, the zero-field oscillations appear as a consequence of having a non-uniform polarizer during a steady-state precession [89]. Going back to Eqs. (1.19) and (1.20), if a non-uniform polarizer is considered, $\mathbf{F_{ST}}(\mathbf{p_{x,y}})$ and $\mathbf{F_{FLT}}(\mathbf{p_{x,y}})$ do not necessarily cancel over the oscillation cycle, since they will vary in accordance with the magnetization distribution of the polarizer. Many experimental reports have already shown that, in the absence of a perpendicular field, it is possible to obtain STT-induced gyrotropic oscillations with a planar polarizer [34, 85, 90–92], which are generally attributed to the non-uniform magnetic distribution of the polarizer. Figure 1.13 shows simulated results, performed in the CPU-based OOMMF software [93], of the oscillation amplitude of a vortex nanodisk as a function of the DC bias current density. The inset illustrates the non-uniform magnetic configuration of the polariser, which allows the vortex steady-state dynamics at zero perpendicular field. Regardless of the exaggeration in defining such a pronounced C-state polariser, experimentally, the manipulation of the polarizer can happen when its magnetization is susceptible to be modified with the same DC current that is used to promote the gyrotropic oscillation in the free layer [91].

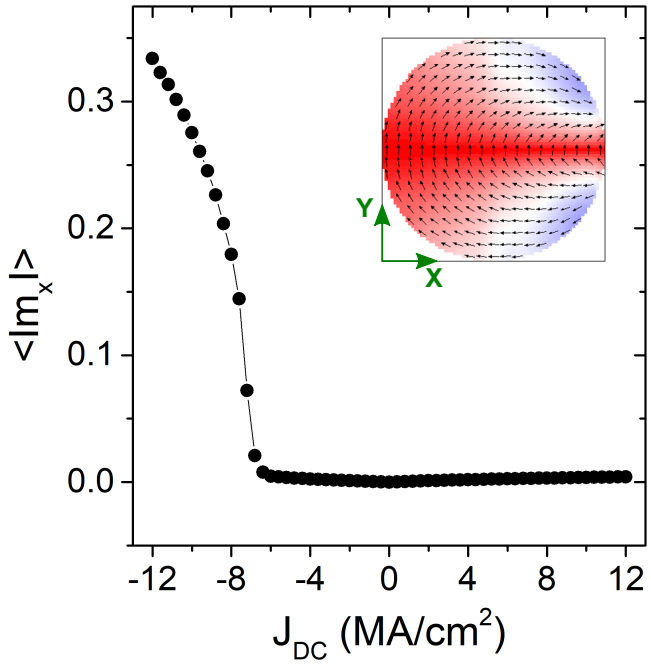


Figure 1.13: Amplitude of the steady-state oscillation (average value of the magnetization component in the xx axis) presented as a function of the applied DC bias current density. The free layer is simulated as a circular nanodisk with a vortex magnetic state, a diameter of 300 nm and a thickness of 9.0 nm. The inset shows the magnetic configuration of the non-uniform polariser. The simulations were performed at zero perpendicular field.

Chapter 2

Experimental techniques

2.1 Sputtering deposition systems

In majority, sputtering systems were used for deposition of the samples presented in this thesis. The working mechanism of the sputtering systems used at INL may be generally illustrated in Fig. 2.1. Sputtering is a physical vapour deposition (PVD) technique based in a linear momentum transfer between ions of a plasma and a target material. The process starts with the insertion of an inert gas flux (usually Ar) inside a vacuum chamber. The use of an inert gas is related with its low chemical reactivity. The plasma is created by applying either a DC or a RF signal, between the target and a grounded shield. In DC sputtering, the target is biased with a negative voltage, so that the electric field favours the acceleration of the Ar cations towards the target. If the linear momentum is large enough, the collision with the target may lead to the removal of material and to its consequent deposition in the substrate, which may be static or moving periodically below the target (as depicted in Fig. 2.1). RF sputtering is used to deposit insulating materials, so the build-up of charges in the target surface can be prevented. In order to optimize the sputtering process, water cooled magnets are placed below the target, thus creating the magnetron configuration. The magnets allow to confine the free electrons of the plasma along the magnetic field lines. Some of these electrons will have enough linear momentum to ionize Ar atoms, so the plasma can be maintained near the target. Two major advantages of the magnetron sputtering are clear: plasma ignition at lower Ar concentration (i.e. at a lower Ar flux) and higher deposition rates. The most visible disadvantage is the formation of an inhomogeneous target as the same is sputtered. As depicted in Fig. 2.1, the magnetic field lines lead to regions where the Ar ionization is higher, which are the same regions above which the target wear is larger.

At INL, two fully computer controlled Timaris sputtering tools were used: the Four-Target-Module (FTM) and the Multi-Target-Module (MTM) clusters.

2.1.1 Timaris sputtering tools

The MTM and FTM sputtering tools are PVD systems by DC/RF magnetron sputtering. At INL, these sputtering tools are constituted by a cassette module, a transport module, a soft-etch/oxidation module and a multi-target PVD module. The cassette module uses a 25-slot cassette for 200 mm wafer insertion. The transport module allows to drive the wafer between modules by using a robot arm. The

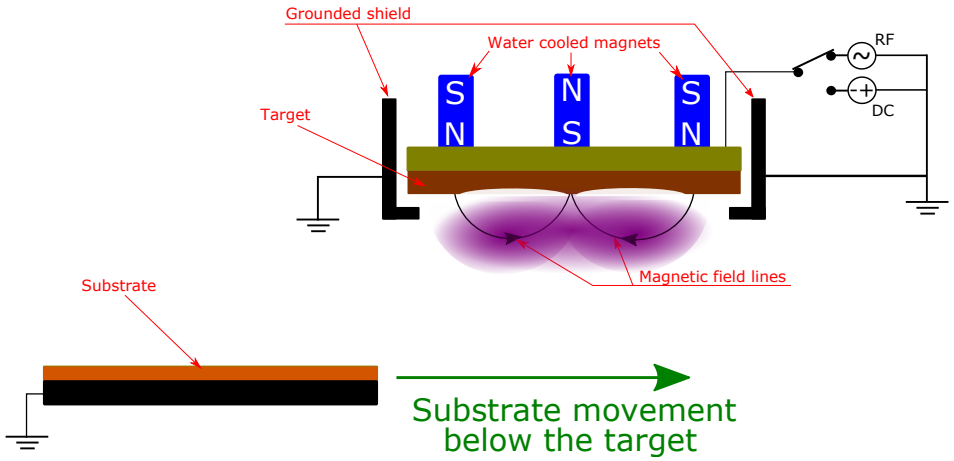


Figure 2.1: Illustration of the magnetron sputtering principle. The purple region below the target represents the plasma ignition. The non-static substrate configuration is in accordance with the sputtering systems used at INL.

soft-etch is a pre-cleaning module for RF sputter etching. It aims to remove undesired molecules (e.g. residual water) or native oxides from the wafer surface that could affect the deposition. Moreover, the pre-cleaning module is combined with an oxidation module, used to oxidize metallic thin films.

In the case of MTM, the multi-target PVD module, an ultra-high vacuum (UHV) deposition chamber (base pressure of $\sim 8 \times 10^{-9}\,\mathrm{Torr}$) allocates 10 cathodes available for sputtering targets (Fig. 2.2a). The MTM was mainly used for the MTJ stack depositions. The targets configuration gives the possibility to perform the MTJ deposition without UHV breaking, since after the deposition of one layer, the sputtering target can be simply switched in order to deposit the next layer.

In the case of FTM, the PVD module is an UHV chamber (base pressure of $\sim 8 \times 10^{-9}\,\mathrm{Torr}$), where four cathodes linearly disposed can host up to four targets (only three are currently mounted, as depicted in Fig 2.2c). The FTM was mainly used for the passivation (i.e. $\mathrm{AlO_x}$) and metalization [i.e. $\mathrm{Al_{98.5}Si_{1.0}Cu_{0.5}}$ and $(\mathrm{Ti_{10}W_{90}})_{100-x}\mathrm{N_x}$ (atomic %)] steps during the nanofabrication process of MTJs. TiWN is deposited by reactive sputtering [94], which means that during the sputtering deposition, a $\mathrm{N_2}$ flux is mixed with Ar in the plasma, thus promoting the nitrogen incorporation in the deposited material. While AlSiCu gives low resistive aluminum-based electric contacts, TiWN has a set of advantages:

1. As the topmost layer, it is a low reactive alloy that prevents the corrosion of the underlying structure, namely in the contact pads and capping structure of the MTJ devices, during different steps of the nanofabrication - e.g. photoresist ashing (section 2.4.2) and optical lithography development (section 2.4.1).

2. Being in majority constituted by tungsten (i.e. a heavy element), it prevents the diffusion of light elements [e.g. aluminum of the sacrificial structure (section 3.2.2)] between layers.

3. The addition of nitrogen gives a dark appearance to the alloy, which minimizes the reflected light during DWL exposures (section 2.4.1). So, TiWN acts as a anti-reflective coating for sharper features in optical lithographies.

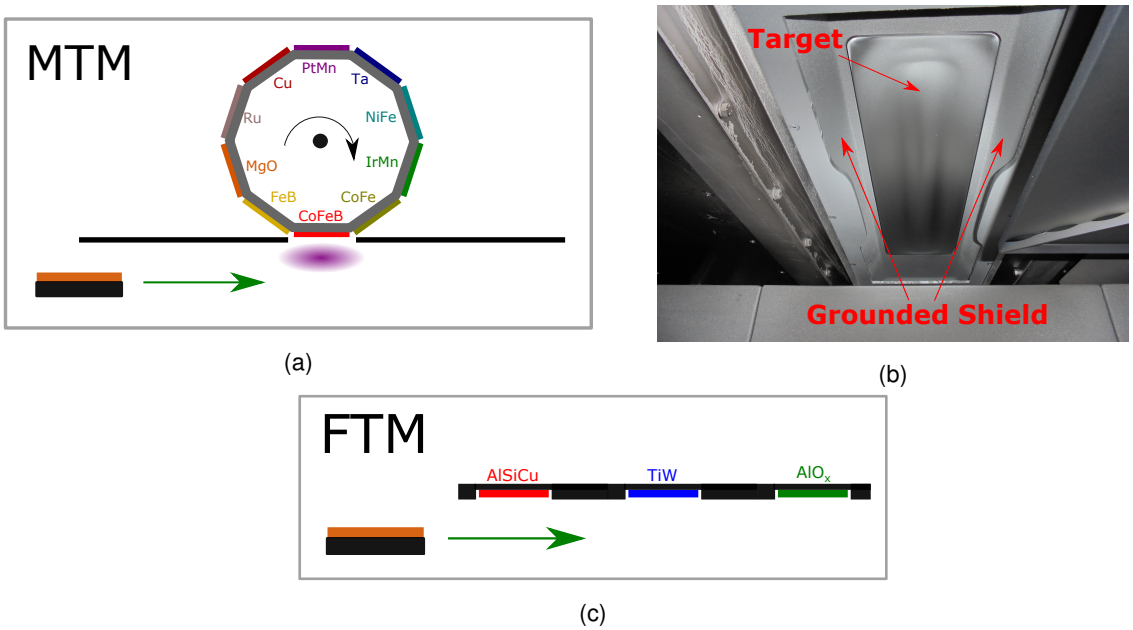


Figure 2.2: (a) Simple illustration of the 10 cathodes configuration in the UHV deposition chamber of MTM. The green arrow indicates the dynamic deposition with a non-static substrate. (b) Image inside the UHV chamber of the MTM selectable target and the corresponding grounded shield. As a consequence of the magnetron configuration, the target wear is not uniform. (c) Illustration of the three linearly disposed cathodes configuration in the UHV deposition chamber of FTM.

For both tools, the deposition goes as the substrate moves in a linear and cyclical path along the chamber, passing periodically below the stationary sputtering target. Therefore, an essential parameter to control the deposition rate is the linear velocity of the substrate (v), while the number of cycles (N) ultimately determines the total film thickness. For a specific power of the sputtering source (P), the final thickness t obtained for a deposited layer is given by

$$t = R_{dyn}\left(\frac{NP}{v}\right). \tag{2.1}$$

$\mathrm{R_{dyn}}$ is the dynamic deposition rate obtained from the calibration process, which is given by

$$R_{dyn} = \frac{t_c v_c}{N_c P_c}, \tag{2.2}$$

where $\mathrm{t_c}$, $\mathrm{N_c}$, $\mathrm{v_c}$ and $\mathrm{P_c}$ are the thickness, number of cycles, velocity and source power used in the calibration process of each material, respectively. A standard calibration process starts with the deposition of the material in a thermally oxidized Si wafer by choosing a set of deposition conditions (i.e. $\mathrm{N_c}$, $\mathrm{v_c}$ and $\mathrm{P_c}$). Then, a four-point-probe system is used to measure the sheet resistance over the wafer surface, thus obtaining $\mathrm{t_c}$ (from the sheet resistance, the thickness is calculated knowing the material resistivity). Table 2.1 shows examples of recipes used in both FTM and MTM tools. From now on, the variable deposition conditions $\mathrm{NP/v}$ (see Eq. 2.1) are referred as exposure, since they give an indication about how much the substrate was exposed to the plasma, so the larger the exposure, the thicker the deposited layer.

Material	t (nm)	N	v (mm/s)	P (kW)	Ar flow (sccm)	N_2 flow (sccm)
Ta	5	2	95	1.10	300	0
Ru	5	2	74	0.60	300	0
CuN_x	50	2	56	3.00	270	30
$IrMn_{80}$	20	1	47	2.60	300	0
$CoFe_{30}$	2	2	62	0.35	300	0
$CoFe_{40}B_{20}$	2	2	66	0.40	300	0
$NiFe_{19}$	7	2	43	0.70	300	0
AlO_x	100	75	20	1.50	200	0
$(TiW_{90})N_x$	15	2	23	1.00	200	40
$AlSi_{1.0}Cu_{0.5}$	250	20	48	2.25	200	0

Material	RA ($\Omega\mu m^2$)	N	v (mm/s)	P (kW)	Ar flow (sccm)
MgO	8.1	2	73	3.00	600
	21.7	2	67	3.00	600

Table 2.1: Examples of standard recipes used for sputtering deposition (nominal thickness t). The materials highlighted in red (blue) correspond to depositions at the MTM (FTM) tool. As explained in the main text, the MgO recipes are defined aiming a specific RA product. Each recipe contains: the number of cyclical paths below the target (N), the linear velocity of the substrate (v), the power of the sputtering source (P), the Ar flow and, for specific cases, the N_2 flow.

The calibration process for the MgO insulating barrier is different. Considering the importance of the RA product for the characterization of an MTJ, the calibration aims to control the RA product of the MTJ, rather than the thickness of the MgO. The well known exponential relation between the RA product and the thickness of the insulating barrier is given by [17, 64]

$$RA = B \cdot \exp(C \cdot t_{MgO}), \tag{2.3}$$

where B is the MTJ RA product without an MgO barrier, C an experimental constant and t_{MgO} the MgO thickness. Both B and C constants may be calculated if an $RA(t_{MgO})$ calibration is performed [64]. Using Eqs. (2.1) and (2.3), the RA product may be written as

$$RA = B \exp\left[D \cdot \frac{NP}{v}\right]. \tag{2.4}$$

Thus, using the CIPT method (section 2.6.3), it is possible to calculate the RA product for MTJs with different MgO exposures. Then, an exponential fit allows to calculate both B and D ($D = C \cdot R_{dyn}$). Table 2.1 shows the recipe parameters, including the exposure, used for the deposition of MgO with two distinct RA values.

A major advantage of the dynamic deposition is the possibility to deposit wedged thin films (i.e. films with a variable thickness along the wafer) by applying an acceleration to the substrate. For instance, the deposition of MTJs with a variable MgO thickness allows to study, in the same wafer, the dependence of several MTJ properties on the RA product [64, 95]. Based on Eq. (2.1), the thickness

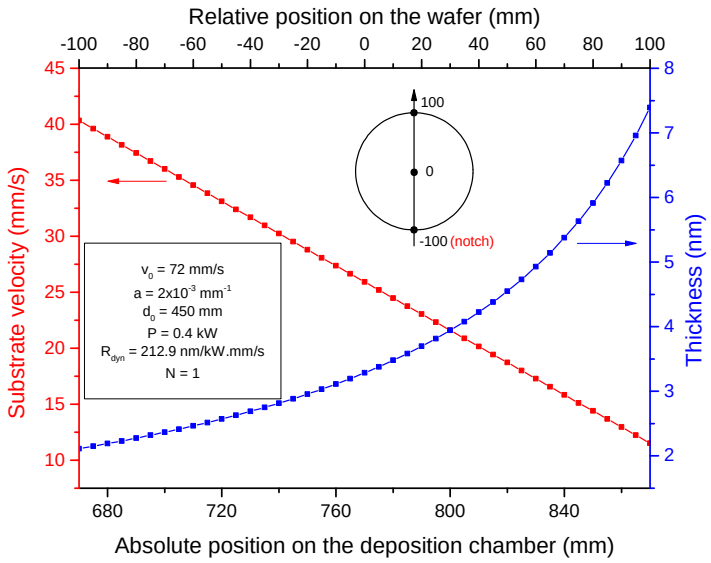


Figure 2.3: Thickness of an FeB layer and substrate velocity as a function of the wafer position along the notch.

as a function of the absolute position of the substrate at the deposition chamber (d) is given by

$$t(d) = R_{dyn}\left(\frac{NP}{v_0[1 - a(d - d_0)]}\right), \tag{2.5}$$

where $\mathrm{v_0}$ is the initial velocity of the substrate and a its spatial acceleration. The substrate starts at the absolute position $\mathrm{d_0}$, slowing down as it passes below the exposure region. A similar equation may be obtained for the RA product using Eq. (2.4). Figure 2.3 shows an example of the thickness profile obtained for the deposition of a wedged FeB layer.

Beyond calibration, the non-uniformity $(\mathrm{t_{nu}})$ of the deposition of each material is also a fundamental parameter to be measured. In a 200 mm wafer, it indicates how much the thickness differs from its average value over the full measurement area and it is given by

$$t_{nu} = \frac{t_{max} - t_{min}}{2 \times t_{av}}, \tag{2.6}$$

where $\mathrm{t_{max}}$, $\mathrm{t_{min}}$ and $\mathrm{t_{av}}$ are the maximum, minimum and average thicknesses over the measurement area, respectively. Figure 2.4 shows a thickness distribution of a Ru layer deposited by MTM in a 200 mm oxidized wafer. The non-uniformity value is in accordance with the best and typical results obtained by MTM deposition, i.e. non-uniformities below 5% in a minimum diameter of 6 inches (154.2 mm).

2.2 Plasma enhanced chemical vapour deposition

In addition to the PVD system, a chemical vapour deposition (CVD) process was also used for oxide deposition. In general, the solid state deposition material is a product of the chemical reaction, taking place in the deposition chamber, between the reactant gases. At INL, an SPTS MPX CVD tool was

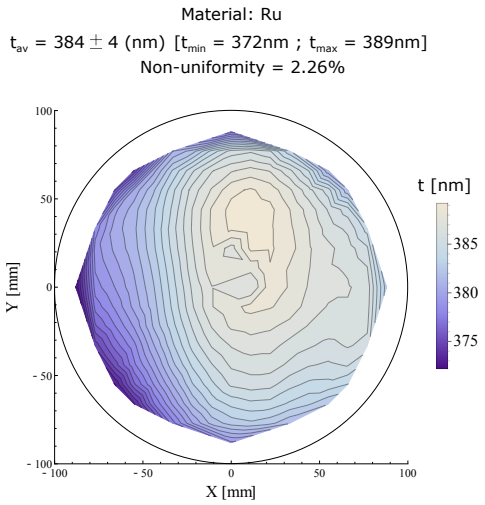


Figure 2.4: Uniformity measurement of a Ru layer deposited by MTM in a 200 mm Si oxidized wafer. The data was obtained by measuring the sheet resistance over the Ru surface. The map comprises an area with a diameter larger than 154.2 mm (i.e. larger than 6 inches).

used for that purpose. It is constituted by a double-slot loadlock, with a defined working pressure of 6×10^{-3} Torr, and a deposition chamber. The tool is set for the deposition of silicon oxide (SiO_2), silicon nitride (SiN_x) and amorphous silicon (a-Si). Specifically, the deposition is assisted by a plasma, in a process called plasma enhanced chemical vapour deposition (PECVD). A general illustration of a PECVD system is shown in Fig. 2.5. In the deposition chamber, a 13.56 MHz RF power is applied on a two parallel plates configuration; at the same time, the gases are introduced in the chamber. The capacitive coupling between the plates excites the reactant gases into a plasma, which promotes a chemical reaction and the consecutive deposition of the solid state material on the substrate below. The main advantage of this system is the decrease of the temperature for deposition, which is

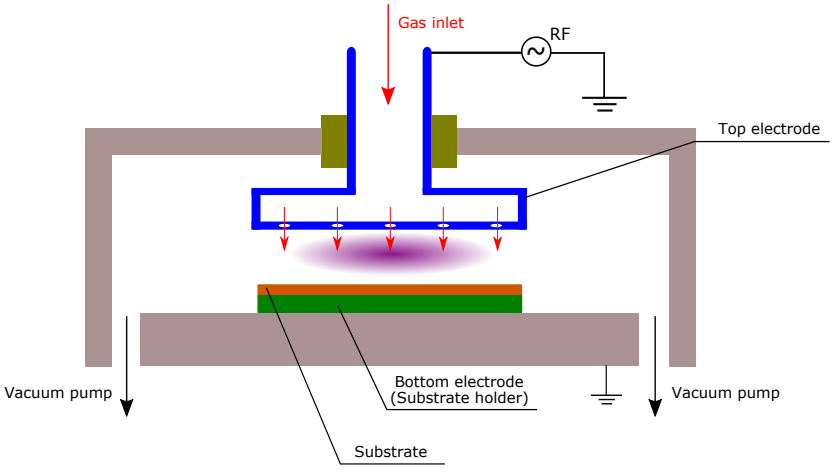


Figure 2.5: General illustration of the deposition chamber of a PECVD system. Insulation parts are represented in yellow.

PECVD conditions	SiO_2
Deposition rate (nm/min)	47
N_2O flux (sccm)	1420
NH_3 flux (sccm)	0
N_2 flux (sccm)	392
SiH_4 flux (sccm)	10
Setpoint pressure (Torr)	0.9
RF (MHz)	13.56
RF power (W)	30
Bottom plate setpoint temperature (°C)	300
Top plate setpoint temperature (°C)	250
Chamber setpoint temperature (°C)	75

Table 2.2: Setpoint conditions at the PECVD tool for the deposition of SiO_2 used in the MTJ fabrication.

below 350 °C for all the three materials. For instance, a temperature of $\sim$ 800 °C is necessary for the deposition of SiN_x by thermally activated CVD [96].

This tool was mainly used for the deposition of SiO_2 as a passivation material between the bottom and top contacts of the MTJ (sections 3.2.5 and 3.2.7). At previous processes, FTM AlO_x was the material used as passivation layer. Nevertheless, its deposition rate ($\sim 3.5\,\mathrm{nm/min}$) makes the sputtering deposition a very time consuming process. So, an oxide transition was made, after proving that the performance of the MTJ devices was not affected. Table 2.2 shows the SiO_2 deposition conditions. As it happens for the PVD systems, non-uniformities below 5% are obtained in a minimum diameter of 6 inches.

2.3 Ion beam milling (Nordiko 7500)

The ion beam milling is a dry etching technique and a purely physical process. In a general perspective, an ion beam is accelerated in a specific direction towards the surface of a target. Like in sputtering, this process leads to the removal of atoms in the target surface, but now the objective is only a controlled removal of the material.

At INL, the Nordiko 7500 ion milling tool is constituted by a cassette module, a transfer module and a working module. The cassette module has a 4-slot cassette for 200 mm wafer insertion, while the transfer module uses an automatic arm to insert and remove wafers from the working module. The working pressure of both modules is $\sim 10^{-6}\,\mathrm{Torr}$.

Figure 2.6 shows an illustration of the ion beam gun, placed inside the working module (standby pressure of $\sim 10^{-8}\,\mathrm{Torr}$, i.e. HV conditions) and responsible for the production of a collimated ion beam. A gas inlet allows the insertion of the inert gas (i.e. Ar) into the discharge vacuum chamber. At atmospheric pressure, an RF source produces an RF field that is transmitted to the chamber through a ceramic window and leads to the creation of the plasma by ionization of the gas. To maximize the power transfer to the plasma, an impedance matching between the RF source circuit and the plasma must be achieved. The matching is automatically performed by two adjustable capacitors, the first connected between the antenna and the RF source and the second between the RF source

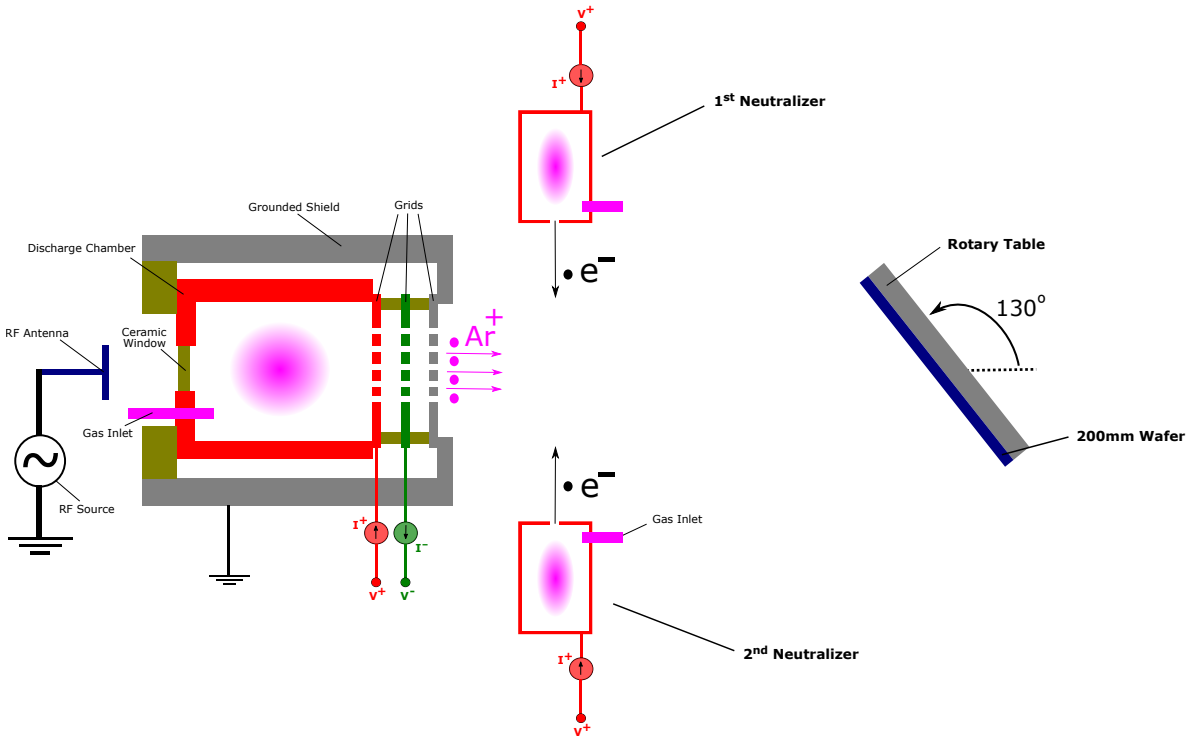


Figure 2.6: Illustration of the Nordiko 7500 ion beam gun, along with both neutralizers and the rotary table. Insulation parts are represented in yellow.

and the ground. A set of three aligned electrostatic grids at different electric potentials is used to accelerate and collimate the ion beam out of the discharge chamber. The acceleration region is located between the first (positively biased at V^{+}) and second (negatively biased at V^{-}) grids. The third grid is at ground state, so that each cation leaves the discharge chamber with an energy of $\mathrm{q_e V}^{+}$ ($\mathrm{q_e} = 1.6 \times 10^{-19}\,\mathrm{C}$). For each accelerated cation, there is an unpaired electron in the discharge chamber that is attracted to the positive biased grid. The electric current I^{+} (flowing between the discharge chamber and the ground) allows to measure the number of unpaired electrons per unit time, so that it indicates the current of the ion beam, which is equivalent to say that the ion beam power is given by $\mathrm{V}^{+}\mathrm{I}^{+}$. On the other hand, the electric current I^{-} (flowing between the negative grid and the ground) is indicative of the ion beam divergence. If an accelerated cation has a divergent trajectory, i.e. its parallel velocity component in relation with the grids is sufficiently large, it may collide or be attracted to the negative grid. For each cation, the negative grid must supply one electron for neutralization, so that an increase of I^{-} is equivalent to say that the divergence is increasing and, per unit time, more cations are being trapped by the negative grid.

Associated with the ion beam gun, Fig. 2.6 also displays two neutralizers disposed in a perpendicular position to the ion beam. Each neutralizer is a small discharge chamber where an applied potential is enough to ionize the inserted Ar gas. The resultant free electrons are then accelerated towards the perpendicular ion beam. The neutralizers allow to solve two main problems. First, they minimize the beam profile change due to the electrostatic repulsion between ions. Second, they cancel the accumulation of charges in the sample surface. This is quite critical when etching insulating or

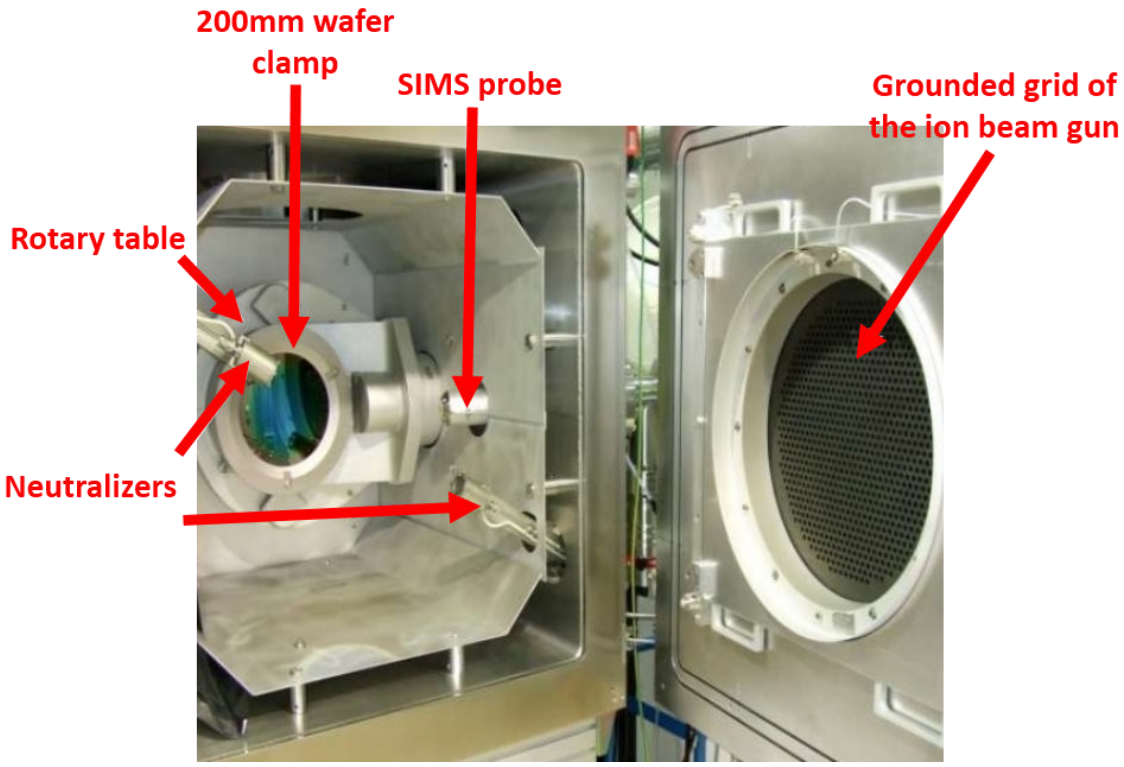


Figure 2.7: Working module of the Nordiko 7500. The ion beam gun is embedded in the chamber door. The rotary table is placed in a 90° position between the sample surface and the ion beam.

coated samples. Without neutralization, the ions bombardment leads to the accumulation of charges in the sample surface. In the limit, the electrostatic repulsion between the ion beam and the sample can be so large that the ions are unable to reach the sample, thus stopping the etching process. Moreover, in the case of coated samples, the accumulation of charges promotes electric discharges through the photoresist (PR), which leads to a brutal increase of temperature in specific regions of the wafer, thus changing the PR properties (e.g. burned PR). In this situation, a PR strip is difficult to achieve or may be even impossible with the standard processes, thus resulting in an aborted nanofabrication process. In some cases, the temperature may be sufficiently high to promote the local PR evaporation, which leads to the removal of material in regions that, in principle, should be protected by the mask.

Figure 2.7 shows the inside of the working module. The sample is fixed to a 200 mm wafer clamp, while a water cooled rotary table allows to rotate the sample (thus improving the milling uniformity) and change the incidence angle between the ion beam and the sample surface. As it is shown in Fig. 2.6, the recipes are always defined with an incidence angle larger than 90° between the beam direction and the horizontal position of the rotary table. This procedure aims to minimize the redeposition of material in the sample surface, after being etched.

The ion milling is a non-selective process, so that it is extremely important to choose the right stopping point by knowing, at each instant, what material is being etched. In the working module (Fig. 2.7), there is a secondary ion mass spectroscopy (SIMS) probe used for detection of the etched

chemical elements. In the probe, after the ionization of a fraction of the etched elements located in the working chamber, an applied magnetic field pushes the ions into parabolic paths that will vary according to their mass-charge ratio, so that different etched materials can be distinguished by the detector. Figure 2.8 shows how the SIMS probe can be used to perform the definition of an MTJ nanopillar. The data can be explained as follows:

- from the start, after 2 minutes, the first TiWN layer is removed;
- after 11 minutes, the AlSiCu is completely removed and the second TiWN layer starts to be etched;
- after 12 minutes, the capping structure is reached with the increase of the Cu and Ru signals;
- after 15 minutes, the buffer is reached, again, with the increase of the Cu and Ru signals;
- the process is stopped after 18 minutes, when the middle Ru layer of the buffer is reached.

Ion beam gun	RF Power (W)	Positive grid voltage (V)	Positive grid current (mA)	Negative grid voltage (V)	Negative grid current (mA)	Ar flux (sccm)
Setpoint	380	1000	370	-3200	-	60
Reading	393	997	369	-3287	-76	60.0

Neutralizer	Ar flux (sccm)	Current (mA)	Voltage (V)
Setpoint	5	430	-
Reading	5.0	439	155

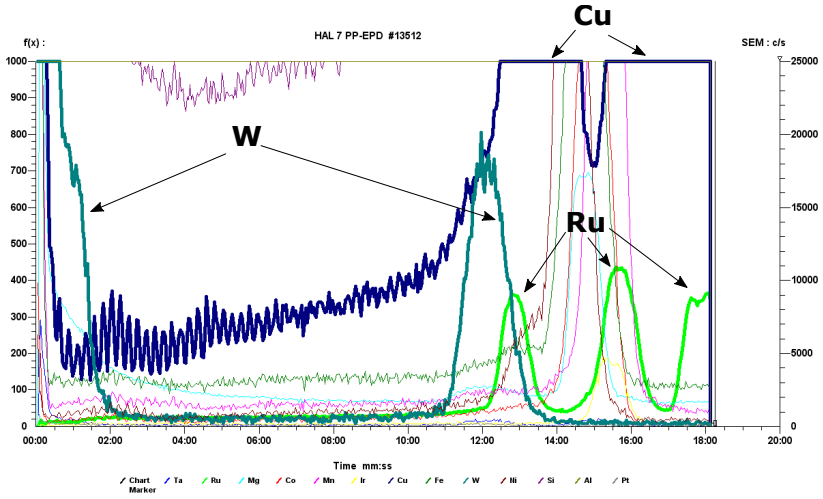
Table 2.3: Standard recipe parameters used at Nordiko 7500. Following the setpoint parameters, an example of a reading during a milling process is presented.

Material	**Etching rate (nm/min)**	
	130°	**170°**
$(Ti_{10}W_{90})_{100-x}N_x$	9	-
$Cu_{100-x}N_x$	13	-
SiO_2	18	8
$Al_{98.5}Si_{1.0}Cu_{0.5}$	25	-

Table 2.4: Etching rates of different materials, obtained using the standard recipe of Table 2.3 at two incidence angles.

Table 2.3 shows the parameters of the standard recipe used on the nanofabrication process. An example of the parameters reading is also shown. Table 2.4 shows the etching rates of different materials at two different angles, using the same recipe. During a milling process, the setpoint RF power is not a constant parameter. The process starts with an RF power of 380 W that changes over time, until the setpoint positive grid current is reached, i.e. the RF power is adjusted to have the setpoint ion beam power. The negative grid current cannot be a setpoint parameter, because it only

gives information about the ion beam divergence. The voltage applied to the neutralizer depends directly on the current and Ar flux chosen as setpoints. Although presenting two neutralizers, the neutralization of the beam was achieved by a single neutralizer. The initial optimization of the recipe parameters was based in two main criteria: etching rate and etching uniformity over a 200 mm wafer. As already referred, the ion beam power is given by $V^{+}I^{+}$, so that an increase of V^{+} and I^{+} leads to an increase of the etching rate. On the other hand, the beam profile, which affects the etching uniformity



(a)



(b)

Figure 2.8: (a) SIMS data obtained from a nanopillar definition process. The milling aims to etch the sample until the bottom contact (i.e. buffer structure below the MTJ). The Cu peaks are not shown in order to highlight the lower W and Ru peak signals. (b) Illustration of the sample stack after definition (thickness in nanometers). The TiWN layers can be recognized by the W signal and the CuN by the Cu signal. The milling definition was stopped at the third Ru peak, which corresponds to the middle Ru layer of the buffer. Starting from the bottom, the MTJ corresponds to the AFM / SAF / insulating barrier / free layer structure.

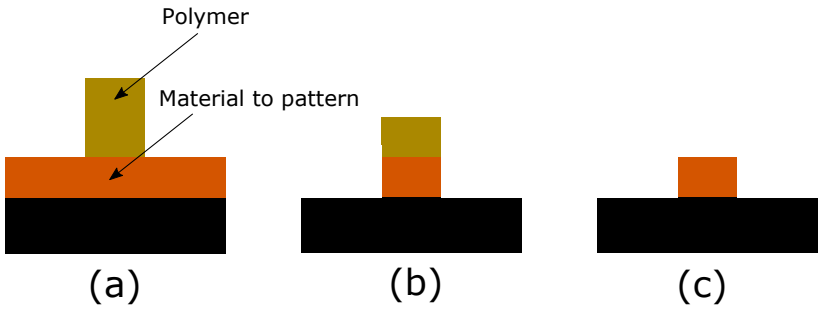


Figure 2.9: Etching fabrication. (a) After coating and according to the design, the polymer mask is set on the sample. (b) An etching technique is performed, removing both the exposed material and the polymer. (c) A strip technique allows to completely remove the polymer, thus obtaining the desired pattern in the sample.

over the wafer, depends on the relation between the setpoint parameters of the electrostatic grids (i.e. V^+, I^+ and V^-). In order to maintain the same profile, the parameters must follow [97, 98]

$$I^+ = \alpha(\Delta V)^{3/2} \ , \ \alpha > 0 \, , \tag{2.7}$$

where $\Delta\mathrm{V} = |\mathrm{V}^- - \mathrm{V}^+|$ and α is a constant that defines the beam profile. For the reading parameters of Table 2.3, $\alpha = 1.3 \times 10^{-6}\,\mathrm{A/V^{3/2}}$. For instance, starting from the standard recipe shown in Table 2.3, if the objective is to create a recipe with a lower etching rate and the same beam profile, both V^+ and I^+ must be chosen by solving a system of two equations where the power of the beam ($\mathrm{P} = \mathrm{V}^+\mathrm{I}^+$) is lower and α of Eq. (2.7) is maintained constant.

2.4 Lithography techniques

The fabrication process of MTJs in 200 mm Si wafers was based on both micro and nanofabrication steps. The microfabrication comprises all the optical lithography steps for the design of the micrometer-range structures ($\geq 2\,\mu$m), such as the MTJ electric contacts and field lines. The nanofabrication is a single electron-beam (e-beam) lithography step for the definition of the MTJ pillars that exhibit a diameter lower than 2 μm. There is a notable exception regarding the work described in chapter 6, where an extra e-beam lithography is performed to define the pillar top contacts.

In this thesis, the fabrication process was based on the ability to selectively remove material from the sample. For an optical (e-beam) lithography, the sample is coated with a photo-sensitive (e-beam-sensitive) polymer. When the etching is performed, the material will be removed only in the regions without the polymer mask (Fig. 2.9).

For the material removal, all the etching steps were performed using ion milling (section 2.3). Again, there is a notable exception described in chapter 7, where the microfabrication of the backside of the substrate is performed with reactive ion etching techniques. Regarding the mask fabrication, the method depends on the lithography type. For an optical lithography, all the fabrication steps made use of a direct write laser tool (section 2.4.1), while for the pillars definition, an e-beam lithography system was used (section 2.4.3).

2.4.1 Direct write laser lithography

A direct write laser (DWL) tool allows to transfer a pattern to a photo-sensitive polymer, generally called photoresist (PR). The first step is to coat the desired PR thickness on top of the process wafer (Fig. 2.10a). At INL, an automatic cluster track (Suss Microtec Gamma Cluster) incorporates a spin coating where recipes may be executed for 200 mm wafers, where the angular velocity of the spin coating controls the PR thickness. The cluster also incorporates two temperature-controlled plates. After coating, a high temperature plate performs the PR soft bake, while a room temperature plate finishes the process by returning the wafer to a lower temperature. It should be emphasized that before each coating step, a vapor prime oven (YES-310TA) performs a thermal treatment (i.e. surface dehydration) with hexamethyldisilazane (HMDS) to improve the PR adhesion to the substrate.

After coating, the wafer is aligned at the DWL table and the laser exposes the PR according to a digital mask made by AutoCAD software (Fig. 2.10b). The lithography is finished by the development step, where a proper developer is used to remove the exposed PR (Fig. 2.10c). The development is also performed in the Suss Microtec Gamma Cluster that also includes a spray development chamber. After development, the sample is ready for the milling (Fig. 2.10d) and strip (Fig. 2.10e) steps, respectively.

In the scope of this thesis, the positive AZ1505 was the most common PR used for DWL lithographies. Being positive means that the exposure makes the PR soluble to the developer (AZ400K with 1:4 dilution in water). Depending on the ion milling step, two different recipes were used, for the coating of 600 nm and 1035 nm of PR. While 600 nm is suitable for most of the steps, 1035 nm is necessary for larger milling times, as it happens for the trenches definition (section 3.2.3). In chapter 7, a thicker positive AZP4110 PR was exceptionally used for the backside patterning of the wafer.

At the INL cleanroom, the optical lithographies were performed using a DWL 2000 tool from Heidelberg Instruments. The tool incorporates an UV laser capable of exposing at 375 nm and 405 nm. In this thesis, all the exposures were performed at 405 nm, which is in accordance with the absorption spectrum of the AZ1505 PR [99]. After mounting the sample, a non-contact proximity sensor allows to perform a pneumatic autofocus on the sample, while two charge-coupled device (CCD) cameras (for macro and micro ranges) show an image of the surface. At each lithography step, cross-shaped marks are designed in the AutoCAD file, in order to guarantee the alignment between the structures to pattern in the present lithography and the structures already fabricated in the previous steps. Although presenting a minimum structure size of 0.7 μm, previous lithographies had shown the need to increase the bottom limit to $2\,\mu$m, in order to prevent overlapped structures after the exposure. At INL, the optimization of the exposure conditions are regularly performed. For each PR coated at a specific thickness, there is a pair of laser parameters that guarantee the best possible exposure: focus and dose (energy/area units) [100].

The main advantage of DWL is its flexibility. Considering the absence of a physical mask, the tool is adaptable to any mask that may be designed with AutoCAD. The main disadvantage is the time needed for exposure. A standard MTJ mask, with an area of $22 \times 22\,\mathrm{mm}^2$, may take between 10 and 15 minutes to expose.

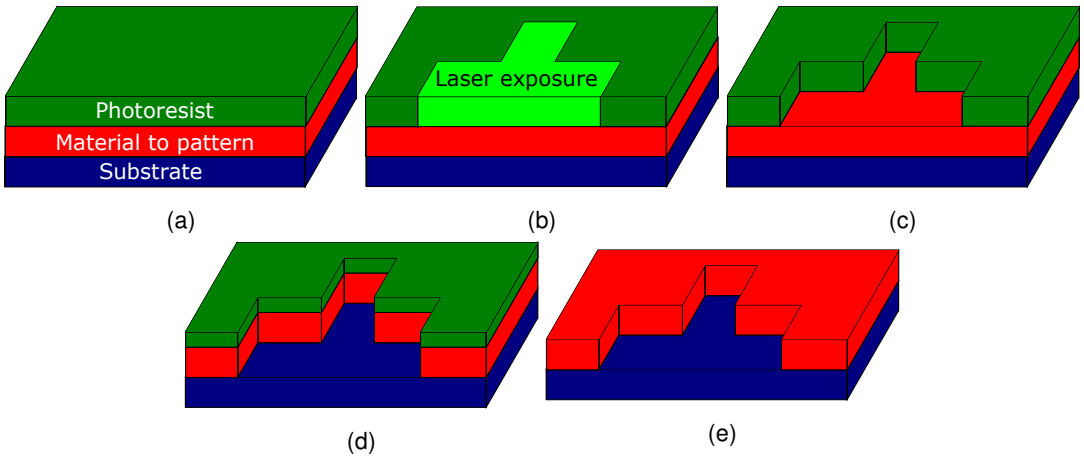


Figure 2.10: Microfabrication step by DWL lithography. (a) The material to pattern is coated with PR. (b) The laser exposure is performed according to the digital mask. (c) Considering a positive PR, the development leads to the removal of the exposed region. (d) The ion milling process removes the material where the PR was removed. (e) Finally, a PR strip (plasma asher or acetone bath) allows to make a complete removal of the PR, thus obtaining the desired pattern in the material.

2.4.2 Photoresist strip by plasma asher

Each optical lithography step is finished with the complete removal of the PR used for the mask design. For this aim, a straightforward wet stripping method is the application of ultrasounds when the sample is in an acetone bath. Although effective, this method takes a long time to be performed (typically, more than 2 h), which may be critical for samples presenting up to eight lithography steps. Thus, a fast dry stripping method was performed. It includes the use of a plasma asher system (PVA Tepla GIGAbatch 360M model) that, by a $2.45\,\mathrm{GHz}$ RF source, produces a plasma able to remove the PR. The process guarantees a good selectivity between the PR organic compounds and the metal and oxide materials of the sample.

In this thesis, unless when the metallic oxidation was critical (section 3.2.9), all of the PR strip steps were performed via plasma asher. Table 2.5 describes the parameters of the ashing recipe. Plasma activated oxygen atoms react vigorously with the organic molecules of the PR, thus promoting their removal from the sample surface. A primary vacuum pump guarantees the evacuation of the unreacted gases and oxidation products (e.g. $\mathrm{CO_2}$) out of the main chamber. The main disadvantage of the process is the possibility to oxidize exposed metals. Nevertheless, if a metallic deposition precedes the PR strip, the deposition recipe is chosen to perform a soft sputter etching before the effective deposition, in order to remove any native oxide on top of pre-existing metal that may have been formed during the PR strip. As described in Table 2.6, an average temperature of $64.6\,^{\circ}\mathrm{C}$ allows to perform the PR strip in less than 10 minutes. The duration of the strip can be made either by inserting a fixed time or by defining a stopping reference. In this case (Table 2.5), the recipe does not have a fixed duration. Instead, the stopping point is found based on the measurement of the instantaneous voltage of the RF source ($\mathrm{V_{RF}}$). The recipe specifies a constant power applied by the RF source, given by $\mathrm{P} = \mathrm{V_{RF}(t)} \cdot \mathrm{I_{RF}(t)}$. Through the strip process, the PR elements contribute to change the impedance of the plasma. In order to maintain a constant power, both current ($\mathrm{I_{RF}}$) and $\mathrm{V_{RF}}$ of the RF

RF power (W)	Start pressure (mbar)	O_2 flux (sccm)	Ar flux (sccm)	Stopping reference	Overashing (%)
500	0.2	600	50	$25\,\%$ variation between V_{RF} and its moving average	100

Table 2.5: Recipe parameters used for PR strip in the plasma asher.

Process time: 2min37sec + 2min37sec of overashing			
Parameters	**Minimum**	**Maximum**	**Average**
O_2 flux (sccm)	593	595	594
Ar flux (sccm)	48	49	48
Process pressure (mbar)	0.923	0.967	0.927
RF power (W)	504	505	505
Temperature (°C)	32.4	94.4	64.6

Table 2.6: Example of the parameters measured during a strip process.

source must vary on time, i.e. the plasma may be considered as a time-varying impedance element of the circuit. Near a complete stripping point, one expects to see a larger variation of V_{RF} due to the low concentration of PR elements in the plasma. When the system detects a decrease larger than $25\,\%$ between the instantaneous V_{RF} and its moving average, the stopping point is reached. For instance, at a specific instant, if the moving average of V_{RF} is $400\,mV$, the stopping point would be reached if the next instantaneous V_{RF} shows a value below $300\,mV$. To prevent an incomplete PR strip, the recipe is defined to repeat the time duration after reaching the stopping point, i.e. an $100\,\%$ overashing is performed. For instance, if the stopping point was reached after 2 minutes and 37 seconds of stripping (Table 2.6), the full duration of the strip will be 5 minutes and 14 seconds.

2.4.3 Direct write electron-beam lithography

At INL, the definition of MTJ nanopillars at the nanometric range cannot be achieved with an optical lithography technique. The minimum feature size of an optical lithography system is directly proportional to the wavelength (λ) of the light used for exposure [101]. As already referred in section 2.4.1, a 405 nm UV laser does not allow the exposure of features presenting dimensions below 2 μm. So, the alternative is to use an e-beam system that takes advantage of the particle-wave duality, using electrons with a sufficient low λ for nanometric exposures.

At INL, a Vistec 5200 ES 100 kV tool was used to perform all the e-beam lithographies. With an energy up to 100 keV, electrons may be accelerated with λ down to $\sim 5\,pm$. An electromagnetic lenses system is used to focus the e-beam on the coated sample. A digital mask is used to expose the sample, one squared pixel at a time, with a width down to 2 nm. The exposure conditions depend on the resist sensitivity (with charge/area units), which is dependent on its chemical composition and thickness. Thus, the exposure dose (D) needs to be calibrated for each resist conditions, which is

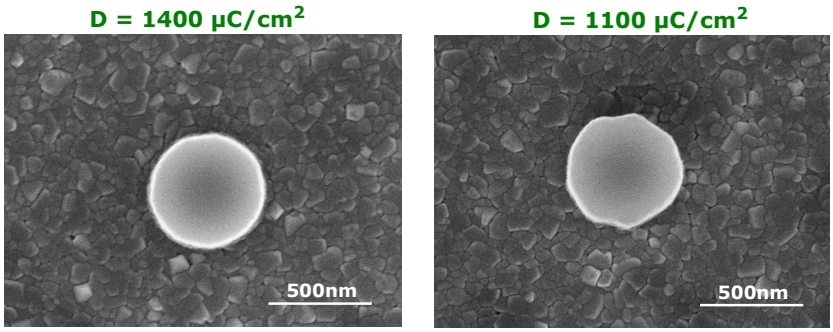


Figure 2.11: SEM top view images of circular 600 nm test structures, obtained after development for two different e-beam doses.

given by

$$D = \frac{I \cdot t}{A}, \tag{2.8}$$

where I is the e-beam current, t the exposure time at each pixel and A the exposed area defined by the beam spot. Figure 2.11 shows SEM images obtained during an optimization of the e-beam exposure for 600 nm circular test structures with a metallic TiWN(15) / AlSiCu(400) / TiWN(15) stack (thickness in nanometers). The test was performed using e-beam doses in the [1100 ; 1400] $\mu\mathrm{C/cm^2}$ range for a 400 nm pure ARN7520.18 negative resist. After development, the results clearly show an improvement of the exposure quality up to $1400\,\mu\mathrm{C/cm^2}$. For the lowest dose ($1100\,\mu\mathrm{C/cm^2}$), the image shows large imperfections of the circular shape, which proves that the same dose is insufficient for the resist sensitivity. Although not being critical inside the circular shape, where the proximity effect [102] allows the exposure beyond the pixel area, on the edges, the number of surrounding pixels is simply not enough to maintain the dose above the sensitivity threshold.

2.5 Magnetic annealing treatment

In section 1.4, it was already emphasized the importance of performing an annealing treatment after deposition. For CoFeB/MgO/CoFeB-based MTJs, an annealing treatment promotes the crystallization of the amorphous CoFeB layers into a body-centered-cubic (bcc) structure which, in association with a NaCl-type MgO barrier, maximizes the TMR performance [18, 62]. The thermal process promotes the diffusion of atoms in solid state materials, thus allowing their reconfiguration in terms of structural and magnetic properties. Moreover, during annealing, the possibility to apply a magnetic field allows to define the magnetic crystalline anisotropy of the MTJ magnetic layers. For instance, Fig. 2.12b shows VSM results (section 2.6.2) of a Ta(10) / $\mathrm{CoFe_{40}B_{20}}$(2.0) / MgO(7.9 $\Omega\mu m^2$) / Ta(10) / Ru(7) nanostructure deposited in a 0.5 $\mathrm{cm^2}$ substrate (thickness in nanometers). The measurement is performed with the field applied along the easy axis, i.e. 0° direction as shown in Fig. 2.12a. The magnetic curves clearly show that, from the crystallization of the FM layer, results an increase of the magnetic moment. It should be emphasized that the quality of the thermal treatment is temperature dependent and may be detrimental for the device performance if the conditions are not well chosen. A problematic behavior is the atoms diffusion between layers and the consequent formation of dead layers in the FM materials [60, 103].

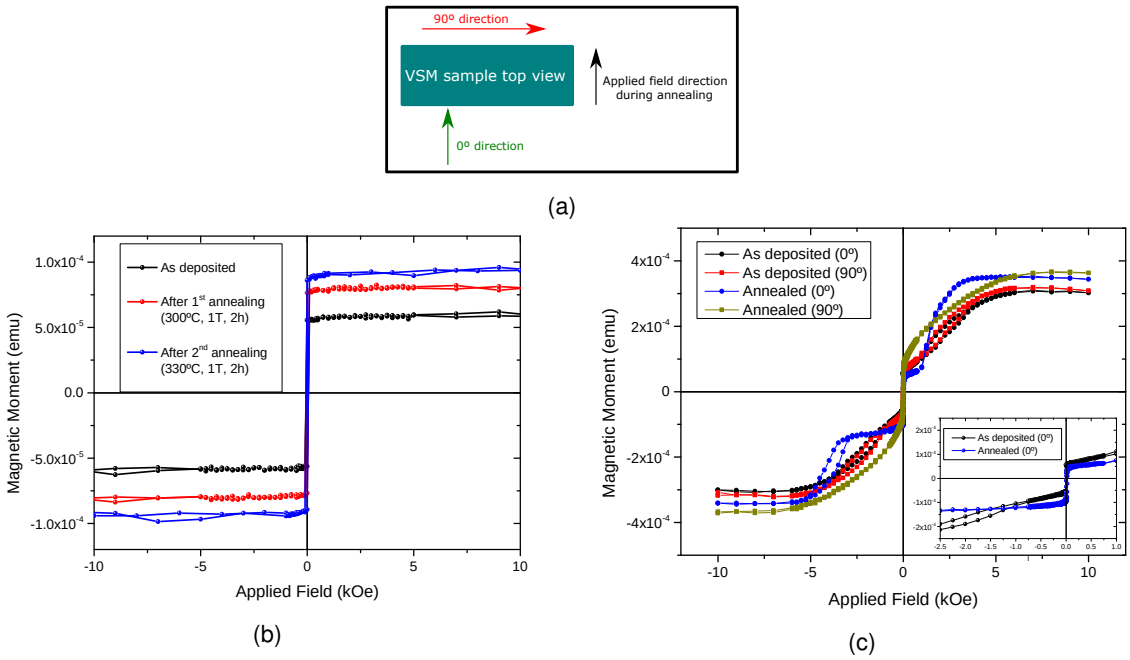


Figure 2.12: (a) Top view of a standard 0.5 cm^2 substrate used for VSM measurements. By definition, the annealing is always performed to define the easy axis in the $0°$ direction. (b) VSM measurements obtained at the easy axis for a Ta(10) / $\mathrm{CoFe_{40}B_{20}}$(2.0) / MgO(7.9 $\Omega\mu m^2$) / Ta(10) / Ru(7) nanostructure, before and after two different annealing conditions. (c) VSM measurements obtained for a Ta(5) / CuN(50) / Ta(5) / CuN(50) / Ta(5) / Ru(5) / IrMn(6) / $\mathrm{CoFe_{30}}$(2.0) / Ru(0.7) / $\mathrm{CoFe_{40}B_{20}}$(2.6) / MgO(9 $\mathrm{k\Omega\mu m^2}$) / $\mathrm{CoFe_{40}B_{20}}$(2.0) / Ta(5) / Ru(10) MTJ, before and after annealing. The sample was annealed at 330 °C for 2 h, with an applied field of 1 T.

Figure 2.12c shows VSM results obtained for a full Ta(5) / CuN(50) / Ta(5) / CuN(50) / Ta(5) / Ru(5) / IrMn(6) / $\mathrm{CoFe_{30}}$(2.0) / Ru(0.7) / $\mathrm{CoFe_{40}B_{20}}$(2.6) / MgO(9 $\mathrm{k\Omega\mu m^2}$) / $\mathrm{CoFe_{40}B_{20}}$(2.0) / Ta(5) / Ru(10) unpatterned MTJ. The results were obtained before and after annealing, with an external field applied at both $0°$ and $90°$ directions. Before annealing, the magnetic curves are almost indistinguishable, which proves the absence of a well defined easy axis. After annealing, there is a clear difference between the hysteresis loops, being the $0°$ direction, parallel to the field applied during annealing, the easy axis. The annealing temperature is chosen to be above the Néel temperature ($\mathrm{T_N}$) of the AFM material used on the MTJ stack ($\mathrm{T_N} \sim 100°\mathrm{C}$ for the 6 nm layer of IrMn, as deposited in the stack analysed in Fig. 2.12c). While cooling down, the material starts to gain its AFM configuration, such that the topmost spin layer aligns according to the pinned FM layer above (CoFe), thus setting up the exchange bias and optimizing the SAF. The inset of Fig. 2.12c shows an amplified view of the VSM measurements obtained before and after annealing at the easy axis. The stability of the SAF increases after annealing, whereas before annealing, the overall MTJ magnetic moment immediately starts to linearly change after the switching of the free layer magnetization.

At INL, the annealing system (MATr 2000 tool) allows to perform annealing treatments up to 400 °C. An integrated superconducting magnet applies an uniform magnetic field up to 2 T. Beyond time, temperature and field intensity, each annealing recipe allows to control both heating and cooling

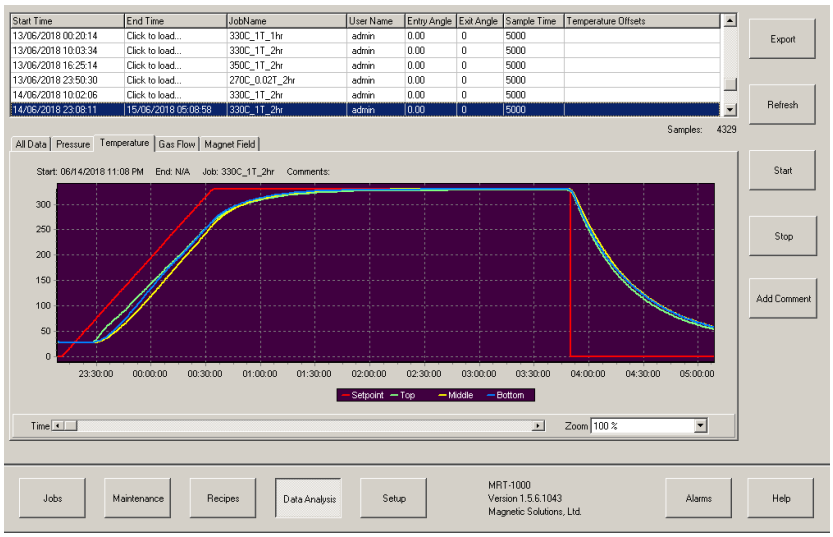


Figure 2.13: Data obtained from the standard recipe used in this thesis. The plot shows the temperature as a function of time.

rates. The tool configuration allows to perform the annealing either in Ar atmosphere or high vacuum (HV) conditions ($\sim 10^{-7}\,\mathrm{Torr}$). In the context of this thesis, annealing at HV conditions was always performed to remove sources of contamination, thus preventing any undesired variation of the sample properties (e.g. oxidation). Considering the HV conditions, the energy transfer between the heating source and the sample is made by radiation. The cooling rate is controlled by an He flux that goes through the annealing chamber to cool down the sample.

Figure 2.13 shows an example of the data obtained from the standard annealing process used in this thesis. The recipe is defined for an annealing at 330 °C for 2 h, with an applied magnetic field of 1 T. The 2 h countdown starts when the setpoint temperature of 330 °C is reached. Beyond the setpoint curve, that is in accordance with the recipe parameters, three more curves in Fig. 2.13 show the data obtained from three thermocouples placed at different positions of the loading cassette. This procedure aims to control the heating uniformity over the cassette region, where the samples are inserted.

2.6 Characterization techniques

2.6.1 Optical interferometer (OPM Nanocalc)

During the planarization step of the fabrication process (section 3.2.5), in order to calculate the etching time to open the pillar top contact, it is necessary to know the $\mathrm{SiO_2}$ thickness on the trenches (section 3.2.3). At that point, the process is designed to create trenches in each die borders with a Si/$\mathrm{SiO_2}$ stack. Considering that $\mathrm{SiO_2}$ is a transparent material, it is possible to measure its thickness by illuminating and studying the interference that occurs naturally between reflected light beams coming from both $\mathrm{SiO_2}$ interfaces (i.e. Si/$\mathrm{SiO_2}$ and $\mathrm{SiO_2}$/air).

The OPM Nanocalc is a setup used to extract the thickness of transparent thin films on different

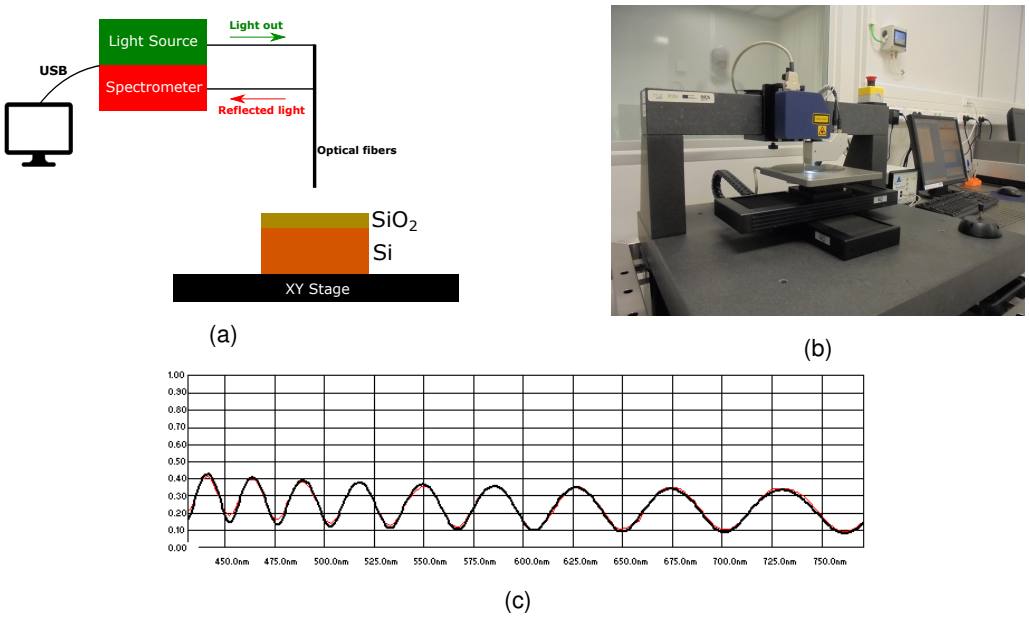


Figure 2.14: (a) Illustration of the OPM Nanocalc setup, measuring the thickness of a SiO_2 layer. (b) XY stage of the Nanocalc setup placed at the INL cleanroom. (c) Nanocalc measurement of a 3μm SiO_2 layer. The reflectance of the sample as a function of the light wavelength is depicted by the black curve. The red curve represents the fit performed by the software from which the thickness is extracted.

substrates. It allows, not only single, but also multiple measurements based on distribution maps specifying the measuring coordinates. This is extremely useful to study the deposition or milling uniformity of transparent materials (e.g. SiO_2) in Si wafers. In a normal incidence configuration (Fig. 2.14a), the target layer is illuminated by white light and a spectrometer measures the reflectance (R) as a function of the light wavelength (λ). Independent optical fiber connections guarantee the light transmission from the source to the sample and from the sample to the spectrometer. A moving stage (Fig. 2.14b) allows to move and position the sample below the light beam. Before measuring the oxide thickness, it is necessary to measure the R(λ) data of a Si substrate as the reference for the Nanocalc software. Then, the Si/SiO_2 stack can be measured, with the software tracing the best possible fit to the R(λ) data (Fig. 2.14c), from which the oxide thickness is extracted.

2.6.2 Vibrating sample magnetometer

All of the magnetic measurements were performed in unpatterned samples ($\sim 0.5\,cm^2$ substrates) using a vibrating sample magnetometer (VSM). As a straightforward definition, a VSM is an electric transducer that allows to measure the magnetic behavior of magnetic materials. Figure 2.15 shows the VSM used at INL (MicroSense EV9 model). The sample is inserted in a region where a uniform magnetic field applied by two water cooled electromagnets is present. The sample holder is connected to a piezoelectric material that, when excited, promotes a periodic vibration of the sample in the vertical direction ($85\,Hz$ is a typical frequency of vibration). Two pick-up coils are incorporated in the gap between the electromagnets, sufficiently close to collect the magnetic stray field of the sample.

The vibration of the sample leads to a periodic variation of the magnetic field flux in the pick-up coils. These conditions lead to the generation of an electromotive force ($\mathrm{V_{coil}}$) in each coil (Faraday's law), whose intensity is proportional to the magnetic moment of the sample (m), so that

$$V_{coil} = S \cdot m. \tag{2.9}$$

The sensitivity S is calculated every time a calibration of the VSM tool is performed using a magnetic sample with a known magnetic moment. After being amplified by a standard amplifier, the electric signal goes as an input to a lock-in amplifier that is tuned to extract an output signal at the vibration frequency of the sample. This step aims to eliminate the noise of the input signal. After the amplification, the magnetic moment can be extracted.

Considering the performed measurements, this setup allows to measure magnetic moments down to $\sim 1 \times 10^{-6}\,\mathrm{emu}$ ($1 \times 10^{-7}\,\mathrm{emu}$ according to the data sheet) and apply fields up to 2 T. Regarding the applied field resolution, the coercivity of the measured samples is high enough to allow measurements with field steps ≥ 1 Oe. Table 2.7 shows the magnetization of three different magnetic materials. The saturation magnetization ($\mathrm{M_{SAT}}$) is calculated based on a magnetic loop, as the one depicted in Fig. 2.16, where the range of the in-plane field is chosen to saturate the sample. The magnetization is simply $\mathrm{M_{SAT}} = \mathrm{m_{SAT}}/(\mathrm{A} \cdot \mathrm{t})$, being $\mathrm{m_{SAT}}$ the saturation magnetic moment obtained from the VSM data, A the area of the sample and t the thickness of the magnetic layer.

2.6.3 Current in-plane tunneling method

The current in-plane tunneling (CIPT) method is a reliable and fast way to characterize MTJs in unpatterned wafers. MTJ properties may be known right after deposition. The technique is based in a series

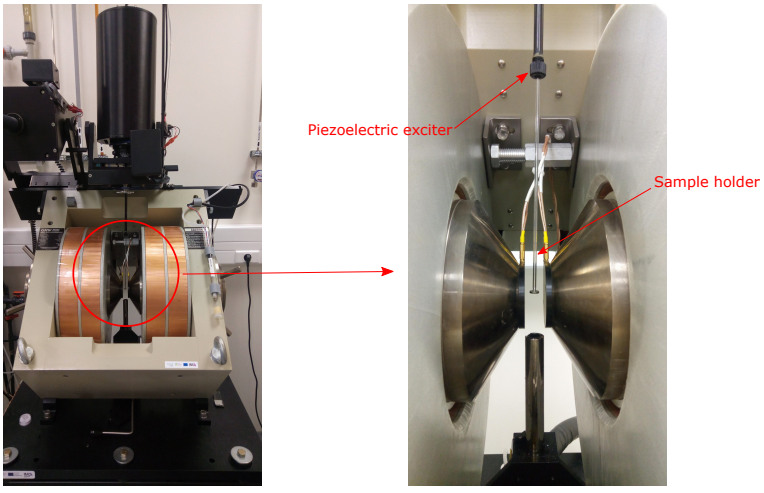


Figure 2.15: (a) Overview of the VSM setup at INL. (b) Amplified view showing the vertical insertion of the sample holder between the pick-up coils. Although covered by the pick-up coils, a Hall probe is also present to measure the magnetic field of the electromagnets.

Magnetic layer	Stack	$\mathbf{M_{SAT}}$ (emu/$\mathbf{cm^3}$)	$\mathbf{M_{SAT} \times 10^6}$ (A/m)
CoFeB	10 Ta / **2.0 $\mathbf{CoFe_{40}B_{20}}$** / MgO [7.9 $\Omega\mu m^2$] / 10 Ta / 7 Ru	1004	1.004
FeB	10 Ta / **2.5 $\mathbf{FeB_{20}}$** / MgO [7.9 $\Omega\mu m^2$] / 10 Ta / 7 Ru	1289	1.289
NiFe	5 Ru / **6.0 $\mathbf{NiFe_{19}}$** / 5 Ru	681	0.681

Table 2.7: Magnetization (M) calculated from VSM data and presented for different magnetic materials. Each magnetic layer is inserted in a specific stack (magnetic layer highlighted in red) that is deposited in the VSM substrates. All the thicknesses shown in the stack column are presented in nanometers. All the three samples were measured as deposited.

of four-point-probe measurements. An external magnetic field is applied to measure the resistance in both MTJ configurations and each resistance measurement is made at a different probe spacing. There are some important considerations regarding the range of the probe spacing. For a thin film, the resistance of a specific volume is given by

$$R = \frac{\rho L}{Wt} = R_s \frac{L}{W}, \tag{2.10}$$

where L is the length, W the width, t the thickness, ρ the resistivity and $\mathrm{R_s}$ the sheet resistance of the material. In both FM layers, the resistance increases with the probe spacing ($\mathrm{R} \propto \mathrm{L}$). In the case of the insulating barrier, the raise of the probe spacing increases the section at which the electric current can tunnel between FM layers, so that the resistance decreases [$\mathrm{R} \propto (\mathrm{Wt})^{-1}$]. Below a certain probe spacing limit (Fig. 2.17a), the resistance of the top FM layer is much smaller than the resistance of the insulating barrier, so all the electric current flows through the top FM layer. Figure 2.17b shows the opposite limit at which the resistance of the insulating barrier is much smaller than the resistance of the

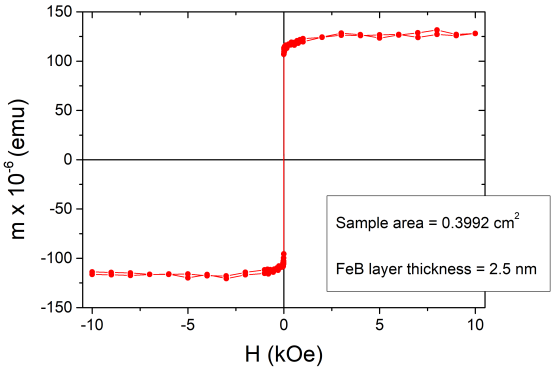


Figure 2.16: VSM measurement performed in a nanostructure with a magnetic layer of FeB, whose stack is presented in Table 2.7. The magnetic moment (m) is presented as a function of the in-plane magnetic field (H). The thickness of FeB and the area of the sample are used to calculate the magnetization presented in Table 2.7.

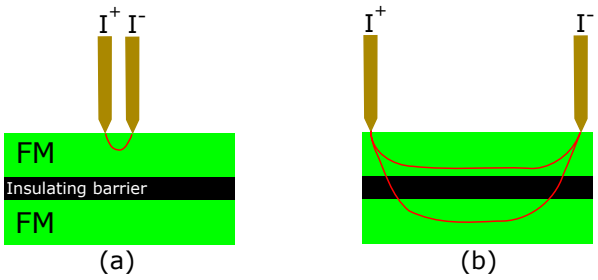


Figure 2.17: Illustration of CIPT measurements, representing the two probe spacing limits. (a) The probes are too close, so the current flows only through the top FM layer. (b) The large probe spacing creates a parallel current propagation through both FM layers.

FM layers, so that the current flows mainly through both FM layers in a parallel resistors configuration. In both limit situations, the TMR cannot be measured. In the case depicted in Fig. 2.17a, for both MTJ configurations, the resistance measured does not change because the current flows only through the top FM layer. In Fig. 2.17b, the contribution of the insulating barrier to the overall resistance of the junction is too small to see a significant resistance variation for different MTJ configurations. However, it is possible to measure TMR for an intermediate probe spacing, whose scale length is given by [104]

$$\lambda = \sqrt{\frac{RA}{(R_T + R_B)}}, \tag{2.11}$$

being RA the resistance-area product of the MTJ and $\mathrm{R_T}$ and $\mathrm{R_B}$ the sheet resistance of the top and bottom FM layers, respectively.

The CIPT method was first proposed by Worledge *et al.* [104]. In that report, an analytical solution describing CIPT is derived, where the resistance of the MTJ is given by

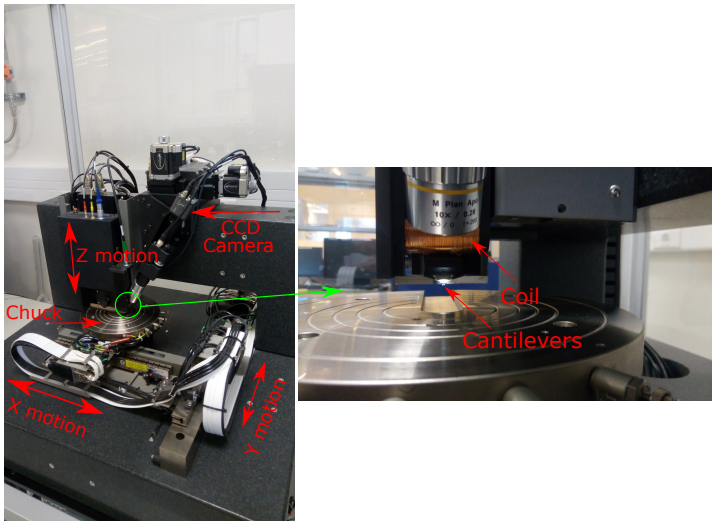


Figure 2.18: Setup of the CIPT tester at INL. On the right side, there is a zoom in at the cantilevers region.

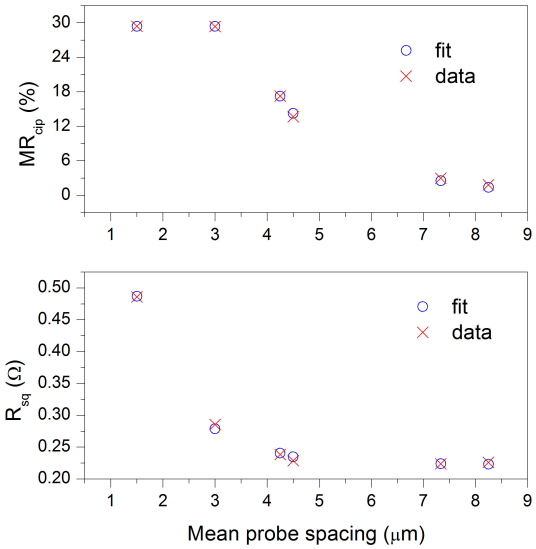


Figure 2.19: Experimental data obtained using the CIPT method and respective fit to the theory based on the analytical solution of Eq. (2.12). $\mathrm{R_{sq}}$ refers to the MTJ sheet resistance in the parallel configuration and $\mathrm{MR_{cip}}$ is the current in-plane magnetoresistance measured as a function of the probe spacing. In this specific measurement, from the fit results $\mathrm{RA} = 1.63\,\Omega\mu\mathrm{m}^2$, $\mathrm{TMR} = 98.04\,\%$, $\mathrm{R_T} = 1.13\,\Omega$, $\mathrm{R_B} = 0.28\,\Omega$ and $\lambda = 1.075\,\mu\mathrm{m}$.

$$R = \frac{R_T R_B}{R_T + R_B}\frac{1}{2\pi}\left[\frac{R_T}{R_B}\left[K_0\left(\frac{a}{\lambda}\right) + K_0\left(\frac{d}{\lambda}\right) - K_0\left(\frac{b}{\lambda}\right) - K_0\left(\frac{c}{\lambda}\right)\right] + \ln\left(\frac{bc}{ad}\right)\right], \tag{2.12}$$

where $\mathrm{K_0}$ is the modified Bessel function of the second kind of zero order. Taking into account the four probes used in the measurements, a is the distance between $\mathrm{I^+}$ and $\mathrm{V^+}$, b between $\mathrm{I^+}$ and $\mathrm{V^-}$, c between $\mathrm{I^-}$ and $\mathrm{V^+}$ and d between $\mathrm{I^-}$ and $\mathrm{V^-}$.

Figure 2.18 shows the CIPT tester at INL. The CIPT tester has 12 cantilever electrodes with a variable spacing, down to $750\,\mathrm{nm}$, for low resistance measurements (i.e. $\mathrm{RA} < 10\,\Omega\,\mu\mathrm{m}^2$). An electromagnet allows to apply an external in-plane field up to 2.5 kOe. An optical system includes a CCD camera, allowing to visualize the cantilevers for each landing on top of the sample. Figure 2.19 shows CIPT experimental data after a landing. The analytical solution of Eq. (2.12) is used to fit to the experimental data using TMR, RA, $\mathrm{R_T}$, $\mathrm{R_B}$ and λ as fit parameters that characterize the MTJ.

2.6.4 Semi-automatic transport measurement setup

After fabrication, the substrate may have hundreds or even thousands of devices. To optimize the accuracy of their characterization, a statistical analysis is performed, where a meaningful number of devices is characterized by a semi-automatic probe station. As illustrated in Fig. 2.20, the setup is controlled by a computer connected through a GPIB bus. Similar to a standard setup for magnetic-transport measurements, a current source and a voltmeter extract information from each sample with the possibility to apply an external in-plane field from a set of coils supplied with a second current

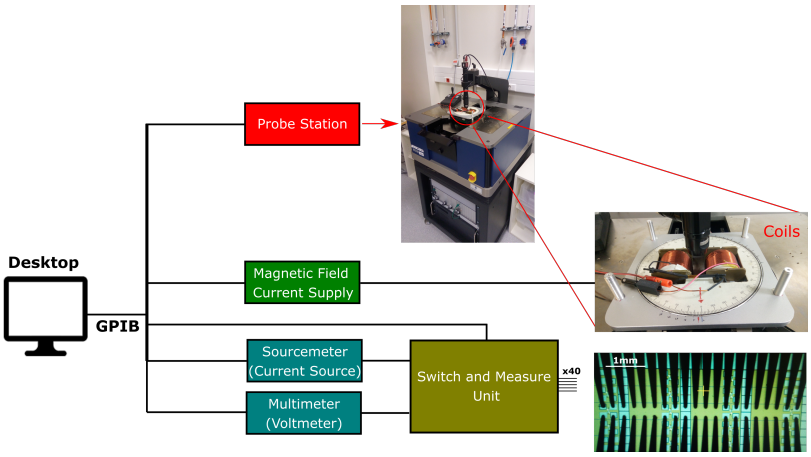


Figure 2.20: Illustration of the setup for measurements at the probe station.

source. The probe station contains a set of forty tips that allow to measure up to ten samples per landing in a four-contacts configuration. Connected by the GPIB bus, the probe station allows to automatize the process by mapping (an homemade software is used for this purpose) and moving the tips over different samples on the same wafer. For each landing, a switch and measure unit (Agilent 34980A) is connected to the current source and voltmeter terminals, which allows to selectively connect them to the forty tips, based on a previous mapping.

As an example, Fig. 2.21a shows a statistical analysis of the TMR as a function of the RA product obtained for a large set of CoFeB/MgO/CoFeB-based MTJ nanopillars from the same substrate, with a diameter of 375 nm. For each MTJ, the results are obtained from a full transfer curve (Fig. 2.21b), where the resistance is probed with a four-contact measurement as a function of the in-plane field created by the setup coils. For this purpose, all the MTJs present the standard four-contact geometry for statistical analysis (see section 3.1). As depicted in Fig. 2.21a, the nanofabrication process

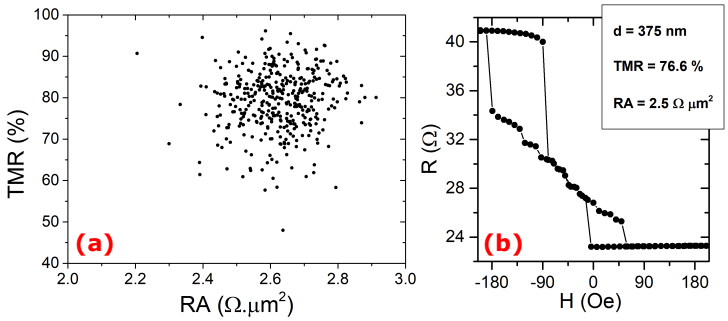


Figure 2.21: (a) TMR ratio a function of the RA product obtained for a set of 379 nanopillars with a nominal diameter of 375 nm. (b) Example of a transfer curve obtained from one of those devices and from which the magnetoresistive parameters are calculated.

leads to a dispersion of the magnetoresistive properties of single nanopillars with the same nominal diameter. It is possible to refer two main contribution for this standard dispersion: (i) formation of conduction paths in the nanopillar sidewall [minimized with a sidewall cleaning after pillar definition (see section 3.2.4)] and (ii) defects of the ultra-thin MgO barrier (already discussed in section 1.5).

2.6.5 RF setup

After the statistical analysis performed in the semi-automatic probe station (section 2.6.4), each device from a die can be characterized individually in the RF setup depicted in Fig. 2.22. A table with pneumatic isolation is used to mount the experimental setup, where a custom designed ground-source microwave probe (picoprobe by GGB Industries) performs the electric contact with the metallic pads of the device. The landing is performed moving the probe with a XYZ stage and following the process with an optical microscope. Figure 2.22a highlights all the instruments used for RF measurements in this thesis. Figure 2.22b is focused in the region where the die is mounted. The sample is placed between the poles of a rotating electromagnet, so that an external magnetic field can be applied

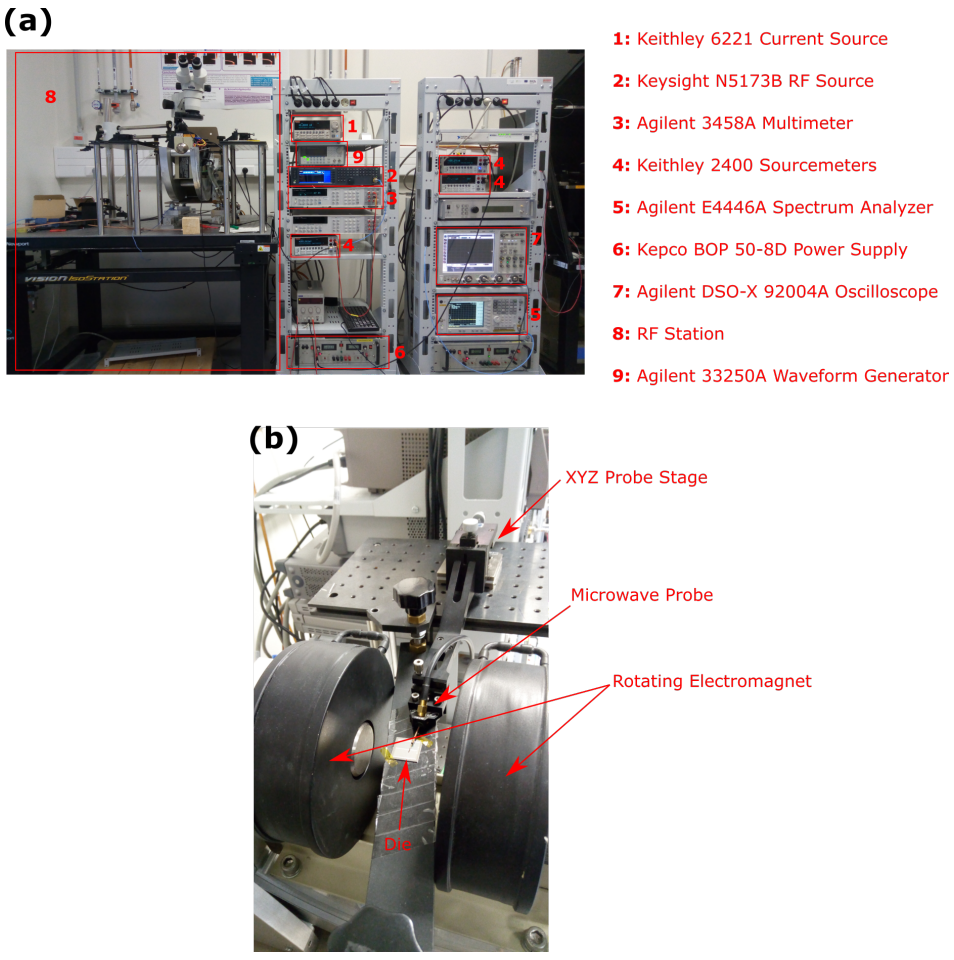


Figure 2.22: (a) Image of all the instruments available for RF measurements. The ones used in this thesis are labelled. (b) Image of the setup mounted in the pneumatic table.

continuously from in-plane to out-of-plane configuration and its intensity can also be controlled by changing the distance between the poles. The measurements are set remotely via GPIB connection, using homemade Labview scripts.

Chapter 3

Micro and nanofabrication

3.1 Device geometries

The broad range of experimental approaches presented in this thesis understandably implies the fabrication of different MTJ designs. Specifically, three distinct device geometries were fabricated: (i) four-contact (Fig. 3.1), (ii) two-contact with an integrated field line (Fig. 3.2) and (iii) independent top contacts (Fig. 3.3). The nanofabrication process developed in this thesis is compatible with all the three designs, meaning that it is possible to fabricate all the designs simultaneously in the same wafer. The details of the geometries used for the patterning of MTJs on top of oxide membranes are described in chapter 7.

The four-contact design is defined in a flexible cross-shaped geometry with a pair of metallic pads for each MTJ contact [bottom (BC) and top (TC) contacts in Fig. 3.1]. This geometry is mainly used to statistically analyse the magnetoresistive properties (i.e. TMR and RA product) of the MTJ pillars in a wafer. This process can be implemented in the semi-automatic probe station by performing a

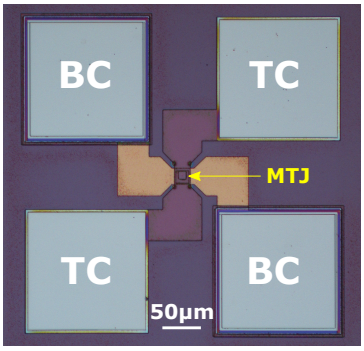


Figure 3.1: Optical microscopy image of a four-contact device. Useful information: bottom contact (BC) and top contact (TC).

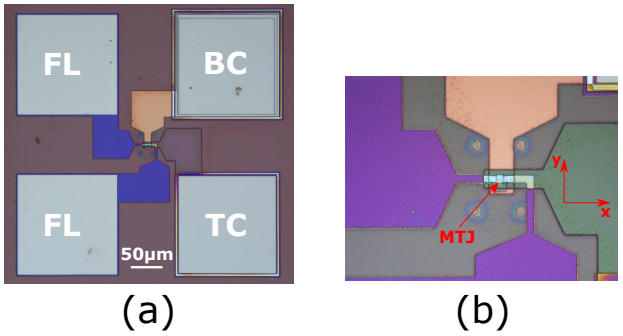


Figure 3.2: (a) Optical microscopy image of a two-contact device. (b) Zoom in at the central region, where the field line is defined on top of the nanopillar. Useful information: bottom contact (BC), top contact (TC) and field line (FL).

four-point R-H measurement to a sufficiently large number of devices (see section 2.6.4).

The two-contact geometry eliminates two MTJ pads to incorporate an integrated field line without compromising the device surface density on the wafer (both four-contact and two-contact designs have an area of $500 \times 500\,\mu\mathrm{m}^2$ per device). As shown in Fig. 3.2b, the field line is fabricated on top of the nanopillar, so that it allows to apply a local magnetic field in the yy direction. This geometry is useful, not only because it discards the need of an external magnetic field (in section 4.5, the chirality of the vortex-based nano-oscillator can be controlled only with the field line), but also because it gives an extra in-plane magnetic field (in section 5.3, the 2D mapping of the pinning sites in the free layer is achieved with both electromagnet and field line).

The independent top contacts (ITCs) geometry shows a higher degree of complexity and it was fabricated to study the synchronization of spin torque nano-oscillators via dipolar coupling, as described in section 6.3. This design allows to electrically connect up to four individual MTJ nanopillars. As shown in Fig. 3.3, while sharing the bottom contact (BC), each nanopillar has an independent top contact $\mathrm{ITC_i}$, where i is the MTJ label (i = 1, 2, 3 or 4), so that it is possible to control individually the DC current passing through each nano-oscillator. Also, the field line is defined with four pads, in this way allowing to apply a local field for both in-plane directions [$\mathrm{FL_x}$ ($\mathrm{FL_y}$) pads for a local field in the xx (yy) direction].

3.2 Process steps

3.2.1 MTJ stack deposition and annealing

The process starts with the substrate preparation. One needs to guarantee the insulation between the MTJ devices and the substrate, so the standard process is to deposit 100 nm of $\mathrm{AlO_x}$ on top of a 200 mm Si wafer. If available, there is the alternative to use directly a thermally oxidized 200 mm Si wafer with a 200 nm layer of $\mathrm{SiO_2}$ on top. Then, the MTJ stack is deposited by magnetron sputtering at the Timaris MTM tool. In general, the MTJ stack is divided into three main structures: bottom contact

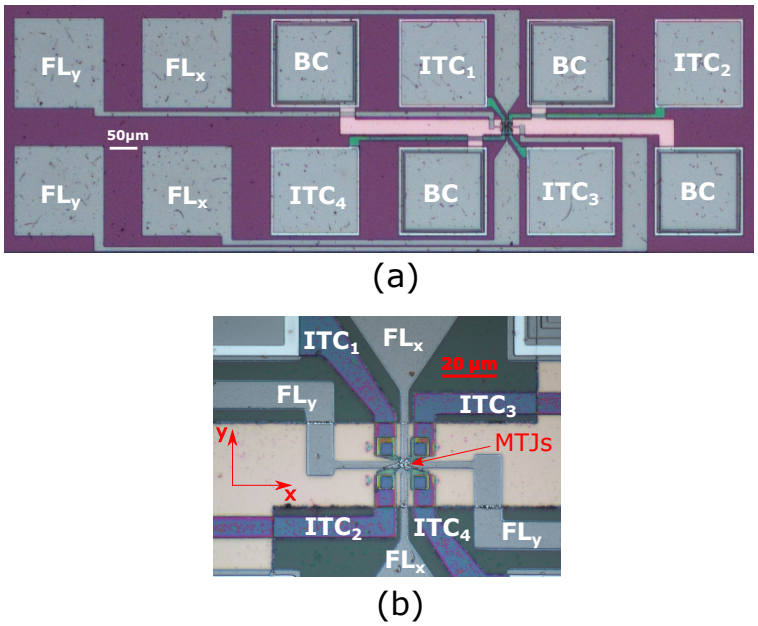


Figure 3.3: (a) Optical microscopy image of a individual top contacts device. (b) Zoom in at the central region, where each nanopillar i is electrically connected with an individual top contact $\mathrm{ITC_i}$ (i = 1, 2, 3 or 4). Useful information: bottom contact (BC), top contact (TC), field line creating a magnetic field in the xx direction ($\mathrm{FL_x}$) and field line creating a magnetic field in the yy direction ($\mathrm{FL_y}$).

/ MTJ / capping structure.

The bottom contact has a two-fold function: (i) provides a surface for the MTJ stack to grow with good adhesion and low stress while promoting the appropriate textures required for good magnetic and electric properties and (ii) constitutes a low resistive electrical path required to contact the bottom electrode for patterned nanopillars in the current-perpendicular-to-plane (CPP) configuration used in MTJ devices. For instance, a Ta(5) / CuN(50) / Ta(5) / CuN(50) / Ta(5) / Ru(5) structure is suitable to be used as bottom contact (thickness in nanometers). It is worth mentioning the two main procedures used to decrease the roughness of the bottom contact structure. First, by reactive DC sputtering [94], Cu deposition is performed as a $\mathrm{N_2}$ flux goes through the deposition chamber. From the insertion of a reactive gas results the deposition of a $\mathrm{CuN_x}$ nitrogen compound with a smoother top interface [105]. Second, the 100 nm CuN layer is laminated in two sheets separated by 5 nm of Ta, in a further attempt to mitigate the grain growth in the buffer, associated with an increase of the surface roughness.

Above the MTJ stack, the capping structure, e.g. a Ta(10) / Ru(7) stack, constitutes the top contact (thickness in nanometers). The choice of Ru as the last layer aims to maintain a conductive sample for prior measurements at the CIPT tester. After deposition, the sample is air exposed, so the Ru layer will partially oxidize. The advantage relies on the fact that Ru-O is still conductive, which is a requirement for the layer in contact with the CIPT probes.

After the stack deposition, the samples are annealed using a previously optimized recipe that maximizes the TMR ratio. As referred in section 2.5, an annealing treatment at 330 °C for 2 h with an

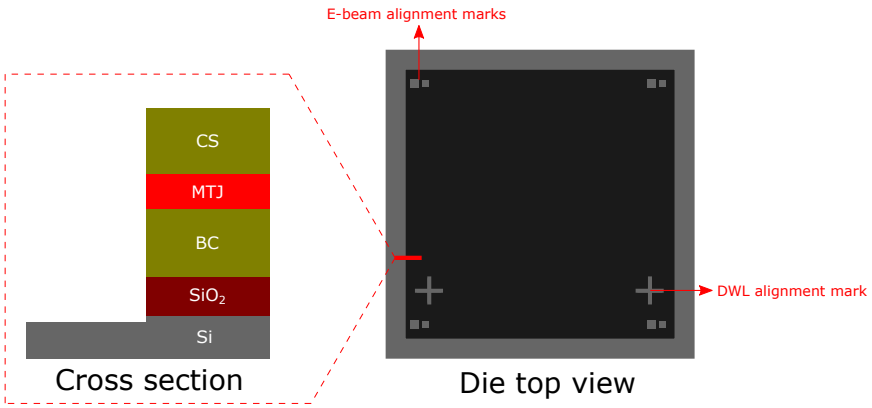


Figure 3.4: Illustration of the mask used at the first optical lithography. On the left side, a cross section of the sample shows the etching performed until the Si substrate at the trench regions. Useful information: capping structure (CS) and bottom contact (BC). The alignment marks are magnified for clarity.

in-plane field of 1 T is performed. Finally, the samples are measured at the CIPT tester to see if the TMR ratio and the RA product are in accordance with the expected results.

3.2.2 Sacrificial structure deposition

In addition to the capping structure deposited at the MTM tool, it is necessary to include a second thick structure, conveniently called sacrificial structure. This requirement comes from the planarization step (section 3.2.5), in which, after the pillars insulation, the top contacts are exposed. The name "sacrificial" gives a hint about the role of the structure: a thick low resistive structure that may be partially removed during planarization to prevent the etching of the functional MTJ. A TiWN(15) / AlSiCu(250) / TiWN(15) metallic structure is deposited at the FTM tool as the sacrificial structure. The bottom TiWN layer prevents the diffusion of aluminum atoms to the underlying MTJ, while the topmost TiWN has a twofold function: (i) gives protection against corrosion and (ii) acts as an anti-reflective coating for the first DWL exposure.

3.2.3 Trenches definition

The first optical lithography consists in the dies definition on the wafer. A die is a macroscopic region (area $\sim 2{\times}2\ \mathrm{cm}^2$, depending on the design) where a specific mask based in an drawing exchange format (DXF) file is fabricated. Beyond that, the trenches are fundamental to control the $\mathrm{SiO_2}$ thickness during the planarization step (section 3.2.5). At the trench regions, a Si / $\mathrm{SiO_2}$ structure will be present after the pillars passivation, so that the $\mathrm{SiO_2}$ thickness is easily measurable with an optical interferometer. Figure 3.4 shows an illustration of the mask used in this lithography. In addition to the trenches, squared alignment marks are also fabricated for the e-beam lithography (section 3.2.4). As a safety measure, cross-shaped alignment marks for DWL exposures are defined for all the lithography steps.

3.2.4 Pillar definition

The pillar definition is the most critical step of the process that will dictate the properties of the MTJ. After an e-beam lithography with a negative ARN7520.18 resist (section 2.4.3), the pillars are defined by ion beam milling (section 2.3). A successful definition implies three main goals:

1. obtain the best possible pillar profile, in order to have the lowest mismatch between the nominal and real diameter of the pillar, mainly above the bottom contact where the functional MTJ is deposited;

2. considering that, after milling, the e-beam resist cannot be removed, guarantee that the definition ends up with the lowest possible thickness of e-beam resist on top (considering the thick sacrificial structure, the most favourable situation would be ending up with no e-beam resist and a small overetch of the sacrificial structure);

3. remove the redeposited material on the sidewall of the pillar, thus minimizing the formation of low resistive conduction paths.

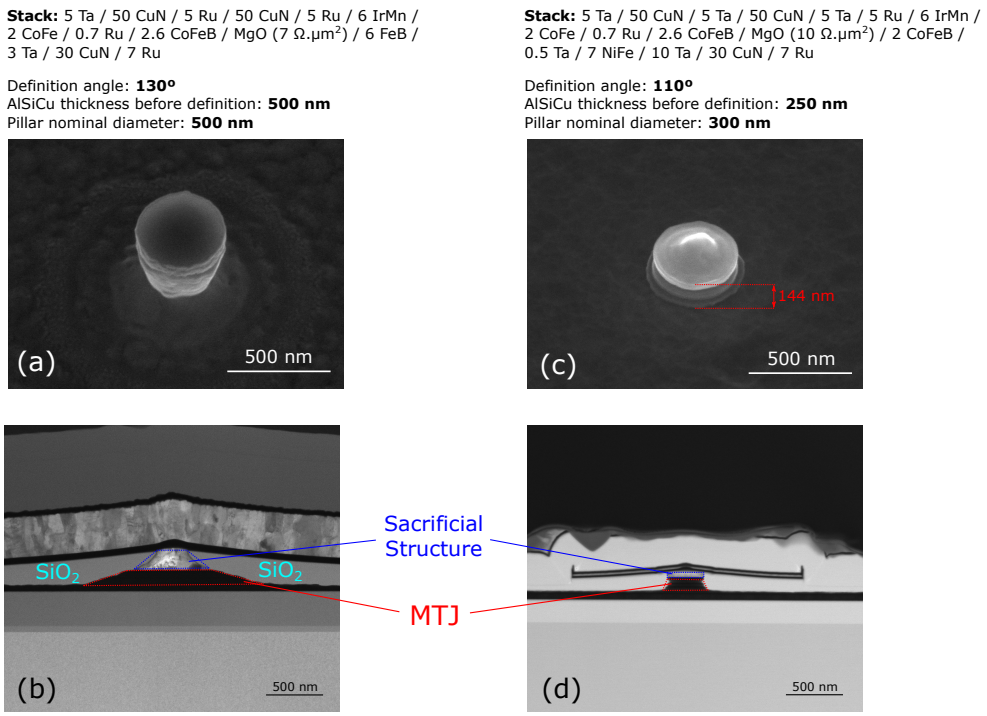


Figure 3.5: (a)-(c) SEM images obtained for two pillars defined with different milling conditions. On top of each image, the pillar stack corresponds to the MTJ composition below the sacrificial structure (thickness in nanometers). The images were saved at a tilting angle of (a) 30° and (b) 40°. From the same two wafers, two identical pillars were chosen for a focus ion beam cut, so that (b)-(d) show the correspondent SEM images of the pillar cross sections.

Regarding the second goal, in fact, the e-beam resist can be removed by plasma asher. Nevertheless, based on previously performed tests [76], it was observed that the ashing process oxidizes the exposed pillar, with a consequent degradation of its profile and electric properties. Figure 3.5a and Fig. 3.5c show SEM images of two pillars defined with different milling conditions. To complete the profile analysis, Fig. 3.5b and Fig. 3.5d show two pillar cross sections, obtained by focus ion beam (FIB), after the nanofabrication of each wafer. It should be emphasized that the pillar shown in the SEM image is not the same as the one used for the cross section. For instance, the pillar shown in Fig. 3.5a is different from the one shown in Fig. 3.5b, but they are fabricated in the same wafer and present the same nominal diameter.

Based on the standard recipe used at Nordiko 7500 (Table 2.3), it was necessary to optimize the angle between the ion beam and the wafer surface. For the profile, 90° appears to be the best option. Nevertheless, the absence of a transversal component of linear moment for the ions (i.e. in the direction parallel to the wafer surface) increases the redeposited material on the sidewall, which may be minimized choosing the standard angle of 130°. Nevertheless, as shown in Fig. 3.5b, the definition at 130° degrades the profile, with a progressive increase of the pillar diameter, from the sacrificial structure to the bottom contact below the MTJ. In this way, one ends up with an MTJ presenting a diameter that is more than twice (i.e. $> 1\,\mu\mathrm{m}$) of the nominal diameter of 500 nm. From all the performed tests, the adoption of an intermediate angle of 110° seems to be the best compromise between profile and redeposition (Fig. 3.5d).

Figure 3.5d shows a profile improvement, but not a complete optimization. After definition, the pillar shows an height of 144 nm. The MTJ alone has a nominal height of ~ 130 nm, meaning that almost all the sacrificial structure was removed during the milling process. This outcome is a consequence of the too thin e-beam resist used in the lithography, i.e. 200 nm of diluted ARN7520.18 (one part of ARN7520.18 plus one part of AR300-12), that is completely removed a long time before finishing the definition step. So, to fulfil the second goal of the definition, 450 nm of pure ARN7520.18 was used for the e-beam lithography. Experimental tests show that a TiWN(15) / AlSiCu(250) / TiWN(15) sacrificial structure (thickness in nanometers) allows the definition down to the bottom contact, with the removal of all the e-beam resist and partially the topmost TiWN layer, in this way leaving almost all the sacrificial structure on top of the MTJ.

At this point, after testing different milling conditions, an optimized pillar definition implies the combination of three requirements: (i) deposition of a TiWN(15) / AlSiCu(250) / TiWN(15) sacrificial structure, (ii) e-beam lithography with 450 nm of pure ARN7520.18 and (iii) pillar definition down to the bottom contact, at a milling angle of 110°. Finally, in the last step, the angle is increased to a grazing angle of 170° for the sidewall cleaning of the pillar.

3.2.5 Ion beam planarization

After definition, the pillars need to be passivated, in order to be physically protected and electrically insulated. The passivation is achieved by an oxide deposition. Figure 3.6 shows a sequence of SEM images from a test sample, where the total $\mathrm{SiO_2}$ thickness was divided into multiple deposition steps. The total thickness of 1.6 μm was chosen, taking into consideration previous samples, where an overall deposition of the same thickness of oxide led to a successful planarization. The $\mathrm{SiO_2}$ growth is translated into the formation of a topographic bump that increases its diameter up to $\sim 2.4\,\mu$m with an oxide nominal thickness of 1.6 μm (Fig. 3.6d), which is four times larger than the original diameter

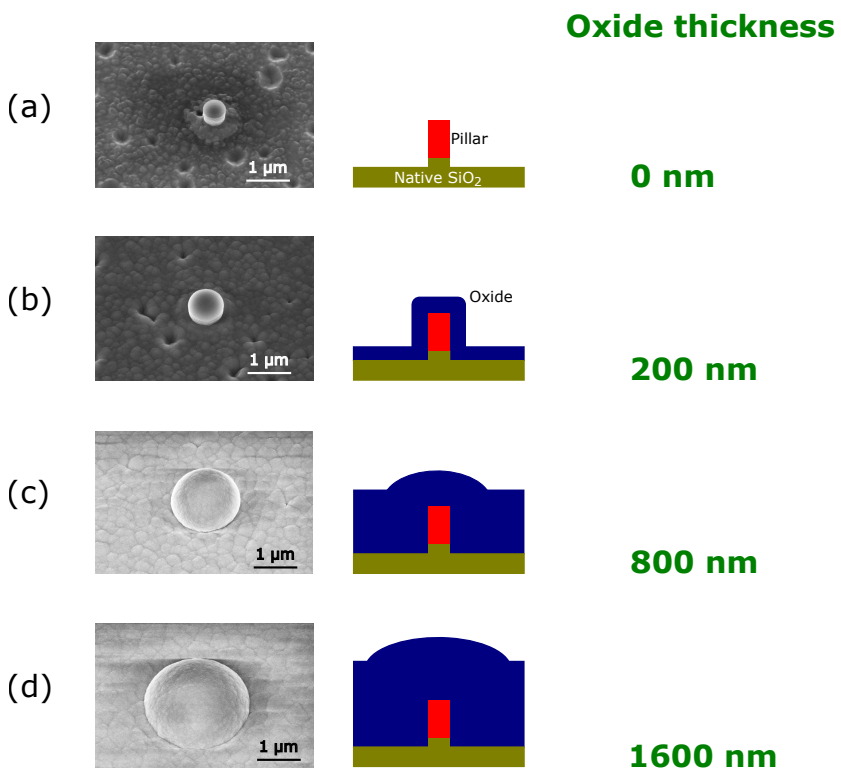


Figure 3.6: SiO_2 deposition sequence before planarization. Each step shows a SEM image and an illustration (not at scale). The test pillars have a TiWN(15) / AlSiCu(400) / TiWN(15) stack and 600 nm of diameter. (a) Starting from a defined pillar, SiO_2 is deposited to fulfil a nominal thickness of (b) 200 nm, (c) 800 nm and (d) 1600 nm.

of the pillar. So, to planarize, one needs to etch the exceeding SiO_2, followed by the flattening of the bump regions above each pillar. An ion milling step at a grazing angle allows to planarize the oxide surface and expose the metallic sacrificial structure.

In the context of this thesis, the planarization was achieved by ion beam milling at a grazing angle of 170°, using the standard milling recipe (Table 2.3). This configuration allows to maximize the etching rate in the horizontal direction, thus decreasing the bump, and minimize the etching rate of the exceeding oxide in the vertical direction. The objective is to perform a complete removal of the bump before reaching the top of the pillar. The grazing angle is limited by the shadow effect caused by the clamp that holds the wafer to the rotary table at Nordiko 7500. After each planarization step (i.e. milling step), the pillars are visualized at SEM to get a qualitative analysis of the planarization progress (Fig. 3.7). Moreover, the oxide thickness is measured on the trenches. For instance, if the oxide is becoming too thin, i.e. close to the functional MTJ height, and the SEM observation does not show a complete planarization, the solution is to deposit more oxide and then continue the milling.

The illustration from Fig. 3.7b shows a real profile near the pillar. Instead of an ideal planarized surface, the process still creates a height gradient near the pillar (particularly clear from the FIB characterization shown Fig. 3.5b, where the SiO_2 insulating the pillar sidewall is labelled), which is a consequence of the shadow effect caused by the initial topographic bump. The oxide thickness

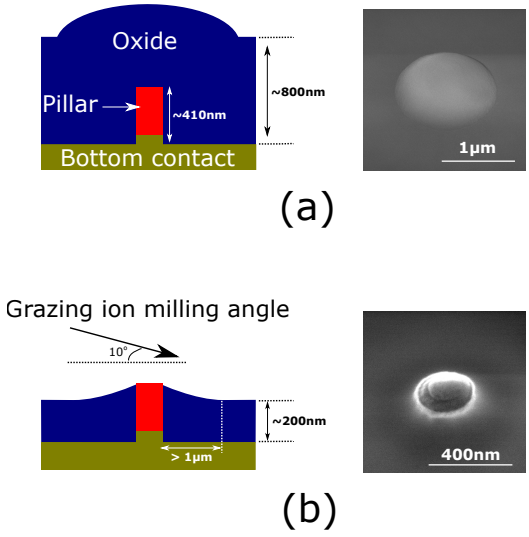


Figure 3.7: Illustration and corresponding SEM images of the planarization process for a real MTJ pillar, (a) after an oxide deposition step and (b) after the last milling when the pillar is open on top for electric contact. The diameter of the pillar is 300 nm.

stabilizes roughly for a distance higher than 1 μm from the edge of the pillar, which means that a successful planarization corresponds to an oxide thickness in the trenches lower than the actual height of the pillar. Typically, as shown in Fig. 3.7, an MTJ pillar with a height of 410 nm and a diameter of 300 nm is open when the oxide remaining on the trenches corresponds to half of its height.

3.2.6 Pillar cap and bottom pads definition

Following the planarization, a thin TiWN(15) / AlSiCu(20) / TiWN(15) metallic structure is deposited at the FTM sputtering tool. The aim is to define an extra capping structure which will establish electric contact between the pillar and the top pads. Figure 3.8 shows the structure defined for each individual device, where the metallic cap is fabricated in the middle region on top of the pillar. Considering that the fabrication comprised more than one design, here, as an example, the choice was to describe the microfabrication of a two-contact design. So, in addition to the cap, a single bottom pad is defined by a large square (if the four-contact design was considered, the bottom pads would be defined in a cross-shaped design by two large squares). After fabrication, these pads will allow to establish contact with the bottom contact of the pillar.

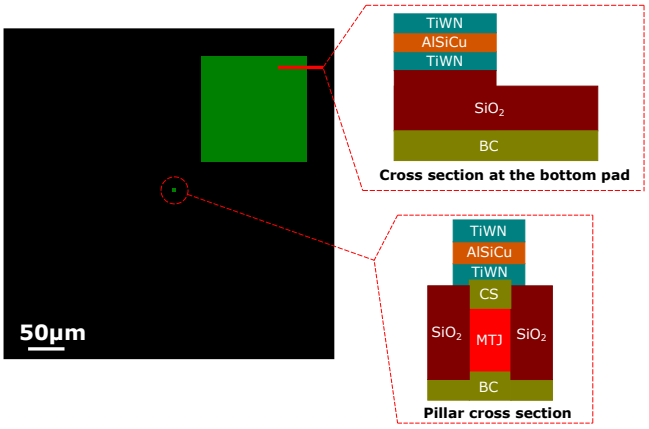


Figure 3.8: Mask used for pillar cap and bottom pad definition (i.e. green regions). On the right, two cross sections show the profile after the etching process. Useful information: capping structure (CS) and bottom contact (BC).

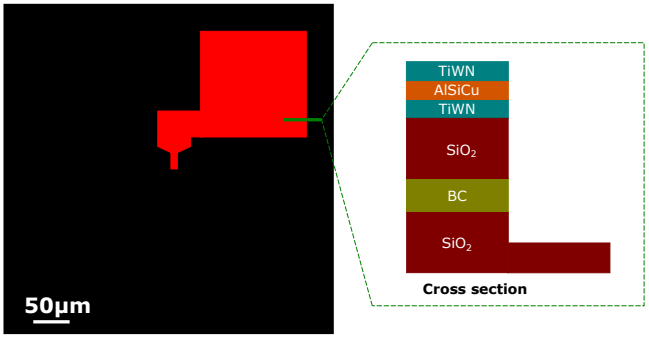


Figure 3.9: Mask used for the bottom contact definition (i.e. red region), along with a cross section at the bottom pad after etching. Useful information: bottom contact (BC).

3.2.7 Bottom contact definition

At this step, the pillars are still not electrically independent. During pillar definition (section 3.2.4), the etching goes down to the middle of the bottom contact, which means that all the pillars end up connected through the bottom contact. So, this lithography aims to revert the last statement by defining the bottom contact individually for each device. Figure 3.9 shows the mask used for the bottom contact definition. The etching removes the remaining metal from the bottom contact and finishes, after an overetch, at the insulating SiO_2 layer. After milling, the cross section from Fig. 3.9 shows that the bottom contact ends up exposed in the sidewall, which may lead to short circuits. This situation may be particularly critical after the deposition of the metal to define the top pads (section 3.2.10). So, after resist strip in the plasma asher, 300 nm of SiO_2 are deposited by PECVD to eliminate any possible low resistive path between top and bottom contacts.

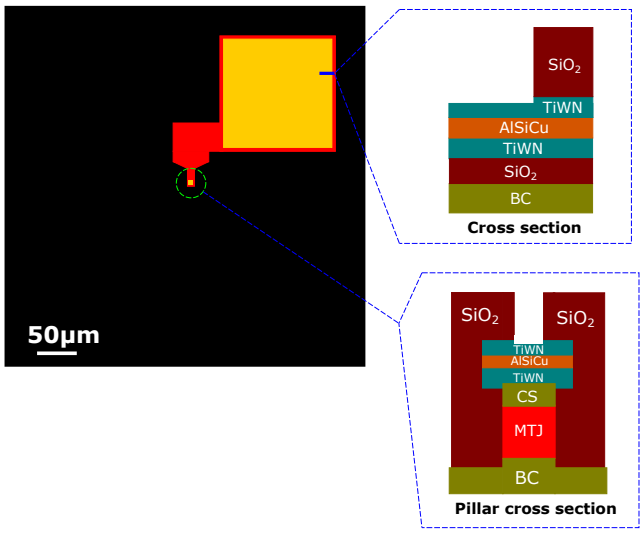


Figure 3.10: Mask used for the via fabrication to the pillar cap (i.e. yellow region), along with a cross section at the bottom pad and pillar region after etching. Useful information: capping structure (CS) and bottom contact (BC).

3.2.8 Via to pillar cap

After insulation of the bottom contact sidewall, it is necessary to re-establish the electrical contact with the pillar. Figure 3.10 shows the mask used to define a via to the pillar cap (i.e. yellow square in the middle). The etching allows to remove the $\mathrm{SiO_2}$ deposited in the last step and access the electrical contact at the topmost TiWN layer.

Another clear aspect from Fig. 3.10 is the simultaneous definition of a via through the bottom contact pad (i.e. a large yellow square). The aim is to maintain the bottom pad at the same etching level of the pillar cap, which is a fundamental requirement for the next lithography step (section 3.2.9). As mentioned in section 2.3, a SIMS probe is used to know the stopping point at each etching step. Nevertheless, if the area at which the material is being removed is too small, the etched material may not be enough to have a sufficiently clear detection. To solve this problem, around the MTJ devices, large 250×250 $\mu\mathrm{m}^2$ squared regions (understandably called SIMS regions) are defined at the same lithographic level, i.e. the material being removed at the MTJ device is exactly the same as the one being removed at the SIMS regions, so that an increase of the area exposed to the ion beam is achieved, followed by an increase of the detection at the SIMS probe. Both lithographies, i.e. to fabricate the via to the pillar (this section) and the via to the bottom contact (section 3.2.9), share the same SIMS regions, so if the via to the bottom pad is not started at this lithography, the next etching step would start with different materials on top of the bottom contact pad ($\mathrm{SiO_2}$ from the last oxide deposition) and on top of the SIMS regions (topmost TiWN layer left from this lithography step).

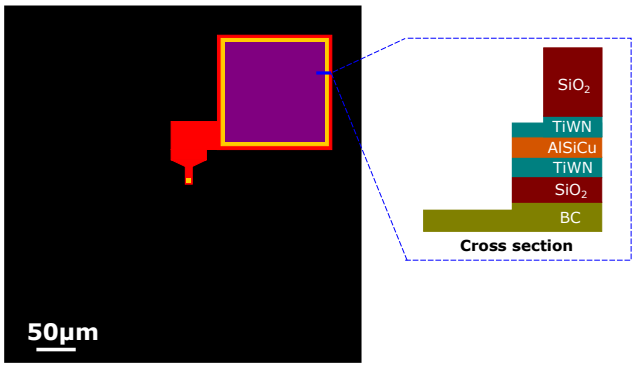


Figure 3.11: Mask used for the via fabrication to the bottom pad (i.e. purple region), along with a cross section at the bottom pad after etching. Useful information: bottom contact (BC).

3.2.9 Via to the bottom contact

To finish the electrical access to the pillar, one still needs to reach the contact at the bottom pad. As mentioned in section 3.2.8 the via to reach the bottom contact was already started, so that SIMS regions and bottom pad are at the same lithography level, i.e. both have the same TiWN layer as the topmost layer. Figure 3.11 shows the mask used to fabricate the via at the bottom pad (i.e. purple square), where, after etching, the metal from the bottom pad definition (section 3.2.6) and the remaining SiO_2 from the planarization (section 3.2.5) are removed. After the milling process, CuN gets exposed in the bottom contact, so, to prevent the oxidation of the pad, this is the only step when, after the dry etching, the resist strip is performed with acetone and ultrasounds.

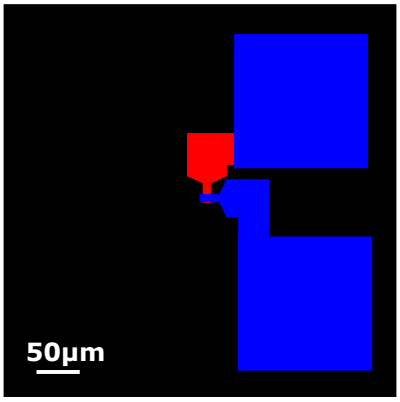


Figure 3.12: Mask used for the top pad definition (i.e. blue regions).

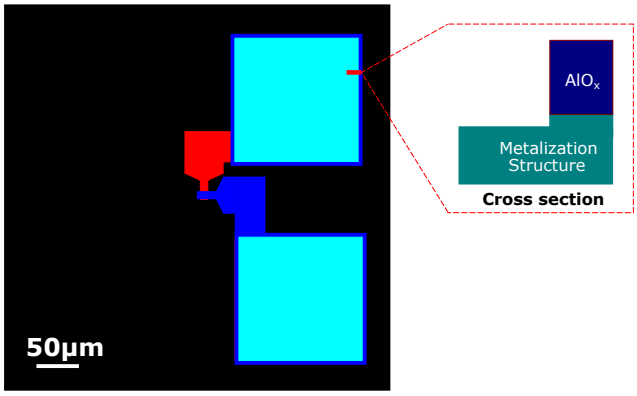


Figure 3.13: Mask used for the vias to MTJ pads (i.e. light blue regions).

3.2.10 Top contact definition

Now, with open vias to bottom and top contacts, it is necessary to define the top pad. The first step is to deposit the metal to be patterned, so a TiWN(15) / AlSiCu (400) / TiWN(30) metalization structure was deposited by magnetron sputtering at the FTM tool (thickness in nanometers). Figure 3.12 shows the mask used in this step, where the blue regions represent the patterned metal. In addition to the top pad, the bottom pad is also patterned to reinforce the electrical contact.

3.2.11 Field line definition

The integration of a field line antenna on top of the MTJ device allows to apply a local in-plane magnetic field without the need of an external electromagnet, which is an important advantage for appli-

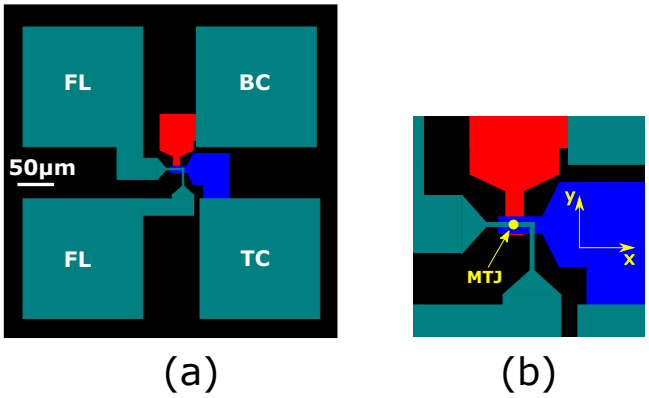


Figure 3.14: (a) Mask used for the field lines definition (i.e. dark blue region). (b) Zoom in at the pillar region showing the field line defined on top of the pillar (the MTJ size is magnified for clarity). Useful information: bottom contact (BC), top contact (TC) and field line (FL).

cations. The first step is to insulate the MTJ contacts from the antenna, so a thick 600 nm layer of AlO_x was deposited by magnetron sputtering at the FTM tool. Then, the fabrication was divided into two lithographies.

The first lithography aims to fabricate a via through the AlO_x layer to recover the MTJ contacts. Figure 3.13 shows the mask used for the vias. The metalization structure denotes the metal deposited before the top pads patterning (section 3.2.10). After opening the vias, a second TiWN(15) / AlSiCu (300) / TiWN(30) metalization structure is deposited by magnetron sputtering at the FTM tool to be patterned as the field lines (thickness in nanometers).

The second lithography finishes the process by defining the field line. Figure 3.14a shows the mask used in this step, where the dark blue regions represent the metal patterning. In addition to the field line, there is metal reinforcement of both MTJ pads. The field line allows the application of an in-plane field in the yy direction (Fig. 3.14b), which is typically the MTJ easy axis defined by the annealing treatment.

Chapter 4

Bio-inspired capabilities for vortex-based spin torque nano-oscillators

In this chapter, a systematic characterization of spin torque vortex oscillators (STVOs) working as rectifiers (i.e. spin diodes) is presented. Experimentally, it is observed that the dynamic response of the STVO depends on the vortex chirality. Consequently, fixing the frequency of the input signal and switching the vortex chirality results in a different rectified voltage. In this way, the chirality can be deterministically controlled via the application of electrical signals injected locally to the device, resulting in a non-volatile control of the output voltage for a given input frequency. Micromagnetic simulations corroborate the experimental results and show the main contribution of the Oersted field created by the input RF current density in defining two distinct spin diode detections for different chiralities. Based on these results, it is proposed to use such devices as programmable non-volatile synapses in artificial neural networks.

4.1 Artificial neural networks

The main results presented in this chapter showing the rectification capabilities of spin torque vortex oscillators are motivated by the scientific hot topic of artificial intelligence [106]. Artificial neural networks (ANNs) are the most studied bio-inspired algorithms, whose main objective is to emulate the transmission and processing capabilities of a biologic neural system. Within the possible tasks, ANNs show excellent results in many domains of science, some more obvious as image [107] and speech [108] recognition and others not so intuitive as precision medicine [109]. Nowadays, the best performance to address real applications is given by deep neural networks. As an example, Fig. 4.1 shows an illustration of a simplified deep neural network for image recognition. The raw input data is an image inserted in the form of an array of pixels that will be processed by the network into an output recognizing the image. Each layer is constituted by a set of non-linear neurons (e.g. four neurons in layer 1) that process the input data and transmit their outputs to all the neurons of the next layer. Each

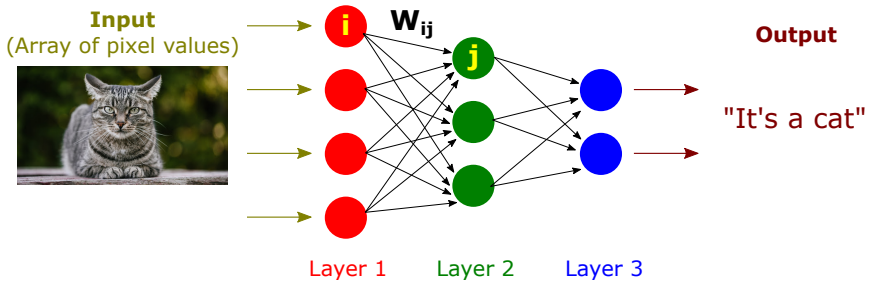


Figure 4.1: Illustration of a simple artificial neural network for image recognition.

neuron has an activation function, which is no more than a non-linear mathematical function applied to the input data. A very popular non-linear function that allows a faster learning in deep neural networks is the rectified linear unit (ReLU) [110]. Every pair of neurons placed in consecutive layers is connected by an artificial synapse that dictates how much of the information is transmitted from one neuron to the other. Considering Fig. 4.1, the input $\mathrm{I_j}$ that the neuron *j* from layer 2 receives from the output $\mathrm{O_i}$ of each neuron *i* from layer 1 results from a multiply-and-accumulate operation given by

$$I_j = \sum_{i=1}^{4} W_{ij} \cdot O_i, \tag{4.1}$$

where $\mathrm{W_{ij}}$ is the synaptic weight that multiplies the information that is being transmitted between neurons. As the name suggests, a deep neural network is much more complex than its simplified version in Fig. 4.1. In reality, it is constituted by a large number of neurons, easily going up to hundreds or thousands of layers [106]. Typically, they take high dimensional input data (as an array of pixels from an image) and the neural processing tends to focus only in some characteristics of the raw input data, in accordance with the desired output. For instance, in Fig. 4.1, if the aim is to recognize a cat from an input image, the network should be sensible to the face features of the animal (e.g. whiskers, ears), whereas its colour can be neglected.

In order to perform its task, the network needs to pass through a machine learning process, in which the synaptic weights are tuned based on the response of the network to different inputs. This process is called supervised learning [106]. Again, considering the network of Fig. 4.1, the supervised training should teach the network to recognize a cat from an input image. For that, different input images are passed through the network and, based on the output, the synaptic weights are tuned to minimize the error. For instance, if the output changes depending on the cat colour, the weights should be changed to neglect the pixel information regarding the colour. After training, a successful network should exhibit the same output (i.e. "it's a cat") for similar inputs (i.e. different cats). A very efficient way to perform supervised learning is by back-propagation [111], where the error is computed backwards, from the output to the input. During training, a single raw input will lead to a specific output that may be different from the target output. From that difference results an error that is computed backwards, layer by layer, until reaching the first layer that receives the raw input. In this backward process, each synaptic weight is modified in proportion to its contribution to the error. This process is repeated until the error is below a minimum of acceptance. At this final stage, the most important

objective is to guarantee that the network will generally perform correctly, even if the input data was not used in the learning process.

4.2 Spintronics hardware for neuromorphic computing

Neural networks need an hardware to be implemented. Nowadays, most of these algorithms run on supercomputers, which are generally constructed in a von-Neumann architecture. Although being dedicated to perform an ANN algorithm, these supercomputers are not power and time efficient, due to the "von-Neumann bottleneck" that results from the continuous data transfer between the separate memory and processing units. Nowadays, this is one of the main challenge for artificial intelligence development, which in turn leads to the natural assumption that electronics needs to be reinvented [112]. In this context, neuromorphic engineering is trying to move forward, taking inspiration in one of the most efficient known hardware: the human brain. Its most important feature is the capacity to surpass the efficiency of any supercomputer nowadays that executes an ANN. On one hand, this fact comes from the multitasking ability of the brain, whereas supercomputers are programmed to execute a specific neuromorphic task. On the other hand, the energy required for brain operation is much smaller, with a power consumption of roughly 20 W. A very clear comparison is done by Marković *et al.* [48], where they show that the deep neural network BERT [113], developed by Google AI for natural language processing, requires an energy of 1000 kWh to train for 80 h, whereas the brain, with the same energy, could operate for 6 years. For this discrepancy contributes the brain architecture, where the memory (i.e. synapses) and processing (i.e. neurons) units are entangled, forming a complex system of 10^{11} neurons interconnected by 10^{15} synapses. So, to build small and efficient neuromorphic chips, research needs to develop a completely new class of hardware inspired by our brain architecture. To date, various hardware schemes have been proposed to implement neuromorphic computing, namely optical [114], CMOS [115] and memristive [116] devices. All of these approaches share the necessity to have in-memory computing by designing systems that compute within the memory, in this way removing the need of a constant data transfer between separate processing and memory units. Some architectures were already scaled up to chips with more than one million of memristors [117–119], with an accuracy efficiency of 94.4 % for handwritten digit recognition [119].

Due to their functional flexibility, non-linear characteristics, high endurance and nanoscale dimensions, spintronic devices are also presented as promising hardware for the development of neuromorphic computing [42–44, 46, 120–126]. Significant advances have been made experimentally, with reports showing STNO neural capabilities in reservoir computing systems [43, 123, 124], where the transient dynamic state of the oscillator (i.e. short-term memory) is used to compute time-varying input signals. Recognition of spoken digits (0 to 9) pronounced by five different people has been shown in a single STNO, with recognition rates up to 99.6 $\%$ [43]. The transition from digits to vowel recognition was achieved in a synchronization-based computing system [44], where the recognition is performed based on the synchronization state between the input signal and a chain of four STNOs representing artificial neurons (Fig. 4.2c). Specifically in the same report, during the learning steps, the DC current applied to each STNO is constantly tuned as a synaptic weight, which in turn changes the steady-state oscillation frequency and the synchronization map with the input RF signals $\mathrm{f_A}$ and $\mathrm{f_B}$. Before any training (Fig. 4.2a), the system is not suitable for the task, since most of the vowel distributions still overlap over more than one synchronization region. After 86 training steps (Fig. 4.2b),

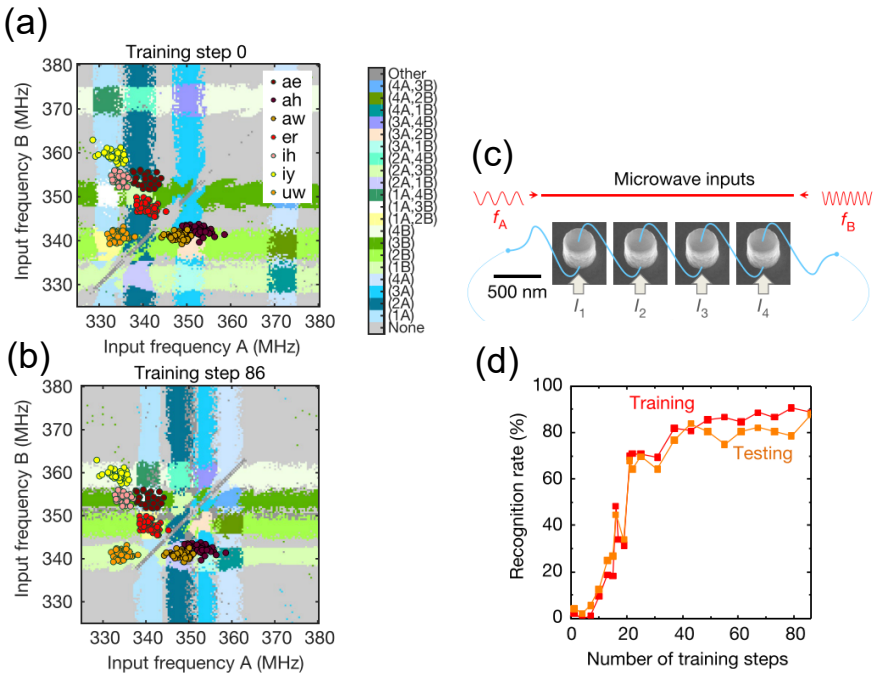


Figure 4.2: (a)-(b) Experimental synchronization maps, measured as a function of the input RF signals $\mathrm{f_A}$ and $\mathrm{f_B}$, (a) before and (b) after 86 training steps. Each colour region corresponds to a different synchronization state between the four oscillators and the input. Dots with different colours correspond to different vowels and their spread is a consequence of being spoken by different people. (c) Illustration of the experimental setup, where four oscillators working as neurons are connected in series. The inputs $\mathrm{f_A}$ and $\mathrm{f_B}$ are transmitted by a field line as two microwave fields. (d) The vowel recognition rate is presented as a function of the number of training steps. Adapted from [44].

each vowel distribution tends to be confined to a distinct synchronization region, which naturally increases the recognition rate (Fig. 4.2d). In the end, the objective is to obtain the same output for similar inputs, meaning that the neuromorphic system should recognize the same vowel spelled by different people.

MTJs working as resonators (see section 4.3) have also been proposed to be integrated in neuromorphic systems as artificial synapses for input microwave signals [46, 125]. The nano-oscillator performs a non-linear spin diode rectification to the input signal, being its synaptic weight dependent on the frequency difference between the input RF signal and the resonator. This means that two nano-oscillators with different resonance frequencies will apply two distinct weights to the same input signal, meaning that each resonator will return a different rectified voltage. In the learning process, the tuning of the synaptic weights implies changing the spin diode response (see section 4.3) of the nano-oscillators working as synapses. In STVOs, it was already demonstrated that the tuning of the synaptic weight of a single oscillator can be achieved simply by applying an external in-plane field that changes its frequency of resonance [46]. Nevertheless, in addition to the tuning capability, the synapse needs to have a memory to avoid loosing its weight update after each tuning step. This

means that the spin diode detection needs to be changed in a non-volatile scheme. The work presented in this chapter comes in line with the necessity of giving a memory to STVOs working as artificial synapses. The aim is to show that the non-volatile capability of an STVO is present in the vortex magnetic state of the free layer, specifically in its chirality. Starting in section 4.6, it is demonstrated that the synaptic weight of an STVO by spin diode effect depends on the vortex chirality and can be persistently changed upon fabrication by means of a proper initialization applied to the device alone.

4.3 RF detection in magnetic tunnel junctions

The experimental results presented in this chapter are based on an important RF detection phenomenon, generally called the spin diode effect [36], where an RF signal goes as an input through a

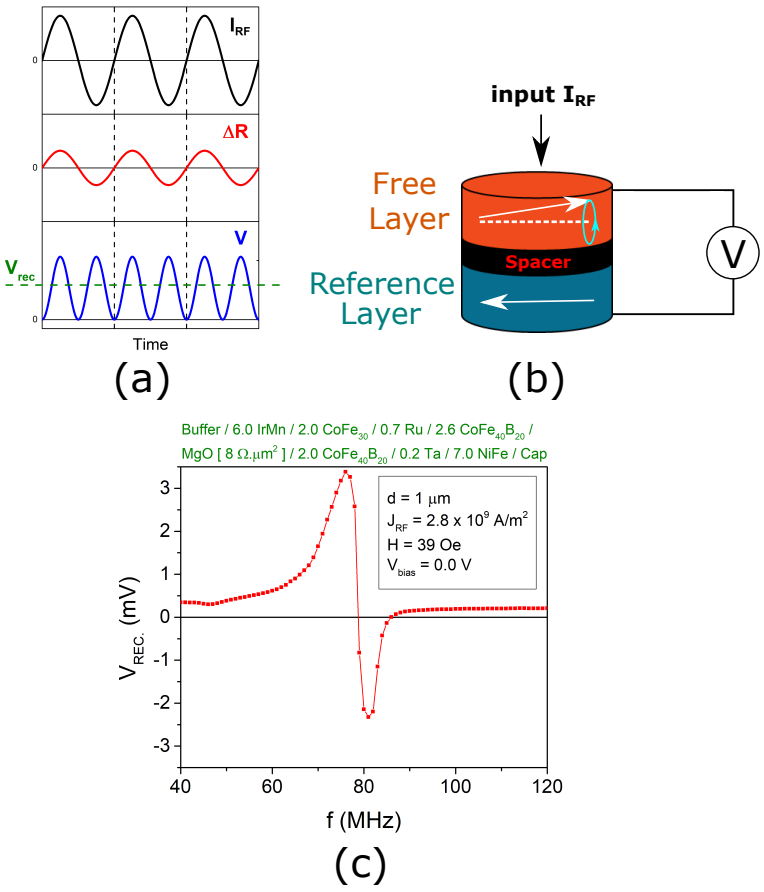


Figure 4.3: (a) Illustration of the spin diode concept. (b) RF detection performed by a nanopillar acting as a spin torque nano-detector (V labels a voltmeter). (c) Example of a spin diode measurement performed at INL for a vortex-based magnetic tunnel junction with a diameter of 1 μm. An in-plane magnetic field of 39 Oe was applied in the easy axis during the measurement.

FL	RL	S (mV/mW)	f (GHz)	Operation regime	Ref.
$\rightarrow$	$\rightarrow$	1.4	5 - 10	Passive	[36] (1st report)
$\uparrow$	$\rightarrow$	1.2×10^4	1.5 - 1.6	Active	[37]
$\uparrow$ (canted)	$\rightarrow$	2.1×10^5	0.4 - 1	Active	[39]
vortex	$\rightarrow$	8.0×10^4	0.44 - 0.48	Active	[41]
$\uparrow$ (canted)	$\rightarrow$	70 (at zero field)	broadband (up to 1.2)	Passive	[129]

Table 4.1: Summary of STND performances from the literature, where the sensitivity (S) and frequency of operation (f) are the indicative parameters. Regarding the magnetic properties of the MTJ, FL and RL refer to the free and reference layers, respectively, which may present an in-plane ($\rightarrow$), a perpendicular ($\uparrow$) or a vortex magnetic state. The operation regime indicates the resonance conditions: passive for a spin diode and active for a bias-assisted phenomenon. It should be emphasized that, considering the way that each reference exposes its experimental results, some of them above are approximations. Except for Ref. [129], the sensitivities correspond to the best result obtained at each reference.

magnetic multilayer, such as a spin valve or an MTJ, and delivers an output signal based on a rectification mechanism. Figure 4.3b shows the RF detection performed by a nanopillar acting as a spin torque nano-detector (STND). If an alternating current $\mathrm{I_{RF}(t) = A\,sin(2\pi ft)}$ is applied as an input, the STT effect will promote the magnetization precession in the free layer, according to the same frequency. The magnetoresistive effect leads to a periodic variation of the resistance $\mathrm{\Delta R(t) = B\,sin(2\pi ft)}$. In these conditions, the output voltage $\mathrm{V(t) = \Delta R(t) \cdot I_{RF}(t)}$ becomes

$$V(t) = \frac{A \cdot B}{2} \cdot [1 - \cos(2\pi \cdot 2ft)]\,. \tag{4.2}$$

As confirmed in Fig 4.3a, the output voltage has an AC component oscillating at $\mathrm{2f}$ and a rectified DC component, which is the signature of the detection. Experimentally, the rectified voltage can be measured with a voltmeter (Fig. 4.3b) while injecting the RF signal through the nanopillar. The spin diode effect is a resonance phenomenon, meaning that the magnetization precession can be strongly amplified if the frequency of the input signal approaches the natural frequency of the detector. Figure 4.3c shows an example of a spin diode measurement performed for an MTJ with a vortex magnetic state in the free layer, where the frequency of the input RF signal is swept while measuring the output. The rectification is characterized by a peak function centered at the resonance frequency of the vortex gyrotropic mode ($\sim 78\,\mathrm{MHz}$), showing the typical lineshape obtained for the vortex-based STNDs fabricated in this thesis (more details will be given through this chapter).

Since the first experimental demonstration of the spin diode effect [36], MgO-based magnetic tunnel junctions have become the standard device for STNDs. The two most important parameters to evaluate an STND performance are the sensitivity (i.e. the ratio between the rectified voltage and the power of the input signal) and the frequency bandwidth of operation. Nowadays, the sensitivity of STNDs already surpasses the performance of standard Schottky diodes ($\sim 10^3\,\mathrm{mV/mW}$ [37]) by roughly two orders of magnitude [39]. Table 4.1 shows a small summary of important experimental reports for the optimization of STNDs.

In MTJs with a uniform magnetized free layer, the detection has been optimized by switching from

a passive to an active regime. In fact, an STND does not need a power supply to rectify according to the spin diode effect. Nevertheless, an active regime, i.e. the application of a DC current during the resonance process, increases the amplitude of the oscillation, which in turn increases the resistance variation and the sensitivity [37]. Along with a bias-assisted detection, the control of the perpendicular magnetic anisotropy of the free FM layer leads to a canted magnetization from the perpendicular direction at the remanent state, due to the stray magnetic field created by the FM layers of the SAF structure [38,39]. The result is the possibility to obtain large sensitivities in the absence of an external magnetic field (up to $\sim 10^5\,\mathrm{mV/mW}$) [39]. In a different approach, an STND with a weak perpendicularly magnetized free layer may also operate in a broadband regime, characterized by a large amplitude out-of-plane precession of the magnetization [130]. This non-resonant mode only appears when the input RF current exceeds a specific frequency-dependent threshold value. Considering the broadband characteristics of the phenomenon [131], the detector can rectify all the input RF signals with a frequency falling in the broadband regime, which makes it suitable for energy harvesting [129].

In vortex-based MTJs, the spin torque exerted by the input RF signal excites the large variety of vortex modes [75, 132], including its fundamental gyrotropic mode [133]. The sensitivity can be enhanced by promoting the vortex core expulsion with a combination of a DC bias and an RF signal [40,41]. So, in the resonance bandwidth, the core expulsion transforms the vortex into a quasi-uniform state, whose main consequence is a sharp variation of the MTJ resistance. Above the threshold, the detection is independent of the input power, i.e. the core expulsion always leads to the same variation of the output voltage.

4.4 MTJ design and stack

In this chapter, the characterization was performed in MTJs with a 5 Ta / 50 CuN / 5 Ta / 50 CuN / 5 Ta / 5 Ru / 6 IrMn / 2 $\mathrm{CoFe_{30}}$ / 0.7 Ru / 2.6 $\mathrm{CoFe_{40}B_{20}}$ / MgO ($8\,\Omega\mu\mathrm{m}^2$) / 2 $\mathrm{CoFe_{40}B_{20}}$ / 0.2 Ta / 7 NiFe / 10 Ta / 7 Ru stack (thickness in nanometers), whose fabrication process is in accordance with chapter 3. In reality, the free layer is a 2 $\mathrm{CoFe_{40}B_{20}}$ / 0.2 Ta / 7 NiFe structure, where the CoFeB and the NiFe layers are magnetically coupled. The nanopillars were defined with a nominal diameter ranging from 0.3 μm to 1.0 μm. For all diameters, the aspect ratio of the free layer induces a vortex magnetic state at remanence. Deposited on top of the insulating barrier, the CoFeB layer allows to maintain the large TMR values already expected for CoFeB/MgO/CoFeB-based MTJs. The NiFe layer ($\mathrm{Ni_{81}Fe_{19}}$) decreases the threshold current density for gyrotropic motion, due to its lower magnetization. The ultra thin Ta layer aims to eliminate the possibility of the CoFeB layer to crystallize according to the fcc structure of the NiFe layer [62], whose immediate consequence is an abrupt decrease of the TMR value.

Figure 4.4 shows a top view of the MTJ design, composed by two contacts and an integrated field line fabricated approximately 600 nm on top of the free layer, with a width of 3 μm (the same design as shown in Fig. 3.2). The field line includes two contact pads, giving the possibility to apply a wide set of signals (e.g. DC current, RF signal, pulse) through the metallic TiWN(15) / AlSiCu (300) / TiWN(30) field line structure (thickness in nanometers) that in turn sets the local magnetic field applied to the MTJ device. In this geometry, the field line is capable of producing a local magnetic field, large enough to saturate the magnetization of the free layer. The main advantage of the field line comes from its integration in the MTJ geometry, which discards the need for an extra setup element, as an

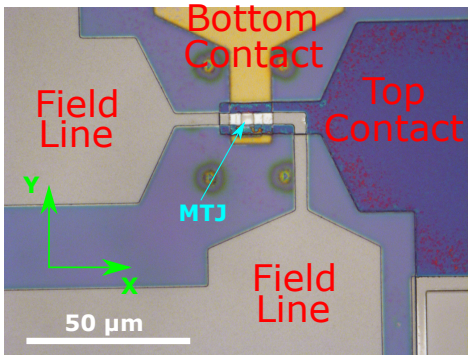


Figure 4.4: Top view of the fabrication design with the integrated field line fabricated on top of the MTJ pillar.

electromagnet, to apply the in-plane field.

4.5 Vortex initialization

In section 1.7.2, it was already emphasized the importance of the vortex chirality in its dynamics. Specifically, the theory predicts a steady-state oscillation at different frequencies for vortices with opposite chiralities [83, 88], which is experimentally demonstrated in Fig. 1.12. As it will be clear through this chapter, the vortex chirality is also fundamental to program the proposed non-volatile synapse (see section 4.6.1). So, before characterization, the MTJ device under study needs to be initialized, according to a protocol aiming to set the chirality of the vortex state in the free layer.

Figure 4.5a shows a transfer curve that summarizes how the initialization is performed with the field line, in conjugation with a local DC bias current applied to the MTJ (see the setup in Fig. 4.5b). Here, a positive DC bias current corresponds to electrons travelling from the free to the reference layer and a positive chirality (C = +1) corresponds to a clockwise rotation of the free layer magnetization as seen from the bottom (see inset of Fig. 4.5a). The protocol can be described as a three-step initialization of the vortex. In the first step, a DC bias current $\mathrm{I_{DC}}$ is applied directly through the MTJ, together with a field line DC current $\mathrm{I_{FL}}$, producing a local magnetic field $\mathrm{H_{FL}}$ large enough to saturate the free layer (point 1 in Fig. 4.5a). In the second step, the magnetic field is reduced down to a value that results in the renucleation of the vortex (point 2 in Fig. 4.5a). In this example, the magnetic field was reduced down to zero (but a range of other values is possible in accordance to the specific transfer curve of the device), while maintaining the MTJ bias current amplitude. At this point, the chirality of the vortex is defined by the direction of the Oersted field associated with the MTJ bias current [134]. A positive bias current results in the nucleation of the vortex with a positive chirality, while a negative bias current results in the nucleation of the vortex with a negative chirality. In the third step, the magnetic field and bias current are set to zero. In the end, the vortex chirality is defined and remains stable, so that switching the vortex to the opposite chirality is achieved simply by repeating

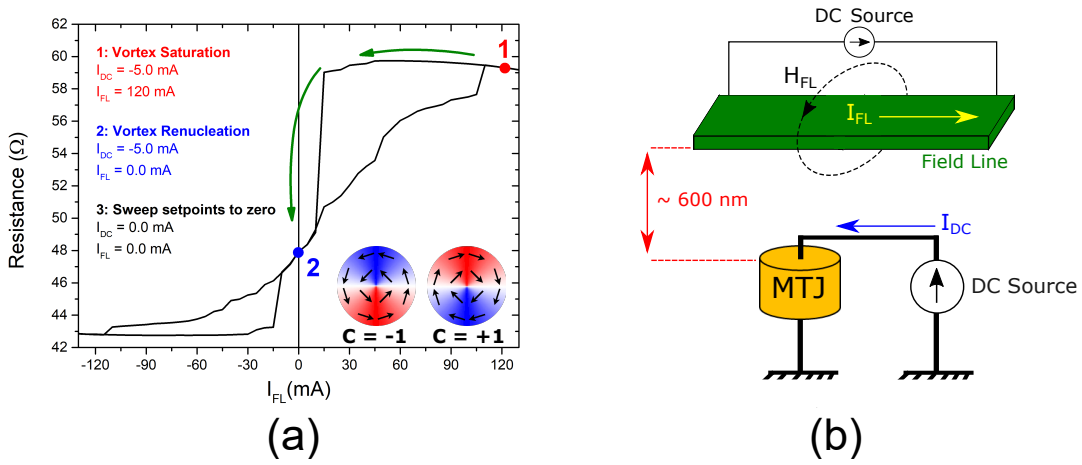


Figure 4.5: (a) Transfer curve explaining the three-step initialization process for an MTJ with a diameter of 1.0 μm. The resistance of the MTJ is depicted as a function of the DC current $\mathrm{I_{FL}}$ applied through the integrated field line. In this example, an applied DC current of -5.0 mA sets the vortex with a negative chirality (C = -1). The insets show how each chirality is associated with a different circulation of the in-plane magnetic moments of the vortex. (b) Illustration of the experimental setup used for initialization. The field line is roughly 600 nm on top of the free layer.

the process with an MTJ bias current applied in the opposite direction.

Following the protocol illustrated in Fig. 4.5a, the saturation and consecutive renucleation of the vortex can also be achieved with a fast pulse applied to the field line (Fig. 4.6a). While applying $\mathrm{I_{DC}}$ to the MTJ, the pulse creates a short in-plane magnetic field, with an amplitude large enough to saturate the vortex. In this context, the main advantage of the pulses is to allow the initialization of the MTJs with smaller diameters. Experimentally, it is observed that the field line withstands a DC current roughly up to 130 mA ($\sim 2\,\mathrm{V}$ measured across the field line) before being destroyed by Joule heating (i.e. open circuit for the field line contact), which limits the use of the field line to MTJ devices where the vortex annihilation occurs for $\mathrm{I_{FL}} < 130\,\mathrm{mA}$. This constraint immediately reduces the available MTJ devices, leaving the two largest diameters, 0.9 μm and 1.0 μm (in this aspect ratio range, the smaller the free layer diameter, the larger the vortex annihilation field [84]), as the only possibilities to work with a field line. A fast pulse allows to apply a larger amplitude signal (up to 5.2 V) in a short period of time without compromising the field line. So, for MTJs with a diameter smaller than 0.9 μm, the initialization with the field line can only be achieved with pulses. Figure 4.6b shows the pulse parameters that were used to optimize the initialization. Beyond the width (w) and amplitude ($\mathrm{V_A}$), the pulse is also defined with an offset amplitude ($\mathrm{V_{off}}$) that is turned off after the initialization. This offset is tuned depending on the MTJ device and it is used to guarantee that the vortex renucleates after saturation. For instance, the MTJ device whose R-H loop is shown in Fig. 4.5a does not need an offset (i.e. $\mathrm{V_{off}} = 0\mathrm{V}$), because going from saturation to remanence is enough for a transition to the vortex region, but this is not generally the case, so it should be evaluated individually for each MTJ device. To be successful, the initialization needs to be deterministic, i.e. the protocol must give a

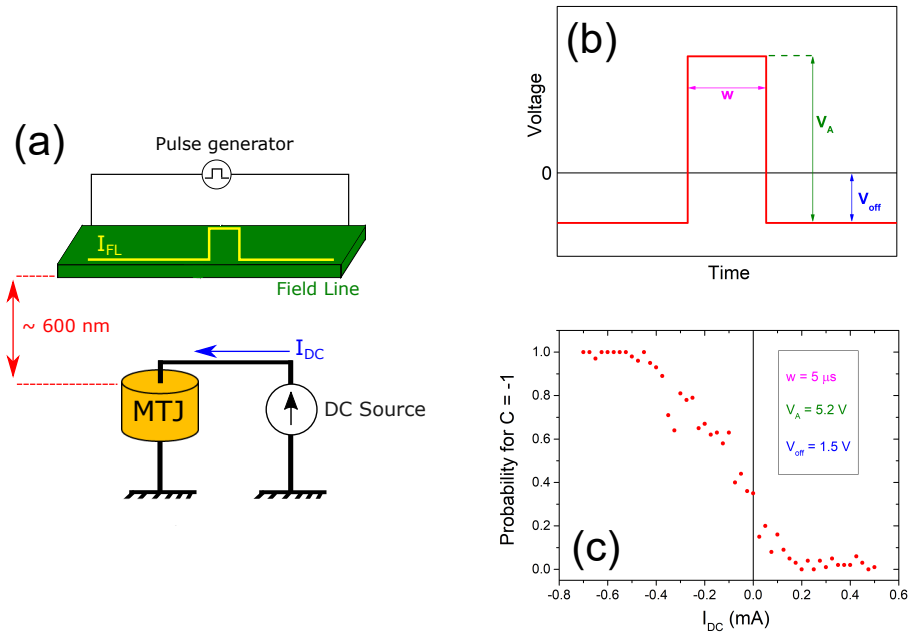


Figure 4.6: (a) Again, an illustration of the experimental setup used for initialization is presented, now with a pulse generator. (b) The initialization is performed with pulses controlled by three main parameters: width (w), amplitude ($\mathrm{V_A}$) and offset ($\mathrm{V_{off}}$). (c) Probability of having a negative chirality, presented as a function of the DC current applied to the MTJ during the initialization. For each $\mathrm{I_{DC}}$ setpoint, the probability is calculated based on 100 repetitions of the initialization. The pulse parameters were constant over the full measurement.

full control over the vortex chirality. To do that, the chosen method was to evaluate the deterministic degree of the protocol as a function of the DC current applied to the MTJ device. In Fig. 4.6c, the probability of having a negative vortex chirality after initialization is presented as a function of $\mathrm{I_{DC}}$. These results were obtained from the MTJ device with a diameter of 300 nm whose dynamics were already presented in Fig. 1.12. For each $\mathrm{I_{DC}}$ setpoint, 100 repetitions of the initialization were performed. After each repetition, the chirality can be easily checked by measuring the frequency of the steady-state dynamics that is different for opposite chiralities (see Fig. 1.12a). At zero bias, the results show an expected stochastic behaviour, since there is no Oersted field breaking the symmetry. The process evolves to deterministic as the intensity of $\mathrm{I_{DC}}$ increases. From a practical point of view, this analysis is necessary to know the $\mathrm{I_{DC}}$ range at which the initialization is safely deterministic.

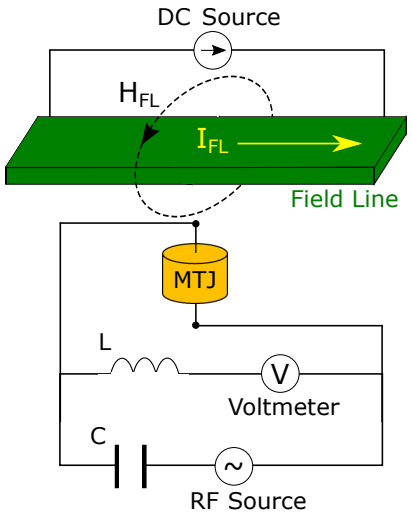


Figure 4.7: Illustration of the experimental setup used for spin diode measurements.

4.6 Non-volatile synapse based on a vortex nano-oscillator

4.6.1 Experimental synaptic weights

After the vortex initialization, the first measurement to be done aims to study the effect of the vortex chirality in the spin diode response. Figure 4.7 shows the setup used for the spin diode measurements. Based on a standard setup [36], a bias tee [represented by an inductance (L) and a capacitance (C) elements] allows to apply an RF signal with a sweeping frequency directly to the MTJ and measure its output rectified voltage simultaneously with a voltmeter. The field line allows to measure the spin diode response as a function of the in-plane field, as will be described in section 4.6.3. As already emphasized in section 4.5, the field line withstands a DC current roughly up to 130 mA before being destroyed by Joule heating. The study of the spin diode response as a function of the in-plane field implies the core displacement up to expulsion, so the use of the field line is limited to the larger MTJs, with diameters of 0.9 μm and 1.0 μm. This is the reason why, in the discussion that follows, the focus goes to MTJ devices with larger diameters. Nevertheless, it is observed that even for the largest diameters, the field line may also be destroyed. Typically, in these situations, the MTJ device without a field line continues to be measured, now using the electromagnet to apply the external magnetic field.

Figures 4.8a-b show spin diode measurements obtained from an MTJ with a diameter of 1.0 μm, as a function of the input RF current density ($\mathrm{J_{RF}}$) at zero external magnetic field. There is an obvious dependence of the spin diode output on the vortex chirality. The difference between the two chiralities is made evident in Fig. 4.8c, obtained by measuring the spin diode voltage output as a function of frequency for a fixed RF amplitude, corresponding to a current density of $2.8 \times 10^9\,\mathrm{A/m^2}$ across the MTJ. The output obtained for each chirality shows two distinct lineshapes, i.e. peak-to-valley for C = +1

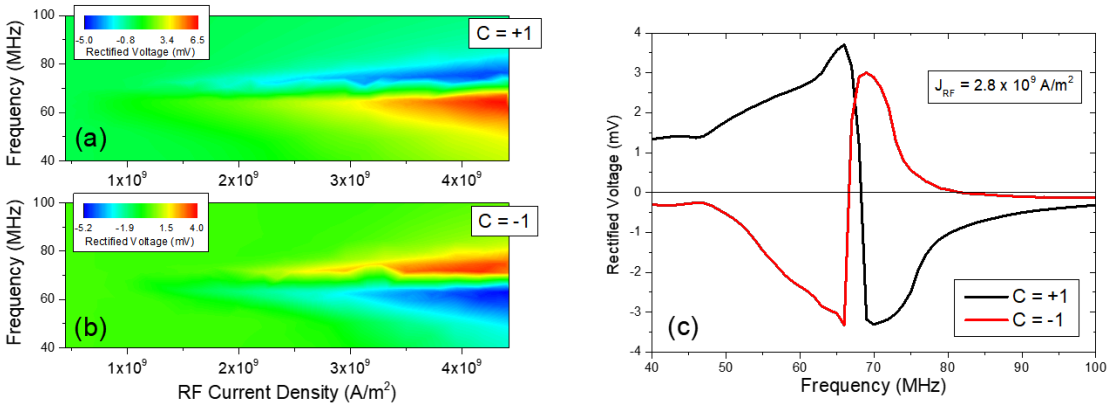


Figure 4.8: Spin diode measurements presented as a function of the input RF current density for (a) positive and (b) negative chiralities. (c) Spin diode measurement obtained for an input RF current density of $2.8 \times 10^9\,\mathrm{A/m^2}$.

and valley-to-peak for C = -1.

Before looking at the opportunities given by these spin diode results, the focus goes to the shape of the spin diode spectrum as presented in Fig. 4.8c. Since the first report of the spin diode effect in MTJs [36], research tried to give a quantitative description of the phenomenon, namely understanding the spin diode lineshapes [71, 135–137]. Fundamental results were presented in symmetric MgO-based MTJs (i.e. both reference and free layers are fabricated with the same materials), showing that the Slonczewski and field-like torque efficiencies (η_{ST} and η_{FLT}, as defined in section 1.7.1) show different dependencies with the bias voltage ($\mathrm{V_{bias}}$), leading to two different regimes, for positive and negative biases, characterized by different spin diode lineshapes, where η_{ST} (η_{FLT}) contributes to a Lorentzian (anti-Lorentzian) peak function [71, 135]. Moreover, the results indicate that zero bias conditions lead to a pure Lorentzian response, as a consequence of a full contribution of η_{ST} (i.e. η_{FLT} is quadratic and symmetric in relation with the bias polarity, so that $\eta_{FLT} = 0$ for $\mathrm{V_{bias}} = 0$ V). On the other hand, for asymmetric MTJs, it was also demonstrated that a relevant contribution from η_{FLT} may also exist at zero bias, due to its symmetry breaking [136, 137]. In fact, the MTJs fabricated in this thesis are also asymmetric, where the reference layer is CoFeB and the free layer is in reality two layers (CoFeB and NiFe) magnetically coupled. Nevertheless, the results shown in Fig. 4.8c cannot be fitted with a peak function translating a combination of a symmetric and an anti-symmetric Lorentzian, as successfully performed in Ref. [137]. The spin diode spectrum is a consequence of the different mechanisms promoting the precession in the free layer, meaning that the resonance of the vortex core in our system is not completely described by considering only the STT effect. As will be further described in section 4.6.2, the extra mechanism to be considered is the Oersted field created by the RF signal injected through the STVO.

Based on the results shown in Fig. 4.8, the synaptic performance of the STVO can be measured. As already emphasized in section 4.2, the working principle of a neuromorphic STVO is that its synaptic weight is a function of the difference between the frequency of the input signal and the resonance frequency of the device [46, 125]. In Fig. 4.9a, the frequency of the RF signal is fixed at 60 MHz as the output voltage is presented as a function of the RF signal amplitude. These results

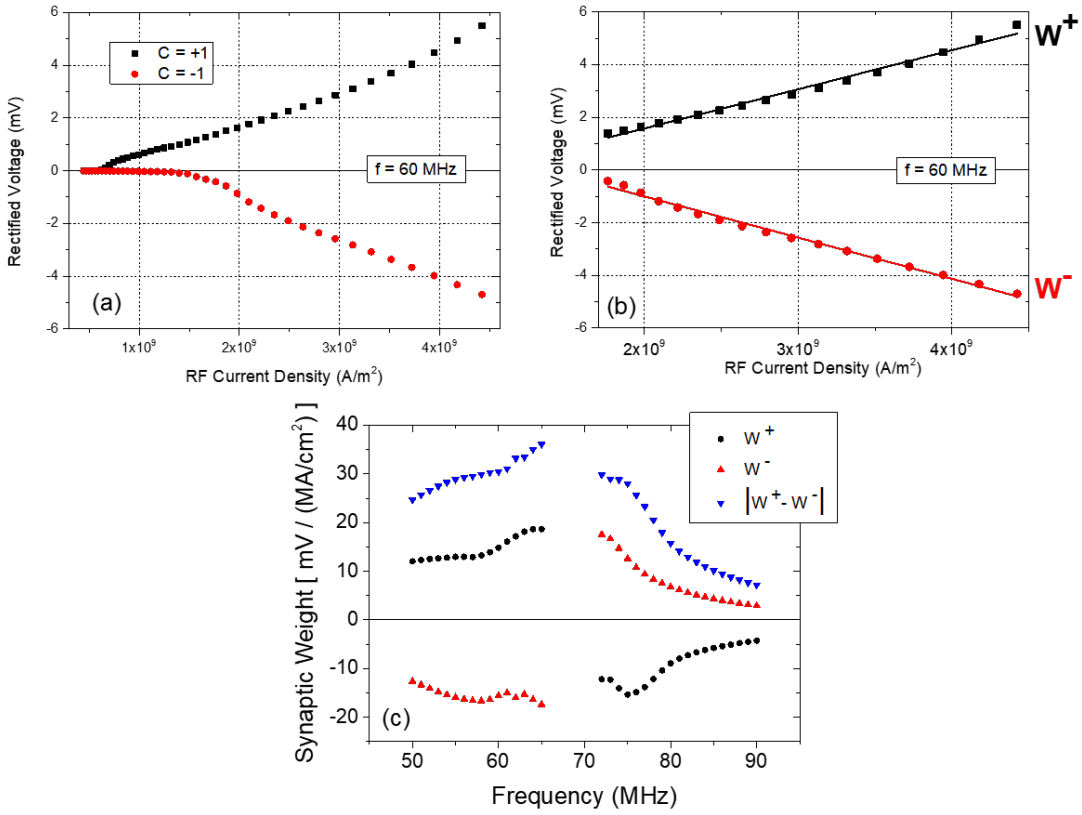


Figure 4.9: (a) Rectified voltage measured at a fixed frequency of 60 MHz and presented as a function of the input RF current density. (b) The same results are now presented in the operational window, where the synaptic weights are defined by the slope of each linear fit. (c) Synaptic weights presented as function of the input frequency for both chiralities. The absolute difference between the two weights is also depicted.

are presented for the same device whose spin diode measurements are depicted in Fig. 4.8, so that the fixed frequency value was chosen to be close to the central frequency of the detection spectrum. The voltage dependencies show that each chirality presents a different critical RF amplitude for a sustained gyrotropic resonance. For a positive (negative) chirality, the threshold is below (above) an RF current density of $1.0 \times 10^9\,\mathrm{A/m^2}$. This is a result already predicted in the literature, where the different critical amplitudes are a consequence of the vortex stiffness variation with the chirality [83]. Here, the choice is to have non-zero synaptic weights for both chiralities, so these conditions imply a restriction to the synaptic operation, since it can only be performed for input signals with an RF amplitude above the largest critical value. In the case of Fig. 4.9a, the operational window is roughly above $1.7 \times 10^9\,\mathrm{A/m^2}$, due to the critical amplitude presented for a negative chirality. In this way, the same results are presented in Fig. 4.9b, now in the new operational amplitude domain, i.e. $\mathrm{J_{RF}} > 1.7 \times 10^9\,\mathrm{A/m^2}$. From each chirality results a rectification with a different sign, coming from the different spin diode spectra shown in Fig. 4.8c. It is also worth noting that a linear fit shows a good agreement with the voltage dependency, indicating that the non-linear characteristics of the

nano-oscillator [138] have a small effect in this operational window. Thus, the STVO can function as an artificial synapse whose weight can be persistently changed in a binary and non-volatile scheme, so that the rectified voltage measured for positive (V^{+}) and negative (V^{-}) chiralities is given by [125]

$$V^{+} = W^{+} \cdot J_{RF} \tag{4.3}$$

or

$$V^{-} = W^{-} \cdot J_{RF} \tag{4.4}$$

where W^{+} and W^{-} are the synaptic weights (i.e. slope of each linear fit in Fig. 4.9b) for each chirality. Similar to an STT-MRAM [139] , where a large current density is used to set MTJs between two possible states that are read at low current densities, the initialization step allows to switch the chirality of the vortex, which in turn changes the spin diode output at fixed values of input RF signal amplitude and frequency. Figure 4.9c extends the calculation of the synaptic weights through the frequency domain. As expected, the module of the difference between the synaptic weights is maximized as the frequency approaches the center of the spin diode spectrum, where the output voltage tends to have its maximum value. A small frequency domain in the center was not considered, because it is an unstable region, characterized by a change of the output voltage sign. In the same region, even for a fixed frequency, the voltage value for a specific chirality can easily switch between positive and negative as function of the RF amplitude, which makes it difficult to define a constant weight.

The synaptic weight is proportional to the output voltage measured for a given $\mathrm{J_{RF}}$. In turn, the output voltage depends on the amplitude of the vortex core oscillation during resonance, in a way that, by the TMR effect, a larger orbit of the core leads to a larger output voltage. Thus, to maximize the synaptic weights, it is required to maximize the radius of the vortex orbit. From a material point of view, that radius depends in a complex way on a large number of properties [40] but, as an example, a possible path is to decrease the Gilbert damping of the free layer [140].

As said before, the programming of the STVO was performed in an RF amplitude domain where both chiralities show a non-zero synaptic weight, but it does not mean that it is the only possible configuration. For smaller RF amplitudes, although having $\mathrm{V}^{-} = 0$ (Fig. 4.9a), there are still two different weights ($\mathrm{W}^{-} = 0$ and $\mathrm{W}^{+} > 0$) , which means that the conditions for a binary programming still exist.

Once a non-volatile control of the synaptic weight is achieved for a single STVO, this mechanism can be extended to a set of STVOs with different geometries and dynamic properties. Figures 4.10a-b demonstrate this possibility for a pair of circular STVOs with different diameters, where the spin diode outputs are presented for each pillar individually. Due to its lower dimensions, the MTJ with a diameter of 0.9 μm presents a larger resonance frequency than the MTJ with a diameter of 1.0 μm [86, 141], meaning that it is straightforward to program a fixed input frequency, so that the rectified voltage measured by each pillar is different. Figure 4.10c shows four possible spin diode outputs calculated as the sum of the output voltage measured individually for each pillar when subjected to a variable amplitude RF signal injected with a fixed input frequency of 60 MHz. Considering that each pillar has two possible synaptic weights (i.e. two possible chirality configurations), the system ends up with four possible programmable outputs (N non-identical STVOs lead to 2^{N} programmable outputs) that may vary depending on the frequency and power of the input signal. In addition to fabricate MTJ pillars with different diameters, there are other possible ways to obtain non-identical detectors. An alternative is to change the thickness of the free layer by deposition of a free layer wedge during the

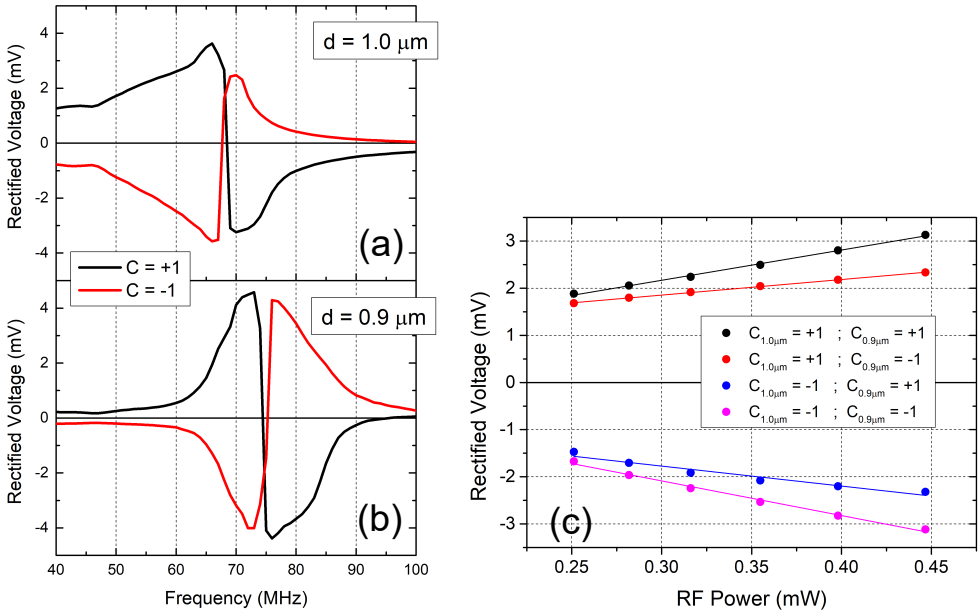


Figure 4.10: Spin diode measurements obtained for an STVO with a diameter of (a) 1.0 μm and (b) 0.9 μm, for an RF input power of 0.398 mW. The four possible programmable sums of the output voltages are presented in (c) as a function of the input RF power for a frequency of 60 MHz.

nanofabrication process, i.e. changing the vortex aspect ratio L/R, being L the thickness and R the radius of the free layer [75]). This step would lead not only to a smooth variation of the resonance frequency over the wedge, but also to a smaller variation of the resistance between non-identical STVOs, which would be essentially dependent on the sample-to-sample variability. The resistance variability between STVOs should be minimized to make sure that, for the same input RF power, all the STVOs receive approximately the same RF current density.

4.6.2 Simulated synaptic weights

To have a physical insight of the experimental results, micromagnetic simulations were performed using the GPU-based MuMax3 software [142]. The simulations comprised a circular nanodisk with a diameter of 1.0 μm and a thickness of 9.0 nm, divided into $5 \times 5\ \mathrm{nm}^2$ unit cells in the xy plane and a cell size of 9 nm in the z direction. The reference layer is set with an in-plane magnetization along the yy axis of the simulation plane. Based on experimental VSM data taken from NiFe films and standard values, the physical parameters were chosen as: saturation magnetization $\mathrm{M_S} = 680 \times 10^3\,\mathrm{A/m}$, uniaxial anisotropy constant along the yy axis $\mathrm{K_u} = 340\,\mathrm{J/m^3}$, Gilbert damping $\alpha = 0.01$ and exchange stiffness $\mathrm{A} = 1.3 \times 10^{-11}\,\mathrm{J/m}$. An RF current density $\mathrm{J_{RF}}$ was applied in the direction perpendicular to the nanodisk plane, with a spin-polarization P = 0.4 and a secondary spin-torque term $\epsilon' = 0.4$, so

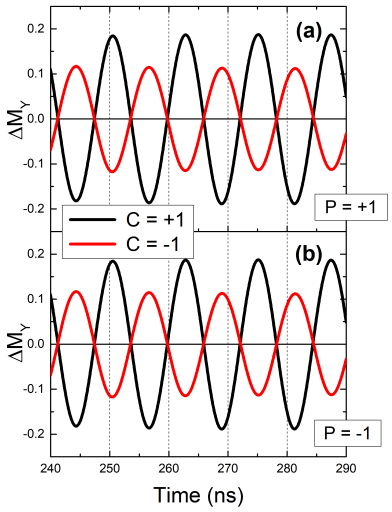


Figure 4.11: Simulated $\Delta \mathrm{M_Y}$ time traces obtained for both chiralities at an in-plane field of 39.8 Oe, for (a) positive and (b) negative polarities. Both OFT and STT are considered. The results are obtained for a frequency of 81 MHz and an RF current density of $3.0 \times 10^9\,\mathrm{A/m^2}$.

both Slonczewski and field-like torques are considered. In addition to the STT terms, the Oersted magnetic field created by the current is also considered. The Oersted field is simulated as an external radial magnetic field that creates a radial magnetic field flux $\mathbf{B_{Oe}}$ inside the nanodisk, in this way satisfying the Ampère's law from electromagnetism

$$\nabla \times \mathbf{B_{Oe}} = \mu_0 \cdot \mathbf{J_{RF}}. \tag{4.5}$$

These conditions imply that the simulated gyrotropic motion is driven, not only by the spin-transfer torque (STT) [68] that naturally arises from the spin-polarized current, but also by a realistic Oersted field torque (OFT) coming from the RF current [143–145]. The initial magnetization configuration for the micromagnetic simulations was set as a vortex with the two possible chiralities and a positive polarity. The polarity switching does not change the spin diode results, since it only dictates the direction of the vortex core trajectory (i.e. clockwise or counter-clockwise) [146], which has no effect in the oscillation of $\Delta \mathrm{M_Y}$ (Fig. 4.11) to which the spin diode response is sensible to.

The effective field (i.e. sum of all the internal and external magnetic fields) acting on the free layer [64,95] leads to a displacement of the vortex core position from the geometric center of the pillar, so it needs to be considered (i.e. in-plane magnetic field along the yy direction) to properly simulate the experimental conditions. The effective field ($\mathrm{H_{eff}}$) can be estimated based on experimental data from MTJ devices with a diameter of 1.0 μm. Figure 4.12 shows the R-H loop of the STVO whose results are presented in Fig. 4.8. The data is used to calculate $\mathrm{H_{eff}}$ applied to the free layer, which is the in-plane field in the yy direction used in the simulations. The effective field leads to an offset of the vortex core from the center of the nanopillar in the remanent state. Moreover, when the core is at the center of the pillar, the resistance of the MTJ is given by $\mathrm{R_C} = (\mathrm{R_{AP}} - \mathrm{R_P})/2$, where $\mathrm{R_P}$

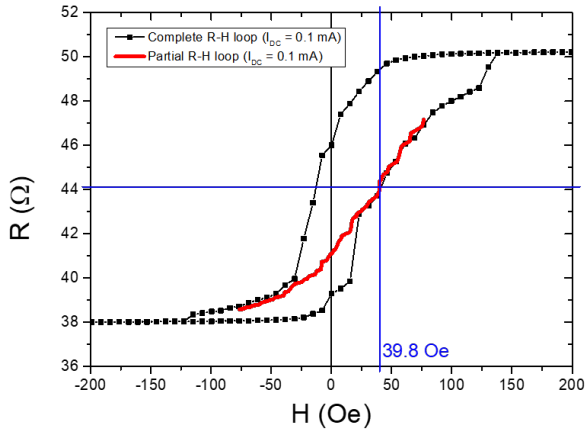


Figure 4.12: Complete and partial R-H loops obtained for a bias DC current of 0.1 mA. These results are obtained from the MTJ device whose spin diode measurements are presented in Fig. 4.8.

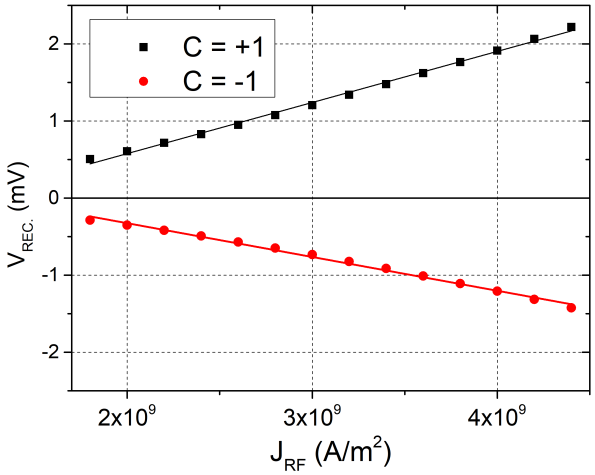


Figure 4.13: (a) Simulated rectified voltage calculated as a function of the input RF current density for the two different vortex chiralities at a fixed frequency of 81 MHz. An in-plane magnetic field of 39.8 Oe is applied in the yy direction.

($\mathrm{R_{AP}}$) is the MTJ resistance in the parallel (antiparallel) configuration. The complete R-H loop allows to calculate the averaged values of $\mathrm{R_P} = 38.0\,\Omega$ and $\mathrm{R_{AP}} = 50.2\,\Omega$, whereas the partial R-H loop is used to calculate the field at which the core is located at the center of the pillar. Before measuring the partial R-H loop, the vortex is initialized according to the initialization illustrated in Fig. 4.5. Then, the partial loop is measured in a field range not enough to annihilate the vortex where there is an absence of coercivity. Finally, based on the partial loop, the effective field $\mathrm{H_{eff}} = 39.8 \pm 0.3\,(\mathrm{Oe})$ corresponds to the setpoint at which $\mathrm{R_{MTJ}}$ = $\mathrm{R_C}$ = 44.1 Ω, being $\mathrm{R_{MTJ}}$ the resistance of the MTJ device.

Figure 4.13 shows the amplitude of the simulated spin diode results, calculated as a function of the RF current density for both chiralities. The results are calculated at a fixed frequency of 81 MHz.

The effective field is considered by applying an in-plane field of 39.8 Oe in the yy direction. The simulated nanodisk does not give a complete description of the real MTJ nanopillar, so that the frequency discrepancy between experimental and simulated data is expected. The rectified voltage ($\mathrm{V_{REC}}$) is estimated based on experimental data, so that

$$V_{REC} = \frac{R_{AP} - R_P}{2} \cdot S \cdot \frac{1}{T} \int_0^T \Delta M_Y(t) \cdot J_{RF}(t)\, dt \tag{4.6}$$

where $\mathrm{R_P}$ ($\mathrm{R_{AP}}$) is the resistance of the MTJ in the parallel (antiparallel) configuration, S the area of vortex (S = $\pi \mathrm{d}^2/4$, being $\mathrm{d} = 1.0\,\mu\mathrm{m}$ the diameter of the nanodisk) and $\Delta \mathrm{M_Y}$ the variation in time of the normalized magnetization in the yy direction. To estimate $\mathrm{V_{REC}}$, values of $\mathrm{R_P}$ and $\mathrm{R_{AP}}$ are measured with a bias DC current of 0.1 mA from the results shown in Fig. 4.12. For each frequency value, the simulations are performed for a time period T = 300 ns. Similar to the experimental results, the voltage presents different signs, as a result of the two different lineshapes given by different chiralities (see OFT + STT curve from Figs. 4.14a-b). In order to study the role of the OFT in the gyrotropic motion, Figs. 4.14a-b also show the simulated spin diode detection only when one excitation mechanism is considered at a time: a pure STT-driven oscillation (red data) and a pure OFT-driven oscillation (blue data). For an STT-driven oscillation, the spin diode response is the same for both chiralities. Moreover, the spin diode spectrum is easily fitted by a peak function combining both Lorentzian and anti-Lorentzian components (see inset of Fig. 4.14a), given by [137]

$$V_{REC}(f) = \frac{A(f_R^2 - f^2) + Bf^2}{(f_R^2 - f^2)^2 + (\Delta f)^2 f^2}, \tag{4.7}$$

where A is the amplitude of the anti-Lorentzian component, B the amplitude of the Lorentzian component, $\mathrm{f_R}$ the resonance frequency and $\Delta \mathrm{f}$ the linewidth of the spin diode spectrum. On the other hand, the OFT-driven output shows two symmetric lineshapes that depend on the vortex chirality and cannot be fitted with Eq. (4.7). As described in Eq. (4.6), $\mathrm{V_{REC}}$ is calculated according to the time-averaged phase difference between $\Delta \mathrm{M_Y}$ and $\mathrm{J_{RF}}$, meaning that a chirality switching results in a 180° phase shift of the OFT-driven $\Delta \mathrm{M_Y}$ oscillation. This behaviour has also been reported for the OFT-driven excitation of high-order spin wave modes (i.e. GHz range) in vortex-based MTJs [132]. In the end, while the amplitude of the gyrotropic oscillation (i.e. $\Delta \mathrm{M_Y}$) dictates the intensity of the spin diode response, the phase difference between $\Delta \mathrm{M_Y}$ and $\mathrm{J_{RF}}$ defines its lineshape. That same phase difference is presented in Figs. 4.14c-e, as a function of the $\mathrm{J_{RF}}$ frequency for different oscillation-driven mechanisms. For each frequency, the time-averaged phase difference Ψ is calculated as

$$\Psi = \frac{1}{T} \int_0^T [\varphi_{\Delta M_Y}(t) - \varphi_{J_{RF}}(t)]\, dt \tag{4.8}$$

being $\varphi_{\Delta \mathrm{M_Y}}$ the phase of the $\Delta \mathrm{M_Y}$ oscillation and $\varphi_{\mathrm{J_{RF}}}$ the phase of $\mathrm{J_{RF}}$. The calculation is performed for a time period when the gyrotropic oscillation stabilizes its amplitude, between 200 ns and 300 ns [i.e. T = 100 ns, as defined in Eq. (4.8)]. Again, Fig. 4.14c confirms the 180° shift of the OFT-driven oscillation, with a 180° offset in the Ψ axis between the phases calculated for opposite chiralities. On the other hand, the results for the STT-driven oscillation overlap perfectly, since the same is not sensible to the vortex chirality. To understand the major role of the Oersted field in defining distinct spin diode lineshapes for opposite chiralities, the focus goes to one specific frequency value. Figures 4.14f-g show time traces of the simulated gyrotropic motion, again for different oscillation-driven

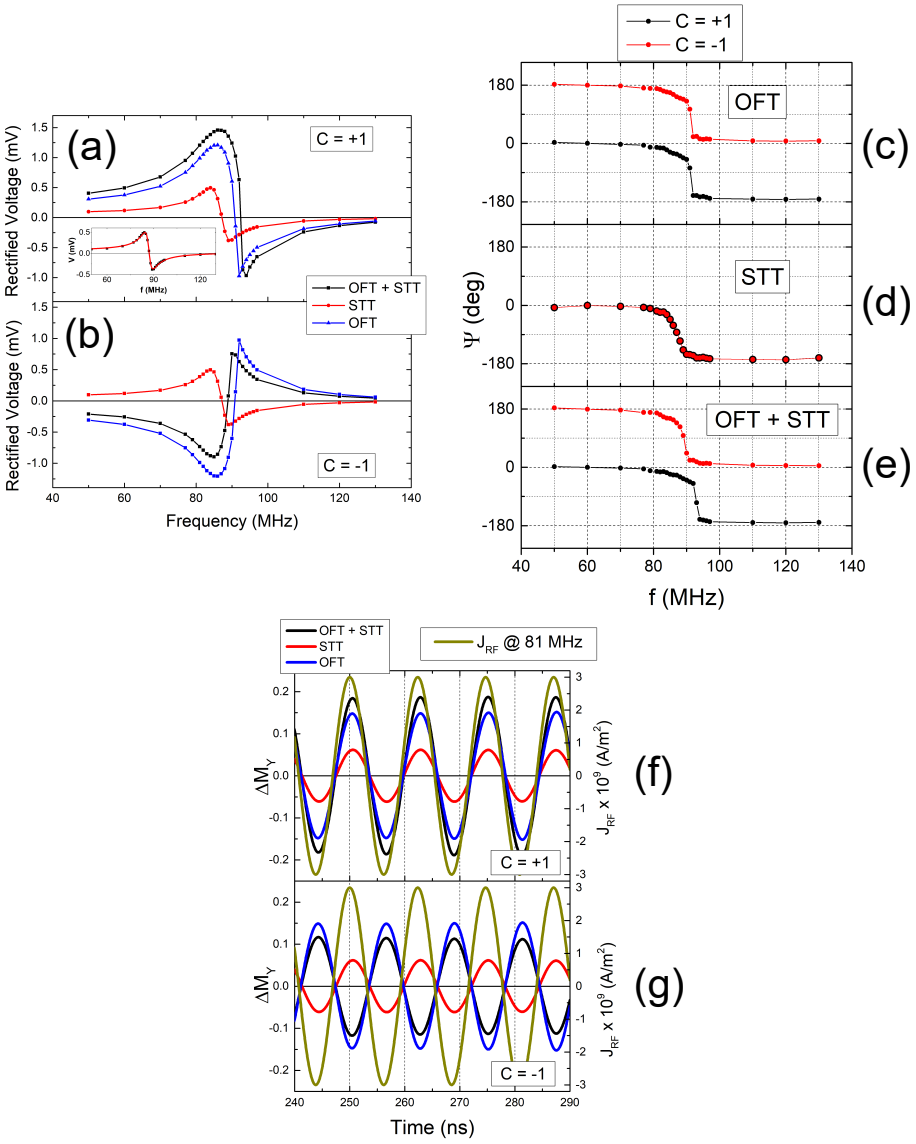


Figure 4.14: The simulated spin diode spectra for (a) positive and (b) negative chiralities are presented for different excitation mechanisms: spin-transfer torque (STT), Oersted field torque (OFT) and for both mechanisms (OFT + STT). The results were obtained for an RF current density of $3.0 \times 10^9\,\mathrm{A/m^2}$. The inset in (a) shows the STT-driven resonance fitted with Eq. (4.7). (c)–(e) Time-averaged phase difference between $\Delta \mathrm{M_Y}$ and $\mathrm{J_{RF}}$, as defined in Eq. (4.8), presented as a function of the $\mathrm{J_{RF}}$ frequency for different oscillation-driven mechanisms and chiralities. (f)–(g) Simulated $\Delta \mathrm{M_Y}$ time traces obtained for both chiralities. Similar to (a) and (b), different excitation mechanisms are considered. The results were obtained for an RF current density of $3.0 \times 10^9\,\mathrm{A/m^2}$ at a frequency of 81 MHz whose time traces are also presented.

mechanisms. The frequency of J_{RF} is 81 MHz and the results are presented for the two chiralities. For C = +1, the OFT ($\Psi = -12°$ in Fig. 4.14c) and STT ($\Psi = -18°$ in Fig. 4.14d) oscillations are almost in-phase, so that their combination results in a larger gyrotropic orbit with $\Psi = -13°$ (Fig. 4.14e) and a positive voltage of 1.2 mV (Fig. 4.14a). For C = -1, the STT oscillation is unchanged, but due to the 180° shift of the OFT-driven oscillation ($\Psi = 168°$ in Fig. 4.14c), now they are almost out-of-phase, which damps the oscillation to a smaller orbit with $\Psi = 167°$ (Fig. 4.14e), leading to a negative voltage of -0.7 mV (Fig. 4.14b). It is clear from Fig. 4.14g that the combined oscillation is driven by the OFT oscillation, meaning that it is the STT that damps the combined oscillation and the OFT that dominates the resonance phenomenon. The last statement will be clarified in section 4.6.3, where a complete description of the OFT dependence with the vortex core displacement is presented.

4.6.3 Evolution of the non-volatile effect with the core displacement

It should be emphasized the importance of having a displacement of the vortex core at the remanent state. In fact, if the core is at the center, the spin diode output for C = +1 and C = -1 should be the same. The Oersted field creates magnetic field lines whose center is also the central point of the pillar. When the core is at the center, the vortex in-plane magnetization will be collinear with the Oersted field lines, so no oscillation of the vortex core is expected [74]. If there is no OFT-driven oscillation, STT would be the only mechanism responsible for the gyrotropic motion, so that the M_Y oscillation would be the same for both chiralities.

Figures 4.15a-f show the module of the rectified voltage (V_{REC}) obtained from simulations as a function of the in-plane field applied in the yy direction of the simulation plane. These results are similar to the analysis depicted in Figs. 4.14a-b, but for different vortex core displacements. Also, as depicted in Fig. 4.15g, V_{REC} is calculated as the peak-to-valley or valley-to-peak voltage. As expected, the OFT alone (Fig. 4.15a and Fig. 4.15d) does not promote a sustained oscillation at zero field, which is only overcome by the progressive offset of the vortex core from the center. For the same field, both chiralities show the same V_{REC}, which are calculated from two symmetric spin diode curves characterized by two distinct lineshapes. As an example, for $H_Y = 6.0\,Oe$, both chiralities show the same $V_{REC} = 0.6\,mV$, but taken from a spin diode curve with a peak-to-valley (light green region in Fig. 4.15a) or a valley-to-peak (light blue region in Fig. 4.15d) lineshape. These results were already discussed in Figs. 4.14c-d, where the OFT-driven oscillation for different chiralities shows a 180° shift. Moreover, the OFT results are symmetric in relation with the field at $H_Y = 0.0\,Oe$, indicating that the 180° shift also happens when the vortex core moves from the right to the left side of the nanodisk and vice-versa (movement in the xx direction, according to Fig. 4.15i). For the STT-driven oscillation (Fig. 4.15b and Fig. 4.15e), V_{REC} shows the same symmetry. Moreover, the spin diode response is only sensitive to the magnitude of the in-plane field, regardless the core position in relation with the center.

The results become quite interesting when both OFT and STT are considered (Fig. 4.15c and Fig. 4.15f). To simplify, this analysis will only consider the positive field domain. For C = +1, V_{REC} increases continuously, as a result of the phase relation between the OFT-driven ΔM_Y and J_{RF} (i.e. both OFT and STT oscillations show a peak-to-valley lineshape). For C = -1, one may define two main regions of the field domain. In the first region ($H < 15\,Oe$), there is a continuous decrease of V_{REC} before reaching a zero oscillation setpoint. Now that the OFT-driven ΔM_Y shows a valley-to-peak response, the increase of the OFT contribution with the field damps the oscillation to a smaller orbit, in this way decreasing V_{REC}. This behaviour leads to a field setpoint where a perfect balance between

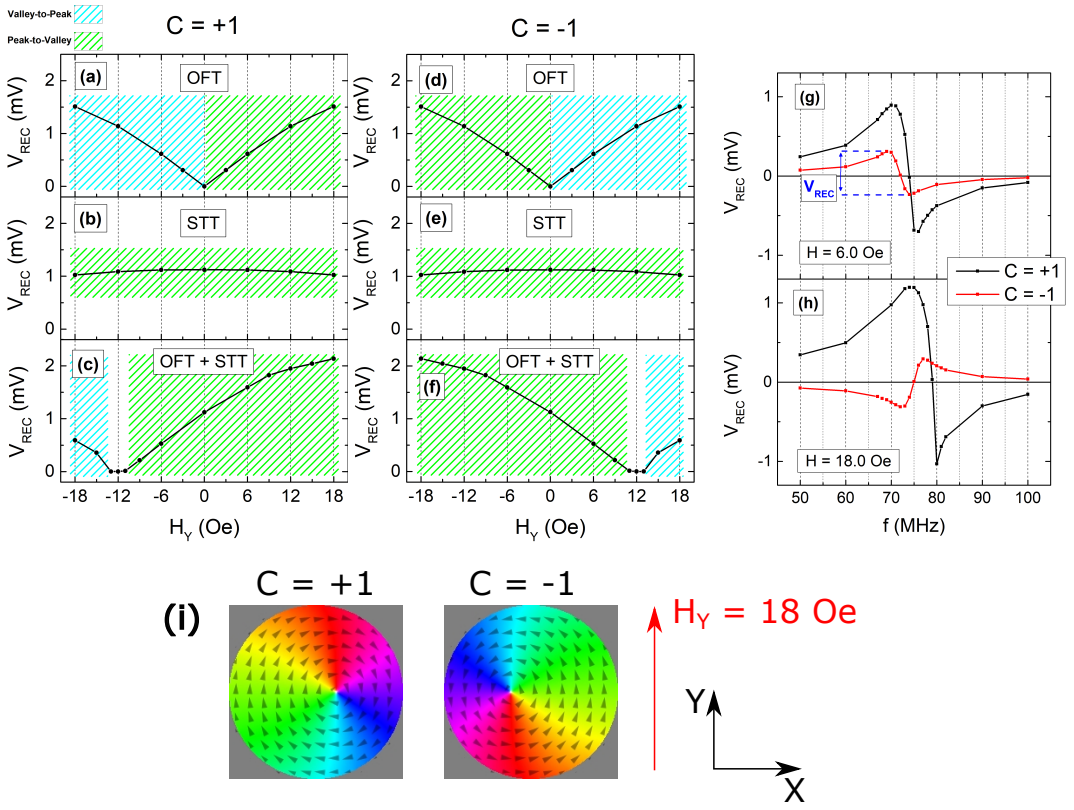


Figure 4.15: (a)-(f) Simulated rectified voltage calculated as a function of the in-plane magnetic field applied in the yy direction for the two different vortex chiralities. Again, the simulated spin diode measurements are presented for different excitation mechanisms: spin-transfer torque (STT), Oersted field torque (OFT) and both (OFT + STT). The results were obtained for an RF current density of $2.8 \times 10^9\,\mathrm{A/m^2}$. The simulated spin diode outputs are presented for a setpoint field of (g) 6.0 Oe and (h) 18.0 Oe. Both OFT and STT are considered. The calculation of $\mathrm{V_{REC}}$ is explained in (g) as the module of the peak-to-valley voltage. (i) Illustration of the simulated nanodisk, showing the vortex core offset for both chiralities when an in-plane field of 18 Oe is applied.

the OFT and STT contributions stops the gyrotropic oscillation. In the same region, before reaching the zero oscillation setpoint, the STT contribution is still dominant over the OFT, meaning that, as depicted in Fig. 4.15g, the spin diode curves for both chiralities still show the same peak-to-valley lineshape, only with different amplitudes. In the second region ($\mathrm{H} \geq 15\,\mathrm{Oe}$), the OFT becomes the dominant resonance mechanism, so that $\mathrm{V_{REC}}$ starts to increase and the lineshape of the spin diode curve for C = -1 is inverted (valley-to-peak lineshape in Fig. 4.15h). Considering the full field domain, it becomes clear that results with a realistic excitation in Fig. 4.15c and Fig. 4.15f are also symmetric in relation with the field at $\mathrm{H_Y} = 0.0\,\mathrm{Oe}$, translating the effect of both OFT and STT contributions.

These spin diode measurements were also performed experimentally as a function of the in-plane

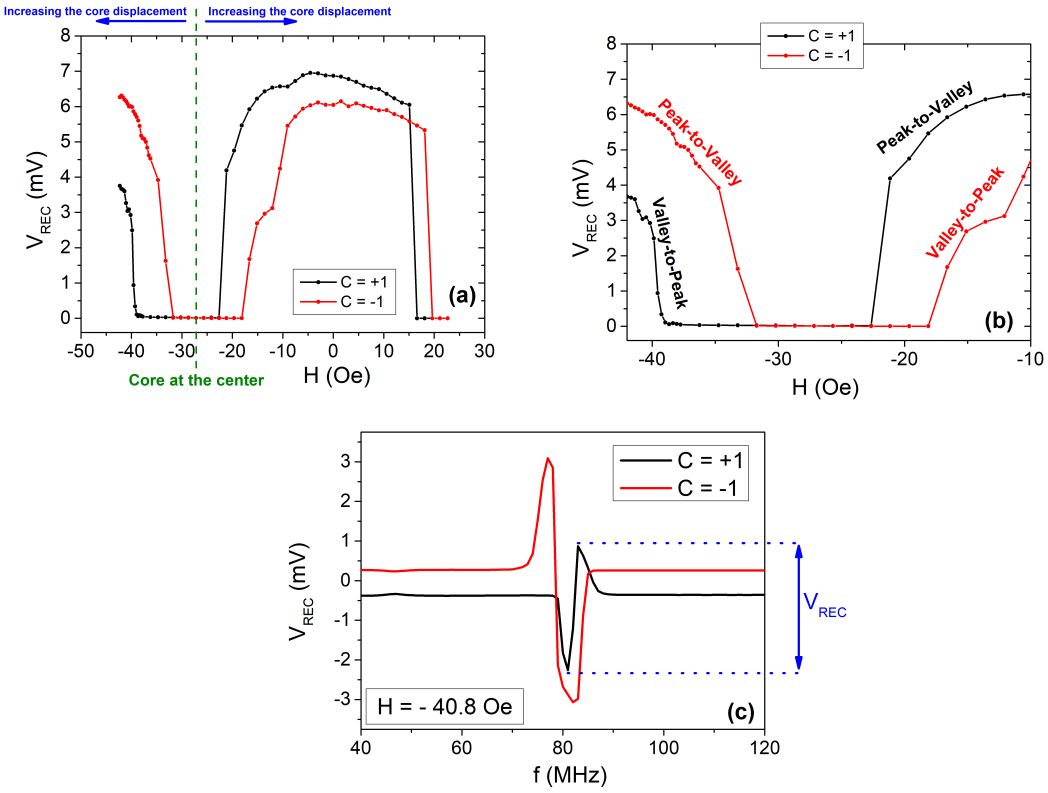


Figure 4.16: (a) Rectified voltage calculated as a function of the in-plane magnetic field applied according to the in-plane easy axis for the two different vortex chiralities. The results were obtained for an MTJ device with a diameter of 1.0 μm and an RF input power of 0.398 mW. (b) The results are zoomed in at the field range where the vortex core passes through the center of the nanopillar. (c) As an example, the spin diode outputs are presented for a setpoint field of -40.8 Oe and $\mathrm{V_{REC}}$ is calculated as the peak-to-valley or valley-to-peak voltage.

magnetic field. The results are presented in Fig. 4.16 for an MTJ device with a diameter of 1.0 μm and an input RF power of 0.398 mW, where $\mathrm{V_{REC}}$ is calculated as illustrated in Fig. 4.16c. The magnetic field is applied according to the in-plane easy axis and, in Fig. 4.16a, its range is chosen so that the vortex core travels from the center of the nanopillar (roughly at $\mathrm{H} \sim -27\,\mathrm{Oe}$) to expulsion (for $\mathrm{H} > 20\,\mathrm{Oe}$ the rectification drops to zero as a result of the core expulsion for both chiralities). The same results are presented in Fig. 4.16b, now zoomed in at the field range where the vortex core moves near the center of the nanopillar. In accordance with the simulations, both chiralities show a plateau in the field domain characterized by an absence of the gyrotropic oscillation and it is also the boundary that dictates the switching of the spin diode lineshape. Nevertheless, there are two main differences that should be explained. As in Fig. 4.15c and Fig. 4.15f, Fig. 4.16b shows a symmetric behaviour, but now with an offset in the field axis ($\mathrm{H} \sim -27\,\mathrm{Oe}$), which is a consequence of the effective field acting on the free layer that moves the vortex core from the center at the remanent state. Also, the plateaus are extended through a larger field range, so that they overlap from -31 Oe to -23 Oe. In our

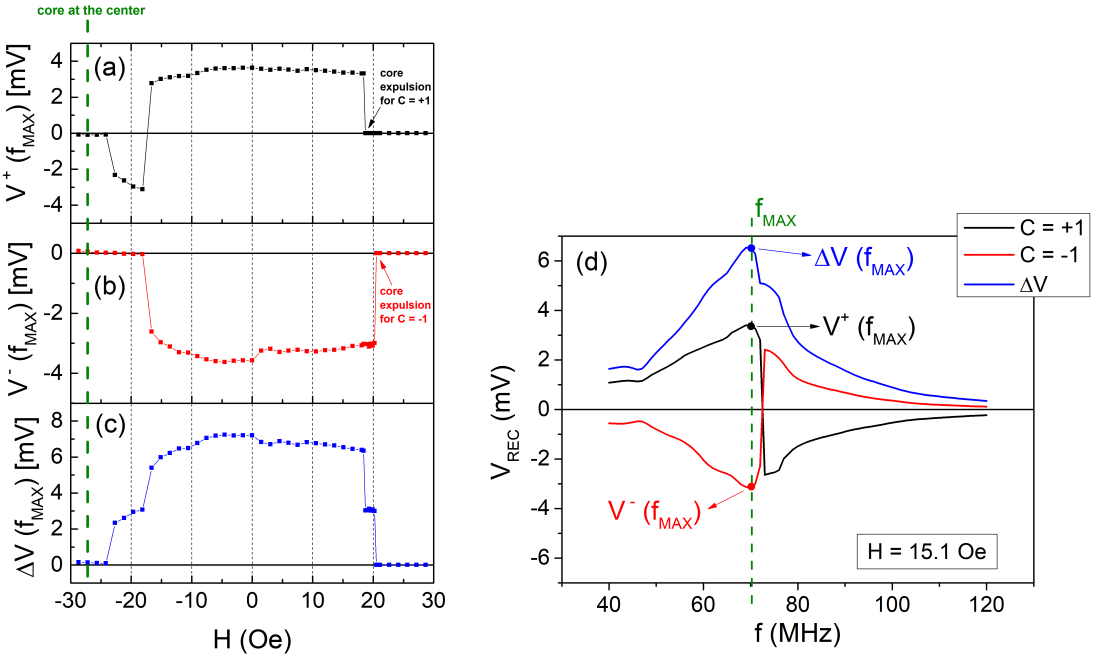


Figure 4.17: (a) The experimental $\Delta V(f_{MAX})$ is depicted in (c) as a function of the in-plane field. (a) and (b) show $V^{+}(f_{MAX})$ and $V^{-}(f_{MAX})$, respectively, used to calculate $\Delta V(f_{MAX})$. For each field setpoint, $\Delta V(f_{MAX})$ is calculated at the frequency f_{MAX} that maximizes the difference. (d) Example of the ΔV calculation for a field setpoint of 15.1 Oe.

understanding, the main contribution for this discrepancy comes from the polycrystalline structure of the free layer that is not considered in the simulations. This subject is the focus of chapter 5, where a distinction between local and collective dynamics is formulated. For a low RF power, the vortex core tends to be trapped by pinning sites where it oscillates locally at a larger frequency (roughly at the GHz range). Naturally, this creates a threshold RF power, above which the core escapes from the pinning site and starts to oscillate at its collective mode. So, the extension of the plateaus seen in Fig. 4.16b is a consequence of the threshold created by the pinning sites, i.e. a larger core displacement is needed, so that the OFT efficiency is enough to promote the transition from a local to a collective mode. Another difference between the simulations and the experiment is related with the OFT efficiency dependence with the RF current density injected through the MTJ. Considering that a constant input RF power of 0.398 mW is applied, the effective current density will vary according to the MTJ resistance that also varies with the in-plane field. This means that the RF current density is constantly changing as the in-plane field is swept, whereas in the simulations, the same is constant. In the future, this is possible to be solved by adapting the RF current density to be applied in the simulations based on the resistance that the MTJ to be compared presents at each field setpoint.

In section 4.6.1, it was demonstrated that the STVO synaptic weights tend to be maximized for a frequency of the input signal close to the resonance frequency of the device (see Fig. 4.9c). Nevertheless, there are other parameters that may influence the synaptic performance, namely the vortex core

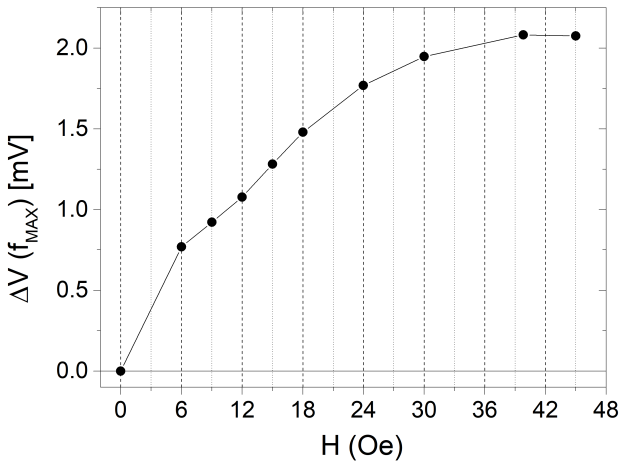


Figure 4.18: Simulated difference of the output voltage (ΔV) calculated for C = +1 and C = -1.

displacement that can be tuned by an in-plane magnetic field applied to the free layer. Specifically, it is interesting to study how the synaptic weights evolve with the core displacement, with particular focus on the difference between W^+ and W^-, since it is that difference the source of the non-volatile effect. The role of the core displacement is clarified in Figs. 4.17a-c, where the results were calculated from the experimental data shown in Fig. 4.16a. Those results show that the core is at the center of the pillar for an in-plane field of $\sim -27\,Oe$ so, to study the effect of the core displacement, the field range $H \geq -27\,Oe$ was chosen. For each value of the external magnetic field, the spin diode spectrum is measured for the two chiralities at a fixed RF input power, as shown in Fig. 4.17d for the particular case of a setpoint field of 15.1 Oe. The interest relies on the frequency f_{MAX} that maximizes the difference $\Delta V(f_{MAX}) = |V^+(f_{MAX}) - V^-(f_{MAX})|$, where $V^+(f_{MAX})$ (Fig. 4.17a) and $V^-(f_{MAX})$ (Fig. 4.17b) are the output voltages calculated at f_{MAX} for C = +1 and C = -1, respectively. Out of these results, $\Delta V(f_{MAX})$ is calculated for each value of the effective field acting on the free layer (Fig. 4.17c). As expected, for a small core displacement ($H < -23\,Oe$), the OFT and STT mechanisms cannot promote a sustainable gyrotropic oscillation, leading to no distinction between the spectra for different chiralities ($\Delta V = 0$). There is a sudden increase of ΔV in the $-23\,Oe < H < -17\,Oe$ field range, due to the appearance of the rectification for C = +1. For $H > -17\,Oe$, the appearance of the rectification for C = -1 leads to another jump and consecutive increase of ΔV with the core displacement, until reaching a plateau region as the core gets close to the edge. Then, due to the different rectification amplitudes, for each chirality, the core is expelled at different fields. For instance, as seen in Fig. 4.16a for $H > -17\,Oe$, the rectification for C = +1 is larger, meaning that the amplitude of the core gyration is larger, which makes it more susceptible to be expelled for a smaller field. That is effectively the case in Fig. 4.17a, where the vortex expulsion [i.e. $V^+(f_{MAX})$ drops to zero] occurs at H = 18.7 Oe, before the expulsion at H = 20.5 Oe for a negative chirality (Fig. 4.17b). After the vortex expulsion for both chiralities, naturally ΔV drops to zero, since the fundamental gyrotropic mode cannot be excited.

Considering that the synaptic weight is proportional to the measured output voltage, these results suggest that the difference between W^+ and W^- (i.e. non-volatile effect) can be optimized by increasing the core displacement until the plateau region ($-5\,Oe < H < 19\,Oe$ in Fig. 4.17a), where

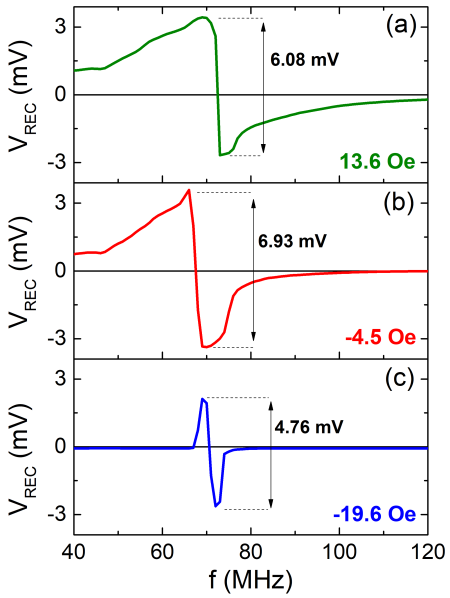


Figure 4.19: Spin diode spectra obtain for an in-plane field of (a) 13.6 Oe, (b) -4.5 Oe and (c) -19.6 Oe. These results were obtained at C = +1 and for the MTJ device whose results are also shown in Fig 4.16.

ΔV stabilizes. These results are confirmed by simulations showed in Fig. 4.18 and based on the simulated data used to plot Fig. 4.15c and Fig. 4.15f, now extended to the range $0\,\mathrm{Oe} \leq \mathrm{H} \leq 45\,\mathrm{Oe}$. Although not reaching the vortex expulsion, the simulations confirm the tendency to reach a plateau. The full understanding of this phenomenon is still an ongoing work. The stabilization of the non-volatile effect for large core displacements is a direct consequence of the stabilization of $\mathrm{V_{REC}}$ as calculated in Fig. 4.16c. Figure 4.16a clearly shows the tendency of $\mathrm{V_{REC}}$ to reach a plateau as the core displacement increases for a positive applied field. Figure 4.19 shows three of the spin diode spectra obtained experimentally for C = +1 in Fig. 4.16. The increase of the core displacement, by applying an in-plane field from -19.6 Oe in Fig. 4.19c to 13.6 Oe in Fig. 4.19a, is followed by a broader lineshape, which in turn mitigates the increase of $\mathrm{V_{REC}}$. Particularly in Fig. 4.19a, the rectification spread over the frequency domain is so pronounced that it leads to a smaller peak-to-valley voltage when compared with Fig. 4.19b, in this way explaining the smooth decrease in the plateau region seen in Fig. 4.16a. So, the non-volatile effect stabilizes because the rectification gets progressively more spread over the frequency domain.

4.7 Conclusion

It was shown that a spin torque vortex oscillator (STVO) working as a rectifier can be used as a binary non-volatile synapse, enabling learning in artificial neural networks making use of these devices. The synaptic weight can be persistently changed by switching the chirality of the vortex induced in the free

layer. Micromagnetic simulations showed that the Oersted field created by the RF current density is the main responsible for the symmetry breaking. In this way, the results indicate that the vortex core displacement at the remanent state is actually an advantage, since there is no contribution of the Oersted field for the gyrotropic resonance when the core is at the center of the nanopillar. It was also proposed to scale up the programming outputs by using two STVOs with different resonance frequencies, in this way opening new perspectives to a full integration of spintronic devices in neuromorphic hardware.

Chapter 5

Collective versus local oscillations linked to the granular nanostructure of a vortex nano-oscillator

Based on the characterization of spin torque vortex oscillators (STVOs) performed in this thesis, one major consequence has been to understand that the granular nanostructure of the free layer plays a fundamental role in defining the vortex magnetic behaviour. So, this chapter is a contribution to clarify this phenomenon. It is shown that the polycrystalline structure creates a map of local energy minima or pinning sites that can be identified simply by measuring the STVO resistance as a function of the in-plane magnetic field. These pinning sites clearly change the expected vortex dynamics. By measuring the spin diode response of an individual STVO, it is possible to define two coexistent gyrotropic modes: (i) a high frequency ($\sim 1\,\mathrm{GHz}$) and low amplitude ($\sim 1\,\mu\mathrm{V}$) local oscillation that appears when the vortex core is "trapped" in a pinning site and (ii) a low frequency ($\sim 100\,\mathrm{MHz}$) and high amplitude ($\sim 1\,\mathrm{mV}$) collective oscillation that is detected above a specific threshold, when the power of the excitation is large enough to overcome the energy potentials created by the pinning sites.

5.1 Effect of structural defects on the dynamics of a vortex-based nano-oscillator

Deposition techniques are ubiquitous in nanotechnology. The deposition of crystalline thin films is typically a source of structural defects that, not only disrupt the geometric regularity of the lattice at the microscopic level, but also has substantial implications in the material properties, such as chemical reactivity [147], electric performance [148] and magnetic dynamics (the focus of this chapter). In general, multiple types of defects coexist in the same material, such as point (e.g. impurities, vacancies), line (e.g. dislocations) and surface (e.g. grain boundaries, roughness) defects. If desirable, there are techniques allowing the deposition of single-crystal materials, namely MTJs by molecular-beam epitaxy [17], that minimize surface defects. Nevertheless, that is not generally the case for

large scale applications, where polycrystalline materials are generally obtained by more efficient deposition techniques, such as magnetron sputtering. In fact, the optimization of sputtered MgO-based MTJs [60, 149] has shown that the growth of a polycrystalline multilayer is not a roadblock for applications [150]. Nevertheless, structural defects should not always be neglected and, for particular conditions, the interaction between the domain structure and local fluctuations of the magnetic properties due to defects can significantly change the behaviour of polycrystalline magnetic materials. This is particularly relevant for materials with a sub-micron geometry showing a vortex state. Typically, a vortex state presents an eigenfrequency, associated with its fundamental collective mode, that is determined by its magnetic properties and geometrical aspect ratio [146]. Nevertheless, the dynamics can be much more complex, depending on the vortex core position in the magnetic medium and on the amplitude of the excitation mechanism. It has been shown in patterned NiFe nanodisks that structural defects create a net of pinning sites able to trap the vortex core in local potential wells, thus changing its dynamics [145, 151–153]. The main consequence of the core trapping is a sudden increase of the oscillation frequency and a decrease of its amplitude [145], as a result of the transition to a local gyrotropic mode. This phenomenon is also expected in spin torque vortex oscillators (STVOs), where the vortex dynamics is induced in a magnetic free layer with a polycrystalline structure. In fact, this spatial dependence of the vortex dynamics was briefly reported for MgO-based MTJs, where the DC bias-induced dynamics in the free NiFe layer (i.e. frequency of the output microwave signal) varies as a function of the in-plane magnetic field [29]. Moreover, in our interpretation, these local gyrotropic modes have also been proved to be relevant in STVOs working as artificial synapses [46]. Specifically, a multiply-and-accumulate operation (see section 4.1) was demonstrated in a chain of two similar STVOs in series, based on a significant difference between the resonance frequencies of each oscillator. In addition to that, the low magnitude of the rectified voltage ($\sim 1\,\mu\mathrm{V}$) indicates that the origin of the different spectra comes from different local gyrotropic modes excited for each individual STVO. So, these results ask for a systematic understanding of the local gyrotropic modes in STVOs, namely their mapping in the magnetic medium. This chapter goes towards that purpose, showing both static and dynamic studies of the local gyrotropic modes in individual STVOs.

5.2 Nanofabrication and experimental setup

The experimental measurements were performed in circular nanopillars with diameters ranging from 300 nm to 800 nm, patterned from a 5 Ta / 50 CuN / 5 Ta / 50 CuN / 5 Ta / 5 Ru / 6 IrMn / 2 $\mathrm{CoFe_{30}}$ / 0.7 Ru / 2.6 $\mathrm{CoFe_{40}B_{20}}$ / MgO ($8\,\Omega\mu\mathrm{m}^2$) / 2 $\mathrm{CoFe_{40}B_{20}}$ / 0.2 Ta / 7 NiFe / 10 Ta / 7 Ru MTJ stack (thickness in nanometers), whose fabrication process is in accordance with chapter 3. The magnetization dynamics is manipulated in the 2 $\mathrm{CoFe_{40}B_{20}}$ / 0.2 Ta / 7 NiFe free layer, presenting a remanent vortex state and the thickness of the MgO barrier determines a resistance-area (RA) product of $8\,\Omega\mu\mathrm{m}^2$. The role of the free layer stack was already explained in section 4.4.

The devices were fabricated according to the two-contact design (see section 3.1), so that a field line antenna with a width of 3 μm is vertically integrated with the nanopillar, approximately 600 nm on top of the free layer (Fig. 5.1). The field line antenna allows the application of a local in-plane magnetic field $\mathrm{H_{FL}}$ along the in-plane direction perpendicular to the reference direction (yy axis as the reference direction in Fig. 5.1) set by the SAF structure. For this purpose, the devices were re-annealed (see section 2.5) with a rotation of 90° in relation with the in-plane field of 1 T. In addition to the field line,

an electromagnet is set to apply an external in-plane field H_{EM} along the reference direction. So, by sweeping the (H_{FL} , H_{EM}) field coordinates, it is possible to have two-dimensional dislocations of the vortex core over the grain landscape of the free layer. For each (H_{FL} , H_{EM}) setpoints, the experimental setup shown in Fig. 5.1 allows to measure the resistance and the spin diode response of individual MTJ devices. For the latter, a bias tee allows to apply an RF signal with a sweeping frequency directly to the MTJ and measure its output rectified voltage simultaneously [36]. Here, a positive DC bias current corresponds to electrons travelling from the free to the reference layer.

5.3 Identification of pinning sites based on static measurements

The first clue of the existence of pinning sites in the free layer appears in the static measurements. The inset of Fig. 5.2a shows a typical transfer curve of the resistance of an STVO with a diameter of 500 nm, as a function of the in-plane field applied by the electromagnet (H_{EM}). Now, if the measurement is repeated in the field range where the vortex is nucleated (Fig. 5.2a), it is clear that the resistance variation with the field shows a step-like behaviour, meaning that the vortex core movement is characterized by a set of pinning-unpinning phenomena, as it moves through the magnetic medium. This phenomenon is common to all MTJ diameters. The resistance is measured with a small DC current of 0.1 mA to avoid any contribution of the DC current to the movement of the core. These results are in accordance with previous data from the literature, obtained for NiFe nanodisks [154]. Considering the periodicity of the resistance jumps, the pinning sites are associated with surface defects, in

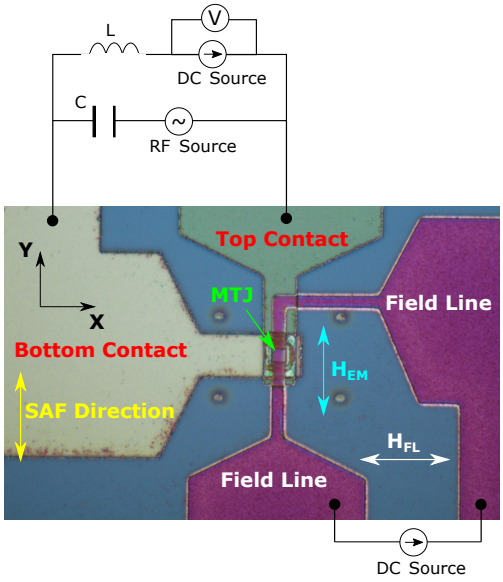


Figure 5.1: The top view of the two-contact design is used to illustrate the experimental setup, which allows to measure both static and dynamic characteristics of each individual nanopillar.

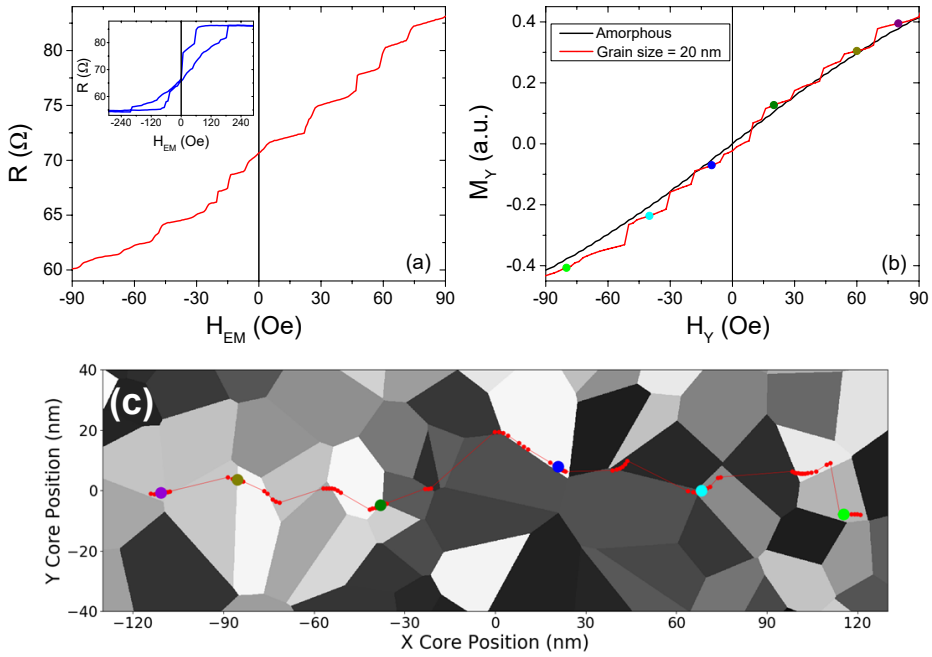


Figure 5.2: (a) Resistance of an STVO measured as a function of the in-plane field applied by the electromagnet ($\mathrm{H_{EM}}$). The results are presented in a field range where the vortex is nucleated and a small DC current of 0.1 mA is applied to the MTJ. The inset shows the complete transfer curve, where a DC current of -5.0 mA is applied to the nanopillar. (b) Simulated $\mathrm{M_Y}$ calculated as a function of the in-plane field in the yy direction, for a nanodisk with a diameter of 500 nm, showing two possible structures: amorphous and polycrystalline. (c) Simulated position of the vortex core calculated as a function of the in-plane field in the yy direction. Some colour dots make the connection between the core position in (c) and $\mathrm{M_Y}$ in (b).

particular with the polycrystalline or granular structure of the free layer.

To sustain the role of the grain structure on the static results, micromagnetic simulations were performed using the GPU-based software MuMax3 [142]. The simulations comprise a circular nanodisk with a diameter of 500 nm and a thickness of 9.0 nm, divided into $5 \times 5\ \mathrm{nm}^2$ unit cells in the xy plane and a cell size of 9 nm in the z direction. The nanodisk is simulated with a vortex magnetic state induced in a grain structure. The reference layer is set with an in-plane magnetization along the yy axis of the simulation plane. Based on experimental data taken from NiFe and standard values, the physical parameters were chosen as: saturation magnetization $\mathrm{M_S} = 740 \times 10^3\,\mathrm{A/m}$, uniaxial anisotropy constant $\mathrm{K_u} = 340\,\mathrm{J/m^3}$ along the yy axis and exchange stiffness $\mathrm{A} = 1.3 \times 10^{-11}\,\mathrm{J/m}$. The grains were defined using the standard MuMax3 function that creates a grain structure based on a Voronoi tesselation [155–157], with an average grain size of 20 nm, that is comparable with sizes of 30 nm [157] and 40 nm [29] found in the literature. Between grains, two magnetic properties were changed: the saturation magnetization (ranging from $0.9\mathrm{M_S}$ to $\mathrm{M_S}$ and randomly distributed) and the

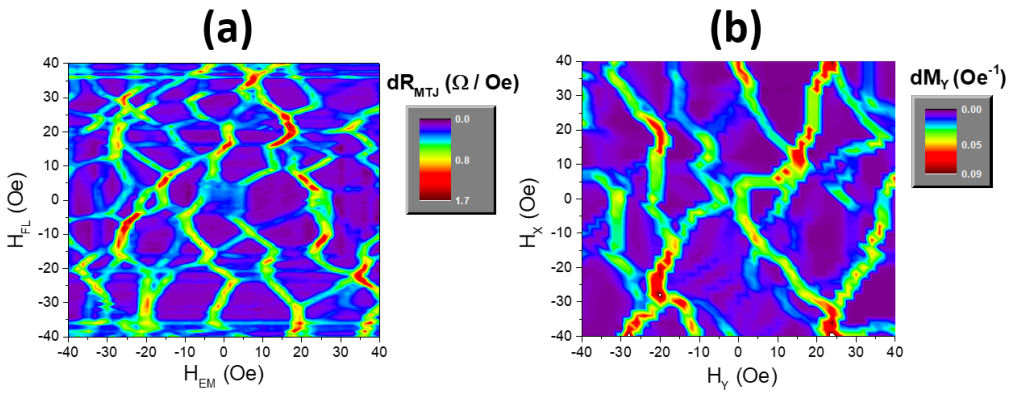


Figure 5.3: (a) $\mathrm{dR_{MTJ}}$ calculated from Eq. (5.1) and presented as a function of both electromagnet and field line in-plane fields. A small DC current of 0.1 mA is applied to the MTJ with a diameter of 500 nm. (b) An equivalent analysis is performed for the simulated nanodisk, also with a diameter of 500 nm.

exchange stiffness at the grain boundaries (exchange reduction of 10%). The variation of the saturation magnetization between grains is suitable to translate a thickness variation of the free layer [158] that is expected in the deposition process due to the roughness accumulation from the seed layer to the top of the MTJ [159]. Reducing the exchange stiffness allows to decrease the magnetic coupling between individual grains. Figure 5.2b shows the simulated magnetization in the yy direction ($\mathrm{M_Y}$) as a function of the in-plane field applied in the same direction ($\mathrm{H_Y}$) for both polycrystalline and amorphous nanodisks. The insertion of the grain structure leads to a step-like behaviour, where the jumps of $\mathrm{M_Y}$ correspond to significant changes of the core position (see Fig. 5.2c) as it switches between pinning sites. So, these calculations show a good qualitative agreement with the experimental results.

The possibility to apply an external field for both in-plane directions allows to perform a 2D mapping of the resistance for an MTJ device ($\mathrm{R_{MTJ}}$). To clarify its behaviour, the gradient of $\mathrm{R_{MTJ}}$ is calculated in the directions of $\mathrm{H_{EM}}$ and $\mathrm{H_{FL}}$. Then, for each ($\mathrm{H_{EM}}$, $\mathrm{H_{FL}}$) setpoints, the sum of the absolute value of each gradient component allows to calculate the absolute variation of $\mathrm{R_{MTJ}}$ as

$$dR_{MTJ}(H_{EM}, H_{FL}) = \left|\frac{\partial R_{MTJ}(H_{EM}, H_{FL})}{\partial H_{EM}}\right| + \left|\frac{\partial R_{MTJ}(H_{EM}, H_{FL})}{\partial H_{FL}}\right|, \tag{5.1}$$

where the first (second) right side term of Eq. (5.1) corresponds to the module of the component of the $\mathrm{R_{MTJ}}$ gradient in the direction of $\mathrm{H_{EM}}$ ($\mathrm{H_{FL}}$). Figure 5.3a shows $\mathrm{dR_{MTJ}}$ as a function of $\mathrm{H_{EM}}$ and $\mathrm{H_{FL}}$ for the same MTJ device as in Fig. 5.2a. Rather than showing the grain structure of the free layer, the results illustrate a map of the pinning sites or local energy minima (i.e. purple regions), where the core is "trapped" as it moves through the polycrystalline landscape. The boundaries (i.e. where the abrupt resistance variations take place) represent the transitions between different pinning sites. In Fig. 5.3a, some parasitic horizontal lines should not be considered in this analysis, since they arise from small movements of the measuring probes due to the external magnetic field. If Eq. (5.1) is applied to the simulated $\mathrm{M_Y}$, now as a function of $\mathrm{H_X}$ and $\mathrm{H_Y}$, it means that $\mathrm{dM_Y}$ will be sensible to the variation of $\mathrm{M_Y}$ as the core travels through the simulated grain structure, so qualitatively, as shown in Fig. 5.3b, it presents an equivalent result to the experimental measurement. A quantitative

comparison (e.g. areal density of pinning sites) between experimental and simulated results is risky, because it is difficult to say how close the grain parameters defined in the simulations (e.g. variation of $\mathrm{M_S}$, exchange reduction at the grain boundaries) are from the real polycrystalline landscape.

5.4 Vortex dynamics in a polycrystalline magnetic medium

5.4.1 Local dynamics

The grain landscape has important implications in the vortex dynamics. Figure 5.4a focus $\mathrm{dR_{MTJ}}$ into a specific field domain, where a well-defined pinning site (i.e. the transition from the center to the neighbour pinning sites is represented by a closed $\mathrm{dR_{MTJ}}$ boundary) appears in the central region for an MTJ device with a diameter of 600 nm. To evaluate how the pinning sites affect the dynamics of the core, spin diode measurements are performed at the same field setpoints, for an input RF power of 10 μW. The resonance frequencies are depicted in Fig. 5.4b, showing a good agreement between the $\mathrm{dR_{MTJ}}$ transitions and the different frequency modes. These results suggest that a change of the pinning site may lead to a massive variation of the resonance frequency (e.g., based on Fig. 5.4b, from 0.4 GHz to 2.4 GHz). In particular, the central region shows stable dynamics (i.e. green frequency island in Fig. 5.4b), which confirms the existence of a central pinning site defined by the $\mathrm{dR_{MTJ}}$ boundary. The wine colour regions correspond to field setpoints where the resonance frequency is not calculated. These regions typically correspond to field setpoints in which a transition between pinning sites occurs (i.e. $\mathrm{dR_{MTJ}}$ boundaries). In these conditions, the vortex core is energetically unstable, which is translated into complex dynamic properties, which makes it difficult to define a single local oscillation frequency. As an example, Fig. 5.4c shows the spin diode measurements performed by fixing $\mathrm{H_{FL}} = -10.4\,\mathrm{Oe}$ and sweeping $\mathrm{H_{EM}}$ as shown by the horizontal line in Fig. 5.4a. From the left to the right, the line passes through three distinct regions: pinning site on the left [starting at point 1 for $(\mathrm{H_{EM}}\,,\,\mathrm{H_{FL}}) = (-42.3\,,\,-10.4)\,\mathrm{Oe}$], transition between pinning sites (illustrated by the boundary) and pinning site on the right [finishing at point 2 for $(\mathrm{H_{EM}}\,,\,\mathrm{H_{FL}}) = (-33.2\,,\,-10.4)\,\mathrm{Oe}$]. Beyond the clear mode transition, from $\sim$0.75 GHz in point 1 to $\sim$1.6 GHz in point 2, in the boundary between pinning sites ($\mathrm{H_{EM}} = -37.8\,\mathrm{Oe}$ in Fig. 5.4c), the rectification shows the coexistence of both modes. So, due to its energy setpoints between two local minima and with the contribution of the thermal fluctuations, as a function of time, the vortex core is switching between the two pinning sites. Figure 5.4b also shows a transition of the local mode, from point 3 to point 4, that is not dictated by a clear $\mathrm{dR_{MTJ}}$ boundary in Fig. 5.4a. This example is used to emphasize the limitations of the static measurements to perfectly translate the energy landscape of the magnetic medium.

The frequency values are quite high when compared with the frequency of the collective gyrotropic mode, which should be below 0.25 GHz [141] for the MTJ device whose results are presented in Fig. 5.4. So, as already discussed in section 5.1, these results suggest that the high frequency modes are the consequence of a small amplitude (i.e. local) gyrotropic oscillation of the vortex core (corroborated by the μV range of the spectra shown in Fig. 5.4c) which, instead of being dictated by the geometry and magnetic properties of the free layer, is defined by each individual local energy minimum. To study this hypothesis, a simplified version of the grain landscape is simulated as a toy model in a circular nanodisk with a diameter of 120 nm, a thickness of 9.0 nm, divided into $2 \times 2\ \mathrm{nm}^2$ unit cells in the xy plane and a cell size of 9 nm in the z direction. The remaining properties of the nanodisk

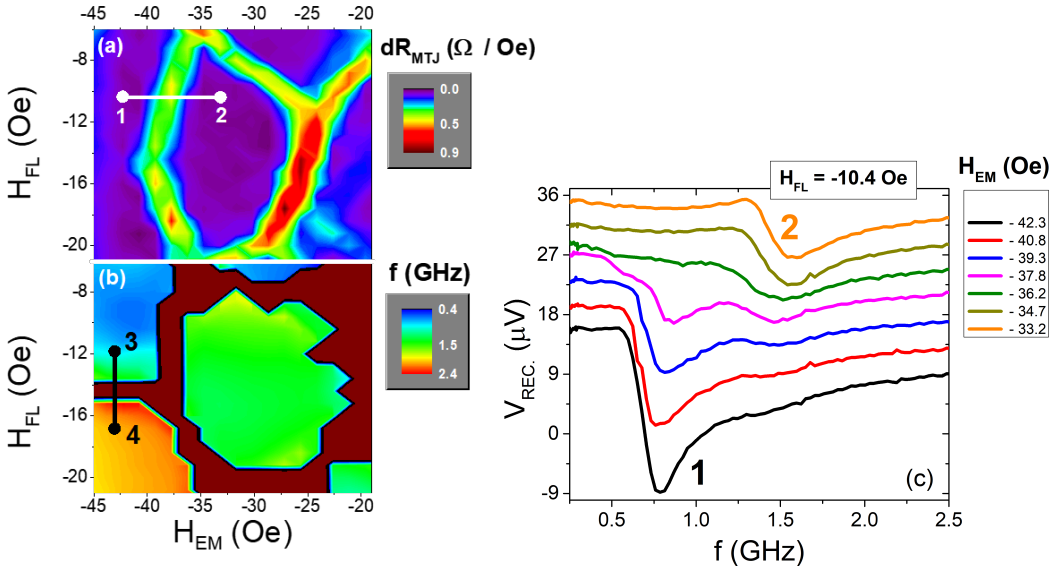


Figure 5.4: (a) $\mathrm{dR_{MTJ}}$ calculated as a function of $\mathrm{H_{EM}}$ and $\mathrm{H_{FL}}$, focused in a central pinning site. (b) For the same field setpoints, the resonance frequency of the local gyrotropic oscillation is calculated from spin diode measurements. (c) Spin diode spectra are presented for different values of $\mathrm{H_{EM}}$, in accordance with the field sweep illustrated in (a) by an horizontal white line. These results are obtained from an MTJ with a diameter of 600 nm, the resistance is measured with a DC current of 0.1 mA and the spin diode spectra are measured with an input RF power of 10 μW.

were defined as described in section 5.3. Here, the aim is to simulate a defect at the center, so that the nanodisk is divided into two concentric regions, where the central region shows a diameter of 20 nm (Fig. 5.5a). Then, the defect is defined by manipulating the two magnetic properties used to simulate the full grain structure in section 5.3: the saturation magnetization of the two regions and the exchange coupling between those two regions. Finally, an in-plane magnetic field $\mathrm{H_Y}$ is swept from -28 Oe to 28 Oe in the yy direction, promoting the movement of the vortex core in the xx direction, in this way passing through both regions (see light blue arrow in Fig. 5.5a). For each field setpoint, the vortex core relaxation allows to calculate the frequency of the gyrotropic oscillation, which is depicted in Fig. 5.5b for different conditions: with (red data) and without (black data) a defect in region 2. The variation (V) of the magnetic properties is performed, so that $\mathrm{M_{S2}} = (1 - \mathrm{V})\mathrm{M_{S1}}$, being $\mathrm{M_{S1}}$ ($\mathrm{M_{S2}}$) the saturation magnetization of region 1 (region 2) and the exchange stiffness at the circular boundary between regions is reduced to $(1 - \mathrm{V}) \times 100\%$. So, a variation of 8% means that $\mathrm{M_{S2}} = 0.92 \times \mathrm{M_{S1}}$ and the exchange stiffness at the boundary is reduced to 92%. The frequency is presented as a function of the core position in the xx direction that is taken after the relaxation of the vortex core for each field setpoint.

When there is no variation of the magnetic parameters ($\mathrm{V} = 0\%$), the oscillation shows the frequency of the collective mode, dictated by the geometry of the nanodisk. The defect definition leads

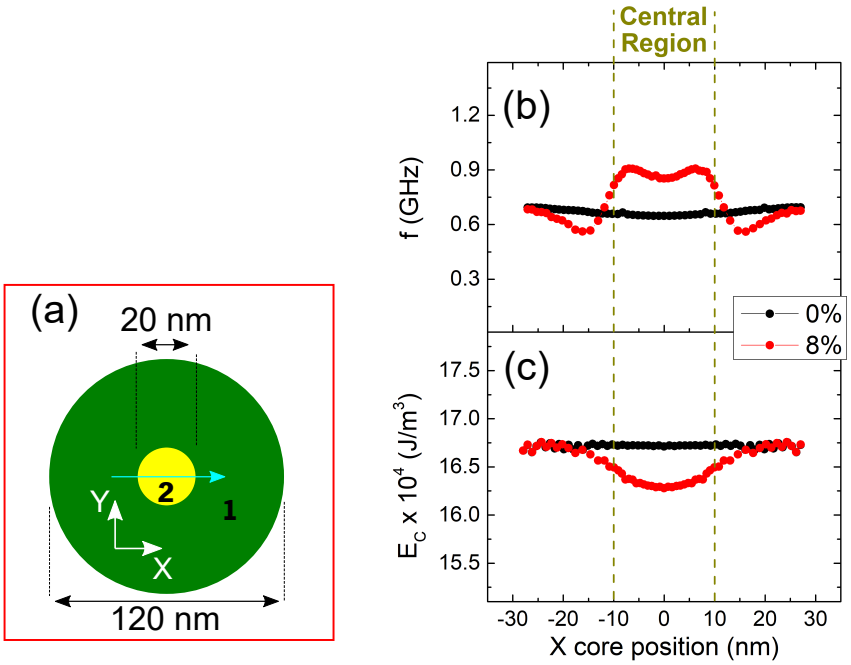


Figure 5.5: (a) Illustration of the nanodisk used in the toy model. Regions 1 and 2 are identified by different colours and the diameters are also indicated. (b) Total energy density of the vortex core and (c) frequency of the gyrotropic oscillation simulated in the toy model as a function of the vortex core position in the xx axis of the simulation plane [the light blue arrow in (a) illustrates the core displacement]. The results are presented for two different conditions: (i) no defect in the center (black) and (ii) 8% variation of both saturation magnetization and exchange coupling in the central region (red).

to a sharp increase of the frequency in the central region, as expected from the experiment. It should be also noted that, before the sharp frequency increase, the data in Fig. 5.5b is characterized by a decrease of the frequency as the core approaches the central region. At this point, this behaviour is not fully understood. A qualitative analysis suggests the link with the out-of-plane magnetic distribution of the vortex core [152]. Nevertheless, our simulations do not indicate any abnormal modification of the vortex core (e.g. core size) at the transition between regions, so it is still considered as an open question. Figure 5.5c also shows the total energy density of the vortex core ($\mathrm{E_C}$) as a function of the core position in the xx direction. Here, it is chosen to neglect the total energy of the nanodisk, since the pinning phenomenon is local, meaning that it is only dictated by the position-dependent energy of the core. So, one expects to measure the same results for a vortex core oscillating in a specific pinning site regardless of the position of the latter in the nanodisk. In fact, as the vortex core travels through the magnetic medium, it gets pinned, not to minimize the energy of the full nanodisk, but to minimize the energy of the core.

A similar approach to the one shown in Fig. 5.5 was already performed by Compton *et al.*, where

the results are successfully explained based on a simple analytical model [152]. They admit a significant variation of the restoring force felt by the vortex core inside a pinning site. For that purpose, the vortex stiffness κ is defined as spatially dependent on the vortex core position in the nanodisk landscape. So, according to Eq. (1.16) and in a small core displacement regime [83], the restoring force is given by

$$\vec{F}_W = -\kappa \vec{X} \tag{5.2}$$

or

$$\vec{F}_W = -(\kappa + \Delta\kappa)\vec{X} \tag{5.3}$$

depending if the core is oscillating inside or outside a spatially defined pinning site. As the core is trapped, there is an immediate increase by $\Delta\kappa$ of the vortex stiffness which, by solving the Thiele equation [152], leads to an increase of the oscillation frequency.

5.4.2 Transition to collective dynamics

The variation of the input RF power allows to measure experimentally the transition from a local to a collective gyrotropic mode. For fixed field setpoints, Fig. 5.6 shows the spin diode response as a function of the input RF power ($\mathrm{P_{RF}}$) for an MTJ device with a diameter of 500 nm. The data is divided into two frequency ranges, each one focusing in a distinct mode. For a low input RF power ($\mathrm{P_{RF}} < 56\,\mu\mathrm{W}$), the spin diode response is characterized by a high frequency mode around 1 GHz, associated with the local pinning site, that is maintained over the full power range, as a result of the non-hysteretic behaviour shown by these devices at the vortex nucleation region (see section 5.5). Above a specific power threshold ($\mathrm{P_{RF}} > 56\,\mu\mathrm{W}$), the energy transfer to the vortex core is enough to overcome the energy potential of the pinning site where the core is trapped, promoting its collective gyrotropic motion, in this case, at a frequency of 0.12 GHz.

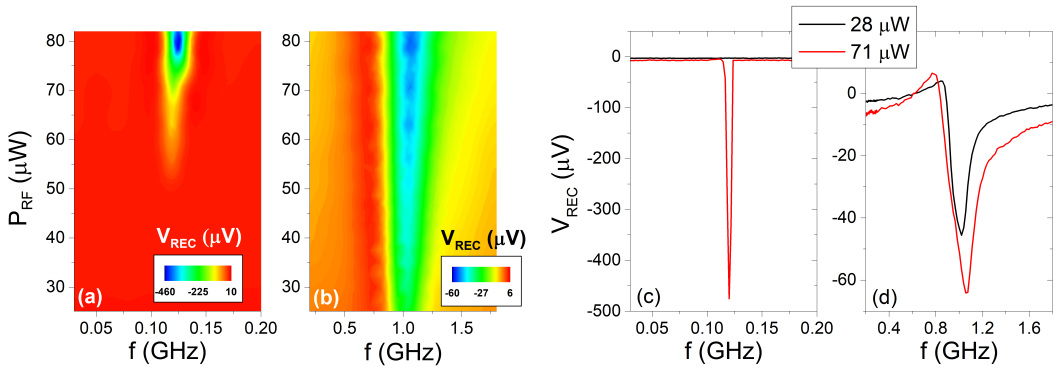


Figure 5.6: Spin diode spectra presented as a function of the input RF power. The MTJ device has a diameter of 500 nm and the field setpoints are $(\mathrm{H_{EM}}\,,\,\mathrm{H_{FL}}) = (5.3\,,\,-18.4)\,\mathrm{Oe}$. For clarity, the data is divided into two frequency domains: (a) collective and (b) local frequency range. The same distinction is made in (c) and (d), where two spin diode spectra are depicted as examples below and above the threshold for a collective oscillation.

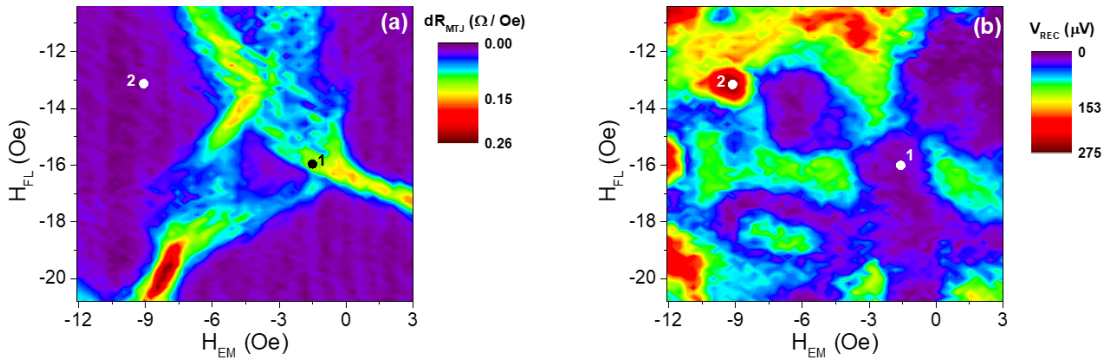


Figure 5.7: (a) $\mathrm{dR_{MTJ}}$ calculated as a function of $\mathrm{H_{EM}}$ and $\mathrm{H_{FL}}$ for a nanopillar with a diameter of 600 nm. The MTJ resistance is monitored by injecting a DC current of 0.1 mA. (d) The amplitude of the rectified voltage of the collective mode is presented for the field window defined in (a). A fixed input RF power of 12.6 $\mu\mathrm{W}$ is applied.

In Fig. 5.6, the focus goes to the oscillation transition, by defining a threshold power for the appearance of the collective mode. Now, in the same way that the local mode dynamics varies with the pinning site (Fig. 5.4), the threshold power for a collective oscillation may also depend on the core position in the magnetic medium. Figure 5.7a shows $\mathrm{dR_{MTJ}}$ as a function of $\mathrm{H_{EM}}$ and $\mathrm{H_{FL}}$ for an MTJ device with a diameter of 600 nm, whereas in Fig. 5.7b, the amplitude of the rectification is measured for a fixed input RF power of 12.6 $\mu\mathrm{W}$ at the same field range. The variation of the threshold over the magnetic medium is complex and does not show a general relation with the $\mathrm{dR_{MTJ}}$ boundaries, where the vortex core is energetically unstable. For instance, as illustrated by points 1 and 2 in Figs. 5.7a and 5.7b, the analysis of the pinning sites based on the measurement of the MTJ resistance does not explain why in point 2 (inside a pinning site) the threshold power for collective oscillation is smaller than in point 1 (in a $\mathrm{dR_{MTJ}}$ boundary). So, these results suggest that the static measurements are insufficient to translate the complexity of the energy landscape.

5.5 Hysteretic behaviour of the vortex displacement

Although not being its main purpose, a second MTJ stack was also deposited and patterned into single MTJ devices. This allows a straightforward comparison between this new stack (stack A) and the standard MTJ (stack B, as described in section 5.2). The composition of the two multilayer structures is described in Table 5.1. Figure 5.8 shows R-H loops obtained for a single device of each stack. Both MTJs have the same nominal diameter of 500 nm and present the same two-contact geometry (see section 3.1). Beyond the complete loop, the illustration also shows partial loops that are obtained in a field range where the vortex is always nucleated. Before the partial loop is measured, an initialization process is performed to nucleate the vortex (see section 4.5). The partial loop clearly demonstrates a major difference between the two devices. Stack A shows a pronounced hysteretic behaviour in the vortex nucleation region, meaning that the path of the vortex core as a function of $\mathrm{H_{EM}}$ depends on its past positions, i.e. a memory effect. Similar results are obtained for all the MTJ devices measured

	Oxide above the substrate	Bottom contact	MTJ	Top contact
Stack A	300 SiN_X	5 Ru / 50 CuN_X / 5 Ru / 50 CuN_X / 5 Ru	6 IrMn / 2.0 $CoFe_{30}$ / 0.7 Ru / 2.6 $CoFe_{40}B_{20}$ / MgO [22.7 $\Omega.\mu m^2$] / 2.0 $CoFe_{40}B_{20}$ / 0.2 Ta / 7 $Ni_{81}Fe_{19}$	30 CuN_X / 7 Ru
Stack B	200 SiO_2	5 Ta / 50 CuN_X / 5 Ta / 50 CuN_X / 5 Ta / 5 Ru	6 IrMn / 2.0 $CoFe_{30}$ / 0.7 Ru / 2.6 $CoFe_{40}B_{20}$ / MgO [8 $\Omega.\mu m^2$] / 2.0 $CoFe_{40}B_{20}$ / 0.2 Ta / 7 $Ni_{81}Fe_{19}$	10 Ta / 7 Ru

Table 5.1: Material composition of stack A and stack B, as described in the main text (thickness in nanometers).

in the same wafer, with a diameter ranging from 300 nm to 500 nm.

The hysteretic behaviour of stack A becomes clear in Fig. 5.9a, where, for the same MTJ device, the resistance is measured in zigzag field sweeps up to 56 Oe. The inset of Fig. 5.9a shows an example of an intermediate zigzag sweep. Starting at zero, the field is swept up to 40 Oe, then decreases to -40 Oe and, finally, it goes back to zero where the next sweep cycle starts (the field step is 4 Oe, meaning that the next cycle will go up to 44 Oe). For each zigzag cycle, the resistance

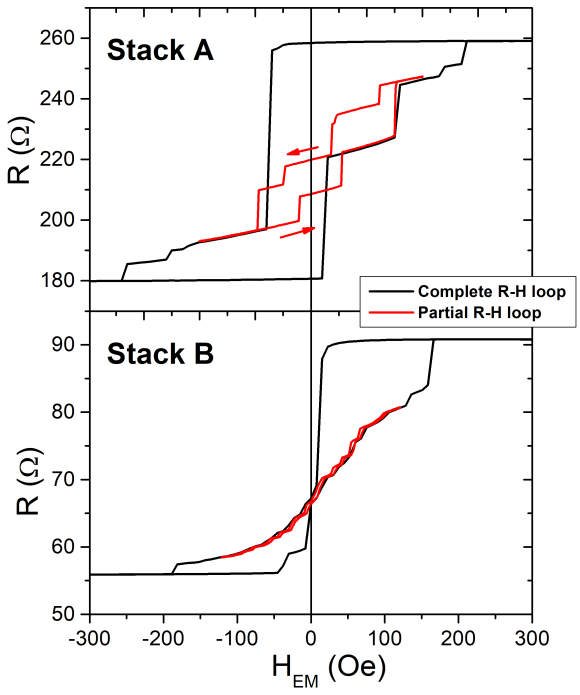


Figure 5.8: MTJ resistance measured as a function of the external field for an MTJ device with the stack A (top) and stack B (bottom). Both measurements are obtained from devices with a nominal diameter of 500 nm and by applying a DC current of 1.0 mA.

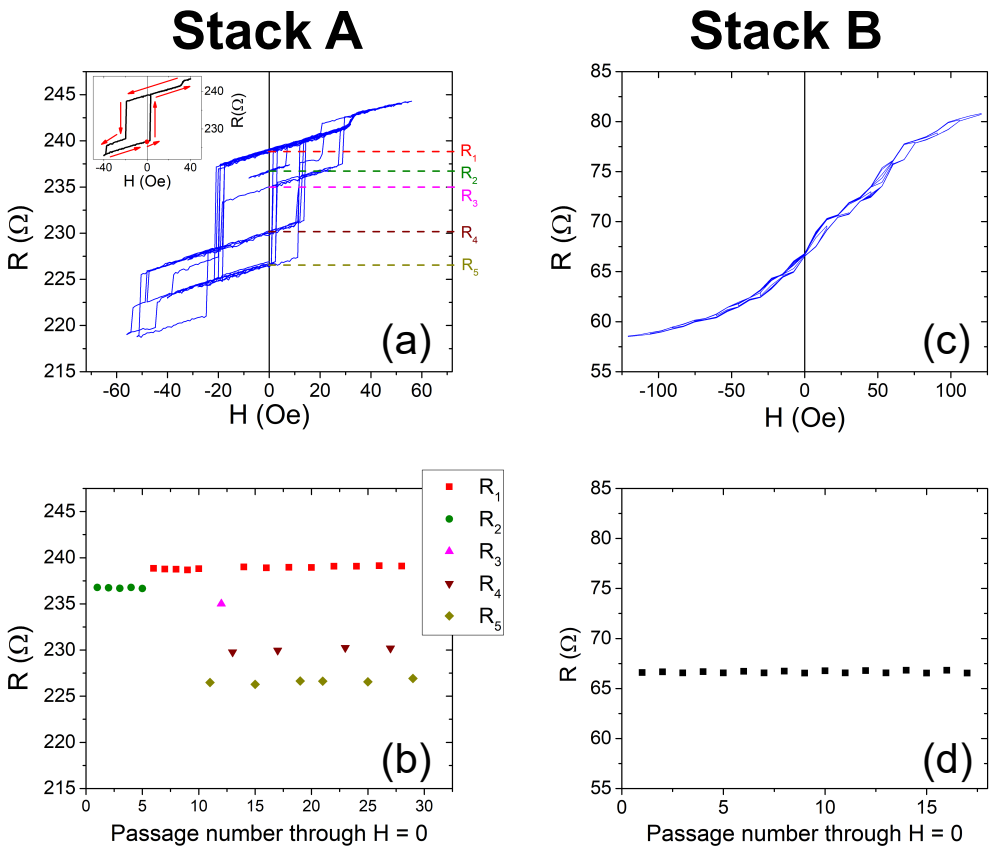


Figure 5.9: (a) Resistance as a function of the external field, measured in the vortex nucleation region for an MTJ device with the stack A. The field sweep is performed in a zigzag fashion, as exemplified in the inset. (b) Resistance of the same MTJ device measured at remanence as a function of the number of passes through zero field. In (c) and (d) the analysis is similar to the one performed in (a) and (b), but now for an MTJ device with the stack B. Here, the MTJ devices are the same as the ones used in Fig. 5.8 and the resistance is measured by applying a DC current of 1.0 mA.

is measured twice at zero field, so Fig. 5.9b shows the MTJ resistance measured at zero field as a function of the passage number through the same field setpoint. It is possible to label five distinct resistances, in this way making evident, not only the memory behaviour, but also that these conditions lead to five different positions of the vortex core at the remanent sate. Similar results (i.e. distinct resistance values at remanence) are also obtained by sweeping the field in the in-plane hard axis, which makes it a 2D phenomenon. Figs. 5.9c-d show the same analysis performed for the MTJ device with stack B, where the effect is negligible.

From a material point of view, stack A and stack B show many differences. Between contacts, Table 5.1 shows that both stacks have a similar MTJ multilayer. The only difference relies on the MgO thickness (RA = 22.7 $\Omega\mu\mathrm{m}^2$ for stack A and RA $\sim$ 8 $\Omega\mu\mathrm{m}^2$ for stack B). Nevertheless, this difference

is discarded as a possible reason for the hysteretic behaviour, because MTJ devices with stack B and an RA = 21.7 $\Omega\mu\mathrm{m}^2$ show similar results as their lower RA counterparts. For the future, there are three main differences between the stacks that are worth to be analysed individually: (i) the oxide below the bottom contact ($\mathrm{SiN_x}$ for stack A and $\mathrm{SiO_2}$ for stack B), (ii) Ru versus Ta as interlayers in the bottom contact (Ru for stack A and, in majority, Ta for stack B) and (iii) the capping layer ($\mathrm{CuN_x}$ for stack A and Ta for stack B). At INL, it was already understood that these changes also have implications in the MTJ electric properties. CIPT measurements show that unpatterned MTJs with stack A (only with a different RA product of 15 $\Omega\mu\mathrm{m}^2$) are characterized by a TMR $\sim 110\,\%$, which is a decrease of more than 30 % of the typical values obtained for unpatterned MTJs with stack B and similar RAs (i.e. TMR $\sim 170\,\%$). As it happens for the hysteretic behaviour presented in this section, at the moment, it is not clear which stack modification contributes the most for the different results. On the other hand, it can be sustained that stack A contributes for the deposition of a free layer where the surface defects are more significant. Chen *et al.* have shown that the pinning of the vortex core is correlated with the roughness of the magnetic layer [153]. So, the changes performed in stack A possibly lead to a larger roughness of the free layer, thus creating a more pronounced vortex pinning.

5.6 Conclusion

By spin diode measurements, it was shown that the polycrystalline structure of the free layer can have a major effect on the static and dynamic behaviour of an STVO. In our devices, the main consequence is that the gyrotropic dynamics depend on the power of the excitation, since below a certain variable threshold (roughly, 10 μW), the collective mode disappears and only a local mode remains, characterized by a vortex oscillation at a smaller amplitude ($\sim 1\,\mu\mathrm{V}$) and larger frequency ($\sim 1\,\mathrm{GHz}$). This phenomenon is partially explained by surface defects caused by the polycrystalline structure that create a landscape of pinning sites to which the vortex core is trapped, since they minimize its energy. Above the threshold power, the energy transmitted to the core allows it to escape from the pinning site, thus oscillating at the expected collective mode, characterized by a vortex oscillation at a larger amplitude ($\sim 1\,\mathrm{mV}$) and smaller frequency ($\sim 100\,\mathrm{MHz}$). It should be noted that only a partial understanding of this subject was achieved, since there is not a general connection between a larger threshold power and the vortex core lying inside a pinning site. This conclusion suggests that our analysis, namely the mapping of the pinning sites by static measurements, shows limitations for a full understanding of the phenomenon.

Chapter 6

Magnetic dipolar synchronization of spin torque vortex oscillators with independent top contacts

In this chapter, a successful synchronization is achieved via dipolar coupling for two spin torque vortex oscillators (STVOs) 100 nm apart. The synchronization state is verified, not only by an analysis of the power spectra, but also measuring the phase of each individual STVO. These results are obtained from a new design that introduces two fundamental features: (i) the nanopillars are defined with an edge-to-edge distance down to 100 nm and (ii) each individual device is fabricated with an independent top contact (ITC), so that it is possible to control individually the DC current applied to each device (giving more flexibility to the synchronization process) and have access to the phase evolution of each individual oscillator.

6.1 Spin torque nano-oscillator

The most widely used spin torque nano-oscillator (STNO) stack is based on a FM / spacer / FM trilayer (Fig. 6.1a), which is generally integrated in two main nanostructures: the spin valve and the MTJ. The reference FM layer acts as the polarizer to promote an STT-driven steady-state magnetization precession in the free layer. The magnetic oscillation delivers an RF output signal (Fig. 6.1b), as the result of the periodic variation of the STNO resistance through the GMR (TMR) effect if a spin valve (MTJ) is considered. The frequency of an STNO is highly tunable by an external magnetic field [160] and, due to its non-linearity, by the intensity of the DC current promoting its dynamics [161]. Moreover, when compared with a standard LC-tank voltage-controlled oscillator (VCO) [162], STNOs can be fabricated in very small sizes. For instance, a functional VCO presents an area of $\sim 10^{-3}\,\mathrm{cm}^2$ [163]. The area of an STNO fabricated at INL may go down to $\sim 10^{-9}\,\mathrm{cm}^2$, so the potential for miniaturization after electronics integration is promising. Over the years, different strategies have been implemented to bring the STNO performance to a level suitable for applications, which mainly comprises the optimization of its output power and spectral purity.

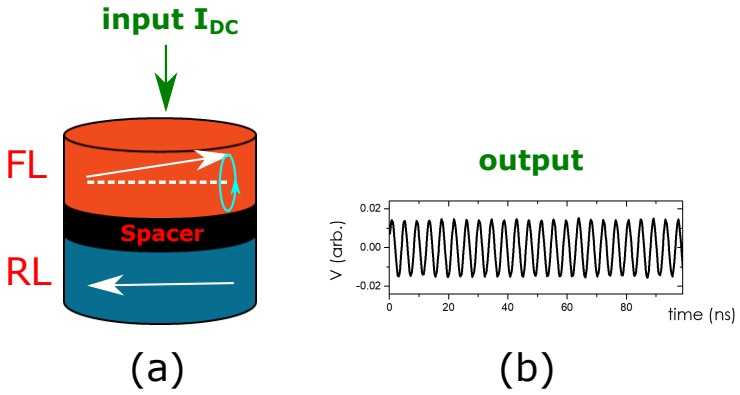


Figure 6.1: (a) Illustration of a simple STNO stack, where the reference layer (RL) acts as the polarizer. A spin-polarized current promotes a steady-state magnetic precession in the free layer (FL). (b) Output voltage obtained from the STNO dynamics.

6.1.1 Device architectures

There are two main geometries used for STNO patterning. For the nanocontact geometry (Fig. 6.2a), a gap in the top insulator ($\sim$100 nm of diameter [164]) creates an electric contact to the extended STNO stack, whereas for a nanopillar (Fig. 6.2b), the multilayer stack is patterned to the desired sectional dimensions. The nanopillar ensures that the electric current propagates through the multilayer, reducing the threshold current density ($\sim 10^6\,\mathrm{A/cm^2}$ [67]) when compared with nanocontacts ($\sim 10^8\,\mathrm{A/cm^2}$ [164]), where a larger current is needed to compensate its spread over the unpatterned stack. On the other hand, due to the smaller magnetic volume, nanopillars are more sensible to shape defects (i.e. sample-to-sample variability) and thermal fluctuations [165, 166], leading to a lower spectral purity [167]. Moreover, due to the patterning of the full MTJ stack, considerable stray magnetic fields are present and need to be considered in the experimental measurements.

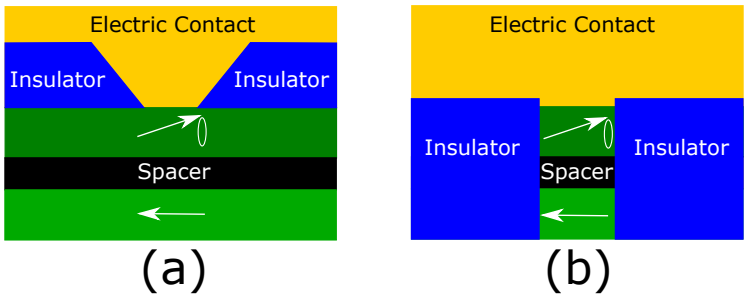


Figure 6.2: Main patterned STNO geometries: (a) nanocontact and (b) nanopillar.

6.1.2 Magnetic and stack configurations

STNOs also differ in the magnetic configuration. Table 6.1 shows a non-exhaustive summary of results obtained for STNOs. Regarding the device type, MTJs present a better performance for the power delivered (i.e. TMR much larger than GMR), while maintaining a linewidth comparable to spin valves. Since the first relevant experimental results in MTJs [67], the focus was directed to the optimization of the STNO performance by using MgO-based MTJ nanopillars. The nanocontact geometry in MTJs is challenging, since its higher resistance leads to shunt currents (see Ref. [167] in Table 6.1 for a non-conventional nanocontact, where a partial etching of the capping layer is performed to minimize the shunt current).

Figure 6.3 shows the main magnetic configurations that have been used over the years for STNO applications. The most straightforward configuration makes use of a fully in-plane magnetic anisotropy (IMA) STNO (Fig. 6.3a, FL : 1), where both FM layers have an in-plane magnetization [7, 22, 67]. To generate the RF signal, it is generally required to apply an external magnetic field to tilt the magnetization of the free layer and promote its oscillation, which is clearly a disadvantage for applications. An alternative combines a reference layer with IMA and a free layer with a perpendicular magnetic anisotropy (PMA, Fig. 6.3a, FL : 2), where STNO oscillations are achieved with [168] and, as a consequence of the remanent misalignment of the magnetizations, even without [169] an external field. A more complex STNO configuration corresponds to the insertion of a magnetic polarizer (Fig. 6.3b) with a strong PMA [170, 171]. The polarizer promotes the propagation of a spin-polarized current, whereas the reference layer acts as an analyser to readout the free layer precession. STNOs based on vortex oscillations (i.e. a free FM layer with a remanent vortex state) were also successfully implemented with (Fig. 6.3b, FL : 3) [172] and without (Fig. 6.3a, FL : 3) [29, 85] a polarizer. As described in Table 6.1, at a lower frequency range, vortex-based MTJs provide a clear advantage, combining a high output power ($\sim 1\ \mu$W) with the narrowest linewidths (~ 100 kHz) obtained to date.

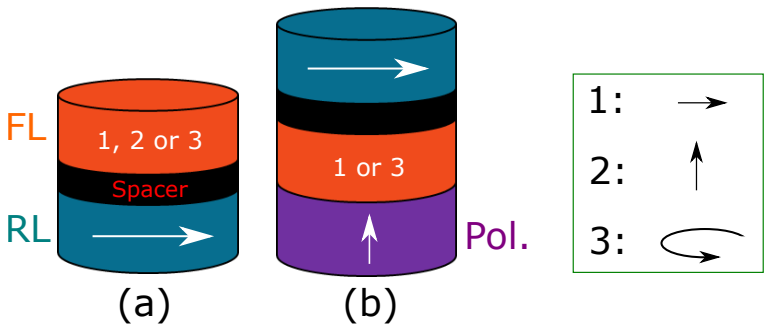


Figure 6.3: Illustration of the main stack configurations used for STNO fabrication: (a) a simple trilayer structure with free (FL) and reference (RL) FM layers and (b) a trilayer structure with insertion of a perpendicular magnetic polarizer (Pol.). For both, the free FM layer may have different magnetic states: 1) in-plane, 2) out-of-plane or 3) vortex.

Device	Geometry	FL	RL	Pol.	f (GHz)	$\mathrm{P_{out}}$ (dBm)	Γ (MHz)	Ref.
Spin valve	nanocontact	$\rightarrow$	$\rightarrow$	-	10 - 30	-70	2	[173]
Spin valve	nanocontact	$\uparrow$	$\rightarrow$	-	4 - 12	-60	6	[168]
Spin valve	nanopillar	$\rightarrow$	$\rightarrow$	$\uparrow$	2 - 4	-80	50	[171]
Spin valve	nanopillar	vortex	$\rightarrow$	-	1 - 2	Not specified	0.3	[85]
MTJ	nanocontact	$\rightarrow$	$\rightarrow$	-	4	-26	12	[167]
MTJ	nanopillar	$\rightarrow$	$\rightarrow$	-	2 - 5	-36	60	[174]
MTJ	nanopillar	$\uparrow$	$\rightarrow$	-	0.6 - 1.5	-47	28	[169]
MTJ	nanopillar	vortex	$\rightarrow$	-	0.2 - 0.5	-24	0.074	[30]
MTJ	nanopillar	vortex	$\rightarrow$	$\uparrow$	0.2	-32	0.105	[172]
8 synchronized MTJs	nanopillars	vortex	$\rightarrow$	-	0.363	-19	0.054	[32]

Table 6.1: Summary of STNO performances from the literature, where the frequency (f), output power ($\mathrm{P_{out}}$) and linewidth (Γ) are the indicative parameters. FL and RL refer to the free and reference layers, respectively, which may present an in-plane ($\rightarrow$), a perpendicular ($\uparrow$) or a vortex magnetic state. The STNO may also have a magnetic polarizer (Pol.). It should be emphasized that, considering the way that each reference exposes its experimental results, some of them above are approximations. The values of $\mathrm{P_{out}}$ and Γ refer to the best result obtained at each reference, which does not imply that both are obtained simultaneously for the same experimental conditions.

6.1.3 Performance parameters

Considering the description presented in Table 6.1, the next step towards the optimization of the STNO performance consists in (i) pushing up the output power above the μW scale and (ii) reduce the linewidth below the top limit for applications ($\sim 10\,\mathrm{kHz}$ [35]).

Output power The output power ($\mathrm{P_{out}}$) is the result of the temporal variation of the STNO resistance [R(t)] due to the magnetoresistance effect, being $\mathrm{R(t) = R_{av} + (\Delta R/2)\cos(\omega t)}$, where $\mathrm{R_{av}}$ is the average STNO resistance, $\Delta\mathrm{R}$ the resistance oscillation amplitude and ω the angular oscillation frequency. $\mathrm{P_{out}}$ delivered to a load with resistance $\mathrm{R_L}$ is given by [27]

$$P_{out} = \frac{R_L}{8}\left(\frac{\Delta R \cdot I}{R_{av} + R_L}\right)^2, \tag{6.1}$$

where I is the DC current flowing through the STNO. Specifically for an MTJ, the DC current is limited by the breakdown voltage ($\sim$1 V), defined as the voltage threshold above which the MTJ looses its TMR properties, with the formation of metallic conductive paths through the insulating barrier. The optimization of $\mathrm{P_{out}}$ in MTJs needs a balance. A lower MTJ resistance allows to apply a larger DC current, but for this purpose, one needs to deposit a thinner insulating barrier, whose effect is the decrease of the TMR ratio (Fig. 1.6). A lower TMR ratio decreases ΔR and, consequently, $\mathrm{P_{out}}$. Another important issue with ultra-thin insulating barriers ($\mathrm{RA} < 5\,\Omega\mu\mathrm{m}^2$) is the sudden increase of the critical current density for sustainable oscillations, which results from the need to compensate the conductive paths naturally created after the deposition of an ultra-thin discontinuous barrier [175]. Beyond the tuning of the barrier, a low critical current density ($\mathrm{J_0}$) demands a free FM layer as sensible as pos-

sible to the STT effect, meaning a thin magnetic layer ($\sim$ 10 nm) with a low saturation magnetization ($J_0 \propto M_S$) [176] and a low damping coefficient [140], without neglecting the need for a high output power and spectral purity. A good strategy is to fabricate a magnetic multilayer instead of a single layer. Specifically in this thesis and already in the literature [172], the free FM structure is constituted by a CoFeB/Ta/NiFe trilayer. While a soft NiFe layer with a low magnetization allows to decrease the critical current density, the CoFeB layer adjacent to the barrier helps to maintain the high TMR values already expected for CoFeB/MgO/CoFeB-based MTJs.

Linewidth For a real STNO, a full coherent precession is impossible, so that a non-zero linewidth, i.e. full width at half maximum of the power spectrum, is always expected. The linewidth measures the phase noise, which refers to the random phase fluctuations that an STNO experiences while precessing. Considering all the parameters on which the linewidth depends upon (e.g. temperature [166], external magnetic field [178–180] and DC current [64, 178, 181]), its optimization is not trivial. In principle, the linewidth of an STNO is larger when compared with a conventional auto-oscillator (e.g. VCO), where the linewidth is determined mostly by the thermal phase noise [182]. The operation frequency of an STNO is strongly dependent on the oscillation amplitude ($d\omega/dP \neq 0$, being ω the angular frequency of the oscillation and P its power), which leads to a coupling between phase and power noises [165]. This phenomenon is illustrated in Fig. 6.4. At t = 2, a perturbation leads to an increase of the oscillation amplitude, from the blue to the red precession, which in turn changes the frequency of oscillation. After the relaxation period, at t = 4, the orbit comes to its initial amplitude. Nevertheless, during the relaxation period, the magnetization experiences a gradient of its oscillation frequency due to the continuous change of the amplitude, which results in a phase shift accumulation in relation with the unperturbed precession (compare the red and blue curves for $t > 4$). In reality, these perturbations lead to a spectral broadening in relation with the nominal frequency, i.e. a significant linewidth appears.

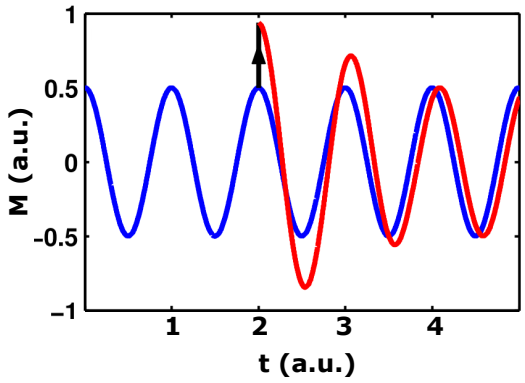


Figure 6.4: Illustration of the magnetization precession of a free FM layer. The blue curve represents a perfect non-realistic precession, whereas the red curve shows a realistic phenomenon, with an amplitude perturbation at t = 2 adding phase noise to the system (adapted from [177]).

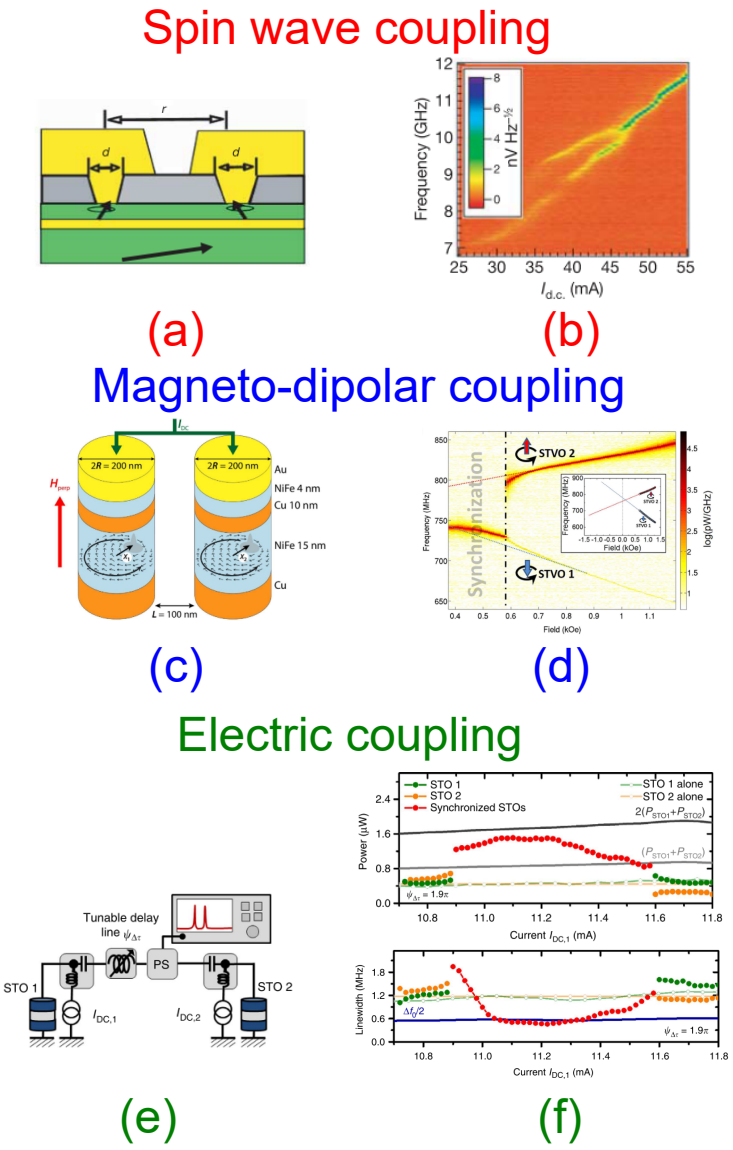


Figure 6.5: (a) Illustration of two nanocontacts fabricated in Ref. [183] for synchronization via spin wave propagation. (b) Power spectral density (PSD) measured as a function of the DC bias current ($\mathrm{I_{DC}}$) applied to a pair of nanocontacts, presented in Ref. [184]. The synchronization is achieved roughly for $\mathrm{I_{DC}} > 45\,\mathrm{mA}$. (c) Illustration of the two adjacent pillars fabricated in Ref. [185] for synchronization via magneto-dipolar coupling. (d) From the same report, the PSD is presented as a function of the perpendicular field ($\mathrm{H_{perp}}$) when the vortices have opposite polarities, showing a synchronized state roughly for $\mathrm{H_{perp}} < 0.6\,\mathrm{kOe}$. (e) Illustration of the setup used in Ref. [31] for synchronization via electric coupling. (f) From the same report, the dynamic properties (output power and linewidth) are presented for the free running oscillations (green and orange) and for the synchronized state (red).

6.2 Synchronization of STNOs

6.2.1 State of the art

The synchronization of STNOs has been performed over the years to improve their performance, thus presenting an alternative when the optimization of a single STNO starts to reach a bottleneck. For a pair of STNOs, the synchronization is achieved when their oscillations are "pushed" to the same frequency and their phases are locked in time (i.e. the difference between the phase of each STNO is constant over time). Theoretical predictions show the possibility to find conditions, so that an array of N synchronized STNOs enhances the spectral linewidth and the output power by a factor of 1/N [186] and N^2 [187], respectively.

The short range synchronization of adjacent STNOs via spin waves propagation was the first method successfully used for experimental synchronization [164, 183, 184]. For a pair of nanocontacts, each STNO precession promotes the propagation of spin waves across the extended free FM layer (Fig. 6.5a). If the distance between nanocontacts is sufficiently small (it may go up to $\sim 1\,\mu$m [188]), the spin waves may reach the opposite STNO, thus leading to an effective coupling (Fig. 6.5b). Moreover, if a vortex nucleation is achieved by a high DC current, the synchronization between nanocontacts is also possible via anti-vortices, as demonstrated by Ruotolo *et al.* [189], where the synchronization of a 2×2 array of vortex state nanocontacts is mediated by the formation of an anti-vortex between each nanocontact.

A second short range synchronization involves the coupling of two STNOs via the common magneto-dipolar field created by each STNO. This method was successfully achieved in vortex-based spin valve nanopillars, with an edge-to-edge distance of 100 nm (Fig. 6.5c) [185] and 50 nm [190]. In these reports, the coupling design comprises the fabrication of two adjacent nanopillars sharing the electric contacts, so that the dynamics are manipulated by a common DC bias current and a perpendicular field. Specifically in Fig. 6.5d, the synchronization of two adjacent nanopillars is achieved based on the distinct dependencies that vortices with different polarities present to the applied perpendicular field [191].

A long range synchronization is also possible via mutual electric coupling, where a non-local electric connection is performed between STNOs, either in parallel (Fig. 6.5e) or in series [31,32,192]. A common method to synchronize a pair of STNOs is to individually control the frequency of each oscillator by an independent DC current source and an additional setup element, as a tunable delay line to control the phase difference [31] or an attenuator to control the coupling strength between STNOs [32]. As shown in Fig. 6.5f, this scheme allows to compare the properties (i.e. linewidth and output power) of the free-running oscillations with the properties of the synchronized state at the same setpoints. Table 6.1 shows the performance for eight electrically synchronized spin torque vortex oscillators, which is the largest number to date.

Naturally, this progress, sustained in a better control and understanding, made synchronization an attractive phenomenon to be implemented in some emergent spintronic fields. Neuromorphic computing is a notable example [42]. In recent years, spintronic devices have been proposed for the hardware implementation of neuromorphic computing systems [43, 44, 46]. Non-trivial tasks such as vowel recognition were achieved in a synchronization-based computing system [44], where the recognition is performed based on the synchronization state between the input signal and a chain of

four STNOs working as artificial neurons. These advances have already been described in section 4.2. More recently, Albertsson *et al.* have proposed a network of synchronized STNOs working as an Ising machine to solve combinatorial optimization problems [193]. Specifically, it is numerically shown that the solution for a nondeterministic polynomial-hard-time (NP-hard) problem [194], as the Max-Cut problem [195, 196], can be found by monitoring the evolution of the synchronization state of each individual STNO as a function of a scheduled second harmonic injection locking [128]. Experimentally, regardless of the coupling mechanism, the full characterization of the synchronization state implies an individual access to the phase of each oscillator.

6.2.2 Synchronization from the universal nonlinear auto-oscillator model

To achieve a successful phase-locking, experiments are typically performed for at least two STNOs with similar unsynchronized frequencies. In fact, the frequency mismatch ($\delta = \omega_1 - \omega_2$) between the free running STNO frequencies (ω_1 and ω_2) is a key parameter for synchronization. Moreover, the phase-locking should be extended to a sufficiently broad and stable frequency range, which may be quantified as the synchronization bandwidth $\Delta\omega_s$. Figure 6.6 shows a common method to lock two STNOs, already performed successfully for nanocontacts [183] and nanopillars [31]. From the inset, it is clear that the unsynchronized oscillators ("1" and "2") have different free running frequencies. While "1" is precessing at a fixed frequency ω_1 (i.e. the applied DC current is constant), the frequency of "2" increases for a DC current variation. At a specific current value, one sees the collapse of both oscillations into a single one (purple solid line), which indicates a locking range characterized by $\Delta\omega_s = w_{max} - w_{min}$. An universal model was developed by Slavin *et al.* [138] to characterize the

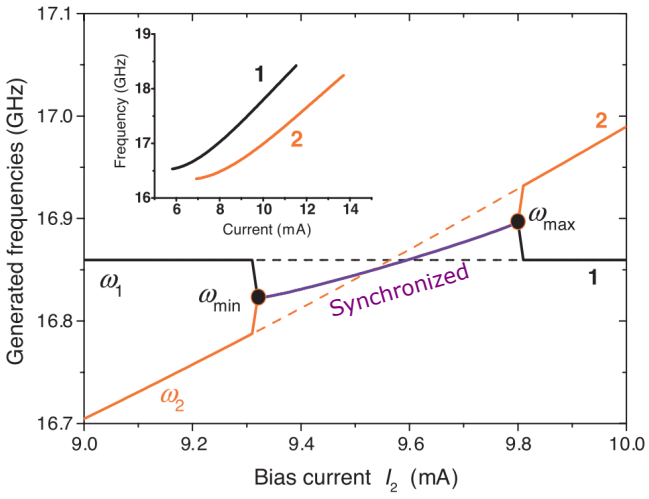


Figure 6.6: Synchronization method of two STNOs, obtained from theory. It shows the frequency of oscillators "1" and "2" as a function of the DC current applied to the oscillator "2". The dashed lines indicate the free running frequencies of each oscillator. The synchronization is represented by a purple solid line, with $\Delta\omega_{synch} = \omega_{max} - \omega_{min}$. The inset shows the free running frequencies of each STNO as a function of the applied DC current. Adapted from [197].

synchronization of two "almost identical" oscillators, i.e. all the parameters are equal, except the free-running frequencies. The synchronization state is described by their phase sum $\phi = \phi_1 + \phi_2$ and phase difference $\Psi = \phi_1 - \phi_2$ as

$$\frac{d\phi}{dt} = -\bar{\omega} + \Omega\sqrt{1+\nu^2}\,\sin[\beta - \arctan(\nu)]\,\cos(\Psi) \tag{6.2}$$

and

$$\frac{d\Psi}{dt} = \delta - 2\Omega\sqrt{1+\nu^2}\,\cos[\beta - \arctan(\nu)]\,\sin(\Psi), \tag{6.3}$$

where $\bar{\omega}$ is the average free-running frequency [i.e. $\bar{\omega} = (\omega_1 + \omega_2)/2$] and ν the normalized coefficient translating the non-linear frequency shift [161]. The coupling is described as a weak external force $\mathrm{f(t)} = \Omega\exp(\mathrm{j}\beta)\,\mathrm{c(t)}$, acting on each oscillator and characterized by a coupling frequency Ω and phase β, where $\mathrm{p} = |\mathrm{c}|^2$ is the power of the oscillation. In the phase-locked regime, $\mathrm{d}\Psi/\mathrm{dt} = 0$, leading to

$$\sin(\Psi) = \frac{\delta}{\Delta\omega_s}, \tag{6.4}$$

with

$$\Delta\omega_s = 2\Omega\sqrt{1+\nu^2}\,|\,\cos[\beta - \arctan(\nu)]\,|, \tag{6.5}$$

which indicates that the mutual phase locking is possible only when the frequency mismatch falls into the synchronization bandwidth, i.e. $|\delta| \leq \Delta\omega_\mathrm{s}$. In the locking regime, both oscillators operate at the same frequency

$$\omega_s = \bar{\omega} - \sqrt{\Delta\omega_s^2 - \delta^2}\,\tan[\beta - \arctan(\nu)]. \tag{6.6}$$

It is clear that even for identical oscillators, ω_s is not necessarily equal to the average of the free running frequencies ($\bar{\omega}$). When $\delta > \Delta\omega_\mathrm{s}$, ω_s becomes imaginary, which physically means the absence of phase-locking.

6.3 Dipolar coupling of STVOs in an ITC geometry

Here, a new integrated design for the synchronization of spin torque vortex oscillators (STVOs) is proposed. The geometry comprises the fabrication of adjacent pairs of STVO nanopillars (MgO-based magnetic tunnel junctions), with an edge-to-edge distance down to 100 nm, together with independent top contacts (ITCs), meaning that, for the first time, the synchronization via magneto-dipolar coupling can be evaluated with a simultaneous access to the phase of each individual oscillator.

6.3.1 ITCs nanofabrication

The fabrication of MTJ devices for synchronization via dipolar coupling follows the process described in section 3.2 with one main difference. Considering that each nanopillar is connected with an ITC, the optical lithography for the pillar cap and bottom pads definition (section 3.2.6) needs to be substituted by an e-beam lithography, defining nano-sized ITCs on top of each pillar, plus the bottom pads that were already defined in the original lithography. Figure 6.7a shows an optical microscope top view image of the new design after process, described in section 3.1. The main features are placed at the central region, that is zoomed in and illustrated in Fig. 6.7b. The design allows the definition up to four nanopillars close together in a vertical line (Fig. 6.7c). While the bottom contact is shared

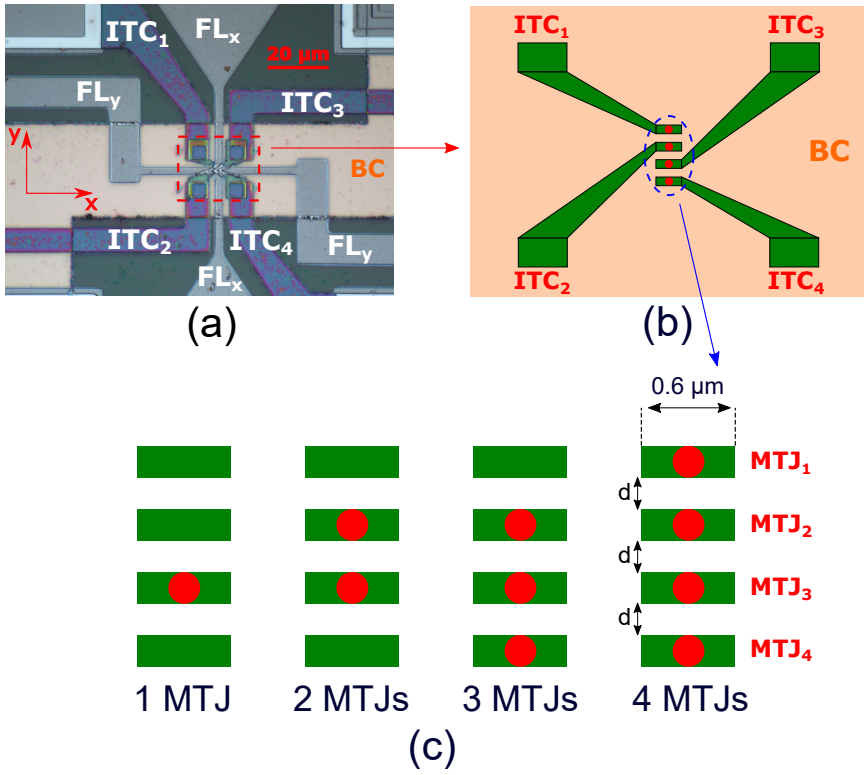


Figure 6.7: (a) Top view of the ITC design in the central region. (b) Illustration of the ITC design near the nanopillars. (c) Each $\mathrm{MTJ_i}$ is electrically connected with an individual top contact $\mathrm{ITC_i}$ (i = 1, 2, 3 or 4). When changing the number of MTJs per device, the design with four ITCs is maintained. Useful information: bottom contact (BC), field line creating a magnetic field in the xx direction ($\mathrm{FL_x}$), field line creating a magnetic field in the yy direction ($\mathrm{FL_y}$) and distance between consecutive nanopillars (d).

by all the nanopillars, four nano-sized ITCs are defined on top (green structures in Fig. 6.7b) and consequently connected to their respective top contact pad. Along with the MTJ contacts, a field line is also defined for both in-plane directions ($\mathrm{FL_x}$ and $\mathrm{FL_y}$ in Fig. 6.7a). In one die, this design is replicated by changing the number of nanopillars (up to four) and the distance between them (d in Fig. 6.7c, down to 100 nm). As an example, Fig. 6.8 shows SEM images of four nanopillars 100 nm apart, after pillar definition (Fig. 6.8a) and after planarization (Fig. 6.8b), in accordance with the description presented in sections 3.2.4 and 3.2.5, respectively. The nanopillars were defined from two MTJ stacks described in Table 6.2, with diameters of 300 nm and 350 nm.

Following the planarization, a TiWN(15) / AlSiCu(20) / TiWN(15) metallic structure is deposited at the FTM sputtering tool for ITC definition (thickness in nanometers). Due to the thin metallic structure, the e-beam lithography is performed with a thinner 200 nm diluted ARN7520.18 e-beam resist (one part of ARN7520.18 plus one part of AR 300-12 organic solvent). Figure 6.9 shows the top view of the closest ITCs fabricated in this thesis (i.e. $\mathrm{d} = 100\,\mathrm{nm}$). The development step is successful (Fig. 6.9a), meaning that the nanometric gaps between ITCs do not prevent the developer from

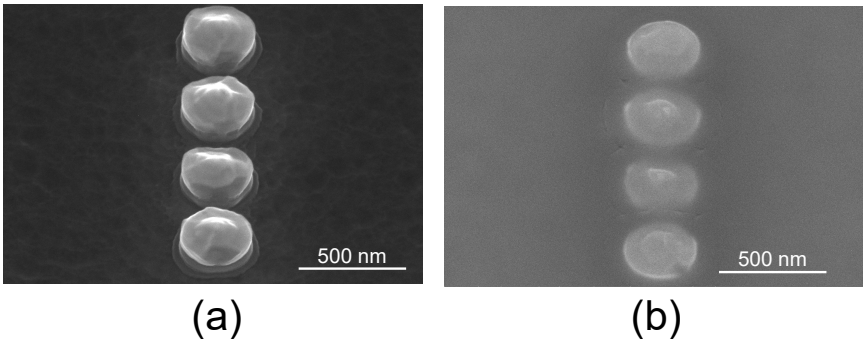


Figure 6.8: SEM images obtained for four MTJ nanopillars with a diameter of 300 nm after (a) definition and (b) planarization. The nominal edge-to-edge distance between pillars is 100 nm. The images are obtained at a tilting angle of 40°.

properly remove the unexposed e-beam resist between ITCs. The contact definition is critical, since an incomplete etching leads to short circuits between consecutive ITCs. As usual, the definition is performed by ion beam milling (Table 6.3), but now with an angle of 100° to minimize the shadow effect in the gaps between ITCs. Moreover, the etching rate is smaller in the gaps between ITCs, so a reasonable overetch of 100% is performed to guarantee the complete ITC insulation. After definition, the e-beam resist strip is performed in plasma asher, according to the recipe described in section 2.4.2 (now that the pillars are insulated and protected, there is no risk in damaging the devices). Figure 6.9b shows an SEM image of the final ITC design after resist strip. To evaluate the yield of the definition (i.e. insulation between consecutive ITCs), electric measurements need to be performed after process. For this purpose, ITCs with an MTJ below cannot be used, because each nanopillar is a conductive path to connect consecutive ITCs. On the other hand, devices with a single MTJ are suitable for this analysis, since they have two consecutive ITCs without establishing contact with

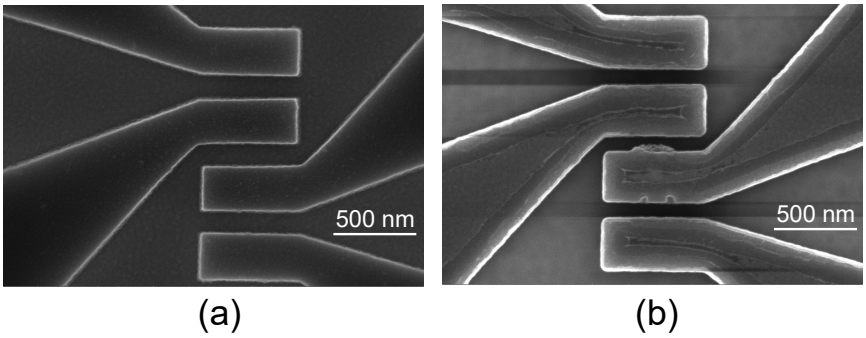


Figure 6.9: Top view SEM images obtained for an ITC device after (a) development and (b) resist strip. The nominal distance between consecutive ITCs is 100 nm.

MTJ label	Stack	Performed measurements
Stack A	5 Ta / 50 CuN / 5 Ta / 50 CuN / 5 Ta / 5 Ru / 6 IrMn / 2.6 $CoFe_{30}$ / 0.85 Ru / 1.8 $CoFe_{40}B_{20}$ / MgO ($3.67\,\Omega\mu m^2$) / 2 $CoFe_{40}B_{20}$ / 0.2 Ta / 7 NiFe / 10 Ta / 30 CuN / 7 Ru	Steady-state dynamics and synchronization
Stack B	5 Ta / 50 CuN / 5 Ta / 50 CuN / 5 Ta / 5 Ru / 6 IrMn / 2.0 $CoFe_{30}$ / 0.7 Ru / 2.6 $CoFe_{40}B_{20}$ / MgO ($21.65\,\Omega\mu m^2$) / 2 $CoFe_{40}B_{20}$ / 0.5 Ta / 7 NiFe / 10 Ta / 30 CuN / 7 Ru	R-H loops for MTJ yield calculation

Table 6.2: Description of the two MTJ stacks used for ITC patterning. The thickness is presented in nanometers.

an MTJ. This is clear in Fig. 6.7c, where a nanopillar is found at the MTJ_3 position, leaving two consecutive ITCs at the MTJ_1 and MTJ_2 positions free to check the ITCs insulation for different gaps. The measurement is performed manually with two micro-size probes, establishing electric contact with ITC_1 and ITC_2 that, in devices with a single MTJ, have no pillar below. In general, all ITC gaps show an open circuit (i.e. for an applied DC current of 1.0 mA, the DC voltage is above 21 V, which is the limit of the sourcemeter), down to 100 nm, in this way proving a successful definition of the nanocontacts.

Considering that the ITCs are not fabricated in a standard design, it is advisable to calculate the yield of the MTJ nanopillars, with particular focus on the ones with a smaller gap, since that can result in nanofabrication issues, namely in the pillar definition (section 3.2.4) due to the shadow effect and in the planarization step (section 3.2.5) due to the formation of a larger oxide bump. The SEM images already give good indications about the nanofabrication, but only the electric measurements can give a complete picture of the MTJ yield. So, the semi-automatic prober was used to obtain a transfer curve for each individual nanopillar through its ITC. Each transfer curve was obtained from a two-contact measurement, since each nanopillar only has one top contact pad. Figure 6.10 shows the yield of the ITC devices, presented as a function of the edge-to-edge distance (d) between them. For each distance, the measurements were performed for 10 ITC devices with stack B from Table 6.2 (5 ITC devices for each MTJ diameter of 300 nm and 350 nm). For instance, in Fig. 6.10a, one is measuring a total of forty individual MTJs (n = 40) fabricated in ITC devices with four pillars. So, for d = 100 nm, the yield is 27.5%, which means that 11 out of the 40 nanopillars fall into the yield filtering of $[5 < \mathrm{MR}\,(\%) < 100]$ and $[10 < \mathrm{RA}\,(\Omega\mu m^2) < 50]$, being MR the magnetoresistance ratio. The upper limit of the RA filter is quite high compared with the nominal value of $21.65\,\Omega\mu m^2$, because it was verified that MTJs with an RA $\sim 50\,\Omega\mu m^2$ still show a vortex-like transfer curve, meaning that the

Ion beam gun	RF Power (W)	Positive grid voltage (V)	Positive grid current (mA)	Negative grid voltage (V)	Ar flux (sccm)	Incidence angle (°)
Setpoint	380	500	306	-3200	60	100

Table 6.3: Recipe parameters used at Nordiko 7500 for ITCs definition. The neutralizer setpoints are in accordance with Table 2.3.

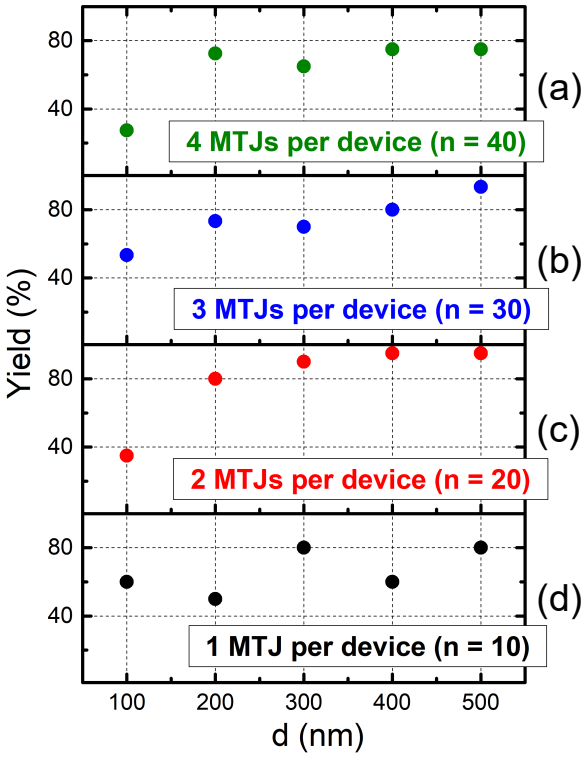


Figure 6.10: Yield of the MTJ nanopillars presented as a function of the edge-to-edge distance. For each distance, the calculation is based on 10 ITC devices with different configurations: (a) four, (b) three, (c) two and (d) one MTJs per device, as illustrated in Fig. 6.7c. The value n represents the number of nanopillars measured in the 10 ITC devices.

ITC resistance is particularly high in these high resistive devices. When the ITC device has more than one nanopillar (Figs. 6.10a-c), the yield clearly decreases as the gap between pillars starts to shrink, with a significant fall at d = 100 nm. This yield degradation is mainly caused by nanopillars showing an open circuit, so one possible explanation may be an incomplete planarization when opening the caps of very close pillars (i.e. these tend to create a larger bump of oxide on top, which naturally makes it more difficult to planarize).

6.3.2 Experimental setup

After process, ITC devices were measured at the station for RF characterization (section 2.6.5). These measurements were only performed in ITC devices from a wafer with stack A, as described in Table

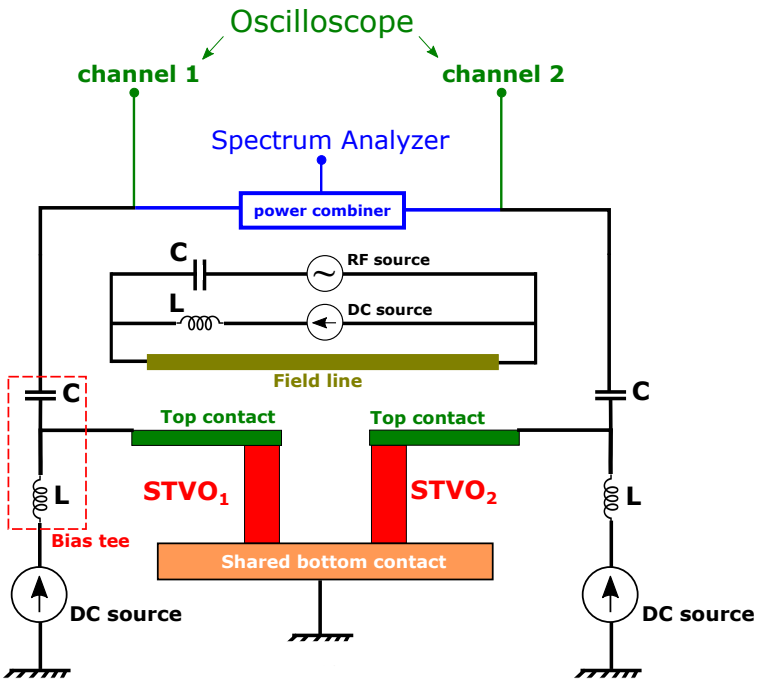


Figure 6.11: Illustration of the experimental setup used for the characterization of MTJ nanopillars with ITCs. Depending on the purpose, the STVO signals can be visualized via a spectrum analyser after power combining or individually via two oscilloscope channels.

6.2. Experimentally, it has been verified that the RA product of stack B is too high for steady-state oscillations, i.e. the most common situation is to reach the breakdown voltage before reaching the threshold for steady-state vortex oscillations.

The dynamics were monitored up to two nanopillars simultaneously. Figure 6.11 shows an illustration of the experimental setup. Independently through a bias tee, each source applies a DC current to an individual STVO. Then, the AC signal from the steady-state oscillation of each STVO is transmitted by the bias tee capacitor to a spectrum analyser, after being combined with the signal of the other STVO. In addition to a direct measurement of the spectra, the setup of Fig. 6.11 also allows the individual connection of each STVO signal to an independent oscilloscope channel, so that both signals can be visualized at the same time domain. There is also a secondary setup associated with the field line fabricated on top of the pillars (see Fig. 3.3). An additional bias tee is used to apply both DC and RF signals through the field line. Finally, an external perpendicular magnetic field is also applied via the electromagnet, as a requirement for steady-state vortex gyrotropic oscillations [29].

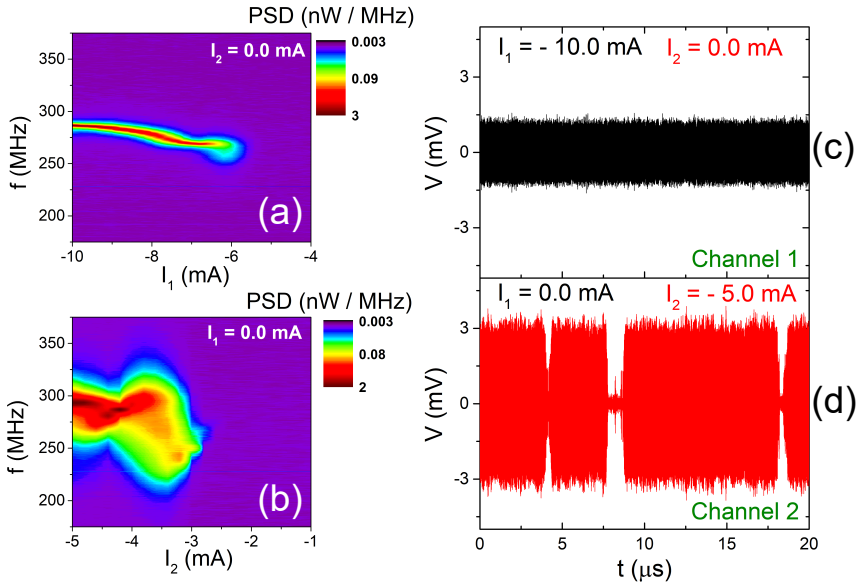


Figure 6.12: (a)-(b) Power spectral density (PSD) individually measured from two STVOs ($\mathrm{STVO_1}$ and $\mathrm{STVO_2}$) with an edge-to-edge distance of 100 nm. (a) Spectrum obtained for $\mathrm{STVO_1}$ as a function of the DC current $\mathrm{I_1}$ (the DC current $\mathrm{I_2}$ applied to $\mathrm{STVO_2}$ is kept at zero). (b) Spectrum obtained for $\mathrm{STVO_2}$ as a function of the DC current $\mathrm{I_2}$ (the DC current $\mathrm{I_1}$ applied to $\mathrm{STVO_1}$ is kept at zero). (c) Time trace obtained for $\mathrm{STVO_1}$ at $\mathrm{I_1} = -10.0\mathrm{mA}$. (d) Time trace obtained for $\mathrm{STVO_2}$ at $\mathrm{I_2} = -5.0\mathrm{mA}$. Each time trace is presented after application of a band pass filter between 150 MHz and 400 MHz. A perpendicular magnetic field of 2.8 kOe was applied during the measurements.

6.3.3 Steady-state dynamics of coupled STVOs

Edge-to-edge distance of 100 nm

Figure 6.12 shows the dynamics of a pair of STVOs ($\mathrm{STVO_1}$ and $\mathrm{STVO_2}$) with an edge-to-edge distance of 100 nm and a diameter of 350 nm. In this first analysis, the dynamics of each STVO are individually measured, meaning that the DC bias current is only applied to one of the devices. Here, a positive DC bias current corresponds to electrons travelling from the reference to the free layer. The spectra measured in the spectrum analyser are depicted in Fig. 6.12a and Fig. 6.12b for the DC current sweep of $\mathrm{STVO_1}$ and $\mathrm{STVO_2}$, respectively. Although nominally similar, the two STVOs have different dynamic properties. $\mathrm{STVO_1}$ shows a larger threshold current for gyrotropic oscillations, which may indicate a more degraded insulating barrier, i.e. a larger current needs to be applied to compensate the current spread through the conductive paths of the barrier [175]. Moreover, the devices present small power emissions, with an output power at the nW range. These results are justified by the small RA product of the MTJ stack ($3.67\,\Omega\mu\mathrm{m}^2$). In fact, a too thin MgO barrier is more susceptible to defects as pinholes [65] and amorphous regions [62], whose main consequences are

the decrease of the spin-polarization of the DC bias current and a larger sample-to-sample variability. $\mathrm{STVO_1}$ was preserved by sweeping the DC current $\mathrm{I_1}$ down to $-10.0\,\mathrm{mA}$, which corresponds to a DC voltage of $\sim 0.8\mathrm{V}$ measured across the MTJ (an irreversible degradation of devices in this wafer is typically observed for a breakdown voltage of $\sim 1\,\mathrm{V}$). On the other hand, $\mathrm{STVO_2}$ shows a smaller threshold but a poorer spectral purity. The dynamics can be understood by looking at the time trace obtained in the oscilloscope, shown in Fig. 6.12d for $\mathrm{STVO_2}$. The vortex oscillation is not continuously sustained over a long time, in contrast with the time trace obtained for $\mathrm{STVO_1}$ (Fig. 6.12c). This behaviour was already reported in the literature and tends to occur near the DC current threshold for vortex oscillations [161]. Although not shown in Fig. 6.12b, it was verified that below $-5.0\,\mathrm{mA}$, the dynamics tend to be suppressed, probably because, in this specific MTJ, the breakdown voltage is reached before having a large enough DC bias current for a more coherent oscillation [161]. So again, the choice was to stop at $\mathrm{I_2} = -5.0\,\mathrm{mA}$ to preserve the device. Nevertheless, the results will prove that the poor spectral purity of $\mathrm{STVO_2}$ does not compromise a successful synchronization.

After the characterization of each individual device, the synchronization between STVOs is evaluated by sweeping the DC current of $\mathrm{STVO_1}$, while maintaining constant the DC current passing through $\mathrm{STVO_2}$. Thus, the coupling strength between the two STVOs is controlled by $\mathrm{I_1}$. The dynamics were measured using the power combiner and the spectrum analyser, as illustrated in Fig. 6.11. The results are presented in Fig. 6.13a, where $\mathrm{I_2} = -5.0\,\mathrm{mA}$ and $\mathrm{I_1}$ is swept down to $-10.0\,\mathrm{mA}$. For $\mathrm{I_1} \leq -6.0\,\mathrm{mA}$, the increase of the $\mathrm{STVO_1}$ frequency tends to decrease the frequency detuning between the two oscillations, until a clear frequency merging for $\mathrm{I_1} \leq -8.2\mathrm{mA}$, where only a single peak is visible. To check if there is an improvement of the dynamics, Figs. 6.13b-c show the linewidth and the output power, respectively, of the system for different conditions, in order to compare the performance of each individual STVO ($\mathrm{STVO_1}$ in black and $\mathrm{STVO_2}$ in red) with the performance of both combined (in blue). The fundamental parameters that characterize the dynamics (i.e. frequency, linewidth and output power) are obtained from a Lorentzian fit performed to the single peak of each spectrum [161, 172]. This calculation was performed for the $\mathrm{I_1} \leq -8.2\,\mathrm{mA}$ range, where the STVOs are oscillating at the same frequency and the synchronization is expected. In this analysis, since $\mathrm{I_2} = -5.0\,\mathrm{mA}$, the parameters of $\mathrm{STVO_2}$ are constant over the full range of $\mathrm{I_1}$. When both STVOs are oscillating, a clear improvement of the output power is verified (blue curve in Fig. 6.13d). As an example, Fig. 6.13b shows the spectra obtained for $\mathrm{I_1} = -10.0\,\mathrm{mA}$ and $\mathrm{I_2} = -5.0\,\mathrm{mA}$ for single (black and red) and combined (blue) oscillations. The output power increases to $\mathrm{P_{synch}} = 41.3\,\mathrm{nW}$, which is significantly larger than the sum of the powers of each STVO oscillating alone ($\mathrm{P_1} = 3.3\,\mathrm{nW}$ and $\mathrm{P_2} = 22.2\,\mathrm{nW}$). Regarding the spectral coherence, the linewidth of the combined oscillation (blue curve in Fig. 6.13c) tends to merge to the values presented by $\mathrm{STVO_1}$ (black curve in Fig. 6.13c), which means that only the noisiest oscillator $\mathrm{STVO_2}$ shows a significant improvement of its spectral coherence, from 8.86 MHz (red dash line in Fig. 6.13c) to 966 kHz (blue data in Fig. 6.13c, at $\mathrm{I_1} = -10.0\,\mathrm{mA}$). The increase of the $\mathrm{I_1}$ module is also followed by an increase of the synchronized state frequency ($\mathrm{f_{SYNCH}}$ in Fig. 6.13e). For $\mathrm{I_1} \leq -9.0\mathrm{mA}$, $\mathrm{f_{SYNCH}}$ goes above both $\mathrm{f_1}$ and $\mathrm{f_2}$ free-running frequencies of $\mathrm{STVO_1}$ and $\mathrm{STVO_2}$, respectively, which is a behaviour already verified in the literature [190]. Although not considering the phase of each oscillator, the results clearly demonstrate the fingerprint of a synchronization of the two STVOs [31, 32]. As already emphasized, going below $-10.0\,\mathrm{mA}$ could be detrimental for $\mathrm{STVO_1}$ (i.e. DC voltage $\sim 1\,\mathrm{V}$ across the MTJ), so it was not possible to measure the synchronization through its entire frequency bandwidth.

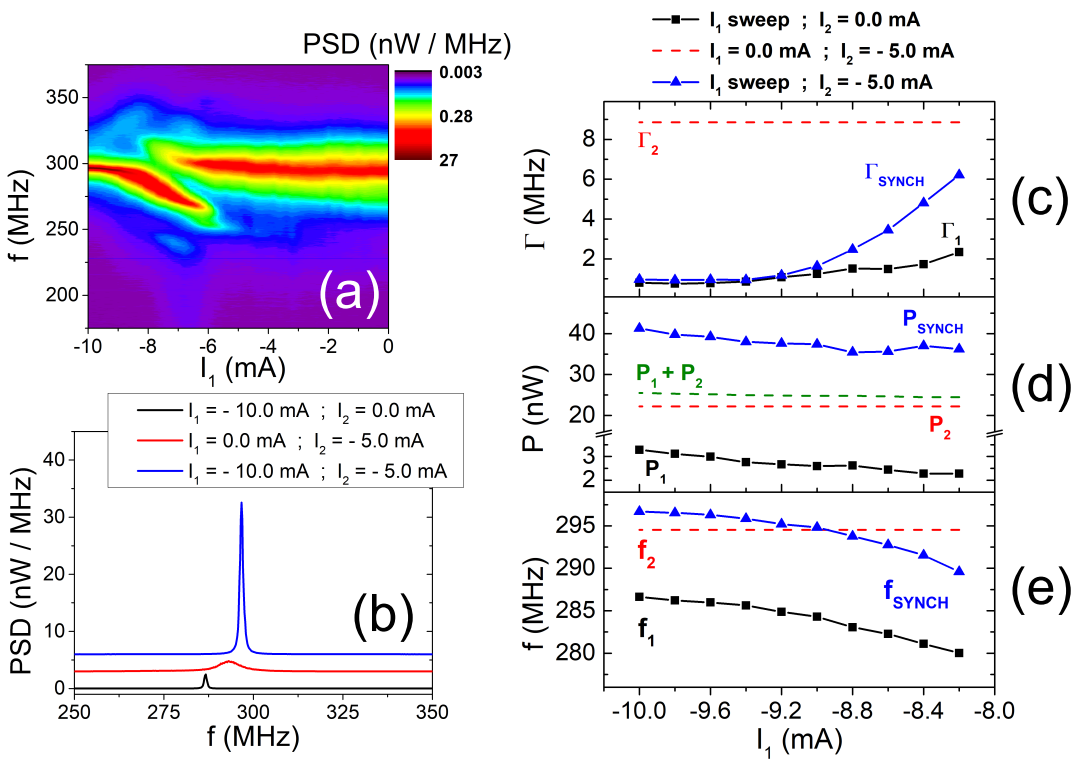


Figure 6.13: (a) Power spectral density (PSD) measured for two STVOs ($\mathrm{STVO_1}$ and $\mathrm{STVO_2}$) with an edge-to-edge distance of 100 nm, as a function of the DC current $\mathrm{I_1}$ passing through $\mathrm{STVO_1}$. The DC current $\mathrm{I_2}$ applied to $\mathrm{STVO_2}$ is $-5.0\,\mathrm{mA}$. (b) Example of the PSD obtained for $\mathrm{I_1} = -10.0\,\mathrm{mA}$ and $\mathrm{I_2} = -5.0\,\mathrm{mA}$ for single (black and red) and combined (blue) oscillations. (c) Linewidth, (d) output power and (e) frequency calculated as a function of $\mathrm{I_1}$ for $\mathrm{I_2} = 0.0\,\mathrm{mA}$ (black) and $\mathrm{I_2} = -5.0\,\mathrm{mA}$ (blue). For an easy comparison, the parameters obtained for an isolated oscillation of $\mathrm{STVO_2}$ at $\mathrm{I_2} = -5.0\,\mathrm{mA}$ (red) are also shown without any connection with the $\mathrm{I_1}$ axis. A perpendicular magnetic field of 2.8 kOe was applied during the measurements.

To complete the synchronization analysis, the ITC fabrication also gives a direct access to the phase of each individual STVO. The phase evolution can be measured using two independent oscilloscope channels as depicted in Fig. 6.11. After measuring the time trace $v(\mathrm{t})$ of an individual STVO, the instantaneous phase can be extracted from its analytic signal [198], given by [199]

$$v_a(t) = v(t) + jH[v(t)] = A(t)e^{j\Psi(t)}, \tag{6.7}$$

where j is the imaginary unit, $\mathrm{H}[v(\mathrm{t})]$ the Hilbert transform of the time trace and $\mathrm{A(t)}$ [$\Psi(\mathrm{t})$] the instantaneous amplitude (phase) of $v(\mathrm{t})$. This signal processing method has also been applied for the noise characterization of STNOs [161, 199–201]. For each value of $\mathrm{I_1}$, the oscillations of $\mathrm{STVO_1}$ and $\mathrm{STVO_2}$ are measured independently in the time domain, so that it is possible to extract the instan-

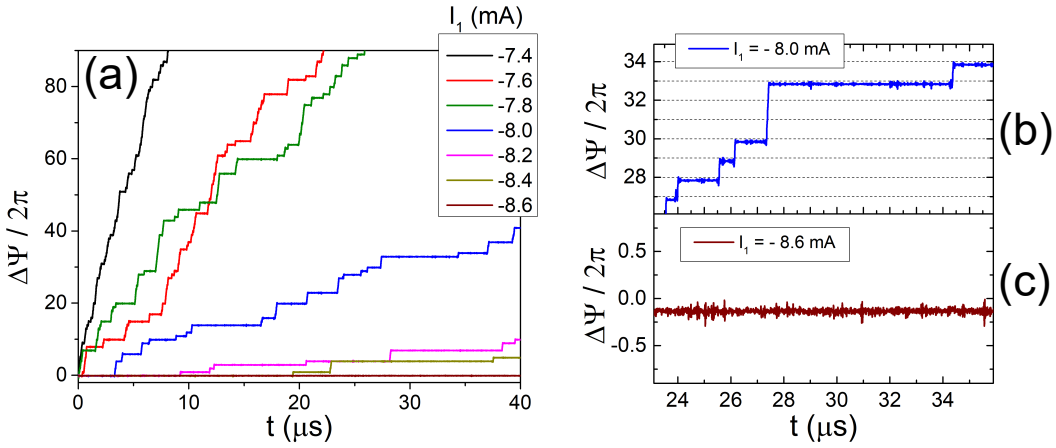


Figure 6.14: (a) The instantaneous phase difference ($\Delta\Psi$) is presented as a function of time, for different values of $\mathrm{I_1}$ passing through $\mathrm{STVO_1}$. The DC current passing through $\mathrm{STVO_2}$ is $-5.0\,\mathrm{mA}$. $\Delta\Psi$ is zoomed in for (b) $\mathrm{I_1} = -8.0\,\mathrm{mA}$ and (c) $\mathrm{I_1} = -8.6\,\mathrm{mA}$. A perpendicular magnetic field of 2.8 kOe was applied during the measurements.

taneous phases of each oscillator, i.e. $\Psi_1(\mathrm{t})$ for $\mathrm{STVO_1}$ and $\Psi_2(\mathrm{t})$ for $\mathrm{STVO_2}$. In addition to the frequency tuning, the second requirement for synchronization is that the phase difference between the two oscillators must be constant over time, i.e. $\Delta\Psi(\mathrm{t}) = \Psi_1(\mathrm{t}) - \Psi_2(\mathrm{t}) = \mathrm{constant}$.

Figure 6.14a shows $\Delta\Psi(\mathrm{t})$ calculated from 40 μs time traces and for different values of $\mathrm{I_1}$. In addition to the frequency domain analysis of Fig. 6.13, these results confirm a successful synchronization. The system evolves from an unsynchronized state, e.g. $\mathrm{I_1} = -7.4\,\mathrm{mA}$ where $\Delta\Psi$ diverges in time, to a stable synchronization at $\mathrm{I_1} = -8.6\,\mathrm{mA}$, that is maintained down to $\mathrm{I_1} = -10.0\,\mathrm{mA}$ (not shown). The time domain analysis gives some details that cannot be clarified by the frequency domain measurements depicted in Fig. 6.13. Considering the measurement period of 40 μs, the phase evolution shows that a stable synchronization is only achieved for $\mathrm{I_1} \leq -8.6\mathrm{mA}$. The output power calculated in Fig. 6.13d suggests a synchronization state starting at $\mathrm{I_1} = -8.2\,\mathrm{mA}$. In fact, at the $-8.6\mathrm{mA} < \mathrm{I_1} < -8.0\mathrm{mA}$ range (i.e. at the edge of the synchronization bandwidth), Fig. 6.14a shows that the coupling strength is not capable of maintaining the synchronization state over significant periods, so that $\Delta\Psi$ shows stable periods separated by desynchronization-resynchronization events (i.e. phase slips). In Fig. 6.13, the consequences of such an unstable state, characterized by short-period synchronization events, are particularly visible in the spectral coherence of the synchronized state (blue data in Fig. 6.13c) that is still far from being optimized at the $-8.6\mathrm{mA} < \mathrm{I_1} < -8.0\mathrm{mA}$ range. Regarding the output power (Fig. 6.13d), that influence is not so significant, since $\mathrm{P_{synch}}$ is much larger than the sum of $\mathrm{P_1}$ and $\mathrm{P_2}$ over the full $\mathrm{I_1}$ range. The existence of phase slips is also visible for $\mathrm{I_1} \geq -8.0\,\mathrm{mA}$. Nevertheless, the conditions are not suitable for synchronization, so $\Delta\Psi$ is now characterized by much shorter stable periods and its divergence in time is much more pronounced. Figure 6.14b shows that the amplitude of the phase slips is a multiple of 2π. This amplitude is associated with the number of synchronization states available over one period [201]. When synchronized, the

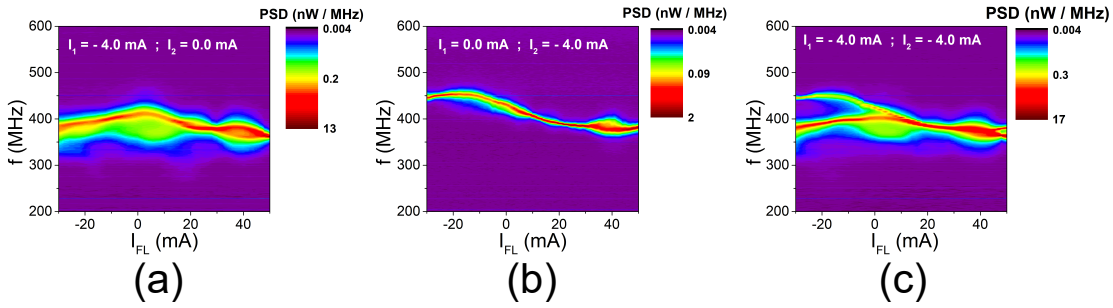


Figure 6.15: Power spectral density (PSD) measured for two STVOs ($\mathrm{STVO_1}$ and $\mathrm{STVO_2}$) 1 μm apart, as a function of the DC current $\mathrm{I_{FL}}$ passing through the field line. The measurement is performed for (a) an individual oscillation of $\mathrm{STVO_1}$ ($\mathrm{I_1 = -4.0mA}$), (b) an individual oscillation of $\mathrm{STVO_2}$ ($\mathrm{I_2 = -4.0mA}$) and (c) the combined dynamics ($\mathrm{I_1 = I_2 = -4.0mA}$). A perpendicular magnetic field of 5.6 kOe was applied during the measurements.

two STVOs are oscillating at the same frequency, so a phase slip of 2πn (being n an integer) indicates a single synchronization state per period.

Another important aspect to consider is that $\Delta\Psi$ of the synchronized state is a non-trivial value, i.e. neither zero, nor π. This is particularly clear in Fig. 6.14c, where the synchronization is characterized by $\Delta\Psi = -0.8 \pm 0.2\,(\mathrm{rad})$ [$\Delta\Psi = -48 \pm 9\,(^\circ)$]. This value is not artificial, since each STVO is connected to the measuring instruments by RF cables with the exact same length. In fact, if two identical STVOs are considered, the theory predicts a synchronized state, via magneto-dipolar interaction, with $\Delta\Psi = 0$ or $\Delta\Psi = \pi$, depending on the magnetic parameters of the vortices [202, 203]. On the other hand, for non-identical oscillators, the theory shows that a non-trivial $\Delta\Psi$ is possible [204, 205]. In this experiment, the two STVOs under study are clearly non identical, as shown by their individual dynamics in Fig. 6.12. The source of this sample-to-sample variability is most probably a combination of different factors, arising from the limitations of the fabrication process (e.g. lithographic accuracy, uniformity of the MgO barrier deposition), as oscillators with different spin torque parameters [205] or with a diameter mismatch [204].

In particular, Chen *et al.* [205] have explained the variation of $\Delta\Psi$ in the synchronized state, admitting the magneto-dipolar coupled pair of oscillators as a Newton-like particle moving in an energy surface that is a function of the phase difference between the oscillators. When the pair is identical, the particle finds an energy minimum for $\Delta\Psi = 0$ or $\Delta\Psi = \pi$, depending on magnetic parameters such as the uniaxial anisotropy. Then, non-identical oscillators are simulated by changing their spin torque parameters, as the spin-polarization. This leads to a tilting of the energy surface that shifts the energy minima in the phase domain, i.e. the particle will find its energy minimum for a $\Delta\Psi$ value different from zero or π.

Edge-to-edge distance of 1 μm

In the ITC geometry, the nanopillars are electrically connected by sharing the bottom contact. So, in addition to the magneto-dipolar interaction, the electric coupling should also be considered as a

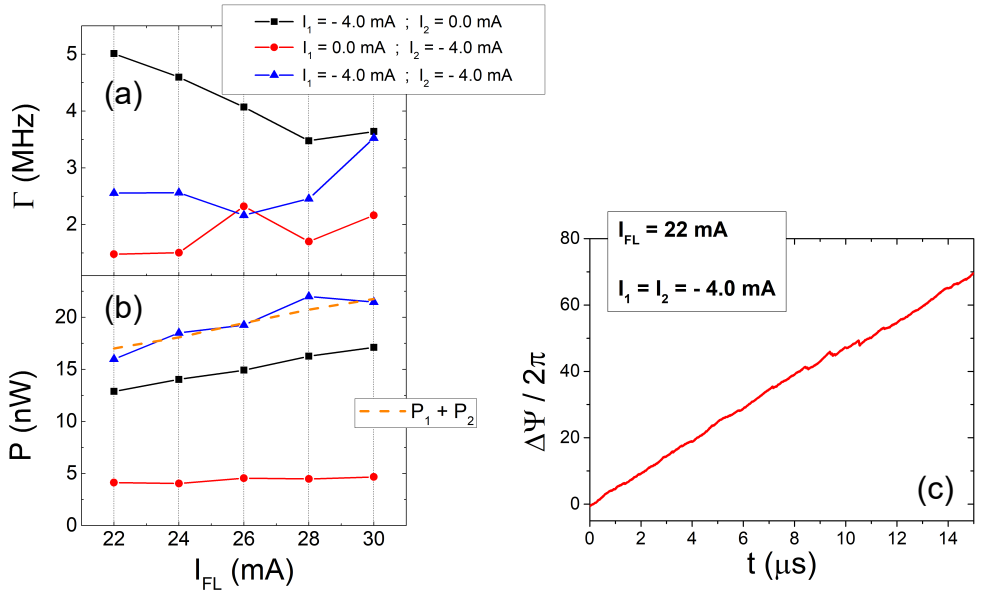


Figure 6.16: (a) Linewidth and (b) output power calculated as a function of $\mathrm{I_{FL}}$ for the individual oscillation of $\mathrm{STVO_1}$ (black) and $\mathrm{STVO_2}$ (red) and for the combined dynamics (blue). The $\mathrm{I_{FL}}$ range is chosen based on the data shown in Fig. 6.15c, where both STVOs merge into the same oscillating frequency. In (b), the orange dashed line corresponds to the sum of the output power of each individual oscillator ($\mathrm{P_1}$ for $\mathrm{STVO_1}$ and $\mathrm{P_2}$ for $\mathrm{STVO_2}$). (c) The instantaneous phase difference ($\Delta\Psi$) is presented as a function of time for $\mathrm{I_{FL}} = 22\mathrm{mA}$. Two channels of the oscilloscope were used to save the time traces of each STVO.

possible synchronization mechanism, which can only be individually evaluated when the magneto-dipolar coupling is minimized. To do that, a pair of STVOs with an edge-to-edge distance of 1 μm was also studied. This comparison is adequate, since one expects a significant decrease of the magneto-dipolar coupling from 100 nm to 1 μm [202]. Figure 6.15 shows the dynamics for each individual STVO (Fig. 6.15a for $\mathrm{STVO_1}$ and Fig. 6.15b for $\mathrm{STVO_2}$) and for their combination (Fig. 6.15c), using the spectrum analyser and the power combiner illustrated in Fig. 6.11. There is a clear difference in this analysis. Instead of merging the dynamics by sweeping the DC current of one of the oscillators, as performed in Fig. 6.13a, the DC current passing through each nanopillar was kept constant and the integrated field line was used to apply a common in-plane magnetic field according to the MTJ easy axis. Thus, the two dynamics can be manipulated and eventually merged, as illustrated in Fig. 6.15c for a DC current applied to the field line ($\mathrm{I_{FL}}$) ranging from 22 mA to 30 mA. The field line is used when the STVO dynamics are very different from each other, to a degree that sweeping the MTJ bias current is not enough to merge the dynamics. Typically, the field line endures a DC current up to $\sim$ 130 mA, allowing the sweeping of the STVOs frequency over a larger bandwidth. As already emphasized, the MTJ breakdown voltage limits the DC current that can be applied to sweep the frequency of each

oscillator. Both STVOs show a complex dependence of their frequency on the in-plane field, to which an undetermined in-plane field applied by the electromagnet also contributes (i.e. the rotation of the electromagnet is performed manually, meaning that a small in-plane magnetic field component coming from it is difficult to avoid).

Figures 6.16a-b show the linewidth and output power calculated at the $\mathrm{I_{FL}}$ range where the oscillators show dynamics at the same frequency (see Fig. 6.15c). The parameters are calculated not only for the combined dynamics, but also for the individual oscillation of each STVO. The results show that, although oscillating at the same frequency, the combined dynamics does not show an improvement of the spectral purity and output power (see blue curves in Figs. 6.16a-b). In particular, the calculation of the output power (Fig. 6.16b) clearly indicates that the values calculated for the combined oscillation (blue curve) are roughly the same as the sum of the powers of the two individual oscillations (orange dashed curve). The existence of two unsynchronized STVOs is finally verified with the calculation of the phase difference $\Delta\Psi$ that diverges in time, for a fixed $\mathrm{I_{FL}} = 22\mathrm{mA}$ (Fig. 6.16c). These results sustain the main contribution of the magneto-dipolar coupling for a successful synchronization in these devices. In fact, mutual electric synchronization requires a strong electric coupling, normally achieved for STVOs with a large emission (i.e. output power of $\sim 1\ \mu$W) [31, 32] to minimize the thermal disturbances and to overcome the frequency detuning of different oscillators.

6.3.4 Second harmonic injection locking with coupled STVOs

In addition to the experimental verification of the STVO synchronization, one last analysis comprised the possibility to use dipolar coupled STVOs for unconventional computing. A notable motivation is given by the work of Albertsson *et al.*, where it is numerically shown that coupled STNOs can be implemented as hardware for an Ising machine, able to solve combinatorial optimization problems [193]. The problem solution is found when the dynamics of a second harmonic injection locked network of coupled STNOs is stabilized in time. From a theoretical point of view, the solution corresponds to the minimization of the Ising Hamiltonian, given by

$$H = -\sum_{k,l}^{N} J_{kl} s_k s_l - h \sum_{k}^{N} s_k, \tag{6.8}$$

where N represents the number of spins in the network, $\mathrm{s_k}$ the spin state (+1 or -1) of spin k and $\mathrm{J_{kl}}$ the coupling strength between spins k and l. The rightmost term is the Zeeman interaction between the spins and the effective magnetic field h that is assumed to be constant over the network. In this context, each $\mathrm{s_k}$ corresponds to the locking state between the $\mathrm{STNO_k}$ of the network and the external signal. An injection RF signal at twice the natural frequency of the STNO leads to a binary scheme with two available locking states over one period of the STNO oscillation [201, 206], corresponding to the +1 and -1 spin states defined in Eq. (6.8). The distinction between states is achieved measuring the phase evolution in time of each STNO. For instance, if two STNO are locked in different states, the phase difference between them over one period should be π. So, while finding its minimum to a scheduled second harmonic injection locking (SHIL), the coupled network allows to its constitutive STNOs to change their locking state until the solution is found.

The second harmonic injection can be easily implemented with the setup of Fig. 6.11, using the integrated field line to apply an RF signal with twice the frequency of the coupled STVOs. Here, the

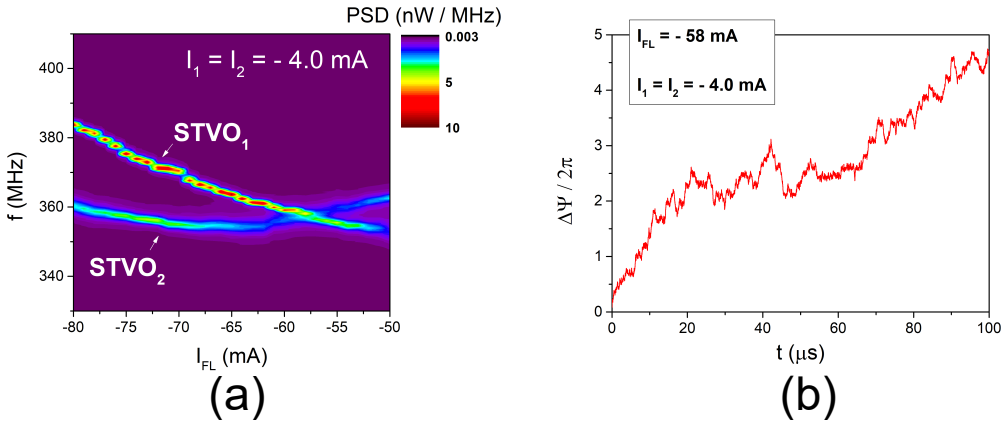


Figure 6.17: Power spectral density (PSD) measured for two STVOs ($\mathrm{STVO_1}$ and $\mathrm{STVO_2}$) 400 nm apart, as a function of the DC current $\mathrm{I_{FL}}$ passing through the field line. The measurement is performed for $\mathrm{I_1 = I_2 = -4.0 mA}$. (b) The instantaneous phase difference ($\Delta\Psi$) is presented as a function of time for $\mathrm{I_{FL} = -58\,mA}$. Two channels of the oscilloscope were used to save the time traces of each STVO. A perpendicular magnetic field of 5.6 kOe was applied during the measurements.

aim is to study the second harmonic injection locking (SHIL) of two dipolar coupled STVOs. Unfortunately, at this stage of the experiment, it was only possible to find a pair of functional STVOs with a functional field line for an edge-to-edge distance of 400 nm. For instance, the synchronized pair with an edge-to-edge distance of 100 nm shown in section 6.3.3 was functional, but the field line was not available for the task (i.e. destroyed by Joule heating).

Figure 6.17a shows the power spectral density (PSD) of an STVO pair ($\mathrm{STVO_1}$ and $\mathrm{STVO_2}$) with an edge-to-edge distance of 400 nm, as a function of the DC current applied through the field line ($\mathrm{I_{FL}}$). Again, the field line was used to tune the dynamics, because the STVO frequencies were very different to be merged with the DC bias current. Although showing a PSD in the same order of magnitude of the results shown for an edge-to-edge distance of 100 nm (see Fig. 6.13a), a successful synchronization is not achieved. The STVO pair is frequency tuned for $\mathrm{I_{FL} = -58\,mA}$, but Fig. 6.17b shows that $\Delta\Psi$ diverges in time. Nevertheless, the phase is more stable when compared with the results obtained for an edge-to-edge distance of 1 μm (Fig. 6.16c). So, the results suggest that the dipolar coupling is still relevant for an edge-to-edge distance of 400 nm, but not enough for an effective synchronization. So, in these conditions, the SHIL was studied for these two weakly coupled STVOs.

Figure 6.18 shows the spectra obtained for the weakly coupled STVOs, as a function of the frequency of the RF signal applied to the field line ($\mathrm{f_{SH}}$). This analysis is performed for individual ($\mathrm{STVO_1}$ in Fig. 6.18a for $\mathrm{I_1 = -4.0\,mA}$ and $\mathrm{I_2 = 0.0\,mA}$; $\mathrm{STVO_2}$ in Fig. 6.18b for $\mathrm{I_1 = 0.0\,mA}$ and $\mathrm{I_2 = -4.0\,mA}$) and simultaneous frequency tuned (Fig. 6.18c for $\mathrm{I_1 = I_2 = -4.0\,mA}$) oscillations. Regarding the setpoints, the frequency tuned dynamics are achieved for $\mathrm{I_{FL} = -66\,mA}$, which is different from the results shown in Fig. 6.17a, where the frequency tuning is achieved for $\mathrm{I_{FL} = -58\,mA}$. This discrepancy appears because, between the data acquisition of Fig. 6.17 and Fig. 6.18, the electro-

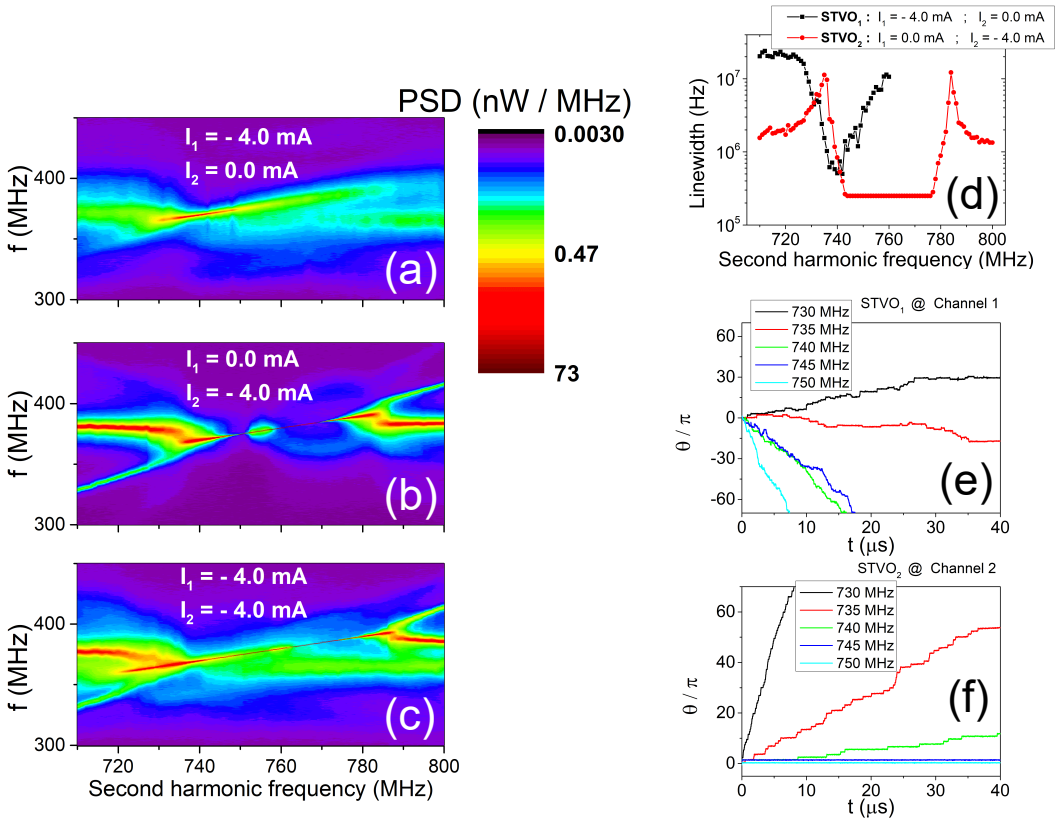


Figure 6.18: (a)-(c) Power spectral density (PSD) measured for two STVOs ($\mathrm{STVO_1}$ and $\mathrm{STVO_2}$) 400 nm apart, as a function of the RF field frequency $\mathrm{f_{SH}}$ applied through the field line with a constant power of 10 mW. The spectra are measured for three different conditions of the DC bias current: (a) $\mathrm{I_1 = -4.0\,mA}$ applied to $\mathrm{STVO_1}$ only, (b) $\mathrm{I_2 = -4.0\,mA}$ applied to $\mathrm{STVO_2}$ only and (c) $\mathrm{I_1 = I_2 = -4.0\,mA}$ applied to both $\mathrm{STVO_1}$ and $\mathrm{STVO_2}$. (d) The linewidth of the locked state is calculated as a function of $\mathrm{f_{SH}}$ for the conditions presented in (a) and (b). (e)-(f) The phase deviation θ translating the locking between each STVO and the external RF field is presented for different values of $\mathrm{f_{SH}}$, considering the conditions in (c). Throughout these measurements, a DC current of -66 mA in the field line and a perpendicular field of 5.6 kOe were applied.

magnet was rotated, so the perpendicular field was similar but not the same in both analyses, which led to the readjustment of the $\mathrm{I_{FL}}$ setpoint for frequency merging. Regarding the individual locking, the STVOs show different behaviours that can be verified in the calculation of the locked state linewidth (Fig. 6.18d). $\mathrm{STVO_2}$ shows an efficient SHIL, characterized by a linewidth of 250 kHz (limited by the resolution bandwidth chosen for the spectrum analyser) between 744 MHz and 776 MHz. On the other hand, $\mathrm{STVO_1}$ shows a poorer spectral quality of its forced oscillation and a much smaller locking range, with a minimum linewidth of 499 kHz for $\mathrm{f_{SH} = 742\,MHz}$. These results are justified by the

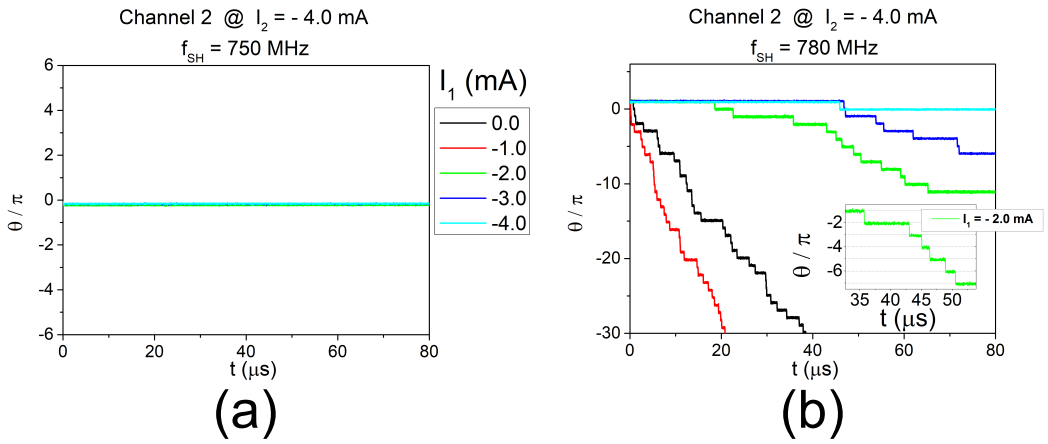


Figure 6.19: The phase deviation θ between $\mathrm{STVO_2}$ and the second harmonic is calculated for different values of the bias DC current $\mathrm{I_1}$ applied to $\mathrm{STVO_1}$. The DC current applied to $\mathrm{STVO_2}$ is constant ($\mathrm{I_2} = -4.0\,\mathrm{mA}$). The results are calculated for two different frequencies of the external RF field: (a) $\mathrm{f_{SH}} = 750\,\mathrm{MHz}$ and (b) $\mathrm{f_{SH}} = 780\,\mathrm{MHz}$. The inset highlights the magnitude of the phase slips.

different spectral purities presented by each STVO before locking. From Fig. 6.18d, it is clear that, before locking ($\mathrm{f_{SH}} < 720\,\mathrm{MHz}$), the two oscillators show very different linewidths, which will naturally play a role in the ability of the oscillator to lock with the external RF field. These results are in accordance with the work of Hamadeh *et al.*, where it is demonstrated that the locking quality (i.e. linewidth of the locked state and locking range) of an STVO to an external RF field depends on the spectral coherence of its free-running oscillation [207]. So, the larger linewidth presented by $\mathrm{STVO_1}$ naturally leads to a poorer locking.

When both STVOs are oscillating, the locking is more complex, since the spectra shown in Fig. 6.18c includes the dynamics of both oscillators. So, an alternative is to look at the time domain using two individual channels of the oscilloscope, as illustrated in Fig. 6.11. For a perfect SHIL, the phase deviation $\theta(\mathrm{t}) = \Psi(\mathrm{t}) - 2\pi\mathrm{ft}$ must be constant over time, being $\Psi(\mathrm{t})$ the phase evolution of the oscillator and f its frequency [201]. Figures 6.18e-f show θ calculated for $\mathrm{STVO_1}$ and $\mathrm{STVO_2}$, respectively, at different frequencies of the locking RF field. Qualitatively, the results show no difference when compared with the locking seen in Figs. 6.18a-b. Again, $\mathrm{STVO_2}$ locks perfectly with the external RF signal, starting at $\mathrm{f_{SH}} = 745\,\mathrm{MHz}$ (see Fig. 6.18f), whereas $\mathrm{STVO_1}$ never shows a constant θ without phase slips (see Fig. 6.18e).

After understanding the behaviour of each STVO to the second harmonic injection, it is important to investigate how the dipolar coupling affects the locking. The coupling strength between STVOs can be controlled by the DC bias current, so a possible experiment comprises the sweeping of the DC bias current for one STVO and simultaneously analyse how this variation affects the SHIL of the other. This idea is illustrated in Fig. 6.19, showing θ associated with $\mathrm{STVO_2}$, as a function of the DC bias current applied to $\mathrm{STVO_1}$ ($\mathrm{I_1}$). This analysis is performed for two distinct setpoints: (i) at $\mathrm{f_{SH}} = 750\,\mathrm{MHz}$, inside of the $\mathrm{STVO_2}$ locking range (Fig. 6.19a) and (ii) at $\mathrm{f_{SH}} = 780\,\mathrm{MHz}$, on the edge

of the $\mathrm{STVO_2}$ locking range (Fig. 6.19b). When $\mathrm{STVO_2}$ is locked to an external RF signal with a frequency $\mathrm{f_{SH}} = 750\,\mathrm{MHz}$, Fig. 6.19a shows that the weak dipolar interaction coming from the $\mathrm{STVO_1}$ has no influence in the locking state. On the other hand, for $\mathrm{f_{SH}} = 780\,\mathrm{MHz}$, $\mathrm{STVO_2}$ is on the edge of the locking range, so that the conditions are not suitable for a perfect locking and θ diverges in time with phase slips (black line in Fig. 6.19b), making it more susceptible to be perturbed by the dipolar interaction coming from $\mathrm{STVO_1}$. The inset highlights the magnitude of the phase slips associated with the SHIL. In fact, for an external RF field with a frequency $\mathrm{f_H} = \mathrm{q f_0}$ that locks to an oscillator with a frequency $\mathrm{f_0}$, the unlocking-locking events are associated with phase slips with an amplitude of $2\pi/\mathrm{q}$ [201]. Considering that $\mathrm{STVO_2}$ is locking to its second harmonic, as already emphasized, one obtains two locking states over one period, so phase slips with an amplitude of π. As the intensity of $\mathrm{I_1}$ increases, it becomes clear that the dynamics of $\mathrm{STVO_1}$ influence the locking of $\mathrm{STVO_2}$, making it more robust with an almost perfect SHIL for $\mathrm{I_1} = -4.0\,\mathrm{mA}$ (see light blue line in Fig. 6.19b). In fact, the setpoints were defined, so that both STVOs oscillate at the same frequency for $\mathrm{I_1} = \mathrm{I_2} = -4.0\,\mathrm{mA}$. Sweeping $\mathrm{I_1}$ changes the coupling between oscillators, which can lead to a variation of the $\mathrm{STVO_2}$ dynamics and of its locking range with the external signal. Romera *et al.* have shown that the locking range between an STVO and an external RF signal can be modified when the first is electrically coupled to a second STVO [208]. Naturally, this modification is easier to identify when measuring the locking capabilities on the edge of the locking range, as it happens in Fig. 6.19b.

6.4 Conclusion

A new nanofabrication design was successfully implemented for the synchronization of an STVO pair with an edge-to-edge distance of 100 nm, via magneto-dipolar coupling. Each nanopillar is electrically connected with an independent top contact (ITC), allowing a direct access to its individual phase. This time domain analysis proved to be more accurate than a frequency domain analysis in defining the range at which a stable synchronization is achieved. The major contribution of the magneto-dipolar coupling over the electric coupling was clarified with an unsuccessful attempt to synchronize a pair of STVOs with an edge-to-edge distance of 1 μm. So, these results suggest that the magneto-dipolar coupling is a viable synchronization method even for STVOs showing a small emission (nW range).

With the same ITC scheme, it was also demonstrated that the dipolar interaction can tune the second harmonic injection locking (SHIL) between the STVOs and an external RF field applied through the integrated field line. For an STVO pair with an edge-to-edge distance of 400 nm, it was shown that the SHIL of the first oscillator can be controlled by the dynamics of the second. It should be clarified that these results show limitations and leave plenty of room for improvement. First, the SHIL was not performed to a pair of synchronized STVOs since, due to the large edge-to-edge distance of 400 nm, they are weakly coupled. Second, due to the poor spectral coherence, a perfect SHIL could only be achieved for one of the STVOs (the other was just too noisy for the purpose).

Chapter 7

Fabrication of spin torque vortex oscillators on top of $\mathrm{SiN_X}$ membranes

Alongside with the main objectives of this thesis, an important fabrication process was developed for spin torque vortex oscillators (STVOs). Specifically, the aim was to fabricate STVOs on top of 300 nm-thick $\mathrm{SiN_x}$ membranes, working as windows for X-ray imaging of the free layer vortex state. This means that the fabrication was performed in a double-side polished wafer, in this way comprising, not only the wafer frontside patterning (as described in chapter 3), but also the fabrication of the $\mathrm{SiN_x}$ membranes on the backside.

7.1 Vortex imaging by transmission X-ray microscopy

Since the first experiments in magnetic materials with a vortex state, imaging techniques have contributed to understand its magnetic properties. Major examples include vortex observation by magnetic force microscopy [77], spin-polarized scanning tunneling microscopy [209, 210] and scanning transmission X-ray microscopy (STXM) [211–216]. Particularly, STXM is a widely used technique for vortex imaging, typically showing spatial resolutions of $\sim$30 nm and temporal resolutions of $\sim$70 ps [215], based on the STXM setup from the beam line 11.0.2 at the Advanced Light Source in Berkeley. This probing performance is specially important to understand the vortex dynamics, namely by presenting space and time-resolved images of the DC bias-induced steady-state oscillation of the vortex gyrotropic mode [215].

The image contrast obtained in STXM comes from the X-ray magnetic circular dichroism (XMCD). By definition, a material shows dichroism when its light absorption spectrum depends on the light polarization. This means that a magnetic material shows XMCD because its X-ray absorption spectrum depends if the incident X-rays have a left or right circular polarization. Based on this effect, the spatial magnetic contrast can be computed from [217]

$$I_N(x,y) = \frac{I^+(x,y) - I^-(x,y)}{I^+(x,y) + I^-(x,y)}, \tag{7.1}$$

where $\mathrm{I^+(x,y)}$ [$\mathrm{I^-(x,y)}$] is the transmitted X-ray intensity for right (left) circularly polarized light. Also,

the (x, y) coordinates correspond to the position in the magnetic material where the X-ray analysis is being performed. $\mathrm{I_N(x,y)}$ is given by the normalized difference between the two different intensities $\mathrm{I^+(x,y)}$ and $\mathrm{I^-(x,y)}$. Although being different, both intensities are affected in the same amount by topographic and chemical properties of the magnetic material, so the difference in Eq. (7.1) allows to cancel all the non-magnetic contrast contributions that are equally observed for both light polarities, ending up with $\mathrm{I_N(x,y)}$ that is fully dependent on the magnetic dichroism. Moreover, $\mathrm{I_N(x,y)}$ is proportional to the dot product $\mathbf{m}\cdot\mathbf{k}$, being $\mathbf{m}$ the normalized magnetization vector and $\mathbf{k}$ the X-ray propagation direction [211]. This means that the X-ray incidence angle needs to be tuned, depending on how one wants to visualize the vortex. For instance, if the sample surface is perpendicular to the X-ray propagation, the measurement will be sensible to the vortex core, so a large contrast is expected between the core region ($|\mathbf{m}\cdot\mathbf{k}|\sim 1$) and the in-plane curled magnetization region ($\mathbf{m}\cdot\mathbf{k}\sim 0$). On the other hand, as one starts to tilt the X-ray incidence angle, so that $\mathbf{0} < |\mathbf{m}\cdot\mathbf{k}| < \mathbf{1}$, the measurement starts to be sensible to the in-plane magnetic moments, which makes it possible, for instance, to identify the vortex chirality [216].

Here, the objective is to fabricate STVOs ready to be probed by STXM. For that purpose, the backside of the Si substrate needs to be completely removed, in order to give optical access to the MTJ device, placed on top of 300 nm-thick transparent $\mathrm{SiN_x}$ membranes [213, 215]. Moreover, the membrane design will allow a maximum angle of 45° between the X-ray propagation direction and the direction perpendicular to the substrate surface, in this way giving the STXM the possibility to be sensible also to the in-plane vortex magnetization. After fabrication, these samples were sent and independently tested in the Swiss Light Source (SLS) synchrotron at the Paul Scherrer Institute (PSI), as a result of the partnership between INL and two research centers: the “Unite Mixte de Physique CNRS/Thales” in France and PSI in Switzerland.

7.2 Geometries

Figure 7.1 shows optical microscope images of the three contact geometries fabricated on top of membranes, after process. All the designs present a four-contact configuration to a single MTJ device, along with a field line for local manipulation of the vortex state (each design was fabricated with and without the field line, in case its X-ray absorption affects the STXM). On top, each image shows the frontside patterning for each design. The images also make evident the existence of an oval-shaped black area at the central region of each design, where the MTJ device is fabricated. The black region corresponds to the $\mathrm{SiN_x}$ membrane, meaning that all the materials fabricated on top of it (including the MTJ device) are suspended on the 300 nm-thick transparent substrate of $\mathrm{SiN_x}$. Due to the transparency of the membrane, it is also possible to visualize each design from the backside of the substrate. On the bottom of Fig. 7.1, optical microscope images show the backside of each design at the membranes region, in this way proving the optical access to the MTJ device from the backside of the substrate.

There is not a perfect design, so the option was to fabricate three different types with their intrinsic advantages and disadvantages. The objective of type 1 is to fabricate contact pads at a safety distance from the membrane, so that the membrane does not collapse easily when establishing contact (e.g. wire bonding, micro-sized tips) with the MTJ device. Due to the size of the contacts, the two main disadvantages are the larger contact resistance and the larger leakage current to the substrate.

These two disadvantages are minimized with type 2, where the contacts are much smaller and closer to the membrane. Here, the main disadvantage is obviously a larger probability of destroying the membrane while establishing contact with the nanopillar. Type 3 is an intermediate solution between type 1 and type 2.

7.3 Fabrication steps

7.3.1 Substrate preparation

This process comprises patterning steps for both sides of the wafer, so 200 mm Si double-side polished wafers were used as substrates. The process starts with the deposition of 3 μm of SiO_2 by PECVD (section 2.2) on the backside of the substrate. This oxide layer will then by used to fabricate an hard mask that will allow the membrane definition. Then, on the frontside, a 50 SiO_2 / 300 SiN_x stack is also deposited by PECVD (thickness in nanometers). The SiN_x layer will be used as the transparent substrate for the membrane, whereas the SiO_2 layer is deposited as a safety procedure. The membrane definition is achieved by fully etching the silicon of the original substrate up to the SiN_x membrane layer. In order to avoid an overetch of the SiN_x layer, the thin SiO_2 is deposited as a sacrificial layer.

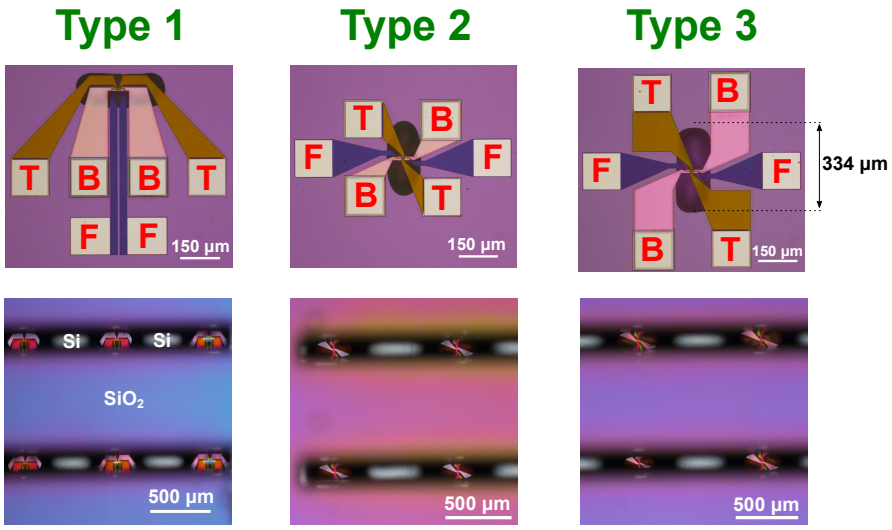


Figure 7.1: Optical microscope images showing the three design types fabricated on top of SiN_x membranes. Both frontside and backside images of each design are shown on top and on the bottom of the figure, respectively. The contact pads refer to the bottom contact (B), top contact (T) and field line (F). On the bottom left side, the main regions are labelled with the backside materials: the 200 μm Si step between consecutive membrane windows and the remaining SiO_2 outside the membrane regions, where the patterning is not performed. As an example, the membrane length is measured for type 3.

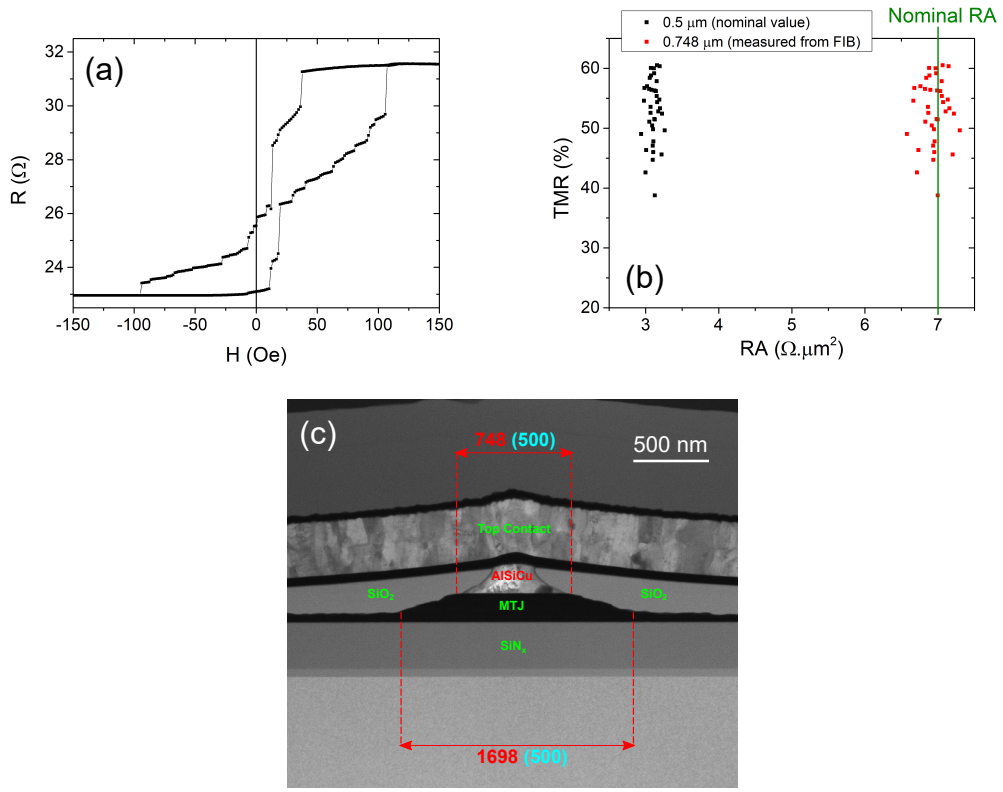


Figure 7.2: (a) R-H loop of an MTJ device with a nominal diameter of 500 nm. The measurement is obtained by applying a DC current of 1.0 mA. (b) Statistical analysis of 38 identical devices, comparing the TMR ratio as a function of the RA product, when the latter is calculated based on the nominal area of the pillar (black scatter) or based in the FIB image (red scatter). (c) SEM image showing the cross section of an STVO after a FIB cut. The MTJ diameter is measured in the bottom contact and on top of the pillar cap (distance in nanometers) and each value is compared with the nominal MTJ diameter of 500 nm. Here, all the MTJs are chosen from the wafer that includes the devices fabricated on top of membranes.

7.3.2 Frontside patterning

The new substrate is used for the deposition of a 5 Ta / 50 CuN / 5 Ru / 50 CuN / 5 Ru / 6 IrMn / 2 $\mathrm{CoFe_{30}}$ / 0.7 Ru / 2.6 $\mathrm{CoFe_{40}B_{20}}$ / MgO ($7\,\Omega\mu\mathrm{m}^2$) / 6.0 $\mathrm{FeB_{20}}$ / 3 Ta / 30 CuN / 7 Ru MTJ stack (thickness in nanometers). The MTJ devices were patterned into circular nanopillars, with a diameter ranging from 300 nm to 600 nm. The free layer is constituted by FeB with a thickness of 6 nm that, considering the chosen diameters, allows an aspect ratio for an induced magnetic vortex at the remanent state. In this context, the choice of FeB as the free layer (requested by our partners) is justified by the increasing interest of this material, with reports showing interesting results in CoFeB/MgO/FeB-based MTJs working as spin torque vortex oscillators [32, 33] and rectifiers [41]. The patterning process

applied to the frontside is in accordance with the description shown in section 3.2.

Along with the membrane fabrication, a fraction of each die was reserved to fabricate MTJ devices with standard geometries (two-contact and four-contact designs, as described in section 3.1) to be measured in our lab setup. Figure 7.2a shows an R-H loop of one of those devices, with a nominal diameter of 500 nm and a two-contact geometry, that clearly demonstrates the existence of a vortex magnetic state in the free layer. Considering the nominal RA product of $7\,\Omega\mu\mathrm{m}^2$, the MTJ resistance shown in Fig. 7.2a is lower than expected (systematically seen for all diameters). These results are confirmed by the magnetoresistive measurements performed in the semi-automatic prober (section 2.6.4) and shown in Fig. 7.2b (black scatter), for identical MTJ devices with a diameter of 500 nm and a four-contact geometry. When the nominal diameter is taken as a reference to calculate the RA product, the values clearly differ from the nominal RA product, in this way showing an RA $\sim 3\,\Omega\mu\mathrm{m}^2$. To check if there is a connection between the electric results and the MTJ profile, Fig. 7.2c shows the cross section of an MTJ device, after a focused ion beam (FIB) cut. This image was already shown in Fig. 3.5b of section 3.2.4, where the optimal conditions for pillar definition are discussed. For this wafer, the deposition of a too thick sacrificial structure (500 nm of AlSiCu) and the pillar definition at 130° lead to a very poor MTJ profile (during the fabrication of this wafer, the optimization of the pillar definition was still an ongoing process). The result is an increase of the MTJ diameter, from the sacrificial structure (748 nm) to the bottom contact (1698 nm), meaning that the effective diameter at the MgO barrier is much larger than the nominal value (in this case, 500 nm). If the diameters measured from the FIB cut are used in the RA calculation, the results start to approach to the expected values. In Fig. 7.2b (red scatter), when the RA product is calculated admitting that the MTJ diameter is the value measured from the FIB cut on top of the pillar cap (i.e. 748 nm), the results become in accordance with the nominal RA product. It should be emphasized that these results are an approximation, because the MgO barrier is some nanometers below the top of the pillar cap.

7.3.3 Backside patterning: membrane definition

Backside alignment

The membrane fabrication implies a backside alignment to center the $\mathrm{SiN_x}$ windows with each individual MTJ device. This step is performed in a Suss MA6 BA6 mask aligner with bottom view optics and image frame grabbing capabilities. To begin with, the chromium mask used to define the first alignment marks on the backside is inserted into the mask aligner. Then, both bottom view microscopes (i.e. left side and right side microscopes) are moved to align the two marks, 20 mm apart, that constitute the mask (the shape of each mark is illustrated on the left side of Fig. 7.3a). Finally, the position of the alignment marks is saved on the screen by using the "grab image" capability of the tool.

After fixing the position of the backside alignment marks, the wafer being processed is loaded into the chuck of the mask aligner with the frontside facing the bottom view optics (see Fig. 7.3b). Then, without moving the back side microscope, the chuck is moved in order to align the grabbed alignment marks on the screen with a pair of compatible alignment marks previously defined during the frontside patterning (the chuck is open in the middle region, in this way allowing the visualization of the frontside by the bottom view microscopes). The shape of each alignment mark defined on the frontside is depicted on the right side of Fig. 7.3a. When this step is successfully achieved, the

exposure is performed, with the coated backside (2.2 μm of AZP4110 photoresist) being exposed through the chromium mask. The exposure conditions are in accordance with standard parameters, resulting from periodic optimizations.

Hard mask definition

The 3 μm layer of SiO_2 deposited on the backside of the substrate is used to fabricate an hard mask from which the membranes are patterned. Figure 7.4 shows the steps until reaching the final hard mask, which comprises two optical lithographies at DWL.

For the first lithography, the 2.2 μm of AZP4110 from the backside alignment is reused to define the first step of the hard mask. By ion beam milling, the oxide is removed to a safety thickness of $\sim$800 nm (Fig. 7.4b), whose aim will be discussed later. In this case, the removed oxide thickness

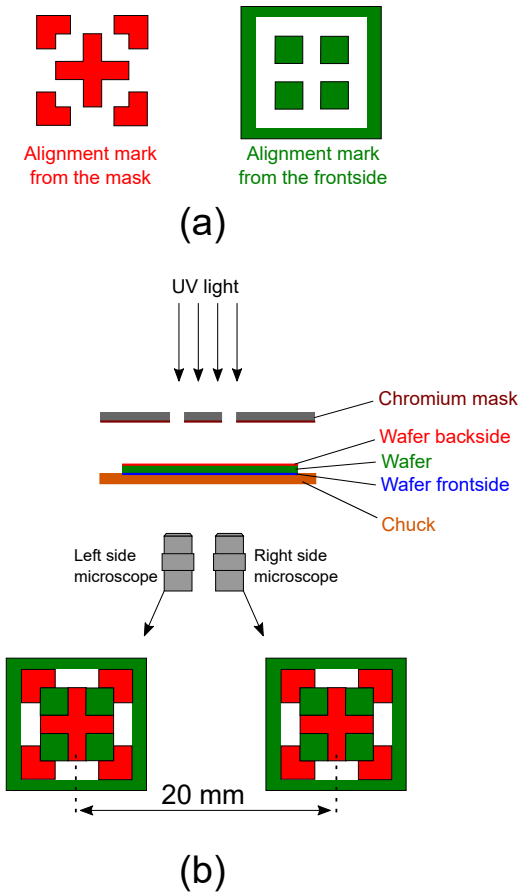


Figure 7.3: (a) Illustration of the marks used for the backside alignment. (b) Simple sketch of the final setup used for the backside alignment. On the bottom, the perfect overlap between the frontside marks (in red) and the screen saved backside marks (in green) represents the configuration that one should see from the bottom view microscopes for a successfully aligned backside exposure.

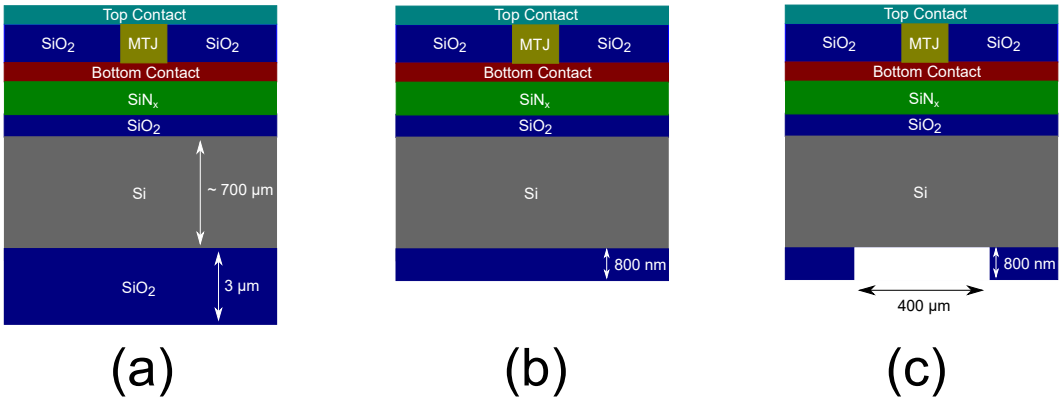


Figure 7.4: Illustrations of the substrate cross section, showing the different steps towards the hard mask definition. Substrate after (a) the backside alignment, (b) the first optical lithography and (c) the second optical lithography. For clarity, the images are not at scale.

is significant, which explains the use of a thicker photoresist. The thickness of $\mathrm{SiO_2}$ is measured in Nanocalc (section 2.6.1) by using regions with a larger area, defined at the same lithographic level as the hard mask. Finally, a second lithography, now with a coating of 1.035 μm of the standard AZ1505, allows to fully remove the oxide in the region below the MTJ device, where the $\mathrm{SiN_x}$ membrane will be defined with a length of 400 μm (Fig. 7.4c).

Silicon substrate removal

Now that the hard mask is defined, it is possible to attend the specific requirements to fabricate the membrane. The most important one is to guarantee a maximum incidence angle of 45° between the X-ray propagation direction and the normal to the membrane surface. Considering that the membrane has a length of 400 μm and the nanopillar is placed at the center, the step between the membrane and the Si substrate needs to have a length of 200 μm (see Fig. 7.5c). So, the process starts by etching 200 μm of Si at the membrane region (Fig. 7.5a). This step is achieved in a SPTS Pegasus tool that performs a deep reactive ion etching process, called the "Bosch Process" [218], that allows the anisotropic etching of Si, with features showing a high aspect ratio. Considering that the etching rate of $\mathrm{SiO_2}$ is $\sim$0.2 % of the etching rate of Si, the hard mask is thick enough to endure this step, ending up with a $\mathrm{SiO_2}$ thickness of $\sim$400 nm.

After the definition of the Si step, the hard mask stops to be useful and must be removed in the membrane regions (Fig. 7.5b). The removal of the remaining oxide is achieved in a SPTS APS tool, which is a $\mathrm{SiO_2}$ etcher, in this way giving an acceptable selectivity between the significant removal of $\mathrm{SiO_2}$ and the neglected removal of the Si substrate (i.e. the Si step of 200 μm is basically unchanged after the oxide etching).

Finally, the SPTS Pegasus tool is used for a second time to remove all the Si substrate up to the oxide below the nanopillar (Fig. 7.5c). Considering the anisotropic nature of the etching process, the

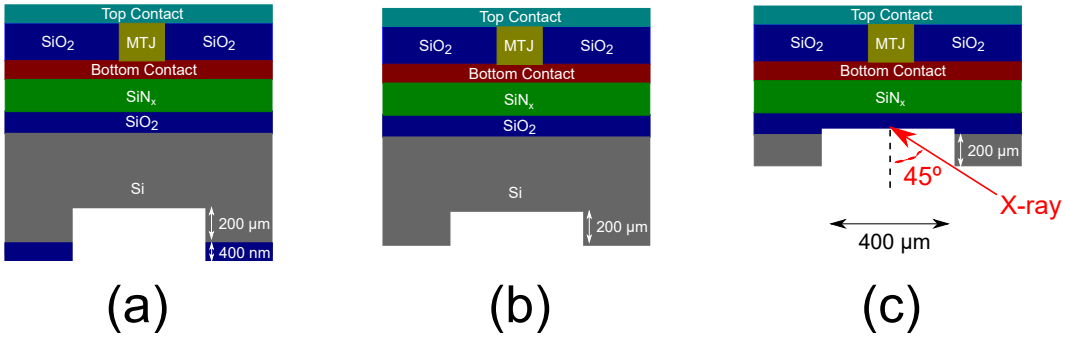


Figure 7.5: Illustrations of the substrate cross section, showing the different steps towards the membrane definition. Substrate after (a) the Si step definition, (b) the hard mask removal and (c) the substrate removal up to the membrane. (c) also illustrates the 200 μm Si step required for a maximum X-ray incidence angle of 45°. For clarity, the images are not at scale.

profile of the Si step should be maintained. The thin $\mathrm{SiO_2}$ layer is used as the stopping point, when it is already possible to see the MTJ device from the backside of the wafer. As shown in the bottom of Fig. 7.1, the process offers individual MTJ devices suspended in $\sim$300 nm-thick membranes, with a 200 μm step of Si substrate between consecutive devices. The oval shape of the $\mathrm{SiN_x}$ windows indicates that the Si etching rate decreases from the center to the wall of the membrane. In the end, as depicted for type 3 in Fig. 7.1, the membranes show an effective length smaller than the nominal value of 400 μm, which decreases the angle range for STXM analysis. Also, the etching process is not uniform over the full wafer, meaning that the process is finished still with some closed membranes (if the process is continued to open these membranes, there is the risk of destroying the ones that are already open). Each die patterned in the frontside of the wafer (constituted by 150 MTJ devices - 50 of each type) shows a yield of $\sim$50%, meaning that, roughly, half of the membranes are open after process. It should be emphasized that outside the membrane regions, where the hard mask definition was not performed, the Si substrate is intact, protected by the initial 3 μm layer of $\mathrm{SiO_2}$. These regions are fundamental for the membrane process, because they give structural support to the wafer. Also, they are a reference surface level to control the thickness of Si removed during the last etching step (Fig. 7.5c). That etching control was performed using the optical profilometer capability of Nanocalc (section 2.6.1).

7.4 Discussion and conclusion

After process, the samples were sent to be probed at the Swiss Light Source (SLS) synchrotron. It was possible to visualize the static vortex state in the free layer, mainly by means of the in-plane magnetization contrast (Fig. 7.6a), obtained by the possibility to sweep the X-ray angle from the perpendicular direction. Nevertheless, the vortex dynamics could not be visualized, since during the STXM experiment, a steady-state oscillation of the gyrotropic mode could not be achieved. At

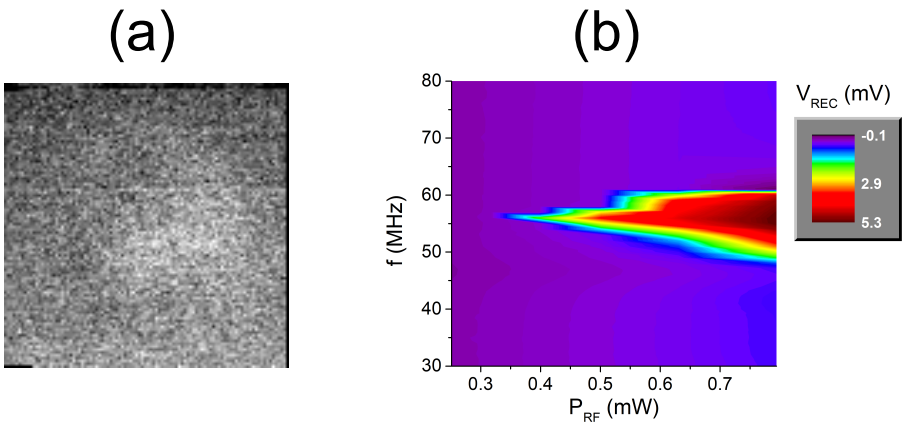


Figure 7.6: (a) STXM image obtained from an STVO fabricated on top of a 300 nm-thick $\mathrm{SiN_x}$ membrane. Courtesy of the "Unite Mixte de Physique CNRS/Thales" center. (b) Spin diode measurements obtained for an MTJ device with a nominal diameter of 600 nm. The measurements are obtained at zero external magnetic field.

INL, spin diode measurements were performed in MTJ devices fabricated in the same wafer (the experimental setup is the same of Fig. 4.7b). Figure Fig. 7.6b shows the rectified voltage measured as a function of the frequency and power of the input RF signal for an MTJ device with a nominal diameter of 600 nm. Considering the significant difference between the nominal and the effective diameter, the rectified voltage is presented as a function of the RF power instead of the RF current density. The resonance frequency is quite low, which again proves the smaller aspect ratio of the free layer coming from the larger effective diameter. For a diameter of 600 nm and a FeB saturation magnetization of $1.289 \times 10^6\,\mathrm{A/m}$ (see Table 2.7), theory predicts a frequency of $\sim 160\,\mathrm{MHz}$ [83]. At SLS, the experimental setup did not allow a continuous frequency sweep of the input RF signal, so no spin diode measurements were performed during STXM. On the other hand, our partners have corroborated the good optical properties of the membranes, as shown in Fig. 7.1.

The poor MTJ profile (i.e. unknown pillar diameter) makes it difficult to compare the performance of these FeB-based STVOs with our standard CoFeB/NiFe-based STVOs. For instance, the critical RF current density for spin diode resonance is a parameter particularly relevant in chapter 4 for the development of an artificial synapse. Nowadays, the pillar definition is optimized at an angle of 110°, so an MTJ profile as presented Fig. 3.5d is expected for future samples.

To conclude, a new fabrication process was developed at INL for the backside processing of Si substrates with patterned spin torque vortex oscillators (STVOs). After process, each STVO can be described as a single MTJ nanopillar suspended in a 300 nm-thick $\mathrm{SiN_x}$ membrane. At the wafer level, the backside process shows a yield of $\sim$50%, with open membranes, so that $45° < \theta \leq 90°$, being θ

the angle between the X-ray propagation direction and the membrane surface.

Chapter 8

Conclusion and outlook

This thesis presents a detailed description of the fabrication and the wide range electric characterization of spin torque vortex oscillators (STVOs) in MgO-based magnetic tunnel junction (MTJ) stacks. In the following, one pretends to summarize the main conclusions and present an outlook for the future.

1. The rectification measurements performed in STVOs were fundamental to perform two main experimental studies. The first is clearly motivated by the emergent field of Neuromorphic Spintronics, where a better understanding and control of the physical properties of spintronic devices have led to the already proved assumption that their integration as neuromorphic computing hardware is a reality [42]. Our results allow to draw the following conclusions:

   - The rectification output shows a direct dependence on the vortex chirality. Experimentally, this is demonstrated by spin diode measurements, where different chiralities lead to two distinct lineshapes of the voltage spectrum. In sum, the vortex chirality breaks the symmetry of the RF detection.
   - Micromagnetic simulations have clarified the origin of the symmetry breaking. The spin-transfer torque (STT), by itself, does not lead to different detections. Instead, the cause of the symmetry breaking is the radial Oersted field [i.e. Oersted field torque (OFT)] created by the input RF current. In fact, the simulations allow to individually study the vortex response to each excitation mechanism, so that,
     (a) when only the STT is considered, the voltage spectrum is the same for both chiralities and can be easily fitted by a peak function combining both Lorentzian and anti-Lorentzian components, as expected from the literature [137];
     (b) when only the OFT is considered, two perfectly symmetric lineshapes (in relation with the frequency domain) are obtained for the voltage spectrum at distinct chiralities. Still, the voltage spectra show an uncommon lineshape that cannot be easily fitted, which is attributed to the dependence of the OFT on the vortex core displacement.
   - Both simulations and experiment demonstrate that a displaced vortex core is mandatory for symmetry breaking. If the core is located at the center of the free layer, the radial Oersted field cannot excite the vortex fundamental mode. The increase of the vortex core

displacement is followed by a competition between the STT (that counteracts the symmetry breaking and shows no significant variation with the displacement) and the OFT (that favours the symmetry breaking and tends to increase with the displacement).

- Based on these rectification capabilities, it is proposed to use such a rectifier as a binary non-volatile synapse to be integrated in artificial neural networks. The synapse is characterized by two weights (W^+ and W^-) associated with distinct vortex chiralities that are stable at remanence and rectify differently (V^+ and V^-) for a fixed frequency of the input RF signal, i.e. $\mathrm{V}^+ = \mathrm{W}^+\mathrm{J}_{\mathrm{RF}}$ and $\mathrm{V}^- = \mathrm{W}^-\mathrm{J}_{\mathrm{RF}}$, being J_{RF} the RF current density of the input signal.

2. The second experimental study based on the rectification measurements shows that the polycrystalline structure of the free layer plays an important role in the static and dynamic properties of the STVO. The following conclusions can be extracted:

   - The static measurements indicate that the vortex core does not move smoothly as a function of the in-plane magnetic field. Instead, its behaviour is characterized by a set of pinning-unpinning phenomena as it moves through the magnetic medium. This conclusion is taken from R-H transfer curves performed in the vortex nucleation field range, where the STVO resistance shows a step-like field dependence. This behaviour is linked with the polycrystalline structure of the free layer and confirmed by a qualitative comparison with a simulated magnetic polycrystalline nanodisk.
   - Due to the pinning sites induced by the polycrystalline structure, the characteristics of the vortex gyrotropic mode (i.e. amplitude and frequency) depend on the power of the RF input signal (P_{RF}). Thus, it is possible to define a threshold power (typically, $\mathrm{P}_{\mathrm{th}} \sim 10\,\mu\mathrm{W}$) to distinguish two different regimes:
     (a) For $\mathrm{P}_{\mathrm{RF}} < \mathrm{P}_{\mathrm{th}}$, the vortex core is easily "trapped" by a short-range energy minimum created by a specific pinning site of the polycrystalline landscape. This setpoint restricts the vortex core dynamics to a local mode, characterized by a lower amplitude ($\sim 1\,\mu\mathrm{V}$) and a larger frequency ($\sim 1\,\mathrm{GHz}$).
     (b) For $\mathrm{P}_{\mathrm{RF}} > \mathrm{P}_{\mathrm{th}}$, the vortex core can overcome the short-range energy well, making it possible to oscillate at its collective mode, characterized by a larger amplitude ($\sim 1\,\mathrm{mV}$) and a lower frequency ($\sim 100\,\mathrm{MHz}$).
   - There is not a general connection between P_{th} and the static measurements, suggesting that the mapping of the pinning sites shows limitations for a full understanding of the phenomenon.

3. The synchronization of STVOs is studied in a new and flexible design, allowing the dipolar coupling between oscillators while having a simultaneous access to the individual dynamics of each one. The experimental measurements performed in this new device geometry allow to draw the following results and conclusions:

   - A successful synchronization via magneto-dipolar coupling is achieved for a pair of STVOs with an edge-to-edge distance of 100 nm. Experimentally, the synchronized state is demonstrated with both frequency (i.e. spectrum analyser) and time (i.e. oscilloscope) domain

analyses. The latter proved to be more accurate than a frequency domain analysis in defining the range at which a stable synchronization is achieved.

- Although sharing the bottom contact, due to their small emission (i.e. an output power in the $\sim 10\,\mathrm{nW}$ range, combined with a linewidth in the $\sim 1\,\mathrm{MHz}$ range), the electric coupling does not play a significant role in the synchronization of the STVO pair. This statement is clarified by an unsuccessful attempt to synchronize a pair of STVOs with an edge-to-edge distance of 1 μm, where the magneto-dipolar coupling is minimized.
- The dipolar interaction can tune the second harmonic injection locking (SHIL) between the STVOs and an external RF field applied through the integrated field line. For a weakly coupled STVO pair with an edge-to-edge distance of 400 nm, it is shown that the SHIL of the first oscillator can be controlled by the dynamics of the second.

4. Although not being one of the main objectives of this thesis, an important fabrication process is also presented. In addition to the standard frontside patterning, it comprises the microfabrication of the substrate backside, in order to obtain STVOs on top of 300 nm-thick oxide membranes working as windows for X-ray imaging of the free layer vortex state. The patterning of a successful membrane (i.e. open membrane) implies the possibility for an X-ray incidence of $45° < \theta \leq 90°$, being θ the angle between the X-ray propagation direction and the membrane surface. At the wafer level, the backside process shows a yield of ~ 50 %, meaning that for each die with 150 devices, approximately 75 STVOs are patterned on top of open membranes.

In the future, it is desirable to fabricate STVOs with a larger output power. In our group, it was already understood that an RA product around $10\,\Omega\mu\mathrm{m}^2$ gives the best conditions for an high emission, a large spectral coherence and a low threshold current density (see Ref. [175] and Fig. 1.12). Focusing on the flexible dipolar design presented in chapter 6, a lower threshold current density would be essential to guarantee the synchronization characterization over its full bandwidth - an analysis that is not possible for the devices presented in this thesis (see Fig. 6.13a), due to the voltage breakdown limitations. The improvement of the STVO properties would also be beneficial for the current status of our SHIL experiment, where STVOs with a larger spectral purity would more easily lock with the external RF signal.

Another important upgrade for the current synchronization design is the use of STVOs showing steady-state oscillations at zero perpendicular field. These results are typically observed for STVOs fabricated at INL with a diameter up to 350 nm, an RA $\sim 10\,\Omega\mu\mathrm{m}^2$ and an MTJ stack as illustrated in Fig. 1.12. For larger diameters, a perpendicular field is required. The literature and our simulations (see Fig. 1.13) clarify this behaviour, showing that a non-uniform polariser is the requirement for zero-field oscillations [34, 85, 90–92]. At INL, the group is still trying to understand why the polariser is more suitable to be modified for smaller STVO diameters. Nevertheless, the results are systematic, with zero-field oscillations measured for the majority of STVOs with a diameter up to 350 nm, so that the incorporation of these devices in the synchronization design is a possibility for the future.

For being polycrystalline, the STVO rectifiers fabricated at INL need a larger power of the input RF signal to operate in the collective mode regime, since an additional power is needed to overcome the energy wells created by the pinning sites. So, the removal of the grain structure is expected to decrease the threshold power, that should be only dictated by the system noise. This upgrade would be extremely useful for the proposed artificial synapse in chapter 4, since a lower threshold

power also means less energy for the synaptic operation. From a material point of view, an important contribution to the surface defects is the roughness, accumulated from the MTJ stack deposition, so the incorporation of a surface smoothing process [159,219] is expected to minimize both areal density and strength of the pinning sites in the free layer. Another alternative is to rethink the properties of the free layer. In the end of 2021, a new target of cobalt-iron-silicon-boron (CoFeSiB) was installed in the MTM sputtering tool. The literature shows the possibility to incorporate a CoFeSiB layer in MTJ stacks without loosing its amorphous structure, even after an annealing treatment ($T \sim 300\,^{\circ}C$) typical to optimize the performance of MgO-based MTJs [220–222]. In the near future, MTJ stacks incorporating CoFeSiB in the free layer will be fabricated and characterized, aiming to evaluate how this modification changes the crystalline structure and the vortex behaviour in the free layer.

Bibliography

[1] W. Thomson, "On the Electro-Dynamic Qualities of Metals : Effects of Magnetization on the Electric Conductivity of Nickel and of Iron," *R. Soc.*, vol. 8, pp. 546–550, 1857.

[2] T. R. Mcguire and R. I. Potter, "Anisotropic Magnetoresistance in Ferromagnetic 3D Alloys," *IEEE Trans. Magn.*, vol. 11, pp. 1018–1038, 1975.

[3] M. N. Baibich, J. M. Broto, A. Fert, F. N. Van Dau, F. Petroff, P. Eitenne, G. Creuzet, A. Friederich, and J. Chazelas, "Giant magnetoresistance of (001)Fe/(001)Cr magnetic superlattices," *Phys. Rev. Lett.*, vol. 61, pp. 2472–2475, 1988.

[4] G. Binasch, P. Grünberg, F. Saurenbach, and W. Zinn, "Enhanced magnetoresistance in layered magnetic structures with antiferromagnetic interlayer exchange," *Phys. Rev. B*, vol. 39, pp. 4828–4830, 1989.

[5] B. Dieny, V. S. Speriosu, S. S. P. Parkin, B. A. Gurney, D. R. Wilhoit, and D. Mauri, "Giant magnetoresistance in soft ferromagnetic multilayers," *Phys. Rev. B*, vol. 43, pp. 1297–1300, 1991.

[6] P. N. Lapa, T. Khaire, J. Ding, J. E. Pearson, V. Novosad, A. Hoffmann, and J. S. Jiang, "Spin valve with non-collinear magnetization configuration imprinted by a static magnetic field," *AIP Adv.*, vol. 6, p. 056107, 2016.

[7] W. Rippard, M. Pufall, S. Kaka, S. Russek, and T. Silva, "Direct-Current Induced Dynamics in $\mathrm{Co_{90}Fe_{10}/Ni_{80}Fe_{20}}$ Point Contacts," *Phys. Rev. Lett.*, vol. 92, p. 027201, 2004.

[8] W. F. Egelhoff, T. Ha, R. D. Misra, Y. Kadmon, J. Nir, C. J. Powell, M. D. Stiles, R. D. McMichael, C. L. Lin, J. M. Sivertsen, J. H. Judy, K. Takano, A. E. Berkowitz, T. C. Anthony, and J. A. Brug, "Magnetoresistance values exceeding 21% in symmetric spin valves," *J. Appl. Phys.*, vol. 78, pp. 273–277, 1995.

[9] J. L. Prieto, N. Rouse, N. K. Todd, D. Morecroft, J. Wolfman, J. E. Evetts, and M. G. Blamire, "Integrated magnetic field sensor based on magnetoresistive spin valve structures," *Sensors Actuators, A Phys.*, vol. 94, pp. 64–68, 2001.

[10] J. R. Childress and R. E. Fontana, "Magnetic recording read head sensor technology," *Comptes Rendus Phys.*, vol. 6, pp. 997–1012, 2005.

[11] M. Julliere, "Tunneling between ferromagnetic films," *Phys. Lett. A*, vol. 54, pp. 225–226, 1975.

[12] T. Miyazaki and N. Tezuka, "Giant magnetic tunneling effect in Fe/Al_2O_3/Fe junction," *J. Magn. Magn. Mater.*, vol. 139, pp. 94–97, 1995.

[13] H. X. Wei, Q. H. Qin, M. Ma, R. Sharif, and X. F. Han, "80% tunneling magnetoresistance at room temperature for thin Al-O barrier magnetic tunnel junction with CoFeB as free and reference layers," *J. Appl. Phys.*, vol. 101, p. 09B501, 2007.

[14] W. H. Butler, X.-G. Zhang, T. C. Schulthess, and J. M. MacLaren, "Spin-dependent tunneling conductance of Fe/MgO/Fe sandwiches," *Phys. Rev. B*, vol. 63, p. 054416, 2001.

[15] J. Mathon and A. Umerski, "Theory of tunneling magnetoresistance of an epitaxial Fe/MgO/Fe(001) junction," *Phys. Rev. B*, vol. 63, p. 220403, 2001.

[16] S. S. P. Parkin, C. Kaiser, A. Panchula, P. M. Rice, B. Hughes, M. Samant, and S.-H. Yang, "Giant tunnelling magnetoresistance at room temperature with MgO (100) tunnel barriers," *Nat. Mater.*, vol. 3, pp. 862–867, 2004.

[17] S. Yuasa, T. Nagahama, A. Fukushima, Y. Suzuki, and K. Ando, "Giant room-temperature magnetoresistance in single-crystal Fe/MgO/Fe magnetic tunnel junctions," *Nat. Mater.*, vol. 3, pp. 868–871, 2004.

[18] D. D. Djayaprawira, K. Tsunekawa, M. Nagai, H. Maehara, S. Yamagata, N. Watanabe, S. Yuasa, Y. Suzuki, and K. Ando, "230% room-temperature magnetoresistance in CoFeB/MgO/CoFeB magnetic tunnel junctions," *Appl. Phys. Lett.*, vol. 86, p. 092502, 2005.

[19] L. Berger, "Emission of spin waves by a magnetic multilayer traversed by a current," *Phys. Rev. B*, vol. 54, pp. 9353–9358, 1996.

[20] J. Slonczewski, "Current-driven excitation of magnetic multilayers," *J. Magn. Magn. Mater.*, vol. 159, pp. L1–L7, 1996.

[21] M. Tsoi, A. G. Jansen, J. Bass, W. C. Chiang, M. Seck, V. Tsoi, and P. Wyder, "Excitation of a magnetic multilayer by an electric current," *Phys. Rev. Lett.*, vol. 80, pp. 4281–4284, 1998.

[22] S. I. Kiselev, J. C. Sankey, I. N. Krivorotov, N. C. Emley, R. J. Schoelkopf, R. a. Buhrman, and D. C. Ralph, "Microwave oscillations of a nanomagnet driven by a spin-polarized current," *Nature*, vol. 425, pp. 380–383, 2003.

[23] E. B. Myers, D. C. Ralph, J. A. Katine, R. N. Louie, and R. A. Buhrman, "Current-induced switching of domains in magnetic multilayer devices," *Science (80-.).*, vol. 285, pp. 867–870, 1999.

[24] J. A. Katine, F. J. Albert, R. A. Buhrman, E. B. Myers, and D. C. Ralph, "Current-Driven Magnetization Reversal and Spin-Wave Excitations in Co/Cu/Co Pillars," *Phys. Rev. Lett.*, vol. 84, pp. 3149–3152, 2000.

[25] https://www.everspin.com/spin-transfer-torque-mram-technology. Access: 16-11-2021.

[26] S. Bhatti, R. Sbiaa, A. Hirohata, H. Ohno, S. Fukami, and S. N. Piramanayagam, "Spintronics based random access memory: a review," *Mater. Today*, vol. 20, pp. 530–548, 2017.

[27] Z. Zeng, G. Finocchio, and H. Jiang, "Spin transfer nano-oscillators," *Nanoscale*, vol. 5, pp. 2219–2231, 2013.

[28] P. N. Skirdkov and K. A. Zvezdin, "Spin-Torque Diodes: From Fundamental Research to Applications," *Ann. Phys.*, vol. 1900460, pp. 1–11, 2020.

[29] A. Dussaux, B. Georges, J. Grollier, V. Cros, A. V. Khvalkovskiy, A. Fukushima, M. Konoto, H. Kubota, K. Yakushiji, S. Yuasa, K. A. Zvezdin, K. Ando, and A. Fert, "Large microwave generation from current-driven magnetic vortex oscillators in magnetic tunnel junctions," *Nat. Commun.*, vol. 1, p. 8, 2010.

[30] S. Tsunegi, H. Kubota, K. Yakushiji, M. Konoto, S. Tamaru, A. Fukushima, H. Arai, H. Imamura, E. Grimaldi, R. Lebrun, J. Grollier, V. Cros, and S. Yuasa, "High emission power and Q factor in spin torque vortex oscillator consisting of FeB free layer," *Appl. Phys. Express*, vol. 7, p. 063009, 2014.

[31] R. Lebrun, S. Tsunegi, P. Bortolotti, H. Kubota, A. S. Jenkins, M. Romera, K. Yakushiji, A. Fukushima, J. Grollier, S. Yuasa, and V. Cros, "Mutual synchronization of spin torque nano-oscillators through a long-range and tunable electrical coupling scheme," *Nat. Commun.*, vol. 8, p. 15825, 2017.

[32] S. Tsunegi, T. Taniguchi, R. Lebrun, K. Yakushiji, V. Cros, J. Grollier, A. Fukushima, S. Yuasa, and H. Kubota, "Scaling up electrically synchronized spin torque oscillator networks," *Sci. Rep.*, vol. 8, p. 13475, 2018.

[33] S. Tsunegi, K. Yakushiji, A. Fukushima, S. Yuasa, and H. Kubota, "Microwave emission power exceeding 10 μW in spin torque vortex oscillator," *Appl. Phys. Lett.*, vol. 109, p. 252402, 2016.

[34] N. Locatelli, V. V. Naletov, J. Grollier, G. De Loubens, V. Cros, C. Deranlot, C. Ulysse, G. Faini, O. Klein, and A. Fert, "Dynamics of two coupled vortices in a spin valve nanopillar excited by spin transfer torque," *Appl. Phys. Lett.*, vol. 98, p. 062501, 2011.

[35] N. Locatelli, V. Cros, and J. Grollier, "Spin-torque building blocks," *Nat. Mater.*, vol. 13, pp. 11–20, 2013.

[36] A. A. Tulapurkar, Y. Suzuki, A. Fukushima, H. Kubota, H. Maehara, K. Tsunekawa, D. D. Djayaprawira, N. Watanabe, and S. Yuasa, "Spin-torque diode effect in magnetic tunnel junctions.," *Nature*, vol. 438, pp. 339–342, 2005.

[37] S. Miwa, S. Ishibashi, H. Tomita, T. Nozaki, E. Tamura, K. Ando, N. Mizuochi, T. Saruya, H. Kubota, K. Yakushiji, T. Taniguchi, H. Imamura, A. Fukushima, S. Yuasa, and Y. Suzuki, "Highly sensitive nanoscale spin-torque diode," *Nat. Mater.*, vol. 13, pp. 50–56, 2014.

[38] B. Fang, M. Carpentieri, X. Hao, H. Jiang, J. A. Katine, I. N. Krivorotov, B. Ocker, J. Langer, K. L. Wang, B. Zhang, B. Azzerboni, P. K. Amiri, G. Finocchio, and Z. Zeng, "Giant spin-torque diode sensitivity in the absence of bias magnetic field," *Nat. Commun.*, vol. 7, p. 11259, 2016.

[39] L. Zhang, B. Fang, J. Cai, M. Carpentieri, V. Puliafito, F. Garescì, P. K. Amiri, G. Finocchio, and Z. Zeng, "Ultrahigh detection sensitivity exceeding 105 V/W in spin-torque diode," *Appl. Phys. Lett.*, vol. 113, p. 102401, 2018.

[40] A. S. Jenkins, R. Lebrun, E. Grimaldi, S. Tsunegi, P. Bortolotti, H. Kubota, K. Yakushiji, A. Fukushima, G. De Loubens, O. Klein, S. Yuasa, and V. Cros, "Spin-torque resonant expulsion of the vortex core for an efficient radiofrequency detection scheme," *Nat. Nanotechnol.*, vol. 11, pp. 360–364, 2016.

[41] S. Tsunegi, T. Taniguchi, K. Yakushiji, A. Fukushima, S. Yuasa, and H. Kubota, "Achievement of high diode sensitivity via spin torque-induced resonant expulsion in vortex magnetic tunnel junction," *Appl. Phys. Express*, vol. 11, p. 053001, 2018.

[42] J. Grollier, D. Querlioz, K. Y. Camsari, K. Everschor-Sitte, S. Fukami, and M. D. Stiles, "Neuromorphic spintronics," jul 2020.

[43] J. Torrejon, M. Riou, F. A. Araujo, S. Tsunegi, G. Khalsa, D. Querlioz, P. Bortolotti, V. Cros, K. Yakushiji, A. Fukushima, H. Kubota, S. Yuasa, M. D. Stiles, and J. Grollier, "letter Neuromorphic computing with nanoscale spintronic oscillators," *Nat. Publ. Gr.*, vol. 547, pp. 428–431, 2017.

[44] M. Romera, P. Talatchian, S. Tsunegi, F. Araujo, V. Cros, P. Bortolotti, J. Trastoy, K. Yakushiji, A. Fukushima, H. Kubota, S. Yuasa, M. Ernoult, D. Vodenicarevic, T. Hirtzlin, N. Locatelli, D. Querlioz, and J. Grollier, "Vowel recognition with four coupled spin-torque nano-oscillators," *Nature*, vol. 563, pp. 230–234, 2018.

[45] A. Mizrahi, T. Hirtzlin, A. Fukushima, H. Kubota, S. Yuasa, J. Grollier, and D. Querlioz, "Neural-like computing with populations of superparamagnetic basis functions," *Nat. Commun.*, vol. 9, p. 1533, 2018.

[46] N. Leroux, A. Mizrahi, D. Markovic, D. Sanz-Hernandez, J. Trastoy, P. Bortolotti, L. Martins, A. Jenkins, R. Ferreira, and J. Grollier, "Hardware realization of the multiply and accumulate operation on radio-frequency signals with magnetic tunnel junctions," *Neuromorphic Comput. Eng.*, vol. 1, p. 011001, 2021.

[47] L. Martins, A. S. Jenkins, L. S. E. Alvarez, J. Borme, T. Böhnert, J. Ventura, P. P. Freitas, and R. Ferreira, "Non-volatile artificial synapse based on a vortex nano-oscillator," *Sci. Rep.*, vol. 11, p. 16094, 2021.

[48] D. Marković, A. Mizrahi, D. Querlioz, and J. Grollier, "Physics for neuromorphic computing," *Nat. Rev. Phys.*, vol. 2, pp. 499–510, 2020.

[49] S. Yuasa and D. D. Djayaprawira, "Giant tunnel magnetoresistance in magnetic tunnel junctions with a crystalline MgO(001) barrier," *J. Phys. D Appl. Phys.*, vol. 40, pp. R337–R354, 2007.

[50] I. A. Campbell, A. Fert, and R. Pomeroy, "Evidence for two current conduction iron," *Philos. Mag.*, vol. 15, pp. 977–983, 1967.

[51] A. Fert and I. A. Campbell, “Two-current conduction in nickel,” *Phys. Rev. Lett.*, vol. 21, pp. 1190–1192, 1968.

[52] P. M. Tedrow and R. Meservey, “Spin-dependent tunneling into ferromagnetic nickel,” *Phys. Rev. Lett.*, vol. 26, pp. 192–195, 1971.

[53] R. Meservey and P. M. Tedrow, “Spin polarization of tunneling electrons from films of Fe, Co, Ni, and Gd,” *Solid State Commun.*, vol. 11, pp. 333–336, 1972.

[54] J. M. De Teresa, A. Barthelemy, A. Fert, J. P. Contour, F. Montaigne, and P. Seneor, “Role of metal oxide interface in determining the spin polarization of magnetic tunnel junctions,” *Science*, vol. 286, pp. 507–509, 1999.

[55] J. C. Slonczewski, “Conductance and exchange coupling of two ferromagnets separated by a tunneling barrier,” *Phys. Rev. B*, vol. 39, pp. 6995–7002, 1989.

[56] R. A. Serway, C. J. Moses, and C. A. Moyer, *Modern Physics*, ch. 10, p. 358. Thomson Learning, Inc., 2005.

[57] C. Tiusan, F. Greullet, M. Hehn, F. Montaigne, S. Andrieu, and A. Schuhl, “Spin tunnelling phenomena in single-crystal magnetic tunnel junction systems,” *J. Phys. Condens. Matter*, vol. 19, p. 165201, 2007.

[58] C. Kittel, *Introduction to Solid State Physics*, ch. 7, p. 167. John Wiley & Sons, Inc., 2005.

[59] W. H. Butler, “Tunneling magnetoresistance from a symmetry filtering effect,” *Sci. Technol. Adv. Mater.*, vol. 9, p. 014106, 2008.

[60] S. Ikeda, J. Hayakawa, Y. Ashizawa, Y. M. Lee, K. Miura, H. Hasegawa, M. Tsunoda, F. Matsukura, and H. Ohno, “Tunnel magnetoresistance of 604% at 300 K by suppression of Ta diffusion in CoFeB/MgO/CoFeB pseudo-spin-valves annealed at high temperature,” *Appl. Phys. Lett.*, vol. 93, p. 082508, 2008.

[61] *Introduction to magnetic random-access memory*, ch. 2, p. 47. John Wiley & Sons, Inc., 2017.

[62] S. Yuasa, Y. Suzuki, T. Katayama, and K. Ando, “Characterization of growth and crystallization processes in CoFeB/MgO/CoFeB magnetic tunnel junction structure by reflective high-energy electron diffraction,” *Appl. Phys. Lett.*, vol. 87, p. 242503, 2005.

[63] R. Matsumoto, A. Fukushima, T. Nagahama, Y. Suzuki, K. Ando, S. Yuasa, R. Matsumoto, A. Fukushima, T. Nagahama, and Y. Suzuki, “Oscillation of giant tunneling magnetoresistance with respect to tunneling barrier thickness in fully epitaxial Fe/MgO/Fe magnetic tunnel junctions,” vol. 90, p. 252506, 2007.

[64] J. D. Costa, S. Serrano-Guisan, J. Borme, F. L. Deepak, M. Tarequzzaman, E. Paz, J. Ventura, R. Ferreira, and P. P. Freitas, “Impact of MgO Thickness on the Performance of Spin-Transfer Torque Nano-Oscillators,” *IEEE Trans. Magn.*, vol. 51, p. 1401604, 2015.

[65] J. Ventura, J. M. Teixeira, J. P. Araujo, J. B. Sousa, P. Wisniowski, and P. P. Freitas, “Pinholes and temperature-dependent transport properties of MgO magnetic tunnel junctions,” *Phys. Rev. B - Condens. Matter Mater. Phys.*, vol. 78, p. 024403, 2008.

[66] S. Ikeda, K. Miura, H. Yamamoto, K. Mizunuma, H. D. Gan, M. Endo, S. Kanai, J. Hayakawa, F. Matsukura, and H. Ohno, "A perpendicular-anisotropy CoFeB-MgO magnetic tunnel junction," *Nat. Mater.*, vol. 9, pp. 721–724, 2010.

[67] A. V. Nazarov, H. M. Olson, H. Cho, K. Nikolaev, Z. Gao, S. Stokes, B. Bharat, A. V. Nazarov, H. M. Olson, H. Cho, K. Nikolaev, and Z. Gao, "Spin transfer stimulated microwave emission in MgO magnetic tunnel junctions," *Appl. Phys. Lett.*, vol. 88, p. 162504, 2006.

[68] M. D. Ralph, D. C. and Stiles, "Spin Transfer Torques," *J. Magn. Magn. Mater.*, vol. 320, pp. 1190–1216, 2008.

[69] *Introduction to magnetic random-access memory*, ch. 3, p. 65. John Wiley & Sons, Inc., 2017.

[70] Z. Li and S. Zhang, "Magnetization dynamics with a spin-transfer torque," *Phys. Rev. B - Condens. Matter Mater. Phys.*, vol. 68, p. 024404, 2003.

[71] J. C. Sankey, Y.-T. Cui, J. Z. Sun, J. C. Slonczewski, R. A. Buhrman, and D. C. Ralph, "Measurement of the spin-transfer-torque vector in magnetic tunnel junctions," *Nat. Phys.*, vol. 4, pp. 67–71, 2007.

[72] A. M. Deac, A. Fukushima, H. Kubota, H. Maehara, Y. Suzuki, S. Yuasa, Y. Nagamine, K. Tsunekawa, D. D. Djayaprawira, and N. Watanabe, "Bias-driven high-power microwave emission from MgO-based tunnel magnetoresistance devices," *Nat. Phys.*, vol. 4, pp. 1–7, 2008.

[73] A. Chanthbouala, R. Matsumoto, J. Grollier, V. Cros, A. Anane, A. Fert, A. V. Khvalkovskiy, K. A. Zvezdin, K. Nishimura, Y. Nagamine, H. Maehara, K. Tsunekawa, A. Fukushima, and S. Yuasa, "Vertical-current-induced domain-wall motion in MgO-based magnetic tunnel junctions with low current densities," *Nat. Phys.*, vol. 7, pp. 626–630, 2011.

[74] A. S. Jenkins, L. Martins, L. Benetti, L. S. E. Alvarez, P. P. Freitas, and R. Ferreira, "Phase variation in the locked state of mutually synchronized spin torque nano-oscillators," *Appl. Phys. Lett.*, vol. 118, p. 172406, 2021.

[75] K. Y. Guslienko, "Magnetic Vortex State Stability, Reversal and Dynamics in Restricted Geometries," *J. Nanosci. Nanotechnol.*, vol. 8, pp. 2745–2760, 2008.

[76] D. Costa, *Spin-Transfer-Torque Nano-Oscillators: Fabrication, Characterization and Dynamics*. PhD thesis, FCUP, 2017.

[77] T. Shinjo, "Magnetic Vortex Core Observation in Circular Dots of Permalloy," *Science*, vol. 289, pp. 930–932, 2000.

[78] R. P. Cowburn, D. K. Koltsov, A. O. Adeyeye, M. E. Welland, and D. M. Tricker, "Single-Domain Circular Nanomagnets," *Phys. Rev. Lett.*, vol. 83, pp. 1042–1045, 1999.

[79] K. Y. Guslienko, V. Novosad, Y. Otani, H. Shima, and K. Fukamichi, "Field evolution of magnetic vortex state in ferromagnetic disks," *Appl. Phys. Lett.*, vol. 78, p. 3848, 2001.

[80] J. Raabe, R. Pulwey, R. Sattler, T. Schweinbock, J. Zweck, and D. Weiss, "Magnetization pattern of ferromagnetic nanodisks," *J. Appl. Phys.*, vol. 88, pp. 4437–4439, 2000.

[81] K. L. Metlov and K. Y. Guslienko, "Stability of magnetic vortex in soft magnetic nano-sized circular cylinder," *J. Magn. Magn. Mater.*, vol. 242, pp. 1015–1017, 2002.

[82] J. Coey, *Magnetism and magnetic materials*, ch. 7, p. 236. Cambridge University Press, 2010.

[83] A. Dussaux, A. V. Khvalkovskiy, P. Bortolotti, J. Grollier, V. Cros, and A. Fert, "Field dependence of spin-transfer-induced vortex dynamics in the nonlinear regime," *Phys. Rev. B - Condens. Matter Mater. Phys.*, vol. 86, p. 014402, 2012.

[84] K. Y. Guslienko, V. Novosad, Y. Otani, H. Shima, and K. Fukamichi, "Magnetization reversal due to vortex nucleation, displacement, and annihilation in submicron ferromagnetic dot arrays," *Phys. Rev. B - Condens. Matter Mater. Phys.*, vol. 65, p. 024414, 2002.

[85] V. S. Pribiag, I. N. Krivorotov, G. D. Fuchs, P. M. Braganca, O. Ozatay, J. C. Sankey, D. C. Ralph, and R. A. Buhrman, "Magnetic vortex oscillator driven by dc spin-polarized current," *Nat. Phys.*, vol. 3, pp. 498–502, 2007.

[86] A. S. Jenkins, L. San Emeterio Alvarez, R. Dutra, R. L. Sommer, P. P. Freitas, and R. Ferreira, "Wideband High-Resolution Frequency-to-Resistance Converter Based on Nonhomogeneous Magnetic-State Transitions," *Phys. Rev. Appl.*, vol. 13, p. 014046, 2020.

[87] A. A. Thiele, "Steady-state motion of magnetic domains," *Phys. Rev. Lett.*, vol. 30, pp. 230–233, 1973.

[88] F. A. Araujo, C. Chopin, and S. de Wergifosse, "Ampere-Oersted Field Splitting of the Nonlinear Spin-torque Vortex Oscillator Dynamics," (In Press).

[89] A. V. Khvalkovskiy, J. Grollier, N. Locatelli, K. A. Zvezdin, and V. Cros, "Nonuniformity of a planar polarizer for spin-transfer-induced vortex oscillations at zero field," *Appl. Phys. Lett.*, vol. 96, p. 212507, 2010.

[90] M. R. Pufall, W. H. Rippard, M. L. Schneider, and S. E. Russek, "Low-field current-hysteretic oscillations in spin-transfer nanocontacts," *Phys. Rev. B - Condens. Matter Mater. Phys.*, vol. 75, p. 140404(R), 2007.

[91] V. S. Pribiag, G. Finocchio, B. J. Williams, D. C. Ralph, and R. A. Buhrman, "Long-timescale fluctuations in zero-field magnetic vortex oscillations driven by dc spin-polarized current," *Phys. Rev. B - Condens. Matter Mater. Phys.*, vol. 80, p. 180411(R), 2009.

[92] T. Devolder, J. V. Kim, P. Crozat, C. Chappert, M. Manfrini, M. Van Kampen, W. Van Roy, L. Lagae, G. Hrkac, and T. Schrefl, "Time-resolved zero field vortex oscillations in point contacts," *Appl. Phys. Lett.*, vol. 95, p. 012507, 2009.

[93] M. J. Donahue and D. G. Porter, "OOMMF user's guide, version 1.0," *Interag. Rep. NISTIR 6376*, 1999.

[94] M. Ohring, *Materials Science of Thin Films*, ch. 5, p. 216. Academic Press, 2002.

[95] E. Paz, R. Ferreira, P. P. Freitas, M. Tarequzzaman, T. Bohnert, A. S. Jenkins, J. Borme, E. Paz, R. Ferreira, and P. P. Freitas, "Influence of MgO Tunnel Barrier Thickness on the Output Power of Three-Terminal Spin Hall Nano-Oscillators," *IEEE Trans. Magn.*, pp. 1–4, 2018.

[96] K. L. Choy, "Chemical vapour deposition of coatings," *Prog. Mater. Sci.*, vol. 48, pp. 57–170, 2003.

[97] J. S. Sovey, "A 30-cm diameter argon ion source," *Twelfth Int. Electr. Propuls. Conf.*, 1976.

[98] R. Ferreira, *Ion Beam Deposited Magnetic Spin Tunnel Junctions targeting HDD Read Heads, Non-volatile Memories and Magnetic Field Sensor Applications*. PhD thesis, IST, 2008.

[99] "AZ 1500 Photoresist." https://microfab.ku.edu/sites/microfab.ku.edu/files/docs/Datasheets/AZ1500SeriesDataPackage.pdf. Accessed: 03-09-2018.

[100] H. J. Levinson, *Principles of Lithography*, ch. 2, p. 36. SPIE, 2010.

[101] H. J. Levinson, *Principles of Lithography*, ch. 2, p. 16. SPIE, 2010.

[102] A. A. Tseng, K. Chen, C. D. Chen, and K. J. Ma, "Electron beam lithography in nanoscale fabrication: Recent development," *IEEE Trans. Electron. Packag. Manuf.*, vol. 26, pp. 141–149, 2003.

[103] S. Y. Jang, C. Y. You, S. H. Lim, and S. R. Lee, "Annealing effects on the magnetic dead layer and saturation magnetization in unit structures relevant to a synthetic ferrimagnetic free structure," *J. Appl. Phys.*, vol. 109, p. 013901, 2011.

[104] D. C. Worledge and P. L. Trouilloud, "Magnetoresistance measurement of unpatterned magnetic tunnel junction wafers by current-in-plane tunneling," *Appl. Phys. Lett.*, vol. 83, pp. 84–86, 2003.

[105] Y. Fang, J. Persson, C. Zha, J. Willman, C. W. Miller, and J. Åkerman, "Utility of reactively sputtered $\mathrm{CuN_x}$ films in spintronics devices," *J. Appl. Phys.*, vol. 111, p. 073912, 2012.

[106] Y. Lecun, Y. Bengio, and G. Hinton, "Deep learning," *Nature*, vol. 521, pp. 436–444, 2015.

[107] A. Krizhevsky, I. Sutskever, and G. Hinton, "ImageNet classification with deep convolutional neural networks," *Proc. Adv. Neural Inf. Process. Syst.*, vol. 25, pp. 1090–1098, 2012.

[108] L. M. Q. D. Santana, R. M. Santos, L. N. Matos, and H. T. Macedo, "Deep Neural Networks for Acoustic Modeling in the Presence of Noise," *IEEE Lat. Am. Trans.*, vol. 16, pp. 918–925, 2018.

[109] H. Y. Xiong, B. Alipanahi, L. J. Lee, H. Bretschneider, D. Merico, R. K. Yuen, Y. Hua, S. Gueroussov, H. S. Najafabadi, T. R. Hughes, Q. Morris, Y. Barash, A. R. Krainer, N. Jojic, S. W. Scherer, B. J. Blencowe, and B. J. Frey, "The human splicing code reveals new insights into the genetic determinants of disease," *Science*, vol. 347, p. 1254806, 2015.

[110] X. Glorot, A. Bordes, and Y. Bengio, "Deep Sparse Rectifier Neural Networks," *Proc. 14th Int. Conf. Artif. Intell. Stat.*, pp. 315–323, 2011.

[111] D. E. Rumelhart, G. E. Hinton, and R. J. Williams, "Learning representations by back-propagating errors," *Nature*, vol. 323, pp. 533–536, 1986.

[112] "Big data needs a hardware revolution," *Nature*, vol. 554, pp. 145–146, 2018.

[113] J. Devlin, M. W. Chang, K. Lee, and K. Toutanova, "BERT: Pre-training of deep bidirectional transformers for language understanding," *Conf. North Am. Chapter Assoc. Comput. Linguist. Hum. Lang. Technol. - Proc. Conf.*, pp. 4171–4186, 2019.

[114] J. Feldmann, N. Youngblood, C. D. Wright, H. Bhaskaran, and W. H. Pernice, "All-optical spiking neurosynaptic networks with self-learning capabilities," *Nature*, vol. 569, pp. 208–214, 2019.

[115] P. A. Merolla, J. V. Arthur, R. Alvarez-icaza, A. S. Cassidy, J. Sawada, F. Akopyan, B. L. Jackson, N. Imam, C. Guo, Y. Nakamura, B. Brezzo, I. Vo, S. K. Esser, R. Appuswamy, B. Taba, A. Amir, M. D. Flickner, W. P. Risk, R. Manohar, and D. S. Modha, "Amillion spiking-neuron integrated circuit with a scalable communication network and interface," *Science*, vol. 345, pp. 668–673, 2014.

[116] D. Ielmini and H. S. Wong, "In-memory computing with resistive switching devices," *Nat. Electron.*, vol. 1, pp. 333–343, 2018.

[117] R. Mochida, K. Kouno, Y. Hayata, M. Nakayama, T. Ono, H. Suwa, R. Yasuhara, K. Katayama, T. Mikawa, and Y. Gohou, "A 4M synapses integrated analog ReRAM based 66.5 TOPS/W neural-network processor with cell current controlled writing and flexible network architecture," *Dig. Tech. Pap. - Symp. VLSI Technol.*, pp. 175–176, 2018.

[118] M. Ishii, U. Shin, K. Hosokawa, M. Brightsky, W. Haensch, S. Kim, S. Lewis, A. Okazaki, J. Okazawa, M. Ito, M. Rasch, W. Kim, and A. Nomura, "On-Chip Trainable 1.4M 6T2R PCM Synaptic Array with 1.6K Stochastic LIF Neurons for Spiking RBM," *Tech. Dig. - Int. Electron Devices Meet.*, pp. 310–313, 2019.

[119] Q. Liu, B. Gao, P. Yao, D. Wu, J. Chen, Y. Pang, W. Zhang, Y. Liao, C.-x. Xue, W.-h. Chen, J. Tang, Y. Wang, M.-f. Chang, H. Qian, and H. Wu, "Compute-In-Memory Chip with Fully Parallel MAC Computing," *2020 IEEE Int. Solid- State Circuits Conf.*, pp. 500–502, 2020.

[120] J. Grollier, D. Querlioz, and M. D. Stiles, "Spintronic nanodevices for bioinspired computing," *Proc. IEEE*, vol. 104, pp. 2024–2039, 2016.

[121] J. Cai, L. Zhang, B. Fang, W. Lv, B. Zhang, G. Finocchio, R. Xiong, S. Liang, and Z. Zeng, "Sparse neuromorphic computing based on spin-torque diodes," *Appl. Phys. Lett.*, vol. 114, p. 192402, 2019.

[122] M. Zahedinejad, A. A. Awad, S. Muralidhar, R. Khymyn, H. Fulara, H. Mazraati, M. Dvornik, and J. Åkerman, "Two-dimensional mutually synchronized spin Hall nano-oscillator arrays for neuromorphic computing," *Nat. Nanotechnol.*, vol. 15, pp. 47–52, 2020.

[123] S. Tsunegi, T. Taniguchi, K. Nakajima, S. Miwa, K. Yakushiji, A. Fukushima, S. Yuasa, and H. Kubota, "Physical reservoir computing based on spin torque oscillator with forced synchronization," *Appl. Phys. Lett.*, vol. 114, p. 164101, 2019.

[124] D. Marković, N. Leroux, M. Riou, F. Abreu Araujo, J. Torrejon, D. Querlioz, A. Fukushima, S. Yuasa, J. Trastoy, P. Bortolotti, and J. Grollier, "Reservoir computing with the frequency, phase, and amplitude of spin-torque nano-oscillators," *Appl. Phys. Lett.*, vol. 114, p. 012409, 2019.

[125] N. Leroux, D. Marković, E. Martin, T. Petrisor, D. Querlioz, A. Mizrahi, and J. Grollier, "Radio-frequency multiply-and-accumulate operations with spintronic synapses," *Phys. Rev. Appl.*, vol. 15, p. 034067, 2021.

[126] M. Zahedinejad, H. Fulara, R. Khymyn, A. Houshang, M. Dvornik, S. Fukami, S. Kanai, H. Ohno, and J. Åkerman, "Memristive control of mutual spin Hall nano-oscillator synchronization for neuromorphic computing," *Nat. Mater.*, vol. 21, pp. 81–87, 2022.

[127] W. H. Rippard, M. R. Pufall, S. Kaka, T. J. Silva, S. E. Russek, and J. A. Katine, "Injection locking and phase control of spin transfer nano-oscillators," *Phys. Rev. Lett.*, vol. 95, p. 067203, 2005.

[128] A. Dussaux, A. V. Khvalkovskiy, J. Grollier, V. Cros, A. Fukushima, M. Konoto, H. Kubota, K. Yakushiji, S. Yuasa, K. Ando, and A. Fert, "Phase locking of vortex based spin transfer oscillators to a microwave current," *Appl. Phys. Lett.*, vol. 98, p. 132506, 2011.

[129] B. Fang, M. Carpentieri, S. Louis, V. Tiberkevich, A. Slavin, I. N. Krivorotov, R. Tomasello, A. Giordano, H. Jiang, J. Cai, Y. Fan, Z. Zhang, B. Zhang, J. A. Katine, K. L. Wang, P. K. Amiri, G. Finocchio, and Z. Zeng, "Experimental Demonstration of Spintronic Broadband Microwave Detectors and Their Capability for Powering Nanodevices," *Phys. Rev. Appl.*, vol. 11, p. 014022, 2019.

[130] O. V. Prokopenko, I. N. Krivorotov, E. Bankowski, T. Meitzler, S. Jaroch, V. S. Tiberkevich, and A. N. Slavin, "Spin-torque microwave detector with out-of- plane precessing magnetic moment," *J. Appl. Phys.*, vol. 111, p. 123904, 2012.

[131] M. Tarequzzaman, A. S. Jenkins, T. Böhnert, J. Borme, L. Martins, E. Paz, R. Ferreira, and P. P. Freitas, "Broadband voltage rectifier induced by linear bias dependence in CoFeB/MgO magnetic tunnel junctions," *Appl. Phys. Lett.*, vol. 112, p. 252401, 2018.

[132] A. S. Jenkins, L. S. E. Alvarez, S. Memshawy, P. Bortolotti, V. Cros, P. P. Freitas, and R. Ferreira, "Electrical characterisation of higher order spin wave modes in vortex-based magnetic tunnel junctions," *Commun. Phys.*, vol. 4, p. 107, 2021.

[133] D. Marković, N. Leroux, A. Mizrahi, J. Trastoy, V. Cros, P. Bortolotti, L. Martins, A. Jenkins, R. Ferreira, and J. Grollier, "Detection of the Microwave Emission from a Spin-Torque Oscillator by a Spin Diode," *Phys. Rev. Appl.*, vol. 13, p. 044050, 2020.

[134] A. S. Jenkins, E. Grimaldi, P. Bortolotti, R. Lebrun, H. Kubota, K. Yakushiji, A. Fukushima, G. De Loubens, O. Klein, S. Yuasa, and V. Cros, "Controlling the chirality and polarity of vortices in magnetic tunnel junctions," *Appl. Phys. Lett.*, vol. 105, p. 172403, 2014.

[135] H. Kubota, A. Fukushima, K. Yakushiji, T. Nagahama, S. Yuasa, K. Ando, H. Maehara, Y. Nagamine, K. Tsunekawa, D. D. Djayaprawira, N. Watanabe, and Y. Suzuki, "Quantitative measurement of voltage dependence of spin-transfer torque in MgO-based magnetic tunnel junctions," *Nat. Phys.*, vol. 4, pp. 37–41, 2008.

[136] S.-c. Oh, S.-y. Park, A. Manchon, M. Chshiev, J.-h. Han, H.-w. Lee, J.-e. Lee, K.-t. Nam, Y. Jo, Y.-c. Kong, B. Dieny, and K.-j. Lee, "Bias-voltage dependence of perpendicular spin-transfer torque in asymmetric MgO-based magnetic tunnel junctions," *Nat. Phys.*, vol. 5, pp. 898–902, 2009.

[137] R. Matsumoto, A. Chanthbouala, J. Grollier, V. Cros, A. Fert, A. Fert, K. Nishimura, Y. Nagamine, H. Maehara, K. Tsunekawa, A. Fukushima, and S. Yuasa, "Spin-Torque Diode Measurements of MgO-Based Magnetic Tunnel Junctions with Asymmetric Electrodes," *Appl. Phys. Express*, vol. 4, p. 063001, 2011.

[138] A. Slavin and V. Tiberkevich, "Nonlinear auto-oscillator theory of microwave generation by spin-polarized current," *IEEE Trans. Magn.*, vol. 45, pp. 1875–1918, 2009.

[139] A. D. Kent and D. C. Worledge, "A new spin on magnetic memories," *Nat. Nanotechnol.*, vol. 10, pp. 187–191, 2015.

[140] S. Tsunegi, H. Kubota, S. Tamaru, K. Yakushiji, M. Konoto, A. Fukushima, T. Taniguchi, H. Arai, H. Imamura, and S. Yuasa, "Damping parameter and interfacial perpendicular magnetic anisotropy of FeB nanopillar sandwiched between MgO barrier and cap layers in magnetic tunnel junctions," *Appl. Phys. Express*, vol. 7, p. 033004, 2014.

[141] S. Menshawy, A. S. Jenkins, K. J. Merazzo, L. Vila, R. Ferreira, M. C. Cyrille, U. Ebels, P. Bortolotti, J. Kermorvant, and V. Cros, "Spin transfer driven resonant expulsion of a magnetic vortex core for efficient rf detector," *AIP Adv.*, vol. 7, p. 056608, 2017.

[142] A. Vansteenkiste, J. Leliaert, M. Dvornik, M. Helsen, F. Garcia-Sanchez, and B. Van Waeyenberge, "The design and verification of MuMax3," *AIP Adv.*, vol. 4, p. 107133, 2014.

[143] B. Krüger, A. Drews, M. Bolte, U. Merkt, D. Pfannkuche, and G. Meier, "Harmonic oscillator model for current- and field-driven magnetic vortices," *Phys. Rev. B - Condens. Matter Mater. Phys.*, vol. 76, p. 224426, 2007.

[144] M. Bolte, G. Meier, B. Krüger, A. Drews, R. Eiselt, L. Bocklage, S. Bohlens, T. Tyliszczak, A. Vansteenkiste, B. Van Waeyenberge, K. W. Chou, A. Puzic, and H. Stoll, "Time-resolved X-ray microscopy of spin-torque-induced magnetic vortex gyration," *Phys. Rev. Lett.*, vol. 100, p. 176601, 2008.

[145] J. S. Kim, O. Boulle, S. Verstoep, L. Heyne, J. Rhensius, M. Kläui, L. J. Heyderman, F. Kronast, R. Mattheis, C. Ulysse, and G. Faini, "Current-induced vortex dynamics and pinning potentials probed by homodyne detection," *Phys. Rev. B - Condens. Matter Mater. Phys.*, vol. 82, p. 104427, 2010.

[146] K. Y. Guslienko, B. A. Ivanov, V. Novosad, Y. Otani, H. Shima, and K. Fukamichi, "Eigenfrequencies of vortex state excitations in magnetic submicron-size disks," *J. Appl. Phys.*, vol. 91, p. 8037, 2002.

[147] S. Seal, A. Jeyaranjan, C. J. Neal, U. Kumar, T. S. Sakthivel, and D. C. Sayle, "Engineered defects in cerium oxides: Tuning chemical reactivity for biomedical, environmental, energy applications," *Nanoscale*, vol. 12, pp. 6879–6899, 2020.

[148] S. Onga, T. Yoshii, K. Hatanaka, and Y. Yasuda, "Effects of crystalline defects on electrical properties in silicon films on sapphire," *Jpn. J. Appl. Phys.*, vol. 15, pp. 225–231, 1976.

[149] Y. Nagamine, H. Maehara, K. Tsunekawa, D. D. Djayaprawira, N. Watanabe, S. Yuasa, and K. Ando, "Ultralow resistance-area product of 0.4 $\Omega\mu m^2$ and high magnetoresistance above 50% in CoFeB/MgO/CoFeB magnetic tunnel junctions," *Appl. Phys. Lett.*, vol. 89, p. 162507, 2006.

[150] S. W. Chung, T. Kishi, J. W. Park, M. Yoshikawa, K. S. Park, T. Nagase, K. Sunouchi, H. Kanaya, G. C. Kim, K. Noma, M. S. Lee, A. Yamamoto, K. M. Rho, K. Tsuchida, S. J. Chung, J. Y. Yi, H. S. Kim, Y. S. Chun, H. Oyamatsu, and S. J. Hong, "4Gbit density STT-MRAM using perpendicular MTJ realized with compact cell structure," *2016 IEEE Int. Electron Devices Meet.*, pp. 27.1.1–27.1.4, 2016.

[151] R. L. Compton and P. A. Crowell, "Dynamics of a pinned magnetic vortex," *Phys. Rev. Lett.*, vol. 97, p. 137202, 2006.

[152] R. L. Compton, T. Y. Chen, and P. A. Crowell, "Magnetic vortex dynamics in the presence of pinning," *Phys. Rev. B - Condens. Matter Mater. Phys.*, vol. 81, p. 144412, 2010.

[153] T. Y. Chen, M. J. Erickson, P. A. Crowell, and C. Leighton, "Surface roughness dominated pinning mechanism of magnetic vortices in soft ferromagnetic films," *Phys. Rev. Lett.*, vol. 109, p. 097202, 2012.

[154] T. Uhlig, M. Rahm, C. Dietrich, R. Höllinger, M. Heumann, D. Weiss, and J. Zweck, "Shifting and pinning of a magnetic vortex core in a permalloy dot by a magnetic field," *Phys. Rev. Lett.*, vol. 95, p. 237205, 2005.

[155] J. Leliaert, B. Van De Wiele, A. Vansteenkiste, L. Laurson, G. Durin, L. Dupré, and B. Van Waeyenberge, "Current-driven domain wall mobility in polycrystalline Permalloy nanowires: A numerical study," *J. Appl. Phys.*, vol. 115, p. 233903, 2014.

[156] J. W. Lau, R. D. Memichael, and M. J. Donahue, "Implementation of two-dimensional polycrystalline grains in object oriented micromagnetic framework," *J. Res. Natl. Inst. Stand. Technol.*, vol. 114, pp. 57–67, 2009.

[157] A. J. Eklund, M. Dvornik, F. Qejvanaj, S. Jiang, S. Chung, J. Åkerman, and B. G. Malm, "Impact of intragrain spin wave reflections on nanocontact spin torque oscillators," *Phys. Rev. B*, vol. 103, p. 214433, 2021.

[158] H. Min, R. D. McMichael, M. J. Donahue, J. Miltat, and M. D. Stiles, "Effects of disorder and internal dynamics on vortex wall propagation," *Phys. Rev. Lett.*, vol. 104, p. 217201, 2010.

[159] A. Sugihara, K. Yakushiji, and S. Yuasa, "Surface smoothing process for high-performance MgO-based magnetic tunnel junctions," *Appl. Phys. Express*, vol. 12, p. 023002, 2019.

[160] P. Villard, U. Ebels, D. Houssameddine, J. Katine, D. Mauri, B. Delaet, P. Vincent, M. C. Cyrille, B. Viala, J. P. Michel, J. Prouvée, and F. Badets, "A GHz spintronic-based RF oscillator," *IEEE J. Solid-State Circuits*, vol. 45, pp. 214–223, 2010.

[161] E. Grimaldi, A. Dussaux, P. Bortolotti, J. Grollier, G. Pillet, A. Fukushima, H. Kubota, K. Yakushiji, S. Yuasa, and V. Cros, "Response to noise of a vortex based spin transfer nano-oscillator," *Phys. Rev. B*, vol. 89, p. 104404, mar 2014.

[162] A. P. Khanna, "State of the art in microwave VCOs," *Microw. J.*, vol. 58, no. 5, pp. 22–42, 2015.

[163] http://ntlab.com/IP/eng/Hard/Analog_Mixed/VCO/250iHP_VCO_01.pdf. Access: 20-08-2020.

[164] S. Sani, J. Persson, S. Mohseni, Y. Pogoryelov, P. Muduli, A. Eklund, G. Malm, M. Käll, A. Dmitriev, and J. Åkerman, "Mutually synchronized bottom-up multi-nanocontact spin–torque oscillators," *Nat. Commun.*, vol. 4, p. 2731, 2013.

[165] J. V. Kim, V. Tiberkevich, and A. N. Slavin, "Generation linewidth of an auto-oscillator with a nonlinear frequency shift: Spin-torque nano-oscillator," *Phys. Rev. Lett.*, vol. 100, p. 017207, 2008.

[166] J. C. Sankey, I. N. Krivorotov, S. I. Kiselev, P. M. Braganca, N. C. Emley, R. A. Buhrman, and D. C. Ralph, "Mechanisms limiting the coherence time of spontaneous magnetic oscillations driven by dc spin-polarized currents," *Phys. Rev. B*, vol. 72, p. 224427, 2005.

[167] H. Maehara, H. Kubota, Y. Suzuki, T. Seki, K. Nishimura, Y. Nagamine, K. Tsunekawa, A. Fukushima, A. M. Deac, K. Ando, and S. Yuasa, "Large Emission Power over 2μW with High Q Factor Obtained from Nanocontact Magnetic-Tunnel-Junction-Based Spin Torque Oscillator," *Appl. Phys. Express*, vol. 6, p. 113005, 2013.

[168] W. H. Rippard, A. M. Deac, M. R. Pufall, J. M. Shaw, M. W. Keller, S. E. Russek, G. E. W. Bauer, and C. Serpico, "Spin-transfer dynamics in spin valves with out-of-plane magnetized CoNi free layers," *Phys. Rev. B*, vol. 81, p. 014426, 2010.

[169] Z. Zeng, G. Finocchio, B. Zhang, P. Amiri, J. Katine, I. N. Krivorotov, Y. Huai, J. Langer, B. Azzerboni, K. L. Wang, and H. Jiang, "Ultralow-current-density and bias-field-free spin-transfer nano-oscillator," *Sci. Rep.*, vol. 3, p. 1426, 2013.

[170] C. H. Sim, S. Y. H. Lua, T. Liew, and J. Zhu, "Current driven oscillation and switching in Co/Pd perpendicular giant magnetoresistance multilayer," *J. Appl. Phys.*, vol. 109, p. 07C905, 2011.

[171] D. Houssameddine, U. Ebels, B. Rodmacq, I. Firastrau, F. Ponthenier, M. Brunet, C. Thirion, J.-P. Michel, L. Prejbeanu-Buda, M.-C. Cyrille, O. Redon, and B. Dieny, "Spin-torque oscillator using a perpendicular polarizer and a planar free layer," *Nat. Mater.*, vol. 6, pp. 447–453, 2007.

[172] A. Dussaux, E. Grimaldi, B. Rache Salles, A. S. Jenkins, A. V. Khvalkovskiy, P. Bortolotti, J. Grollier, H. Kubota, A. Fukushima, K. Yakushiji, S. Yuasa, V. Cros, and A. Fert, "Large amplitude spin torque vortex oscillations at zero external field using a perpendicular spin polarizer," *Appl. Phys. Lett.*, vol. 105, p. 022404, 2014.

[173] W. H. Rippard, M. R. Pufall, S. Kaka, T. J. Silva, and S. E. Russek, "Current-driven microwave dynamics in magnetic point contacts as a function of applied field angle," *Phys. Rev. B*, vol. 70, p. 100406, 2004.

[174] Z. M. Zeng, P. Upadhyaya, P. K. Amiri, K. H. Cheung, J. A. Katine, and J. Langer, "Enhancement of microwave emission in magnetic tunnel junction oscillators through in-plane field orientation," *Appl. Phys. Lett.*, vol. 99, p. 032503, 2011.

[175] J. D. Costa, S. Serrano-Guisan, B. Lacoste, A. S. Jenkins, T. Böhnert, M. Tarequzzaman, J. Borme, F. L. Deepak, E. Paz, J. Ventura, R. Ferreira, and P. P. Freitas, "High power and low critical current density spin transfer torque nano-oscillators using MgO barriers with intermediate thickness," *Sci. Rep.*, vol. 7, p. 7237, 2017.

[176] J. A. Katine and E. E. Fullerton, "Device implications of spin-transfer torques," *J. Magn. Magn. Mater.*, vol. 320, no. 7, pp. 1217–1226, 2008.

[177] B. T. Chen, S. M. Ieee, R. K. Dumas, M. Ieee, A. Eklund, S. M. Ieee, P. K. Muduli, A. Houshang, S. M. Ieee, A. A. Awad, and M. Ieee, "Spin-Torque and Spin-Hall," 2016.

[178] W. H. Rippard, M. R. Pufall, and S. E. Russek, "Comparison of frequency, linewidth, and output power in measurements of spin-transfer nanocontact oscillators," *Phys. Rev. B*, vol. 74, p. 224409, 2006.

[179] K. V. Thadani, G. Finocchio, Z. P. Li, O. Ozatay, J. C. Sankey, I. N. Krivorotov, Y. T. Cui, R. A. Buhrman, and D. C. Ralph, "Strong linewidth variation for spin-torque nano-oscillators as a function of in-plane magnetic field angle," *Phys. Rev. B*, vol. 78, p. 024409, 2008.

[180] K. Mizushima, T. Nagasawa, K. Kudo, Y. Saito, R. Sato, K. Mizushima, T. Nagasawa, K. Kudo, Y. Saito, and R. Sato, "Decrease of nonlinearity and linewidth narrowing in spin-transfer oscillators under the external field applied near the hard axis Decrease of nonlinearity and linewidth narrowing in spin-transfer oscillators under the external field applied near the hard," vol. 94, p. 152501, 2009.

[181] D. Houssameddine, S. H. Florez, J. A. Katine, J. Michel, U. Ebels, D. Mauri, O. Ozatay, B. Delaet, B. Viala, B. D. Terris, M. Cyrille, D. Houssameddine, S. H. Florez, J. A. Katine, J. Michel, U. Ebels, and D. Mauri, "Spin transfer induced coherent microwave emission with large power from nanoscale MgO tunnel junctions," *Appl. Phys. Lett.*, vol. 93, p. 022505, 2008.

[182] A. Blaquiere, *Nonlinear system analysis*, ch. 9. Academic Press, 1966.

[183] S. Kaka, M. R. Pufall, W. H. Rippard, T. J. Silva, S. E. Russek, and J. A. Katine, "Mutual phase-locking of microwave spin torque nano-oscillators," *Nature*, vol. 437, pp. 389–392, 2005.

[184] F. B. Mancoff, N. D. Rizzo, B. N. Engel, and S. Tehrani, "Phase-locking in double-point-contact spin-transfer devices," *Nature*, vol. 437, pp. 393–395, 2005.

[185] N. Locatelli, A. Hamadeh, F. Abreu Araujo, A. D. Belanovsky, P. N. Skirdkov, R. Lebrun, V. V. Naletov, K. A. Zvezdin, M. Muñoz, J. Grollier, O. Klein, V. Cros, and G. de Loubens, "Efficient Synchronization of Dipolarly Coupled Vortex-Based Spin Transfer Nano-Oscillators," *Sci. Rep.*, vol. 5, p. 17039, 2015.

[186] H.-C. Chang, X. Cao, U. K. Mishra, and R. A. York, "Phase noise in coupled oscillators: theory and experiment," *IEEE Trans. Microw. Theory Tech.*, vol. 45, pp. 604–615, 1997.

[187] J. Grollier, V. Cros, and A. Fert, "Synchronization of spin-transfer oscillators driven by stimulated microwave currents," *Phys. Rev. B*, vol. 73, p. 060409, 2006.

[188] A. Houshang, E. Iacocca, P. Dürrenfeld, S. R. Sani, J. Åkerman, and R. K. Dumas, "Spin-wave-beam driven synchronization of nanocontact spin-torque oscillators," *Nat. Nanotechnol.*, vol. 11, pp. 280–286, 2015.

[189] A. Ruotolo, V. Cros, B. Georges, A. Dussaux, J. Grollier, C. Deranlot, R. Guillemet, K. Bouzehouane, S. Fusil, and A. Fert, "Phase-locking of magnetic vortices mediated by antivortices," *Nat. Nanotechnol.*, vol. 4, pp. 528–532, 2009.

[190] Y. Li, X. De Milly, O. Klein, V. Cros, J. Grollier, and G. De Loubens, "Selective control of vortex polarities by microwave field in two robustly synchronized spin-torque nano-oscillators," *Appl. Phys. Lett.*, vol. 112, p. 022405, 2018.

[191] G. De Loubens, A. Riegler, B. Pigeau, F. Lochner, F. Boust, K. Y. Guslienko, H. Hurdequint, L. W. Molenkamp, G. Schmidt, A. N. Slavin, V. S. Tiberkevich, N. Vukadinovic, and O. Klein, "Bistability of vortex core dynamics in a single perpendicularly magnetized nanodisk," *Phys. Rev. Lett.*, vol. 102, p. 177602, 2009.

[192] R. Sharma, R. Mishra, T. Ngo, Y. X. Guo, S. Fukami, H. Sato, H. Ohno, and H. Yang, "Electrically connected spin-torque oscillators array for 2.4 GHz WiFi band transmission and energy harvesting," *Nat. Commun.*, vol. 12, p. 2924, 2021.

[193] D. I. Albertsson, M. Zahedinejad, A. Houshang, R. Khymyn, J. Åkerman, and A. Rusu, "Ultrafast Ising Machines using spin torque nano-oscillators," *Appl. Phys. Lett.*, vol. 118, p. 112404, 2021.

[194] A. Lucas, "Ising formulations of many NP problems," *Front. Phys.*, vol. 2, pp. 1–14, 2014.

[195] P. McMahon, A. Marandi, Y. Haribara, R. Hamerly, C. Langrock, S. Tamate, T. Inagaki, H. Takesue, S. Utsunomiya, K. Aihara, R. Byer, M. Fejer, H. Mabuchi, and Y. Yamamoto, "A fully programmable 100-spin coherent Ising machine with all-to-all connections," *Science*, vol. 354, pp. 614–617, 2016.

[196] J. Chou, S. Bramhavar, S. Ghosh, and W. Herzog, "Analog Coupled Oscillator Based Weighted Ising Machine," *Sci. Rep.*, vol. 9, p. 14786, 2019.

[197] A. N. Slavin and V. S. Tiberkevich, "Theory of mutual phase locking of spin-torque nanosized oscillators," *Phys. Rev. B*, vol. 74, p. 104401, 2006.

[198] B. Picinbono, "On instantaneous amplitude and phase of signals," *IEEE Trans. Signal Process.*, vol. 45, pp. 552–560, 1997.

[199] L. Bianchini, S. Cornelissen, J. V. Kim, T. Devolder, W. Van Roy, L. Lagae, and C. Chappert, "Direct experimental measurement of phase-amplitude coupling in spin torque oscillators," *Appl. Phys. Lett.*, vol. 97, p. 032502, 2010.

[200] M. Quinsat, D. Gusakova, J. F. Sierra, J. P. Michel, D. Houssameddine, B. Delaet, M. C. Cyrille, U. Ebels, B. Dieny, L. D. Buda-Prejbeanu, J. A. Katine, D. Mauri, A. Zeltser, M. Prigent, J. C.

Nallatamby, and R. Sommet, “Amplitude and phase noise of magnetic tunnel junction oscillators,” *Appl. Phys. Lett.*, vol. 97, p. 182507, 2010.

[201] R. Lebrun, A. Jenkins, A. Dussaux, N. Locatelli, S. Tsunegi, E. Grimaldi, H. Kubota, P. Bortolotti, K. Yakushiji, J. Grollier, A. Fukushima, S. Yuasa, and V. Cros, “Understanding of Phase Noise Squeezing under Fractional Synchronization of a Nonlinear Spin Transfer Vortex Oscillator,” *Phys. Rev. Lett.*, vol. 115, p. 017201, 2015.

[202] A. D. Belanovsky, N. Locatelli, P. N. Skirdkov, F. A. Araujo, J. Grollier, K. A. Zvezdin, V. Cros, and A. K. Zvezdin, “Phase locking dynamics of dipolarly coupled vortex-based spin transfer oscillators,” *Phys. Rev. B*, vol. 85, p. 100409, 2012.

[203] F. Abreu Araujo, A. D. Belanovsky, P. N. Skirdkov, K. A. Zvezdin, A. K. Zvezdin, N. Locatelli, R. Lebrun, J. Grollier, V. Cros, G. De Loubens, and O. Klein, “Optimizing magnetodipolar interactions for synchronizing vortex based spin-torque nano-oscillators,” *Phys. Rev. B*, vol. 92, p. 045419, 2015.

[204] A. D. Belanovsky, N. Locatelli, P. N. Skirdkov, F. Abreu Araujo, K. A. Zvezdin, J. Grollier, V. Cros, and A. K. Zvezdin, “Numerical and analytical investigation of the synchronization of dipolarly coupled vortex spin-torque nano-oscillators,” *Appl. Phys. Lett.*, vol. 103, p. 122405, 2013.

[205] H. H. Chen, C. M. Lee, Z. Zhang, Y. Liu, J. C. Wu, L. Horng, and C. R. Chang, “Phase locking of spin-torque nano-oscillator pairs with magnetic dipolar coupling,” *Phys. Rev. B*, vol. 93, p. 224410, 2016.

[206] T. Wang and J. Roychowdhury, “Oscillator-based Ising Machine,” *http://arxiv.org/abs/1709.08102*, 2017.

[207] A. Hamadeh, N. Locatelli, V. V. Naletov, R. Lebrun, G. De Loubens, J. Grollier, O. Klein, and V. Cros, “Perfect and robust phase-locking of a spin transfer vortex nano-oscillator to an external microwave source,” *Appl. Phys. Lett.*, vol. 104, p. 022408, 2014.

[208] M. Romera, P. Talatchian, R. Lebrun, K. J. Merazzo, P. Bortolotti, L. Vila, J. D. Costa, R. Ferreira, P. P. Freitas, M. C. Cyrille, U. Ebels, V. Cros, and J. Grollier, “Enhancing the injection locking range of spin torque oscillators through mutual coupling,” *Appl. Phys. Lett.*, vol. 109, p. 252404, 2016.

[209] A. Wachowiak, J. Wiebe, M. Bode, O. Pietzsch, M. Morgenstern, and R. Wiesendanger, “Direct observation of internal spin structure of magnetic vortex cores,” *Science*, vol. 298, pp. 577–580, 2002.

[210] C. Holl, M. Knol, M. Pratzer, J. Chico, I. L. Fernandes, S. Lounis, and M. Morgenstern, “Probing the pinning strength of magnetic vortex cores with sub-nanometer resolution,” *Nat. Commun.*, vol. 11, p. 2833, 2020.

[211] K. Y. Guslienko, X. F. Han, D. J. Keavney, R. Divan, and S. D. Bader, “Magnetic vortex core dynamics in cylindrical ferromagnetic dots,” *Phys. Rev. Lett.*, vol. 96, p. 067205, 2006.

[212] M. Curcic, B. Van Waeyenberge, A. Vansteenkiste, M. Weigand, V. Sackmann, H. Stoll, M. Fähnle, T. Tyliszczak, G. Woltersdorf, C. H. Back, and G. Schütz, "Polarization selective magnetic vortex dynamics and core reversal in rotating magnetic fields," *Phys. Rev. Lett.*, vol. 101, p. 197204, 2008.

[213] S. Kasai, P. Fischer, M. Y. Im, K. Yamada, Y. Nakatani, K. Kobayashi, H. Kohno, and T. Ono, "Probing the Spin polarization of current by soft X-ray imaging of current-induced magnetic vortex dynamics," *Phys. Rev. Lett.*, vol. 101, p. 237203, 2008.

[214] A. Vansteenkiste, K. W. Chou, M. Weigand, M. Curcic, V. Sackmann, H. Stoll, T. Tyliszczak, G. Woltersdorf, C. H. Back, G. Schütz, and B. Van Waeyenberge, "X-ray imaging of the dynamic magnetic vortex core deformation," *Nat. Phys.*, vol. 5, pp. 332–334, 2009.

[215] X. W. Yu, V. S. Pribiag, Y. Acremann, A. A. Tulapurkar, T. Tyliszczak, K. W. Chou, B. Bräuer, Z. P. Li, O. J. Lee, P. G. Gowtham, D. C. Ralph, R. A. Buhrman, and J. Stöhr, "Images of a spin-torque-driven magnetic nano-oscillator," *Phys. Rev. Lett.*, vol. 106, p. 167202, 2011.

[216] V. Uhlíř, M. Urbánek, L. Hladík, J. Spousta, M. Y. Im, P. Fischer, N. Eibagi, J. J. Kan, E. E. Fullerton, and T. Šikola, "Dynamic switching of the spin circulation in tapered magnetic nanodisks," *Nat. Nanotechnol.*, vol. 8, pp. 341–346, 2013.

[217] G. Schtz, W. Wagner, W. Wilhelm, P. Kienle, R. Zeller, R. Frahm, and G. Materlik, "Absorption of circularly polarized x rays in iron," *Phys. Rev. Lett.*, vol. 58, pp. 737–740, 1987.

[218] https://www.spts.com/resources/tech-insights/intro-to-silicon-DRIE-etching. Access: 08-09-2021.

[219] L. Martins, J. Ventura, R. Ferreira, and P. P. Freitas, "Optimization of the buffer surface of CoFeB/MgO/CoFeB-based magnetic tunnel junctions by ion beam milling," *Appl. Surf. Sci.*, vol. 424, pp. 58–62, 2017.

[220] Y. K. Kim, "Magnetic tunnel junctions comprising amorphous NiFeSiB and CoFeSiB free layers," *J. Magn. Magn. Mater.*, vol. 304, pp. 79–82, 2006.

[221] S. J. Noh, B. S. Chun, Y. K. Kim, and T. Wang, "Effects of Co addition on magneto-transport properties of magnetic tunnel junction consisting of CoFeB or CoFeSiB free layer," *J. Appl. Phys.*, vol. 109, p. 07D346, 2011.

[222] L. Huang, Z. H. Yuan, B. S. Tao, C. H. Wan, P. Guo, Q. T. Zhang, L. Yin, J. F. Feng, T. Nakano, H. Naganuma, H. F. Liu, Y. Yan, and X. F. Han, "Noise suppression and sensitivity manipulation of magnetic tunnel junction sensors with soft magnetic Co70.5Fe4.5Si15B10 layer," *J. Appl. Phys.*, vol. 122, p. 113903, 2017.